



N° d'ordre NNT : xxx

**THESE de DOCTORAT DE L'UNIVERSITE DE LYON**

opérée au sein de

**L'Université Claude Bernard Lyon 1**

**Ecole Doctorale de Lyon**

N° 206

**Spécialité de doctorat : Chimie**

**Discipline : Chimie Industrielle Durable**

Soutenue publiquement le 04/03/2021

par

**M. Medet Zhukush**

---

**Chimie organométallique de surface pour la croissance ALD de films ultra-minces de WS<sub>2</sub> et leurs performances photo(électro)catalytiques**

---

Devant le jury composé de:

*Dr. Francesco DI-RENZO*

CNRS-ICG Montpellier

Rapporteur

*Prof. Hubert RENEVIER*

Université de Grenoble

Rapporteur

*Prof. Michela SIGNORETTO*

Università Ca' Foscari Venezia

Examinator

*Prof. Salvatore ABATE*

Università di Messina

Examinator

*Prof. Giuseppe FORNASARI*

Università di Bologna

Examinator

*Prof. Stéphane DANIELE*

Université Lyon 1

Examinator

*Dr. Elsje Alessandra QUADRELLI*

CNRS-IRCELYON

PhD supervisor

*Prof. Siglinda PERATHONER*

Università di Messina

Co-supervisor

*Dr. Claudio AMPELLI*

Università di Messina

Co-supervisor





Erasmus+

**DOCTORAL THESIS**

---

**Surface Organometallic Chemistry for ALD Growth of Ultra-Thin Films of WS<sub>2</sub> and Their Photo(electro)catalytic Performances**

---

carried at  
**Université Claude Bernard Lyon 1**  
and  
**Università degli Studi di Messina**

**SINCHEM - Sustainable and Industrial Chemistry**  
**Erasmus Mundus - Joint Doctoral Research program**

Ecole Doctorale N° 206  
(Ecole Doctorale de Chimie de Lyon : Chimie, Procédés, Environnement)  
and  
Dottorato di XXXIII ciclo in  
Ingegneria e Chimica dei Materiali e delle Costruzioni

Supervisors  
Dr. Elsje Alessandra QUADRELLI  
and  
Prof.ssa Siglinda PERATHONER

Thesis by  
**Medet ZHUKUSH**  
March 2021

# UNIVERSITE CLAUDE BERNARD - LYON 1

Président de l'Université	M. le Professeur Frédéric FLEURY
Président du Conseil Académique	M. le Professeur Hamda BEN HADID
Vice-président du Conseil d'Administration	M. le Professeur Didier REVEL
Vice-président du Conseil Formation et Vie Universitaire	M. le Professeur Philippe CHEVALIER
Vice-président de la Commission Recherche	M. Fabrice VALLÉE
Directrice Générale des Services	Mme Dominique MARCHAND

## COMPOSANTES SANTE

Faculté de Médecine Lyon Est – Claude Bernard	Directeur : M. le Professeur G.RODE
Faculté de Médecine et de Maïeutique Lyon Sud – Charles Mérieux	Directeur : Mme la Professeure C. BURILLON
Faculté d'Odontologie	Directeur : M. le Professeur D. BOURGEOIS
Institut des Sciences Pharmaceutiques et Biologiques	Directeur : Mme la Professeure C. VINCIGUERRA
Institut des Sciences et Techniques de la Réadaptation	Directeur : M. X. PERROT
Département de formation et Centre de Recherche en Biologie Humaine	Directeur : Mme la Professeure A-M. SCHOTT

## COMPOSANTES ET DEPARTEMENTS DE SCIENCES ET TECHNOLOGIE

Faculté des Sciences et Technologies	Directeur : M. F. DE MARCHI
Département Biologie	Directeur : M. le Professeur F. THEVENARD
Département Chimie Biochimie	Directeur : Mme C. FELIX
Département GEP	Directeur : M. Hassan HAMMOURI
Département Informatique	Directeur : M. le Professeur S. AKKOUCHE
Département Mathématiques	Directeur : M. le Professeur G. TOMANOV
Département Mécanique	Directeur : M. le Professeur H. BEN HADID
Département Physique	Directeur : M. le Professeur J-C PLENET
UFR Sciences et Techniques des Activités Physiques et Sportives	Directeur : M. Y.VANPOULLE
Observatoire des Sciences de l'Univers de Lyon	Directeur : M. B. GUIDERDONI
Polytech Lyon	Directeur : M. le Professeur E.PERRIN
Ecole Supérieure de Chimie Physique Electronique	Directeur : M. G. PIGNAULT
Institut Universitaire de Technologie de Lyon 1	Directeur : M. le Professeur C. VITON
Ecole Supérieure du Professorat et de l'Education	Directeur : M. le Professeur A. MOUGNIOTTE
Institut de Science Financière et d'Assurances	Directeur : M. N. LEBOISNE

*“I’m a great believer in luck, and I find the harder I work the more I have of it.”*

*-Thomas Jefferson*

# Acknowledgments

Although the PhD study requires students to be autonomous and perseverant, this journey was completed by significant support from supervisors, colleagues, administrative staff, friends, and my family. I was lucky to be surrounded by such wonderful people who assisted and steered me through this period.

First of all, I wish to express my sincere gratitude to my supervisor, Dr. Elsjé Alessandra Quadrelli, whose wise guidance and constant inspiration fueled me with steering energy. Whenever I was in a challenging situation, any issue in or out of the laboratory could be solved easily after a conversation with her. Her principles, behavior, superior presentation and planning skills not only motivate me to be a better scientist but also encourage me to train a strong personality. Her professional mentorship will leave an invaluable mark in my future career.

I am grateful to my co-supervisors, Prof. Siglinda Perathoner and Dr. Claudio Ampelli, for their great support during my mobility at the University of Messina. Despite the reconstruction problems of the faculty, I always had the opportunity to conduct my experiments thanks to them. My special thanks go to Dr. Ampelli, who guided me in the laboratory as well as took me to the hospital when I had a health issue. I would also like to mention the important contribution to my thesis by other research team members in Italy. Warm thanks go to Francesco, Daniele, Matteo, and Kaveh for helping me to learn a set of instruments, the Italian language, and sharing cheerful moments.

To be a SINCHEM student also means to challenge administrative obstacles. However, thanks to the excellent planning and strong efforts of Prof. Stefania Albonetti and kind support from Mrs. Emmanuelle Foulhe (CPE, Lyon) and Mrs. Maria Cassella (Unime, Messina), all the difficulties passed seamlessly. I am honored to be a part of the SINCHEM family that allows establishing an international network. I would like to express acknowledgment to the Erasmus Mundus program for

funding this doctoral project and providing an opportunity to extend my network and expertise by attending training schools and conferences every year.

Scientific discussions are an essential part of any research, so was in my doctoral project. I am thankful to Dr. Clément Camp, Dr. Mostafa Taoufik, and Dr. Francesco Di Renzo, who were always happy to share their insightful ideas and motivated me to keep learning more. I must also thank Dr. Kai Szeto, Mr. Laurent Veyre, Mrs. Christine Lucas, Dr. Aimery DeMallmann, and Dr. Nesrine Cherni for their readiness to assist in all characterization and train me whenever it was necessary. Warmest gratitude goes to Dr. Jules Galipaud for conducting the XPS analysis of my samples with strong expertise and permanent enthusiasm to go into more details. I would like to show my gratitude to Dr. Mimoun Aouine from IRCELYON for the environmental HRTEM study, Mr. Ruben Vera from the University of Lyon 1 for the XRD measurements. I wish to recognize the invaluable contribution that you all provided throughout the three years of my PhD study.

I was fortunate to work in the SOMC team among wonderful colleagues who have well contributed to my thesis by supporting me in difficult moments, showing the execution of the classical procedures of an organic chemistry laboratory, sharing their expertise, and giving wise advice. Many thanks must go to my former colleagues Alexis, Marc, Pooja, Ravi, Vittoria, Tapish, Clément, and Valeriia for being my friends and adding joy to my routine days. I wish to pay special regards to my current colleagues, Sebastian, Martin, Isis, Walid, Zijia, Léon, Vincent, Yulan, Isah, and Jessy whose great support is very well appreciated.

My final words of gratitude are dedicated to my family. I express my gratitude to my mom and brother for supporting my decisions and showering me with their love and care. I am exceptionally thankful to my wife, who is always near and helped me to overcome all the challenges.

# Contents

Abbreviations .....	ix
ABSTRACT .....	xi
RESUME SUCCINT .....	xii
RIASSUNTO BREVE .....	xiii
EXTENDED SUMMARY .....	xiv
RÉSUMÉ .....	xxv
RIASSUNTO ESTESO .....	xxxvii
Chapter 1 - GENERAL INTRODUCTION .....	1
1.1 PART 1 Energy conversion devices and the relevance of ALD .....	2
1.1.1. General considerations .....	2
1.1.2. Relevance of ALD .....	3
1.1.3. Interest in WS <sub>2</sub> monolayer and ultrathin deposit .....	5
1.1.4. Growth of WS <sub>2</sub> and other transition metal dichalcogenides (TMD) thin films by Atomic Layer Deposition (ALD) .....	7
1.2 PART 2 SOMC and its connection to ALD .....	15
1.2.1. Molecular level understanding of ALD film growth .....	15
1.2.2. Surface organometallic chemistry and its utility for ALD .....	20
1.2.3. SOMC of tungsten-based catalyst .....	24
1.3 PART 3 Aim and scope of the thesis .....	27
1.3.1. Aim of the present work .....	27
1.3.2. Scope of suitable ALD/CVD molecular precursors for growth of WS <sub>2</sub> and other W-containing phases .....	27

Chapter 2 - ELABORATION of ALD GROWTH of WS <sub>2</sub> USING W <sub>2</sub> (NMe <sub>2</sub> ) <sub>6</sub> and EDT .....	31
2.1 INTRODUCTION .....	32
2.1.1. Use of [W <sub>2</sub> (NMe <sub>2</sub> ) <sub>6</sub> ] as an ALD precursor.....	32
2.1.2. SOMC of [W <sub>2</sub> (NMe <sub>2</sub> ) <sub>6</sub> ] complex on silica .....	33
2.1.3. The goal of this chapter .....	34
2.2 EXPERIMENTAL SECTION.....	35
2.2.1. General procedures.....	35
2.2.2. Synthesis of [W <sub>2</sub> (NMe <sub>2</sub> ) <sub>6</sub> ] .....	35
2.2.3. Reaction of HDMDW with tris(tert-butoxy)silanol .....	36
2.2.4. Reaction of HDMDW with EDT.....	36
2.2.5. ALD-modelling surface reactions using the W <sub>2</sub> (NMe <sub>2</sub> ) <sub>6</sub> and EDT on silica-700 in solution 37	
2.2.6. Characterization instruments .....	43
2.3 RESULTS AND DISCUSSION.....	45
2.3.1. The precursor.....	45
2.3.2. Preliminary study with molecular chemistry.....	48
2.3.3. Modeling ALD via impregnation of W <sub>2</sub> (NMe <sub>2</sub> ) <sub>6</sub> on silica-700 and reaction with EDT 53	
2.4 CONCLUSION.....	67
Chapter 3 - ELABORATION of ALD GROWTH of WS <sub>2</sub> USING W(NMe <sub>2</sub> ) <sub>2</sub> (=N <sup>t</sup> Bu) <sub>2</sub> and EDT	68
3.1 INTRODUCTION .....	69
3.1.1. Details of bis( <i>tert</i> -butylimido)bis(dimethylamido) tungsten (VI) utilization in ALD (and known molecular characteristics).....	69
3.1.2. The goal of the chapter .....	70

3.2	EXPERIMENTAL SECTION.....	71
3.2.1.	General procedures.....	71
3.2.2.	Precursors.....	71
3.2.3.	Preparation of molecular samples.....	72
3.2.4.	ALD-modeling reactions on the surface of silica nanobeads.....	74
3.2.5.	Characterization instruments.....	78
3.3	RESULTS AND DISCUSSION.....	80
3.3.1.	Preliminary study with molecular chemistry.....	80
3.3.1.2.	<i>Exploratory data on the reactivity of (NMe<sub>2</sub>)<sub>2</sub>(=N<sup>t</sup>Bu)<sub>2</sub>W (VI) complex with triphenylsilanol in solution.....</i>	83
3.3.2.	Modeling the 1 <sup>st</sup> pulse via deposition of (NMe <sub>2</sub> ) <sub>2</sub> (=N <sup>t</sup> Bu) <sub>2</sub> W (VI) on nanobeads of silica-700.....	93
3.3.3.	Exploratory SOMC work toward ALD process with 1,2-ethanedithiol and [(=N <sup>t</sup> Bu) <sub>2</sub> (NMe <sub>2</sub> ) <sub>2</sub> W].....	100
3.3.4.	Study of the annealing step.....	107
3.4	CONCLUSION.....	115
Chapter 4 - WS <sub>2</sub> GROWTH by ALD ON SILICON WAFERS.....		116
4.1	INTRODUCTION.....	117
4.1.1.	Silicon wafers as ALD substrate. What do we know of their ultimate surface?.....	117
4.2	EXPERIMENTAL PART.....	119
4.2.1.	XPS studies.....	119
4.2.2.	Environmental TEM studies.....	124
4.3	RESULTS AND DISCUSSION.....	130
4.3.1.	XPS study.....	130
4.3.2.	<i>In situ</i> annealing of ALD grown W and Mo thiolates on SiO <sub>x</sub> @Cu grid in an environmental transmission electron microscope.....	148

4.4	CONCLUSION.....	156
Chapter 5 - PHOTO- and ELECTROCATALYTIC PERFORMANCE OF ALD-GROWN WS <sub>2</sub>		
	158	
5.1	INTRODUCTION.....	159
5.1.1.	TiO <sub>2</sub> as an ALD substrate and its ultimate surface.....	159
5.1.2.	Carbon nanotubes as an ALD substrate and its ultimate surface .....	163
5.2	EXPERIMENTAL SECTION.....	166
5.2.1.	Preparation and characterization of Ti disk-supported samples.....	166
5.2.2.	Preparation and characterization of CNTs-supported samples .....	167
5.3	RESULTS AND DISCUSSION.....	169
5.3.1.	WS <sub>2</sub> films grown on TiO <sub>2</sub> @Ti disk by ALD and their photocurrent production tests	169
5.3.2.	Electrocatalytic reduction of CO <sub>2</sub> by ALD-grown WS <sub>2</sub> on CNT .....	178
5.4	CONCLUSION.....	182
Chapter 6 - GENERAL CONCLUSION AND PERSPECTIVES.....		
	183	
6.1	Summary .....	184
6.2	Perspectives .....	187
	REFERENCES .....	188

# Abbreviations

ALD	atomic layer deposition
asym	asymmetric
br	broad
<sup>t</sup> Bu	<i>tert</i> -butyl, $-\text{CH}(\text{CH}_3)_3$
BTBMW	bis( <i>tert</i> -butylimido)bis(dimethylamido)tungsten (VI)
(MW)CNTs	multi-walled carbon nanotubes
CVD	chemical vapor deposition
DFT	density functional theory
DRIFT	diffuse reflectance infrared Fourier transform
EA	elemental analysis
EDT	1,2-ethanedithiol
EDX	energy-dispersive X-ray
ESI-MS	electrospray ionization mass spectrometry
E-TEM	environmental transmission electron microscopy
EXAFS	extended X-ray absorption fine structure
FFT	fast Fourier transform
FTIR	Fourier-transform infrared spectroscopy
GC	gas chromatography
GPC	growth per cycle
HDMDW	hexakis(dimethylamido)ditungsten (III)
HDMW	hexakis(dimethylamido)tungsten (VI)
HDN	hydrodenitrogenation
HDS	hydrodesulfurization
HRTEM	high-resolution transmission electron microscopy
ICDD	international center for diffraction data
m	medium
Me	methyl, $-\text{CH}_3$
MeOH	methanol
MEMS	microelectromechanical systems
NEMS	nanoelectromechanical systems
NMR	nuclear magnetic resonance
PE-ALD	plasma-enhanced atomic layer deposition

Ph	phenyl
PL	photoluminescence
QCM	quartz crystal microbalance
RBS	Rutherford backscattering spectroscopy
RT	room temperature
s	strong
SEM	scanning electron microscopy
SIMS	secondary ion mass spectrometry
SOMC	surface organometallic chemistry
ss NMR	solid-state nuclear magnetic resonance
STEM	scanning transmission electron microscopy
s	strong
sh	sharp
str	stretching
sym	symmetric
TGA	thermogravimetric analysis
THF	tetrahydrofuran
TMDs	transition metal dichalcogenides
TNTs	titania nanotube arrays
TOF-ERDA	time-of-flight elastic recoil detection analysis
TXRF	total X-ray reflection fluorescence
UHV	ultra-high vacuum
VPD	vapor phase decomposition
vs	very strong
w	weak
WDXRF	Wavelength Dispersive X-ray Fluorescence
XANES	X-ray absorption near-edge spectroscopy
XPS	X-ray photoelectron spectroscopy
XRD	X-ray diffraction

# ABSTRACT

A new Atomic Layer deposition (ALD) method for the growth of ultra-thin films of WS<sub>2</sub> was investigated by testing two tungsten precursors (hexakis(dimethylamido) ditungsten (III) and bis(tert-butylimido)bis(dimethylamido) tungsten (VI)) and one sulfur precursor (1,2-ethanedithiol). The growth chemistry of WS<sub>2</sub> ALD was first studied by model reactions in molecular and surface organometallic chemistry (SOMC). Several SOMC tools (infrared (IR), Raman, solid- and liquid-state nuclear magnetic resonance (NMR), elemental analysis, *in situ* quantitative determinations of by-products at the gas-solid interphase) applicable to high-surface-area powder silica provided an understanding of the surface chemistry during the initial ALD cycles, which allowed to propose possible structures of the surface sites.

A successful ALD-like sequence of reactions with bis(tert-butylimido)bis(dimethylamido) tungsten (VI) and ethanedithiol on porous high-surface-area silica nanobeads afforded to perform the growth of WS<sub>2</sub> on 2D substrates (silica-covered silicon wafers, SiO<sub>2</sub>@Si<sub>wafers</sub>, and silicon oxides-covered copper grids, SiO<sub>x</sub>@Cu<sub>grid</sub>, titania nanotubes on titanium disk, TNTs@Ti<sub>disk</sub>, and carbon nanotubes CNT). X-Ray photoelectron spectroscopy XPS study conducted on the ALD-modified silicon wafers coupled with analogous XPS insight gained on the molecular models brought new insights into the oxidation state evolution and environment of tungsten during the ALD process. Gradual reduction of tungsten's oxidation number from the initial (VI) to targeted (IV) was first observed upon the thiol pulse, and then completed during the annealing step. Monitoring the surface *in situ* by high-resolution transmission electron microscopy (HRTEM) supported the tungsten reduction by the formation of characteristic layered patterns and well-ordered crystalline nanodomains.

Deposition onto (semi)conducting 2D substrates like a Ti disk coated with photoactive TiO<sub>2</sub> nanotubes (TNTs@Ti<sub>disk</sub>) and conducting carbon nanotubes allowed to initiate the photocurrent and CO<sub>2</sub> electro reduction measurement, respectively.

# RESUME SUCCINT

La croissance de couches ultra-minces de WS<sub>2</sub> par un procédé innovant de dépôt par couche atomique ou ALD (pour Atomic Layer Deposition) a été étudié en testant deux précurseurs du tungstène (hexakis(diméthylamido) ditungstène (III) et bis(tert-butylimido)bis(diméthylamido) tungstène (VI)), ainsi qu'un précurseur soufré (1,2-éthanedithiol).

La chimie autour de la croissance par ALD de WS<sub>2</sub> a d'abord été étudiée par des réactions modèles en chimie organométallique moléculaire et de surface. Plusieurs outils de Chimie Organométallique de surface COMS (infrarouge (IR), Raman, résonance magnétique nucléaire (RMN) à l'état solide et liquide, analyse élémentaire et déterminations quantitatives *in situ* des sous-produits à l'interphase gaz-solide) applicables à des poudres de silice à haute surface spécifique ont permis de comprendre la chimie de surface pendant les premiers cycles de l'ALD, ce qui a mené à la proposition des structures possibles des sites de surface.

À partir de la séquence de réactions de type ALD avec le bis(tert-butylimido)bis(diméthylamido) tungstène (VI) et l'éthanedithiol sur des nanoparticules de silice poreuse à haute surface spécifique, il a été possible de réaliser la croissance de WS<sub>2</sub> sur des substrats 2D (plaquettes de silicium recouverte d'oxyde thermique SiO<sub>2</sub>@Si<sub>wafers</sub>, grilles de cuivre recouvertes d'oxyde de silicium SiO<sub>x</sub>@Cu<sub>grid</sub>, nanotubes d'oxyde de titane crûs sur des disque de titane, TNTs@Ti<sub>disk</sub>, et des nanotubes de carbones, CNT). L'étude par spectrométrie de photoélectrons induits par rayons-X (XPS) menée sur les plaquettes de silicium modifiées par ALD, comparée aux données XPS analogues mesurées sur les modèles moléculaires, a permis de mieux comprendre l'évolution de l'état d'oxydation et de l'environnement du tungstène. Une réduction progressive du degré d'oxydation du tungstène, de l'état initial (VI) à l'état ciblé (IV), a d'abord été observée lors de l'ajout de thiol, puis se complète lors de l'étape de recuit. Une étude par microscopie électronique en transmission à haute résolution (HRTEM) a permis d'observer l'étape de recuit *in situ*. La réduction du tungstène par la formation de motifs en couches caractéristiques et de nano-domaines cristallins bien ordonnés a été observée.

Le dépôt sur des substrats photoactifs en 2D, comme un disque de Ti recouvert de nanotubes de TiO<sub>2</sub> (TNTs@Ti<sub>disk</sub>), a permis de lancer de mesure de photocourant et d'électroreduction du CO<sub>2</sub>.

# RIASSUNTO BREVE

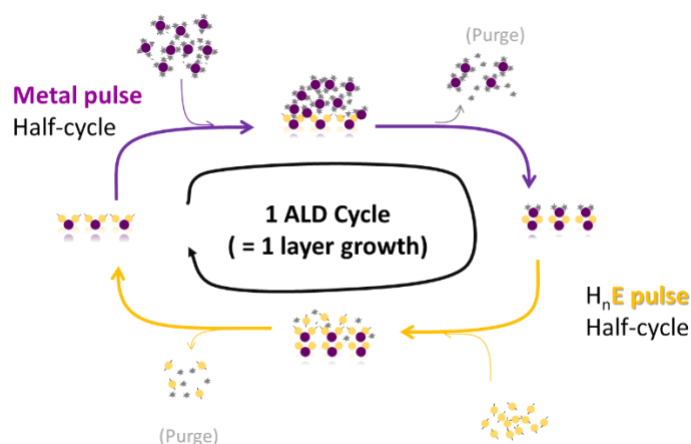
Un nuovo metodo di deposizione a strato atomico (in inglese Atomic Layer Deposition, ALD) per la crescita di film ultrasottili di  $WS_2$  è stato studiato testando due precursori di tungsteno (esa(dimetilammido) tungsteno (III) e bis(ter-butylimmido)bis(dimetilammido) tungsteno (VI)) e un precursore contenente zolfo (1,2-etanditiolo). La chimica della crescita di  $WS_2$  mediante ALD è stata studiata per la prima volta attraverso l'utilizzo di reazioni modello di chimica organometallica di superficie (in inglese Surface Organometallic Chemistry -SOMC). Gli strumenti analitici utilizzati (quali la spettroscopia a infrarossi, IR e Raman, la risonanza magnetica nucleare -NMR- allo stato solido e liquido, l'analisi elementare, le determinazioni quantitative *in situ* dei sottoprodotti all'interfaccia gas-solido) applicabili alla silice in polvere ad alta area superficiale hanno permesso di comprendere la chimica di superficie durante i cicli iniziali di ALD, e suggerito le possibili strutture degli intermedi di superficie ad ogni tappa del processo .

Mediante una sequenza di reazioni tipo ALD con bis(ter-butylimmido)bis(dimetilammido) tungsteno (VI) ed etanditiolo su nano-grani di silice porosa ad alta area superficiale, è stata possibile la crescita di  $WS_2$  su substrati 2D (wafer di silicio ricoperti di silice - $SiO_2@Si_{wafer}$ , griglie di rame ricoperte di ossidi di silicio - $SiO_x@Cu_{grid}$ , nanotubi di titania su dischi di titanio -  $TNTs@Ti_{disk}$  e nanotubi di carbonio, CNT). Lo studio tramite spettroscopia fotoelettronica a raggi X (XPS) condotto sui wafer di silicio modificati mediante ALD, accoppiata all'analisi di dati analoghi ottenuti da modelli molecolari, ha permesso di conoscere l'evoluzione dello stato di ossidazione e della stera di coordinazione del tungsteno durante il processo ALD. La riduzione graduale del numero di ossidazione tungsteno dal valore iniziale (VI) a quello desiderato (IV) è stata osservata sin dalla prima aggiunta del tiolo, e completata durante la fase di annealing. Il monitoraggio *in situ* della superficie tramite la microscopia elettronica a trasmissione ad alta risoluzione (HRTEM) ha confermato la riduzione del tungsteno con la formazione di disposizioni a strati caratteristici e nano-domini cristallini ben ordinati.

La deposizione di  $WS_2$  su substrati 2D (semi)conduttori, come un disco di titanio rivestito da nanotubi  $TiO_2$  ( $WS_2@TNTs@Ti_{disk}$ ) o nonotubi di carbonio ( $WS_2@CNT$ ), ha permesso di effettuare la misurazione della fotocorrente e il testing nell'elettroreduzione della  $CO_2$ , anche se è ancora necessario ottimizzarne il processo.

# EXTENDED SUMMARY

A larger share of sustainable energy to power our society necessitates the development of different types of energy conversion devices (e.g. solar to electrical, solar to chemical, electrical to chemical).<sup>1-6</sup> As the conversion reactions mainly occur on the top surface of the active material, engineering of such materials strives toward a large active surface area while at the same time minimizing recombination between charge carriers. Elongated nanostructures with a high-aspect-ratio are known to afford solutions in striking such balance in energy conversion. Their surface functionalization with a thin catalytic layer can significantly enhance their performance. Crystallinity, conformality, and purity of a deposited film are essential qualities that influence the performance in a final application. Atomic Layer Deposition (ALD), a thin-film growth technique based on the succession of two (or more) different self-limiting surface reactions (see Scheme 1), is a well-adapted method to achieve a uniform coating of high-aspect-ratio surfaces with a conformal thin to ultra-thin film. It affords control over the film thickness down to a monolayer.



Scheme 1. Simplified representation of material growth by atomic layer deposition (ALD), that is a succession of two self-limiting surface reactions at the gas-solid interphase: (above) the half-cycle based on the gaseous metal precursor and the surface followed by (below) the second half cycle pulse (e.g. with  $\text{H}_2\text{O}$ ,  $\text{NH}_3$ ,  $\text{H}_2\text{S}$ , etc.), which through the second self-limiting reactions ideally leads to the desired materials (e.g. metal oxide, nitride or sulfide, respectively).

The ALD showed excellent usefulness not only for energy conversion applications but also in many other areas such as anti-corrosion coating, microelectronics, nano- and microelectromechanical systems, optical coatings, electroluminescent devices, etc. Knowledge of chemistry occurring on the surface during a single ALD cycle can provide excellent control over these qualities. It can

guide the choice of appropriate precursors and substrates, of optimal process conditions so as to avoid undesired side reactions and improve the overall qualities of the deposited material.

Thin films of tungsten disulfide with thickness to be controlled down to the monolayer over nanostructured supports are emerging as a worthy target for the development of performing noble-metal free energy converting devices.<sup>7-14</sup> While some ALD processes to WS<sub>2</sub> thin film exist,<sup>15-17</sup> these have not yet reached monolayer level thickness nor have succeeded to avoid highly toxic H<sub>2</sub>S as a source of sulfur.

The goal of this thesis is firstly to lay the molecular foundation to propose a successful process for the ALD growth of WS<sub>2</sub> and secondly implement this molecular-level model to the ultrathin growth on real 2D supports.

The molecular model part of this doctoral work is centered on Surface Organometallic Chemistry (SOMC)<sup>18</sup>, which brings a large range of spectroscopic and analytic tools to gain insight into the mechanism of ALD reactions, as recently shown by our group on MoS<sub>2</sub> ALD,<sup>19</sup> with an approach that, to the best of our knowledge, has no other precedent in the ALD community nor in the SOMC community.

In this thesis, we tested two tungsten precursors, W<sub>2</sub>(NMe<sub>2</sub>)<sub>6</sub> – HDMDW and W(=N<sup>t</sup>Bu)<sub>2</sub>(NMe<sub>2</sub>)<sub>2</sub> – BTBMW and 1,2-ethanedithiol as a sulfur precursor for the ALD growth of WS<sub>2</sub>.

The first precursor, [(Me<sub>2</sub>N)<sub>3</sub>W≡W(NMe<sub>2</sub>)<sub>3</sub>], hexakis(dimethylamido)ditungsten (HDMDW) was synthesized and purified from the mixture with its monomeric form [(Me<sub>2</sub>N)<sub>6</sub>W]. As the dimer complex was previously applied as an ALD precursor of other tungsten-containing compounds<sup>20,21</sup>, it was thought that HDMDW can also yield WS<sub>2</sub> in the ALD, where the sulfur source is EDT.

A preliminary molecular chemistry study was performed using (<sup>t</sup>BuO)<sub>3</sub>SiOH. SOMC studies were carried using SiO<sub>2-700</sub>. The molecular reactions in solution showed that HDMDW is reactive towards silanol groups, with HNMe<sub>2</sub> as a byproduct, and is reactive towards EDT, leading to a precipitate. Hence, the studies directly switched onto the silica nanobeads' surface, where the surface reactions in suspension (using solvent) modeled solution ALD. The IR spectra recorded after each pulse over two full ALD cycles demonstrated periodicity. Namely, an increase and decrease of SH vibration band (2391 cm<sup>-1</sup>) were observed with each EDT and HDMDW pulse,

respectively. The tungsten pulse increased bands assigned to  $-NMe_2$  ligands, while sulfur pulse decreased these absorption bands. Elemental analyses corroborate this evidence. However, the deposition of HDMDW in vapor-solid interaction did not lead to the consumption of surface hydroxyl groups. In suspension, solvent molecules are known to assist the reactions (e.g. by better diffusion, changing electronic structure) that are not possible or complicated in the gas-solid interphase.<sup>22,23</sup> The possibility to use HDMDW in solution ALD for the growth of  $WS_2$  was still of interest. Therefore, silica powder after 2 full ALD cycles performed in presence of solvent was annealed ex-situ in argon at 800 °C and in hydrogen at 450 °C. HRTEM of the resulting black powder did reveal the formation of worm-like layered patterns and well-ordered crystalline nanoparticles. The estimated distance (0.64 nm) between subsequent layers pointed to  $WS_2$  as it was in good agreement with literature reports. Elemental analysis and EDX of the annealed powder supported the expected S to W ratio, which was found as 2.1:1 and  $2(\pm 0.7):1$ , respectively.

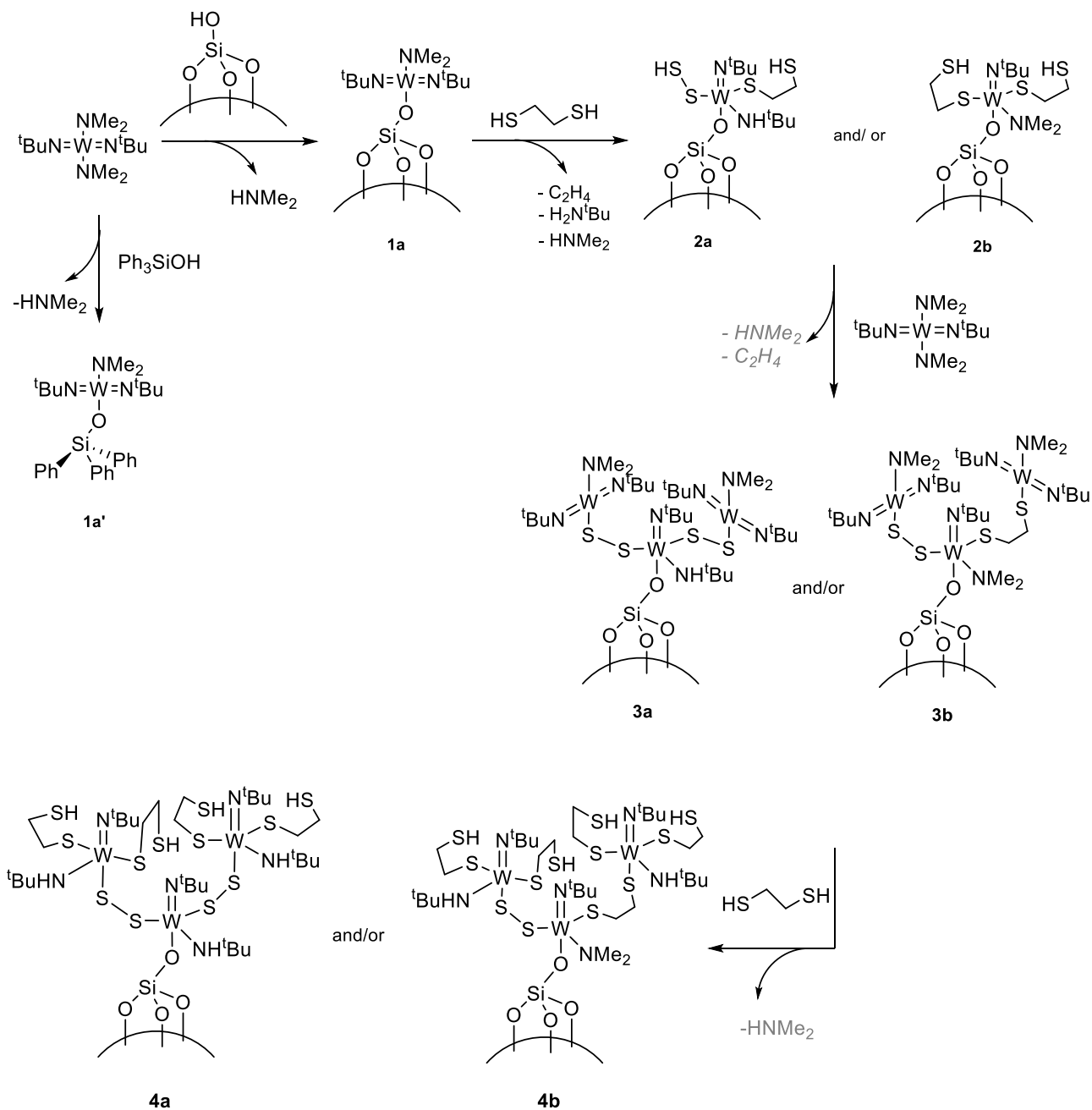
The first spectroscopic and microscopic data point to the successful growth of  $WS_2$  film by a solution ALD method. Self-limiting and periodic features of the surface reactions were observed.

The reactivity of the second precursor studied in this thesis, bis(tert-butylimido)bis(dimethylamido)tungsten (VI) (BTBMW) with silica-modeling molecular compound,  $Ph_3SiOH$ , showed mono-substitution preferentially via a proton exchange with the silanol group and elimination of dimethylamine (see **1a'** in Scheme 2). Dimethylamine gas was observed as the unique by-product when the reaction was carried inside a closed nuclear magnetic resonance (NMR) tube. The reaction in a 10-fold larger scale demonstrated clear mono-substitution to a unique tungsten-based product displaying imido ( $=N^tBu$ ) : amido ( $-NMe_2$ ) in 2:1 ratio. X-ray Photoelectron Spectroscopy (XPS) analysis of the final yellow powder confirmed the  $W^{6+}$  oxidation state and the presence of siloxy, imido, and amido ligands in the tungsten(VI) coordination sphere. The unexpected large O:W atomic ratio as well as the presence of a third nitrogen-based signal at higher binding energies suggest adventitious hydrolysis. The reaction of  $Ph_3SiO-W(=N^tBu)_2(NMe_2)$  with 1,2-ethanedithiol (EDT) yielded a complex mixture of several products containing red-brown precipitation and soluble fraction in toluene. The filtrate was dried, pressed, and studied by XPS which suggested a formal reduction of  $W^{6+}$  to  $W^{5+}$  possibly linked to the formation of persulfido  $S_2^{2-}$  ligand around the tungsten center.<sup>24</sup> The formation of this persulfide ligand is explained through the elimination of ethylene from the bridging dithiolate

ligand,  $-\text{SCH}_2\text{CH}_2\text{S}-$ , as suggested by possible ethylene evolution during the reaction. The ethylene evolution for such a ligand has several literature precedents among which during the annealing of a closely related siloxy-molybdenum ethylene dithiolate system developed in our group.<sup>19</sup> The formal reduction of  $\text{W}^{6+}$  to  $\text{W}^{5+}$  could also be explained by coupling of thiols in an analogy with a precedent, where tungsten in W (VI) oxide nanoparticles is reduced by reaction with thiol.<sup>25</sup> The system at hand is further complicated by the possibility of co-existing thiol and amine groups to form a zwitterion ( $(=\text{NH})(\text{HSR})$  vs.  $(=\text{NH}_2)^+(\text{SR})$ ).<sup>26,27</sup> For both these aspects (relevance of S–S bond formation and zwitterionic forms) further experimental corroborating evidence is necessary.

In summary, the molecular evidence obtained by reaction of  $\text{W}(=\text{N}^t\text{Bu})_2(\text{NMe}_2)_2$  – BTBMW with triphenylsilanol followed by reaction with 1,2-ethanedithiol thus suggests, firstly, that the targeted surface reaction between surface silanol of the pristine substrate and the incoming metal precursor is feasible and, secondly, that ethanedithiol does react with such siloxy W(VI) amido, imido, amino species, bonding well for the desired ALD process to be devised, although complex side reactions linked to forming persulfido species and/or the presence of zwitterionic forms involving the thiol and the amino residues complicate this chemistry.

The second level of modeling was achieved by using a solid, high surface area porous silica, instead of the molecule, triphenylsilanol just discussed, as a proxy for the final 2D substrate to be functionalized. This second level of modeling allows us to investigate the reaction at the gas-solid interphase, as it is usual in ALD processes, rather than in solution, as done with triphenylsilanol. Within 4 ALD pulses modeled on silica, diffuse reflectance infrared Fourier transform (DRIFT) showed periodic repeatability. The first pulse of the vapor deposition of BTBMW consumed all surface hydroxyl groups,  $\equiv\text{Si}-\text{OH}$ , as shown by the disappearance of the absorption band at  $3747\text{ cm}^{-1}$  and brought new bands attributed to alkyl C–H bond vibrations in the range between  $2700$  and  $3000\text{ cm}^{-1}$ . Raman spectrum of the impregnated complex on silica showed a good match with the Raman bands of pure BTBMW. Volatile by-products of the impregnation were analyzed by NMR that showed ca. 98 mol. %  $\text{HNMe}_2$  and 2 mol. % of  $\text{H}_2^t\text{Bu}$ . The solid-state  $^{13}\text{C}$  NMR spectrum of the solid product confirmed the primary (32.6 ppm) and quaternary carbon atoms (66.0 ppm) of the *tert*-butyl group as well as primary carbon atoms (53.9 ppm) of the dimethylamido ligands. Elemental analysis of that 1<sup>st</sup> pulse product was coherent with the other spectroscopy observations and lead to the average formula:  $\equiv\text{SiO}-\text{WC}_{10}\text{N}_3\text{H}_{25}$ . This allowed proposing the structure of grafted sites **1a** (which matches the atomic composition just mentioned) as illustrated in Scheme 2.



Scheme 2. Simplified proposed ALD-modelling reactions of  $\text{WS}_2$  growth on the surface of  $\text{SiO}_{2-700}$  and in solution with the molecular model,  $\text{Ph}_3\text{SiOH}$ , using BTBMW and EDT as precursors. For example, the partial (re)coordination of eliminated amine on the tungsten centers as well as the coexistence of several surface species, among which zwitterionic forms, on top of the main species drawn, are not shown.

The further reaction of the 1<sup>st</sup> pulse product with EDT models the 2<sup>nd</sup> half-cycle reaction of the ALD. Spectral analysis showed that silica-supported BTBMW readily reacts with EDT, which is

also seen by its color change from yellow to red. DRIFT spectrum recorded for the red product shows the disappearance of some bands that is the CH<sub>x</sub> stretching vibration (2786, 2832 cm<sup>-1</sup>) and the appearance of thiol (2572 cm<sup>-1</sup>) and new surface hydroxyl (3747 cm<sup>-1</sup>) groups. It confirms the successful surface reaction of the EDT and the presence of the available functional group for the following tungsten pulse. A broad IR band between 2500 and 3500 cm<sup>-1</sup> is a sign of intramolecular interaction (e.g., hydrogen bonding) between thiol, hydroxyl, siloxy ( $\equiv\text{Si}-\text{O}-\text{Si}\equiv$ ) and amine groups. The latter group could be produced upon proton transfer to amido groups and forming coordinated dimethylamine or *tert*-butylamine. Previous reports on reactions of tungsten and molybdenum alkylamido complexes with thiols and bulky alcohols showed that substitution of alkylamido groups can be incomplete.<sup>28-30</sup> Besides, volatile byproducts trapped in the NMR tube revealed the presence of ethylene, HNMe<sub>2</sub>, and H<sub>2</sub>N<sup>t</sup>Bu. Elimination of ethylene might be a part of the path towards the formation of S<sub>2</sub><sup>2-</sup> which was proposed above based on the XPS data in the analogous molecular product.

The regeneration of surface hydroxyl might be indirect evidence for the coupling of thiol groups (of neighboring sites or free EDT molecules in excess) to make -S-S- bond. Indeed, such oxidative coupling can produce two electrons and two protons capable of reduction of W<sup>6+</sup> and generation of new Si-OH groups by opening  $\equiv\text{Si}-\text{O}-\text{Si}\equiv$  bridges. Although this proposal is still incomplete and needs to be experimentally corroborated, it has the appealing potential to explain the re-appearance of surface silanol observed in the IR study.

Elemental analysis of the solid powder product after the 1<sup>st</sup> pulse of EDT (2<sup>nd</sup> half-cycle) allowed defining the molecular formula as  $\equiv\text{SiO}-\text{WC}_{10}\text{N}_2\text{S}_4\text{H}_{25}$ . It afforded to propose the following extended formulas  $\equiv\text{SiO}-\text{W}(=\text{N}^t\text{Bu})(\text{NH}^t\text{Bu})(\text{SCH}_2\text{CH}_2\text{SH})(\text{SSH})$  (**2a**) and  $\equiv\text{SiO}-\text{W}(=\text{N}^t\text{Bu})(\text{NMe}_2)(\text{SCH}_2\text{CH}_2\text{SH})_2$  (**2b**) as two possible structures. The first option (**2a**) is proposed to contain S<sub>2</sub><sup>2-</sup> persulfide binding both sulfur atoms to the tungsten center. This still needs to be confirmed in deeper characterization (e.g. by EPR). Nevertheless, there is a new absorption band in the Raman spectrum that appeared upon the 2<sup>nd</sup> pulse reaction at 463.3 cm<sup>-1</sup>. This band comes in agreement with some literature reports in the identification of the S-S bond in polysulfides.<sup>31</sup> Two structures for the reaction products were proposed in Scheme 2.

The third pulse that is the second addition of BTBMW, reacts with the 2<sup>nd</sup> pulse products (represented by **2a** and **2b** as main surface species) as well as with the regenerated surface silanols discussed above. Accordingly, the DRIFT spectrum shows the consumption of thiol and surface

hydroxyl groups bands as well as the appearance of bands of  $-\text{NMe}_2$  and  $\text{N}^t\text{Bu}$  ligands. Overall, the IR spectrum resembles one that was acquired upon the 1<sup>st</sup> pulse of BTBMW. So do the Raman spectra of the 1<sup>st</sup> and 3<sup>rd</sup> pulses too. Elemental analysis shows an increase of tungsten loading 2.7-fold leading to the formula as  $\equiv\text{SiO}-\text{W}_3\text{C}_{28}\text{N}_8\text{S}_4\text{H}_{67}$ . This allowed us to propose the reaction products **3a** and **3b** as illustrated in Scheme 2. The new structures are coherent with the IR, Raman spectra as well as with solid-state  $^{13}\text{C}$  NMR.

The 4<sup>th</sup> pulse was expected to proceed similarly to the 2<sup>nd</sup> pulse path in which the W center was bonded to 2 equivalents of EDT. The SS  $^{13}\text{C}$  NMR, IR, and Raman spectra were indeed almost identical to those seen after the 2<sup>nd</sup> pulse showing a periodicity with each ALD cycle. The elemental analysis of the 4<sup>th</sup> pulse product showed an increase of the S/W ratio to 4 and defined the formula as  $\equiv\text{SiO}-\text{W}_3\text{C}_{32}\text{N}_6\text{S}_{12}\text{H}_{75}$ . Following two options of the 3<sup>rd</sup> pulse, the **4a** and **4b** structures were proposed for the 4<sup>th</sup> pulse in Scheme 2.

The silica nanobeads after 4 ALD-modeling pulses were then heated to 500 °C in helium flow, which was monitored *operando* by DRIFT coupled with GC-MS spectrometry. The decrease of absorption bands assigned to C–H bonds vibration begins from 110 °C and completely disappears above 450 °C. The GC-MS graphs showed the release of ethylene, isobutene, ethanethiol, thiophene, and thiirane starts in the range of 200-250 °C. These are all possible fragments and products that could be formed upon decomposition of the proposed structures for the 4<sup>th</sup> pulse. Ex-situ annealing (both in argon at 800 °C and in hydrogen at 450 °C) of the powder revealed the formation of worm-like layered patterns and well-structured nanocrystals. The latter allowed estimating the unit cell parameters via FFT calculation, which came in agreement with theoretical values of  $\text{WS}_2$  in the 2H (hexagonal) phase. Therefore, the desired reduction of tungsten to the targeted  $\text{W}^{4+}$  sulfide is proposed to occur during annealing.

Based on this modeling result, both at the molecular and the SOMC levels, the ALD process was performed on a 2D silicon wafer covered with thermal oxide, and each half-cycle was studied by *in situ* XPS study.

Namely, XPS analysis of the 1<sup>st</sup> pulse product on  $\text{SiO}_2@\text{Si}_{\text{wafer}}$  afforded to confirm the  $\text{W}^{6+}$  oxidation state and  $\text{SiO}-\text{W}$  in the environment of Si. The N 1s core-level demonstrated the presence of not only imido and amido type nitrogen atoms but also nitrogen compatible with an amine group, thus suggesting that some amine by-product of the half-cycle reaction can remain coordinated to the tungsten. As for the molecular model, the wafer-bound product showed a partial formal reduction of

$W^{6+}$  to  $W^{5+}$  upon the EDT pulse. As in the molecular case, where similar XPS signals were observed, the formal reduction is explained by the presence of the  $S_2^{2-}$  group. The atomic fraction of the coordinated amine was increased with respect to imido and amido nitrogen atoms, notwithstanding the zwitterionic forms mentioned above. The XPS signal assigned to the thiol ( $-SH$ ) group overlaps with the XPS signal due to adventitious hydrolysis. The addition of EDT shows the successful addition of sulfur to the solid. The possible proton transfer from the thiol group to amine could also suggest the existence of zwitterions. This latter hypothesis could not be verified yet by other means. A wider range of spectroscopic tools is necessary to assert the formation of the ammonium group, if there is any, over this first half-cycle as well as the three further ones. The results are in most parts very close to the evidence collected on the models described above while revealing some unexpected minority events (e.g. the formation of tungsten silicide).

The ex-situ annealing of the successfully obtained tungsten thiolates was marred by the adventitious exposure to air and the formation of a top layer of tungsten oxide. Nevertheless, after the surface etching with  $Ar^+$  XPS signature for  $WS_2$  could be found alongside residual starting material. To gain better insight into the conversions of the molecular thiolate to the final targeted  $WS_2$ , the annealing was repeated in *operando* conditions directly inside the XPS chamber (in an ultra-high vacuum), which revealed the lowering the binding energy (BE) of the  $W\ 4f_{7/2}$  peak's starting from 300 °C. This decrease of BE pointed to the reduction until  $W^{4+}$  that came in parallel with the loss of carbon, nitrogen, and excess sulfur contents. The spurious formation of  $CuS_x$ , probably due to sample holder contamination, has prevented from observing the full transformation to the expected final phase.

*In situ* annealing in the environmental transmission electron microscope (E-TEM) was conducted to observe the gradual phase transition from amorphous W thiolates to crystalline  $WS_2$ . Although the worm-like shapes and crystalline nanodomains characteristic to  $WS_2$  were spotted starting from 400 °C, at higher temperatures (above 700 °C) some contamination originating from the sample holder marred the observation.

Finally, the developed ALD growth method was applied on TNT's@Ti disks to further investigate photocatalytic performance. The ALD-modified and pristine TNT's@Ti disk samples were compared in the photocurrent generation tests. TNT's growth by anodization of Ti disks and

photocatalytic tests of samples were carried during mobility in the University of Messina. Due to time constrain and pandemic restrictions, a list of the studied samples remained short. Improvement of the photocurrent generation with respect to pristine TNT's could not be achieved. Although various conditions including a different number of ALD cycles (3 and 5), the temperature of BTBMW deposition (RT and 60 °C), and Ti disk purity (99.96 and 99.8 %) were tried, thorough optimization is still required.

Electrocatalytic reduction of CO<sub>2</sub> measurements were performed in collaboration with Humboldt University in Berlin. Several samples of WS<sub>2</sub> thin film grown by ALD on multiwalled carbon nanotubes (MWCNTs) were prepared using BTBMW and H<sub>2</sub>S by the research group of Prof. N. Pinna in Berlin. The resulting powders were sprayed onto the gas diffusion layer carbon electrode and tested in electrocatalytic reduction of CO<sub>2</sub> as a cathode in chronoamperometry mode. Formic acid, carbon monoxide and hydrogen gas were observed as main products. The faradaic efficiency towards the formation of carbon-based products from CO<sub>2</sub> was low, although WS<sub>2</sub>@CNT composites are expected to be interesting in the electrocatalysis based on literature precedents. Further studies are necessary.

In conclusion, this thesis has contributed to further assessing SOMC as a valuable tool for the investigation, understanding, and design of novel ALD process aiming at precise chemistry from the first half pulse and final thickness as challenging as monolayers. Besides the capacity to lay the foundation for promising ultrathin WS<sub>2</sub> growth, this work has also explored the powerful contribution that *in situ* and *operando* XPS can give when simultaneously gaining molecular level understanding via model molecules, via SOMC on 3D high surface area beads and device-oriented 2D supports like wafers. The first timid study using environmental microscopy to similarly witness the atomic level transformation during the annealing step is also reported. This unique combination of molecular chemistry, *operando* ultra-high vacuum analytic techniques, and chemistry at the gas-solid interphases on high surface area powders is therefore showing promise in advancing our capacity to modify nanostructured 2D substrates toward thin films deposition, which can be crucial for efficient energy converting devices.

## REFERENCES:

1. Molaei, M. J. The optical properties and solar energy conversion applications of carbon quantum dots: A review. *Solar Energy* **196**, 549–566 (2020).
2. Ismael, M. Ferrites as solar photocatalytic materials and their activities in solar energy conversion and environmental protection: A review. *Solar Energy Materials and Solar Cells* **219**, 110786 (2021).
3. Dong, C. R., Wang, Y., Zhang, K. & Zeng, H. Halide perovskite materials as light harvesters for solar energy conversion. *EnergyChem* **2**, 100026 (2020).
4. Yu, X. & Sivula, K. Layered 2D semiconducting transition metal dichalcogenides for solar energy conversion. *Current Opinion in Electrochemistry* **2**, 97–103 (2017).
5. Yu, X. & Sivula, K. Toward Large-Area Solar Energy Conversion with Semiconducting 2D Transition Metal Dichalcogenides. *ACS Energy Letters* **1**, 315–322 (2016).
6. Iqbal, M. Z., Alam, S., Faisal, M. M. & Khan, S. Recent advancement in the performance of solar cells by incorporating transition metal dichalcogenides as counter electrode and photoabsorber. *International Journal of Energy Research* **43**, 3058–3079 (2019).
7. Tsai, M. L. *et al.* Monolayer MoS<sub>2</sub> heterojunction solar cells. *ACS Nano* **8**, 8317–8322 (2014).
8. Yin, Z. *et al.* Single-layer MoS<sub>2</sub> phototransistors. *ACS Nano* **6**, 74–80 (2012).
9. Krasnozhan, D., Lembke, D., Nyffeler, C., Leblebici, Y. & Kis, A. MoS<sub>2</sub> transistors operating at gigahertz frequencies. *Nano Lett.* **14**, 5905–5911 (2014).
10. Bertolazzi, S., Krasnozhan, D. & Kis, A. Nonvolatile Memory Cells Based on MoS<sub>2</sub>/Graphene Heterostructures. *Am. Chem. Soc. Nano* **7**, 3246–3252 (2013).
11. Sun, P., Zhang, W., Hu, X., Yuan, L. & Huang, Y. Synthesis of hierarchical MoS<sub>2</sub> and its electrochemical performance as an anode material for lithium-ion batteries. *J. Mater. Chem. A* **2**, 3498–3504 (2014).
12. Xiang, Q., Yu, J. & Jaroniec, M. Synergetic effect of MoS<sub>2</sub> and graphene as cocatalysts for enhanced photocatalytic H<sub>2</sub> production activity of TiO<sub>2</sub> nanoparticles. *J. Am. Chem. Soc.* **134**, 6575–6578 (2012).
13. Yan, Y., Xia, B., Xu, Z. & Wang, X. Recent development of molybdenum sulfides as advanced electrocatalysts for hydrogen evolution reaction. *ACS Catal.* **4**, 1693–1705 (2014).
14. Sobczynski, A. *et al.* Tungsten Disulfide: A Novel Hydrogen Evolution Catalyst for Water Decomposition. *J. Phys. Chem* **92**, 2311–2315 (1988).
15. Wu, Y. *et al.* A Self-Limited Atomic Layer Deposition of WS<sub>2</sub> Based on the Chemisorption and Reduction of Bis(t-butylimino)bis(dimethylamino) Complexes. *Chem. Mater.* **31**, 1881–1890 (2019).
16. Scharf, T. W., Prasad, S. V., Mayer, T. M., Goeke, R. S. & Dugger, M. T. Atomic layer deposition of tungsten disulfide solid lubricant thin films. *J. Mater. Res.* **19**, 3443–3446 (2004).
17. Nandi, D. K., Sen, U. K., Dhara, A., Mitra, S. & Sarkar, S. K. Intercalation based tungsten disulfide (WS<sub>2</sub>) Li-ion battery anode grown by atomic layer deposition. *RSC Adv.* **6**, 38024–

- 38032 (2016).
18. Copéret, C. *et al.* Surface Organometallic and Coordination Chemistry toward Single-Site Heterogeneous Catalysts: Strategies, Methods, Structures, and Activities. *Chem. Rev.* **116**, 323–421 (2016).
  19. Cadot, S. *et al.* A novel 2-step ALD route to ultra-thin MoS<sub>2</sub> films on SiO<sub>2</sub> through a surface organometallic intermediate. *Nanoscale* **9**, 538–546 (2017).
  20. Dezelah IV, C. L. *et al.* Atomic layer deposition of tungsten(III) oxide thin films from W<sub>2</sub>(NMe<sub>2</sub>)<sub>6</sub> and water: Precursor-based control of oxidation state in the thin film material. *J. Am. Chem. Soc.* **128**, 9638–9639 (2006).
  21. Dezelah IV, C. L. *et al.* A low valent metalorganic precursor for the growth of tungsten nitride thin films by atomic layer deposition. *J. Mater. Chem.* **17**, 1109–1116 (2007).
  22. Koch, V. M. *et al.* A solution-based ALD route towards (CH<sub>3</sub>NH<sub>3</sub>)(PbI<sub>3</sub>) perovskite: Via lead sulfide films. *J. Mater. Chem. A* **7**, 25112–25119 (2019).
  23. Wu, Y. *et al.* Atomic Layer Deposition from Dissolved Precursors. *Nano Lett.* **15**, 6379–6385 (2015).
  24. Dupin, J.C., Gonbeau, D., Martin-Litas, I., Vinatier, P. & Levasseur, A. Amorphous oxysulfide thin films MO<sub>y</sub>S<sub>z</sub> (M=W, Mo, Ti) XPS characterization: structural and electronic peculiarities. *Appl. Surf. Sci.* **173**, 140–150 (2001).
  25. Mukherjee, A., Sengupta, S. K., Steeves, D. M., Soares, J. W. & Whitten, J. E. Mechanism of thiol-induced color change of tungsten oxide nanoparticles. *Chem. Phys. Lett.* **752**, (2020).
  26. Bachrach, S. M., Nguyen, T. T. & Demoin, D. W. Microsolvation of cysteine: A density functional theory study. *J. Phys. Chem. A* **113**, 6172–6181 (2009).
  27. Ataman, E., Isvoranu, C., Andersen, J. N., Schnadt, J. & Schulte, K. Unconventional zwitterionic state of l-cysteine. *J. Phys. Chem. Lett.* **2**, 1677–1681 (2011).
  28. Coutelier, O. *et al.* A new donor-stabilized ditungsten amido alkoxido species: Synthesis, crystal structure, fluxionality, and grafting onto silica. *Eur. J. Inorg. Chem.* 5541–5547 (2007). doi:10.1002/ejic.200700732
  29. Chisholm, M. H., Corning, J. F. & Huffman, J. C. Bis(dimethylamine)tetrakis(tert-butyl mercaprido)di-μ-sulfido-dimolybdenum(IV). *Inorg. Chem.* **21**, 286–289 (1982).
  30. Chisholm, M. H., Corning, J. F. & Huffman, J. C. The molybdenum-molybdenum triple bond. 14.<sup>1</sup> preparation and characterization of mixed alkoxy-thiolate compounds of formula Mo<sub>2</sub>(OR)<sub>2</sub>(SAr)<sub>4</sub> (M≡M). *Inorg. Chem.* **23**, 754–757 (1984).
  31. Yu, X. G. *et al.* Lithium storage in conductive sulfur-containing polymers. *J. Electroanal. Chem.* **573**, 121–128 (2004).

# RÉSUMÉ

Le développement de différents types de dispositifs de conversion d'énergies (par exemple, solaire en électrique, solaire en chimique, électrique en chimique) est nécessaire pour permettre la meilleure et plus large utilisation d'énergies dites renouvelables.<sup>1-6</sup> Comme les réactions de conversion se produisent principalement sur la surface ultime du dispositif, l'ingénierie de ces matériaux tente de maximiser la surface active. Les nanostructures allongées à fort rapport d'aspect sont connues pour être efficaces dans la conversion d'énergie. Leur fonctionnalisation avec une couche catalytique peut améliorer considérablement leurs performances. Le dépôt de couches atomiques (ALD) ne permet d'obtenir un revêtement uniforme des surfaces à fort rapport d'aspect avec un film ultra-fin conforme. Technique de croissance de film unique basée sur la succession de deux (ou plus) réactions de surface auto-limitantes différentes (voir schéma 1), avec une précision sur l'épaisseur du film pouvant aller jusqu'à la monocouche.

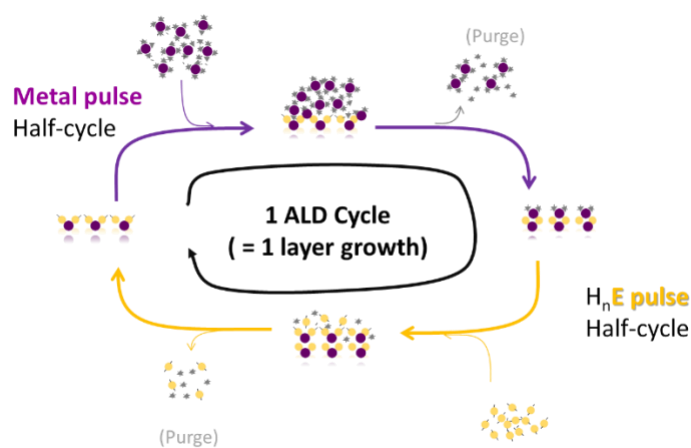


Schéma 1. Représentation simplifiée de la croissance des matériaux par dépôt de couche atomique (ALD), c'est-à-dire une succession de deux réactions de surface auto-limitantes à l'interphase gaz-solide : (en haut) le demi-cycle basé sur le précurseur métallique gazeux et la surface, suivi (en bas) de la deuxième impulsion de demi-cycle (par exemple avec  $\text{H}_2\text{O}$ ,  $\text{NH}_3$ ,  $\text{H}_2\text{S}$ , etc.), qui, grâce aux deuxièmes réactions auto-limitantes, conduit idéalement aux matériaux souhaités (par exemple oxyde, nitrure ou sulfure métallique, respectivement).

La cristallinité, la conformité et la pureté du film déposé sont des qualités essentielles qui influencent les performances finales. L'ALD a montré une excellente utilité non seulement pour les applications de conversion d'énergie mais aussi dans de nombreux autres domaines tels que le revêtement anticorrosion, la microélectronique, les systèmes nano- et microélectromécaniques, les

revêtements optiques, les dispositifs électroluminescents, etc. La connaissance de la chimie se produisant à la surface au cours d'un seul cycle ALD peut permettre de maîtriser ces propriétés. Elle peut guider le choix des précurseurs et des substrats appropriés, des conditions optimales du processus afin d'éviter des réactions secondaires indésirables et d'améliorer les qualités globales du matériau déposé. Les couches minces de disulfure de tungstène dont l'épaisseur doit être contrôlée jusqu'à la monocouche sur des supports nanostructurés apparaissent comme une cible digne d'intérêt pour le développement de dispositifs performants de conversion d'énergie sans métaux nobles.<sup>7-14</sup> S'il existe des procédés ALD pour les couches minces WS<sub>2</sub><sup>15-17</sup>, ceux-ci n'ont pas encore atteint l'épaisseur d'une monocouche ni réussi à éviter le H<sub>2</sub>S hautement toxique comme source de soufre.

Le but de cette thèse est d'une part de poser les bases moléculaires pour proposer un processus de croissance WS<sub>2</sub> par ALD et d'autre part de mettre en œuvre ce modèle au niveau moléculaire pour la croissance ultra-mince sur de véritables supports 2D.

La partie modèle moléculaire de ce travail de doctorat est centrée sur la chimie organométallique de surface (COMS)<sup>18</sup>, qui apporte un large éventail d'outils spectroscopiques et analytiques qui peuvent aider à explorer les mécanismes des réactions de l'ALD, comme l'a récemment montré notre groupe sur l'ALD du MoS<sub>2</sub><sup>19</sup>, avec une approche qui, à notre connaissance, n'a pas de précédent dans la communauté de l'ALD ni dans celle de la COMS.

Dans cette thèse, nous avons testé deux précurseurs du tungstène, W<sub>2</sub>(NMe<sub>2</sub>)<sub>6</sub> - HDMDW et W(=N<sup>t</sup>Bu)<sub>2</sub>(NMe<sub>2</sub>)<sub>2</sub> - BTBMW, et le 1,2-éthanedithiol comme précurseur soufré pour la croissance par ALD du WS<sub>2</sub>.

Le premier précurseur, [(Me<sub>2</sub>N)<sub>3</sub>W≡W(NMe<sub>2</sub>)<sub>3</sub>], l'hexakis(diméthylamido)ditungstène (HDMDW) a été synthétisé et purifié à partir du mélange avec sa forme monomère [(Me<sub>2</sub>N)<sub>6</sub>W]. Puisque le complexe dimère a été précédemment utilisé comme précurseur d'autres composés contenant du tungstène,<sup>20,21</sup> on a émis l'hypothèse que l'HDMDW pouvait également donner du WS<sub>2</sub> par ALD, où la source de soufre est l'EDT.

Une étude préliminaire en chimie moléculaire a été réalisée à l'aide de (tBuO)<sub>3</sub>SiOH et des études COMS ont été effectuées à l'aide de SiO<sub>2-700</sub>. Les réactions moléculaires en solution ont montré que l'HDMDW réagit avec les groupes silanol, avec HNMe<sub>2</sub> comme sous-produit et que HDMDW réagit avec le groupe thiol de l'EDT. Les études ont ensuite porté sur la surface des nanoparticules de silice. Les spectres IR enregistrés après chaque impulsion ont montré une périodicité sur les 2

cycles d'ALD. À savoir, une augmentation et une diminution de la bande de vibration SH ( $2391\text{ cm}^{-1}$ ) ont été observées avec chaque impulsion EDT et HDMDW, respectivement. L'impulsion de tungstène a augmenté les bandes attribuées aux ligands  $-\text{NMe}_2$  ( $2777$  et  $2821\text{ cm}^{-1}$ ), tandis que l'impulsion de soufre a diminué ces bandes d'absorption. Cependant, le dépôt d'HDMDW par interaction vapeur-solide n'a pas entraîné la consommation de groupes hydroxyles de surface. En suspension, les molécules de solvant sont connues pour faciliter les réactions (par exemple par une meilleure diffusion, un changement de structure électronique) qui peuvent ne pas être possibles ou compliquées à l'interphase gaz-solide.<sup>22,23</sup> La possibilité d'utiliser l'HDMDW en solution ALD pour la croissance de  $\text{WS}_2$  est toujours intéressante. Par conséquent, la poudre de silice après 2 cycles ALD complets effectués en présence de solvant a été recuite ex-situ dans de l'argon à  $800\text{ }^\circ\text{C}$ . L'analyse HRTEM de la poudre noire obtenue a révélé la formation de motifs en couches lamellaire et de nanoparticules cristallines ordonnées. La distance estimée ( $0,64\text{ nm}$ ) entre les couches a indiqué la présence de  $\text{WS}_2$ . L'analyse élémentaire et l'EDX de la poudre recuite ont confirmé le rapport S/W attendu, qui était de  $2,1:1$  et  $2(\pm 0,7):1$ , respectivement.

Les premières données spectroscopiques et microscopiques indiquent une bonne croissance du film  $\text{WS}_2$  par une méthode ALD en solution. Des caractéristiques auto-limitantes et périodiques des réactions de surface ont été observées.

La réactivité du second précurseur étudié dans cette thèse, bis(tert-butylimido)bis-(diméthylamido)tungstène (VI) (BTBMW) avec le composé moléculaire modélisant la silice,  $\text{Ph}_3\text{SiOH}$ , a montré une mono-substitution préférentielle avec l'élimination de la diméthylamine via un échange de protons avec le groupe silanol (voir **1a'** dans le schéma 2). La libération de diméthylamine gazeuse a été observée lorsque la réaction a été réalisée en tube RMN en rapport de 1:1. La réaction à une échelle 10 fois plus grande a démontré une mono-substitution claire avec élimination exclusive du  $\text{HNMe}_2$  et absence de tert-butylamine. La poudre jaune, le produit de la réaction, a été séchée, pressée en pastille et analysée par spectroscopie photoélectronique à rayons X (XPS) qui a confirmé l'état d'oxydation  $\text{W}^{6+}$  et la présence de ligands imidures, amidures et aminés dans la sphère de coordination du tungstène(VI) du complexe siloxy. L'observation de ligand amino conduit à suspecter une hydrolyse partielle du produit. Le produit majoritaire de la réaction,  $\text{Ph}_3\text{SiO}-\text{W}(=\text{N}^t\text{Bu})_2(\text{NMe}_2)$  est néanmoins identifié. La réaction de  $\text{Ph}_3\text{SiO}-\text{W}(=\text{N}^t\text{Bu})_2(\text{NMe}_2)$  avec le 1,2-éthanedithiol (EDT) a donné un mélange complexe de

plusieurs produits contenant un précipité rouge-brun et une fraction soluble dans le toluène. Le filtrat a été séché, pressé et étudié par XPS qui a suggéré une réduction formelle de  $W^{6+}$  à  $W^{5+}$ , probablement liée à la formation du ligand persulfido  $S_2^{2-}$  autour du centre du tungstène.<sup>24</sup> La formation de ce ligand persulfide s'explique par l'élimination spontanée de l'éthylène du ligand dithiolate pontant,  $-SCH_2CH_2S-$ , comme le corrobore l'observation directe de l'évolution de l'éthylène en phase gazeuse au cours de la réaction. L'évolution de l'éthylène pour un tel ligand a également plusieurs précédents dans la littérature, parmi lesquels le recuit d'un système de dithiolate d'éthylène siloxy-molybdène étroitement apparenté, développé dans notre groupe.<sup>19</sup> La réduction formelle de  $W^{6+}$  en  $W^{5+}$  pourrait également être expliquée par le couplage de thiols, par analogie avec un précédent où le tungstène dans les nanoparticules d'oxyde W (VI) est réduit par réaction avec des thiols.<sup>25</sup> Le système actuel est encore compliqué par la possibilité de coexistence de groupes thiol et amine pour former un zwitterion,  $((=NH)(HSR))$  par opposition à  $((=NH_2)^+(RS)^-)$ .<sup>26,27</sup> Pour ces deux aspects (possibilité de la formation de liaisons S-S et de formes zwitterioniques), des preuves expérimentales supplémentaires de corroboration sont nécessaires.

En résumé, les preuves moléculaires obtenues par la réaction de  $W(=N^tBu)_2(NMe_2)_2$  – BTBMW – avec le triphénylsilanol suivie d'une réaction avec le 1,2-éthanedithiol suggèrent donc, premièrement, que la réaction de surface ciblée entre le silanol de surface du substrat de départ et le précurseur métallique est possible et, deuxièmement, que la réaction de l'éthanedithiol bien avec des espèces siloxy W(VI) amido, imido est possible. Des réactions secondaires complexes liées à la perte d'éthylène des ponts thiolates, pour former des espèces persulfido et/ou la présence de formes zwitterioniques impliquant le thiol et les résidus amino pourraient compliquer cette chimie.

Le deuxième niveau de modélisation a été atteint en utilisant une silice poreuse solide à haute surface spécifique au lieu de la molécule triphénylsilanol dont nous venons de parler, comme substitut du substrat 2D final à fonctionnaliser. Ceci nous permet d'étudier la réaction à l'interphase gaz-solide, comme habituellement dans les processus ALD, plutôt qu'en solution, comme c'est le cas avec le triphénylsilanol. Au cours de modélisation des quatre premières pulses type ALD étudiés sur la silice, la spectroscopie infrarouge à réflexion diffuse avec transformée de Fourier (DRIFT) a montré une répétabilité périodique. La première impulsion de BTBMW a consommé tous les groupes hydroxyles de surface,  $\equiv Si-OH$ , représentée comme indiqué par la disparition de la

bande d'absorption à  $3747\text{ cm}^{-1}$  et par l'apparition de nouvelles bandes attribuées aux vibrations des liaisons C–H des alkyles dans la région comprise entre  $2700$  et  $3000\text{ cm}^{-1}$ .

Le spectre Raman du complexe imprégné sur la silice a démontré une bonne correspondance avec les bandes Raman du BTBMW uniquement. Les sous-produits volatils de l'imprégnation ont été analysés par RMN qui a montré environ 98 % molaire de  $\text{HNMe}_2$  et 2 % molaire de  $\text{H}_2^t\text{Bu}$ . Le spectre RMN  $^{13}\text{C}$  du produit solide a confirmé la présence d'atomes de carbone primaires ( $32,6\text{ ppm}$ ) et quaternaires ( $66,0\text{ ppm}$ ) du groupe tert-butyle ainsi que les atomes de carbone primaires ( $53,9\text{ ppm}$ ) des ligands diméthylamidure. L'analyse élémentaire de ce premier produit d'impulsion est cohérente avec les autres observations spectroscopiques, et a conduit à la formule moyenne suivante :  $\equiv\text{SiO}-\text{WC}_{10}\text{N}_3\text{H}_{25}$ . Cela a permis de proposer la structure des sites greffés **1a** (qui correspond à la composition atomique qui vient d'être mentionnée) comme illustré dans le schéma 2.

La réaction ultérieure du produit  $\equiv\text{SiO}-\text{WC}_{10}\text{N}_3\text{H}_{25}$  avec l'EDT modélise la réaction de la seconde demi-période du cycle ALD. L'analyse spectrale a montré que le BTBMW à base de silice réagit facilement avec l'EDT, ce qui se voit également par son changement de couleur du jaune au rouge. Le spectre DRIFT enregistré pour le produit rouge montre la disparition des bandes qui étaient auparavant attribuées au ligand  $-\text{NMe}_2$  ou  $\text{N}^t\text{Bu}$  et l'apparition de groupes thiol ( $2572\text{ cm}^{-1}$ ) et de nouveaux groupements hydroxyles de surface ( $3747\text{ cm}^{-1}$ ). Ceci confirme la réussite de la réaction de surface de l'EDT et la présence du groupe fonctionnel disponible pour le greffage de métal à l'impulsion de tungstène suivante. Un large pic entre  $2500$  et  $3500\text{ cm}^{-1}$  est le signe d'une interaction intramoléculaire de type la liaison hydrogène. Les atomes d'hydrogène au soufre peuvent former une liaison hydrogène avec le soufre dithiolate, l'azote amido et les atomes d'oxygène de surface (dans les ponts  $\equiv\text{Si}-\text{O}-\text{Si}\equiv$ ). Des rapports précédents sur les réactions de complexes alkylamido de tungstène et de molybdène avec des thiols et des alcools volumineux ont montré que la substitution des groupes alkylamido peut être incomplète.<sup>28–30</sup> En outre, les sous-produits volatils piégés dans le tube RMN ont révélé la présence d'éthylène, de  $\text{HNMe}_2$  et de  $\text{H}_2\text{N}^t\text{Bu}$ . L'élimination de l'éthylène pourrait faire partie de la voie vers la formation de  $\text{S}_2^{2-}$  qui a été proposée ci-dessus sur la base des données XPS dans le produit moléculaire analogue.

Le modèle moléculaire et le produit lié à la plaquette ont également montré une réduction formelle partielle de  $\text{W}^{6+}$  à  $\text{W}^{5+}$  lors de l'impulsion EDT. Comme dans le cas moléculaire, où des signaux XPS similaires ont été observés, la réduction formelle s'explique par la présence du ligand  $\text{S}_2^{2-}$ .

L'amine coordonnée a augmenté sa fraction atomique par rapport aux atomes d'azote imido et amido, malgré les formes zwitterioniques mentionnées ci-dessus.

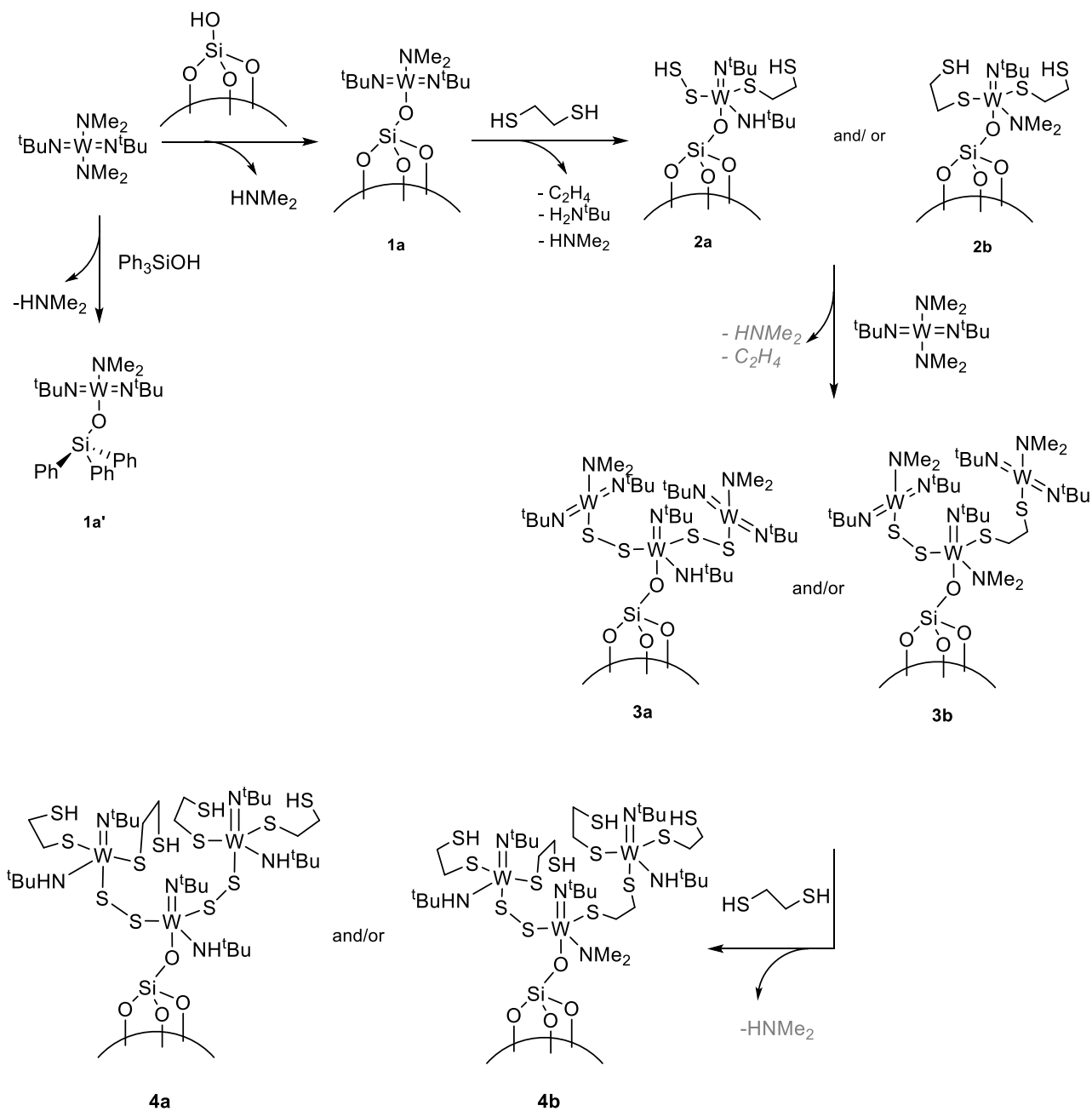


Schéma 2. Proposition simplifiée de réactions de modélisation ALD de la croissance de WS<sub>2</sub> à la surface de SiO<sub>2-700</sub> et en solution avec le modèle moléculaire, Ph<sub>3</sub>SiOH, en utilisant BTBMW et EDT comme précurseurs. Par exemple, la (re)coordination partielle de l'amine éliminée sur les centres du tungstène ainsi que la coexistence de plusieurs espèces de surface, en plus des principales espèces dessinées, ne sont pas indiquées.

La régénération de l'hydroxyle de surface pourrait être la preuve indirecte du couplage des groupes thiol (de sites voisins ou de molécules EDT libres en excès) pour former une liaison –S–S–. En effet, un tel couplage oxydatif peut produire deux électrons et deux protons capables de réduire  $W^{6+}$  et de générer de nouveaux groupes Si–OH en ouvrant des ponts  $\equiv Si-O-Si\equiv$ . Bien que cette proposition soit encore incomplète et doive être corroborée expérimentalement, elle a le potentiel intéressant d'expliquer la réapparition du silanol de surface observée dans l'étude IR.

L'analyse élémentaire du produit en poudre solide après la 1ère impulsion de l'EDT (2ème demi-cycle) a permis de définir la formule moléculaire  $\equiv SiO-WC_{10}N_2S_4H_{25}$ . Elle a permis de proposer les formules étendues suivantes  $\equiv SiO-W(=N^tBu)(NH^tBu)(SCH_2CH_2SH)(SSH)$  (**2a**) et  $\equiv SiO-W(=N^tBu)(NMe_2)(SCH_2CH_2SH)_2$  (**2b**) comme deux structures principales possibles. En même temps, elle est en accord avec les données analytiques disponibles pour les composés liés à la silice, et les preuves XPS acquises sur les espèces moléculaires de triphénylsilanol. La première option (**2a**) peut contenir du persulfure  $S_2^{2-}$  liant les deux atomes de soufre au centre du tungstène. Cela doit encore être confirmé par une caractérisation plus approfondie (par exemple par la RPE). Néanmoins, il existe une nouvelle bande d'absorption dans le spectre Raman qui est apparue lors de la réaction de la deuxième impulsion à  $463,3\text{ cm}^{-1}$ . Cette bande est en accord avec certains rapports de la littérature sur l'identification de la liaison S–S dans les polysulfures.<sup>31</sup> Deux structures pour les produits de réaction ont été proposées dans le schéma 2.

La troisième impulsion, qui est la deuxième addition de BTBMW, réagit avec les produits de la deuxième impulsion (représentés par **2a** et **2b** comme principales espèces de surface) ainsi qu'avec les silanols de surface régénérés dont il a été question plus haut. Le spectre DRIFT montre la consommation de thiols et de bandes de groupes hydroxyles de surface ainsi que l'apparition de bandes de ligands –NMe<sub>2</sub> et =N<sup>t</sup>Bu. Dans l'ensemble, le spectre IR ressemble à celui qui a été acquis lors de la première impulsion de BTBMW. Il en va de même pour les spectres Raman des 1ère et 3ème impulsions. L'analyse élémentaire montre une augmentation de la charge de tungstène de 2,7 fois et a permis d'estimer la formule comme  $\equiv SiO-W_3C_{28}N_8S_4H_{67}$ . Cela nous a permis de proposer les produits de réaction **3a** et **3b** comme illustré dans le schéma 2. Les nouvelles structures sont cohérentes avec les spectres IR et Raman ainsi qu'avec la RMN <sup>13</sup>C à l'état solide.

La 4ème impulsion se déroule de manière similaire à la 2ème impulsion dans laquelle le centre W était lié à 2 équivalents d'EDT. Les spectres RMN <sup>13</sup>C ss, IR et Raman sont en effet presque identiques à ceux observés après la 2ème impulsion, montrant une sorte de périodicité avec chaque

cycle d'EDT. L'analyse élémentaire du produit de la 4e impulsion a montré une augmentation du rapport S/W à 4 et a conduit à la formule suivante :  $\equiv\text{SiO}-\text{W}_3\text{C}_{32}\text{N}_6\text{S}_{12}\text{H}_{75}$ . Les structures **4a** et **4b** ont été proposées pour la 4e impulsion dans le schéma 2.

Les nanoparticules de silice obtenues après 4 impulsions de type ALD ont ensuite été chauffées à 500 °C dans un flux d'hélium, qui a été suivi par DRIFT *operando* couplé à la spectrométrie GC-MS. La diminution des bandes d'absorption attribuées à la vibration des liaisons C-H commence à partir de 110 °C et disparaît complètement au-dessus de 450 °C. Les GC-MS ont montré que la libération d'éthylène, d'isobutène, d'éthanethiol, de thiophène et de thiirane commence dans la plage de 200-250 °C. Ce sont tous des fragments et produits qui pourraient être formés lors de la décomposition des structures proposées pour la 4ème impulsion. Le recuit ex-situ (à la fois sous l'argon à 800 °C et sous l'hydrogène à 450 °C) a révélé la formation de motifs en couches et de nano-domaines cristallins bien structurés. Ces derniers ont permis d'estimer les paramètres des cellules unitaires par calcul FFT, qui sont en accord avec les valeurs théoriques de WS<sub>2</sub> dans la phase 2H (hexagonale). Il est donc proposé que la réduction souhaitée du tungstène en sulfure W<sup>4+</sup> ciblé se produise pendant le recuit.

Sur la base de ce résultat de modélisation, tant au niveau moléculaire qu'au niveau COMS, le processus ALD a été réalisé sur une plaquette de silicium 2D recouverte d'oxyde thermique, et chaque demi-cycle a été étudié par une étude XPS *in situ*. L'analyse XPS du premier produit d'impulsion sur SiO<sub>2</sub>@Si<sub>waf</sub>er a permis de confirmer l'état d'oxydation du W<sup>6+</sup> et du SiO-W dans l'environnement du Si. Le niveau du noyau N 1s a démontré la présence non seulement d'atomes d'azote de type imido et amido, mais aussi d'azote caractéristique d'un groupe amine, ce qui suggère hydrolyse partielle, qu'une partie du sous-produit amine peut rester coordonnée au tungstène. La formation de zwitterions dus au transfert de protons de résidus thiol vers l'amine. Cette dernière hypothèse n'a pas pu être vérifiée par d'autres moyens. Une gamme plus large d'outils spectroscopiques est nécessaire pour étayer ces hypothèses. Les résultats sont en grande partie très proches des preuves recueillies sur les modèles décrits ci-dessus tout en révélant quelques événements mineurs inattendus (par exemple la formation de siliciure de tungstène).

Le recuit ex-situ des thiolates de tungstène ainsi obtenus a été entaché par l'exposition accidentelle à l'air et la formation d'une couche supérieure d'oxyde de tungstène. Néanmoins, après le etching par Ar<sup>+</sup> de la surface, la signature XPS pour WS<sub>2</sub> a pu être trouvée. Pour mieux comprendre les conversions du thiolate moléculaire en WS<sub>2</sub> final, le recuit a été répété directement à l'intérieur de la

chambre XPS (sous ultravide), ce qui a révélé l'abaissement de l'énergie de liaison (BE) du pic  $W_{4f_{7/2}}$  à partir de 300 °C. Cette diminution de BE a mis en évidence la réduction jusqu'au  $W^{4+}$  qui s'est produite parallèlement à la perte des teneurs en carbone, azote et soufre excédentaire. La formation de  $CuS_x$ , probablement due à la contamination du porte-échantillon, a empêché d'observer la transformation complète vers la phase finale prévue.

Lors du recuit *in situ* au microscope électronique à transmission environnementale (E-TEM), les formes lamellaires ont été repérées à 400 °C. La FFT des images a montré que des paramètres de maille correspondent aux paramètres théoriques de la phase 2H de  $WS_2$  ont été observés .

Enfin, la méthode de croissance ALD développée a été appliquée sur les disques de nanotubes d'oxyde de titane TNT's@Ti pour étudier plus en détail les performances photocatalytiques. Les échantillons de disques TNT's@Ti modifiés par l'ALD ont été comparés à des nanotubes non fonctionnalisés dans les tests de génération de photo-courant. La croissance de TNT par anodisation des disques Ti et les tests photo-catalytiques des échantillons ont été effectués pendant la mobilité à l'université de Messine. En raison des contraintes de temps et des restrictions liées à la pandémie, la liste des échantillons étudiés est restée courte. L'amélioration de la génération de photo-courants par rapport aux TNT purs n'a pas pu être réalisée. Bien que diverses conditions, dont un nombre différent de cycles ALD (3 et 5), la température de dépôt du BTBMW (RT et 60 °C) et la pureté du disque de Ti (99,96 et 99,8 %), aient été essayées, une optimisation approfondie est toujours nécessaire.

Les mesures de réduction électrocatalytique du  $CO_2$  ont été réalisées en collaboration avec l'Université Humboldt de Berlin et l'Université de Messine. Plusieurs échantillons de films minces  $WS_2$  crûs par l'ALD sur des nanotubes de carbone multi-parois (MWCNT) ont été préparés à l'aide de BTBMW et  $H_2S$  par le groupe de recherche du Prof Pinna à Berlin. Les poudres résultantes ont été déposées sur la cathode en carbone et testées en réduction électrocatalytique du  $CO_2$  en mode chronoampérométrie. L'acide formique, le monoxyde de carbone et l'hydrogène gazeux ont été observés comme produits principaux. L'efficacité faradique pour la formation de produits à base de carbone à partir du  $CO_2$  était faible bien que les composites testés de  $WS_2@CNT$  soient censés être intéressants en électrocatalyse. Une étude plus approfondie est nécessaire.

En conclusion, cette thèse a contribué à placer la chimie organométallique de surface comme un outil pour l'investigation, la compréhension et la conception d'un nouveau processus ALD visant une chimie précise à partir de la première demi-impulsion et une épaisseur finale aussi difficile que

celle des monocouches. Outre la capacité à jeter les bases d'une croissance prometteuse de WS<sub>2</sub> ultra-mince, ce travail a également permis d'explorer la puissante contribution que les XPS *in situ* et *operando* peuvent apporter lorsqu'on acquiert simultanément une compréhension au niveau moléculaire via des molécules modèles, COMS sur des billes 3D à haute surface spécifique et des supports 2D comme les wafers. Une étude préliminaire timide utilisant la microscopie environnementale pour observer de façon similaire la transformation au niveau atomique pendant l'étape de recuit est également rapportée. Cette combinaison unique de chimie moléculaire, de techniques analytiques sous ultravide et de chimie aux interphases gaz-solide sur des poudres à haute surface spécifique est donc prometteuse pour faire progresser notre capacité à modifier des substrats 2D nanostructurés vers le dépôt de couches minces, ce qui peut être utile pour élaborer des dispositifs de conversion d'énergie efficaces.

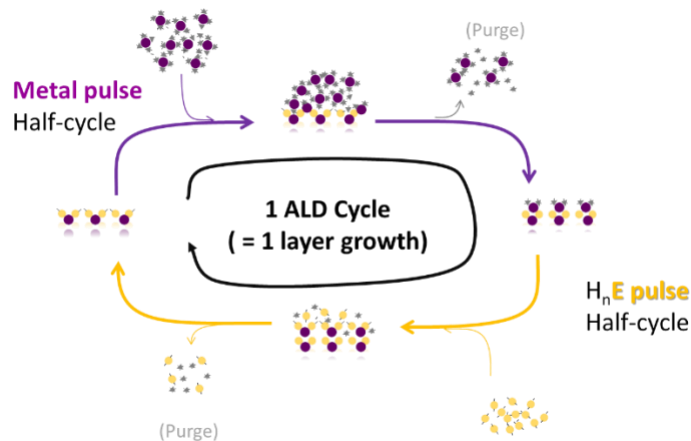
## RÉFÉRENCES :

1. Molaei, M. J. The optical properties and solar energy conversion applications of carbon quantum dots: A review. *Solar Energy* **196**, 549–566 (2020).
2. Ismael, M. Ferrites as solar photocatalytic materials and their activities in solar energy conversion and environmental protection: A review. *Solar Energy Materials and Solar Cells* **219**, 110786 (2021).
3. Dong, C. R., Wang, Y., Zhang, K. & Zeng, H. Halide perovskite materials as light harvesters for solar energy conversion. *EnergyChem* **2**, 100026 (2020).
4. Yu, X. & Sivula, K. Layered 2D semiconducting transition metal dichalcogenides for solar energy conversion. *Current Opinion in Electrochemistry* **2**, 97–103 (2017).
5. Yu, X. & Sivula, K. Toward Large-Area Solar Energy Conversion with Semiconducting 2D Transition Metal Dichalcogenides. *ACS Energy Letters* **1**, 315–322 (2016).
6. Iqbal, M. Z., Alam, S., Faisal, M. M. & Khan, S. Recent advancement in the performance of solar cells by incorporating transition metal dichalcogenides as counter electrode and photoabsorber. *International Journal of Energy Research* **43**, 3058–3079 (2019).
7. Tsai, M. L. *et al.* Monolayer MoS<sub>2</sub> heterojunction solar cells. *ACS Nano* **8**, 8317–8322 (2014).
8. Yin, Z. *et al.* Single-layer MoS<sub>2</sub> phototransistors. *ACS Nano* **6**, 74–80 (2012).
9. Krasnozhan, D., Lembke, D., Nyffeler, C., Leblebici, Y. & Kis, A. MoS<sub>2</sub> transistors operating at gigahertz frequencies. *Nano Lett.* **14**, 5905–5911 (2014).
10. Bertolazzi, S., Krasnozhan, D. & Kis, A. Nonvolatile Memory Cells Based on MoS<sub>2</sub>/Graphene Heterostructures. *Am. Chem. Soc. Nano* **7**, 3246–3252 (2013).
11. Sun, P., Zhang, W., Hu, X., Yuan, L. & Huang, Y. Synthesis of hierarchical MoS<sub>2</sub> and its electrochemical performance as an anode material for lithium-ion batteries. *J. Mater. Chem. A* **2**, 3498–3504 (2014).
12. Xiang, Q., Yu, J. & Jaroniec, M. Synergetic effect of MoS<sub>2</sub> and graphene as cocatalysts for enhanced photocatalytic H<sub>2</sub> production activity of TiO<sub>2</sub> nanoparticles. *J. Am. Chem. Soc.* **134**, 6575–6578 (2012).
13. Yan, Y., Xia, B., Xu, Z. & Wang, X. Recent development of molybdenum sulfides as advanced electrocatalysts for hydrogen evolution reaction. *ACS Catal.* **4**, 1693–1705 (2014).
14. Sobczynski, A. *et al.* Tungsten Disulfide: A Novel Hydrogen Evolution Catalyst for Water Decomposition. *J. Phys. Chem* **92**, 2311–2315 (1988).
15. Wu, Y. *et al.* A Self-Limited Atomic Layer Deposition of WS<sub>2</sub> Based on the Chemisorption and Reduction of Bis(t-butylimino)bis(dimethylamino) Complexes. *Chem. Mater.* **31**, 1881–1890 (2019).
16. Scharf, T. W., Prasad, S. V., Mayer, T. M., Goeke, R. S. & Dugger, M. T. Atomic layer deposition of tungsten disulfide solid lubricant thin films. *J. Mater. Res.* **19**, 3443–3446 (2004).
17. Nandi, D. K., Sen, U. K., Dhara, A., Mitra, S. & Sarkar, S. K. Intercalation based tungsten disulfide (WS<sub>2</sub>) Li-ion battery anode grown by atomic layer deposition. *RSC Adv.* **6**, 38024–

- 38032 (2016).
18. Copéret, C. *et al.* Surface Organometallic and Coordination Chemistry toward Single-Site Heterogeneous Catalysts: Strategies, Methods, Structures, and Activities. *Chem. Rev.* **116**, 323–421 (2016).
  19. Cadot, S. *et al.* A novel 2-step ALD route to ultra-thin MoS<sub>2</sub> films on SiO<sub>2</sub> through a surface organometallic intermediate. *Nanoscale* **9**, 538–546 (2017).
  20. Dezelah IV, C. L. *et al.* Atomic layer deposition of tungsten(III) oxide thin films from W<sub>2</sub>(NMe<sub>2</sub>)<sub>6</sub> and water: Precursor-based control of oxidation state in the thin film material. *J. Am. Chem. Soc.* **128**, 9638–9639 (2006).
  21. Dezelah IV, C. L. *et al.* A low valent metalorganic precursor for the growth of tungsten nitride thin films by atomic layer deposition. *J. Mater. Chem.* **17**, 1109–1116 (2007).
  22. Koch, V. M. *et al.* A solution-based ALD route towards (CH<sub>3</sub>NH<sub>3</sub>)(PbI<sub>3</sub>) perovskite: Via lead sulfide films. *J. Mater. Chem. A* **7**, 25112–25119 (2019).
  23. Wu, Y. *et al.* Atomic Layer Deposition from Dissolved Precursors. *Nano Lett.* **15**, 6379–6385 (2015).
  24. Dupin, J.C., Gonbeau, D., Martin-Litas, I., Vinatier, P. & Levasseur, A. Amorphous oxysulfide thin films MO<sub>y</sub>S<sub>z</sub> (M=W, Mo, Ti) XPS characterization: structural and electronic peculiarities. *Appl. Surf. Sci.* **173**, 140–150 (2001).
  25. Mukherjee, A., Sengupta, S. K., Steeves, D. M., Soares, J. W. & Whitten, J. E. Mechanism of thiol-induced color change of tungsten oxide nanoparticles. *Chem. Phys. Lett.* **752**, (2020).
  26. Bachrach, S. M., Nguyen, T. T. & Demoin, D. W. Microsolvation of cysteine: A density functional theory study. *J. Phys. Chem. A* **113**, 6172–6181 (2009).
  27. Ataman, E., Isvoranu, C., Andersen, J. N., Schnadt, J. & Schulte, K. Unconventional zwitterionic state of l-cysteine. *J. Phys. Chem. Lett.* **2**, 1677–1681 (2011).
  28. Coutelier, O. *et al.* A new donor-stabilized ditungsten amido alkoxido species: Synthesis, crystal structure, fluxionality, and grafting onto silica. *Eur. J. Inorg. Chem.* 5541–5547 (2007). doi:10.1002/ejic.200700732
  29. Chisholm, M. H., Corning, J. F. & Huffman, J. C. Bis(dimethylamine)tetrakis(tert-butyl mercaprido)di-μ-sulfido-dimolybdenum(IV). *Inorg. Chem.* **21**, 286–289 (1982).
  30. Chisholm, M. H., Corning, J. F. & Huffman, J. C. The molybdenum-molybdenum triple bond. 14.<sup>1</sup> preparation and characterization of mixed alkoxy-thiolate compounds of formula Mo<sub>2</sub>(OR)<sub>2</sub>(SAr)<sub>4</sub> (M≡M). *Inorg. Chem.* **23**, 754–757 (1984).
  31. Yu, X. G. *et al.* Lithium storage in conductive sulfur-containing polymers. *J. Electroanal. Chem.* **573**, 121–128 (2004).

# RIASSUNTO ESTESO

Un più ampio uso di energia sostenibile per soddisfare la richiesta energetica della nostra società necessita lo sviluppo di diverse tipologie di dispositivi per la conversione dell'energia (ad esempio da energia solare ad elettrica, da solare a chimica, da elettrica a chimica).<sup>1-6</sup> Poiché le reazioni di conversione avvengono principalmente sulla superficie del materiale attivo, l'ingegneria applicata a tali materiali cerca di massimizzarne l'area superficiale attiva. Le nanostrutture allungate con un alto rapporto di aspetto sono note per essere efficienti nella conversione di energia. La loro funzionalizzazione superficiale con un sottile strato catalitico può migliorarne significativamente le prestazioni. Il rivestimento uniforme di superfici ad alto rapporto di aspetto con un film ultrasottile può essere ottenuto mediante la tecnica di deposizione a strato atomico (in inglese Atomic Layer Deposition -ALD). L'ALD è una tecnica basata sulla successione di due (o più) diverse reazioni superficiali autolimitanti (vedi Schema 1), che permette di controllare lo spessore del film fino ad un monostrato.



Schema 1. Rappresentazione semplificata della crescita del materiale tramite la deposizione a strato atomico (ALD), cioè una successione di due reazioni superficiali autolimitanti all'interfaccia gas-solido: (sopra) il semiciclo basato sul precursore gassoso del metallo e la superficie seguito da (sotto) l'impulso del secondo semiciclo (ad esempio con H<sub>2</sub>O, NH<sub>3</sub>, H<sub>2</sub>S, ecc.), che attraverso le successive reazioni autolimitanti porta idealmente ai materiali desiderati (ad esempio rispettivamente all'ossido, il nitrato o il solfuro di metallo).

La cristallinità, la conformità e la purezza di una pellicola depositata sono qualità essenziali che influenzano le prestazioni in un'applicazione finale. L'ALD si è dimostrata di eccellente utilità non solo per le applicazioni di conversione dell'energia ma anche in molti altri settori come il

rivestimento anticorrosione, la microelettronica, i sistemi nano- e microelettromeccanici, i rivestimenti ottici, i dispositivi elettroluminescenti, ecc. La conoscenza della chimica che si verifica sulla superficie durante un singolo ciclo ALD fornisce il miglior controllo di queste qualità. Può guidare la scelta di precursori e substrati appropriati, di condizioni di processo ottimali in modo da evitare reazioni collaterali indesiderate e migliorare le qualità complessive del materiale depositato. La possibilità di creare film sottili di solfuro di tungsteno,  $WS_2$ , a spessore controllato fino ad un monostrato su supporti nanostrutturati rappresenta sempre di più un valido obiettivo per poter sviluppare dei dispositivi di conversione dell'energia che non prevedono l'utilizzo di metalli nobili.<sup>7-14</sup> Mentre alcuni processi ALD per la crescita di un film sottile di  $WS_2$  già esistono<sup>15-17</sup>, ad oggi però questi non hanno ancora raggiunto il livello di spessore del monostrato né sono riusciti ad evitare l'altamente tossico  $H_2S$  come fonte di zolfo.

L'obiettivo di questa tesi è in primo luogo di porre le basi molecolari per proporre un processo efficace per la crescita ALD del  $WS_2$ , e in secondo luogo di implementare questo modello a livello molecolare alla crescita ultrasottile su supporti reali 2D.

La parte del modello molecolare di questo lavoro di dottorato è incentrata sulla Chimica Organometallica di Superficie (COMS)<sup>18</sup>, che offre una vasta gamma di strumenti spettroscopici e analitici per aiutare a comprendere il meccanismo delle reazioni ALD, come recentemente dimostrato dal nostro gruppo per l'ALD di  $MoS_2$ ,<sup>19</sup> con un approccio che, per quanto a nostra conoscenza, non ha precedenti nella comunità ALD né nella comunità COMS.

In questa tesi, abbiamo testato due precursori del tungsteno,  $W_2(NMe_2)_6$  – HDMDW e  $W(=N^tBu)_2(NMe_2)_2$  - BTBMW, e 1,2-etanditiolo come precursore dello zolfo per la crescita ALD di  $WS_2$ .

Il primo precursore,  $[(Me_2N)_3W \equiv W(NMe_2)_3]$ , hexakis(dimetilammido)ditungsteno (HDMDW) è stato sintetizzato e purificato dalla miscela con la sua forma monomerica  $[(Me_2N)_6W]$ . Poiché il complesso dimerico è stato precedentemente applicato come precursore ALD di altri composti contenenti tungsteno<sup>20,21</sup>, si è pensato che l'HDMDW potesse anche produrre  $WS_2$  nell'ALD, dove la fonte di zolfo è l'EDT.

Uno studio preliminare di chimica molecolare è stato eseguito utilizzando  $(^tBuO)_3SiOH$  e gli studi COMS sono stati effettuati utilizzando  $SiO_2-700$ . Le reazioni molecolari in soluzione hanno mostrato che HDMDW è reattivo verso i gruppi di silanolo, con  $HNMe_2$  è come sottoprodotto. Il prodotto HDMDW reagisce con il gruppo tiolo di EDT precipitando. Gli studi sono quindi passati alla

superficie delle nanosfere di silice, dove le reazioni superficiali in sospensione (con solvente) hanno modellato la ALD in soluzione. Gli spettri IR registrati dopo ogni impulso hanno dimostrato una periodicità in 2 cicli ALD. Vale a dire, un aumento e una diminuzione della banda di vibrazione SH ( $2391\text{ cm}^{-1}$ ) sono stati osservati con ogni impulso EDT e HDMDW, rispettivamente. Al contrario, l'impulso di tungsteno ha aumentato le bande assegnate ai ligandi  $\text{-NMe}_2$ , mentre l'impulso di zolfo ha diminuito queste bande di assorbimento. Tuttavia, la deposizione di HDMDW dalla fase vapore non ha portato al consumo di gruppi idrossilici di superficie. In sospensione, le molecole di solvente sono note per assistere le reazioni (ad esempio, via una migliore diffusione, cambiando la struttura elettronica) che non sono possibili o complicate nella interfase gas-solido.<sup>22,23</sup> La possibilità di utilizzare HDMDW in soluzione ALD per la crescita di  $\text{WS}_2$  resta interessante. Pertanto, la polvere di silice dopo 2 cicli completi di ALD eseguiti in presenza di solvente è stata ricotta ex-situ in argon a  $800\text{ }^\circ\text{C}$ . L'HRTEM della polvere nera ottenuta ha rivelato la formazione di sistemi lamellari e di nanoparticelle cristalline ben ordinate. La distanza stimata ( $0,64\text{ nm}$ ) tra gli strati successivi puntava a  $\text{WS}_2$ , in buon accordo con i dati della letteratura. L'analisi elementare e l'EDX della polvere ricotta hanno mostrato il rapporto S a W previsto, di 2,1:1 e  $2 (\pm 0,7):1$ , rispettivamente.

I primi dati spettroscopici e microscopici indicano la buona crescita positiva della pellicola  $\text{WS}_2$  con il metodo ALD in soluzione. Sono state osservate caratteristiche autolimitanti e periodiche delle reazioni superficiali. Tuttavia, rimane la questione dell'evoluzione dello stato di ossidazione del tungsteno con impulsi ALD e fase di ricottura. Pertanto, sarebbe interessante condurre uno studio XPS per i campioni supportati su silicio o wafer.

La reattività del secondo precursore studiato in questa tesi, bis(tert-butylimido)bis(dimetilammido)tungsteno (VI) (BTBMW) con il composto molecolare modello per la silice,  $\text{Ph}_3\text{SiOH}$ , ha mostrato una mono-sostituzione preferenzialmente attraverso uno scambio di protoni con il gruppo del silanolo e l'eliminazione della dimetilammina (vedi **1a'** nello Schema 2). Quando la reazione è stata condotta in una provetta NMR chiusa, è stato osservato il rilascio di gas dimetilammina. La reazione in una scala 10 volte superiore ha mostrato una chiara mono-sostituzione ad un unico prodotto a base di tungsteno, con un rapporto immido ( $=\text{N}^t\text{Bu}$ ) : ammido ( $\text{-NMe}_2$ ) di 2:1. La polvere gialla, il prodotto di reazione, è stata essiccata, pressata in pellet e analizzata mediante spettroscopia fotoelettrica a raggi X (XPS), che ha confermato lo stato di ossidazione  $\text{W}^{6+}$  e la presenza di immido amido e ammino ligandi nella sfera di coordinazione del

tungsteno (VI) del complesso silossico. La presenza di ammine lascia pensare a reazioni di idrolisi non volute. Ciononostante, il prodotto principale  $\text{Ph}_3\text{SiO}-\text{W}(\text{N}^t\text{Bu})_2(\text{NMe}_2)$  è osservato. La sua ulteriore reazione con 1,2-etanditiolo (EDT) ha prodotto una miscela complessa di diversi prodotti contenenti precipitazione rosso-marrone e frazione solubile in toluene. Il filtrato è stato essiccato, pressato e studiato mediante XPS che ha mostrato una riduzione formale di  $\text{W}^{6+}$  a  $\text{W}^{5+}$  eventualmente dovuta alla formazione di un ligando persolfuro  $\text{S}_2^{2-}$  intorno al centro del tungsteno.<sup>24</sup> La formazione di questo ligando persolfuro si spiega con l'eliminazione spontanea dell'etilene dal ligando ditiolato a ponte,  $-\text{SCH}_2\text{CH}_2\text{S}-$ , come confermato dall'osservazione diretta dell'evoluzione dell'etilene in fase gassosa durante la reazione. L'evoluzione dell'etilene per tale ligando ha anche diversi precedenti in letteratura, come durante la calcinazione di un sistema di ditiolato di etilene di silossil-molibdeno molto simile sviluppato nel nostro gruppo.<sup>19</sup> La riduzione formale di  $\text{W}^{6+}$  a  $\text{W}^{5+}$  potrebbe anche essere spiegata dall'accoppiamento di tioli, in analogia con un precedente in cui il tungsteno in nanoparticelle di ossido W (VI) di tungsteno è ridotto per reazione con i tioli.<sup>25</sup> Il sistema studiato in questa tesi è ulteriormente complicato dalla possibilità di coesistenza tra gruppi di tioli e ammine per formare uno zwitterione  $(=\text{NH})(\text{HSR})$  vs.  $(=\text{NH}_2)^+(\text{SR})$ .<sup>26,27</sup> Per entrambi questi aspetti (rilevanza della formazione del legame S-S e delle forme zwitterioniche) sono necessarie ulteriori prove sperimentali di conferma.

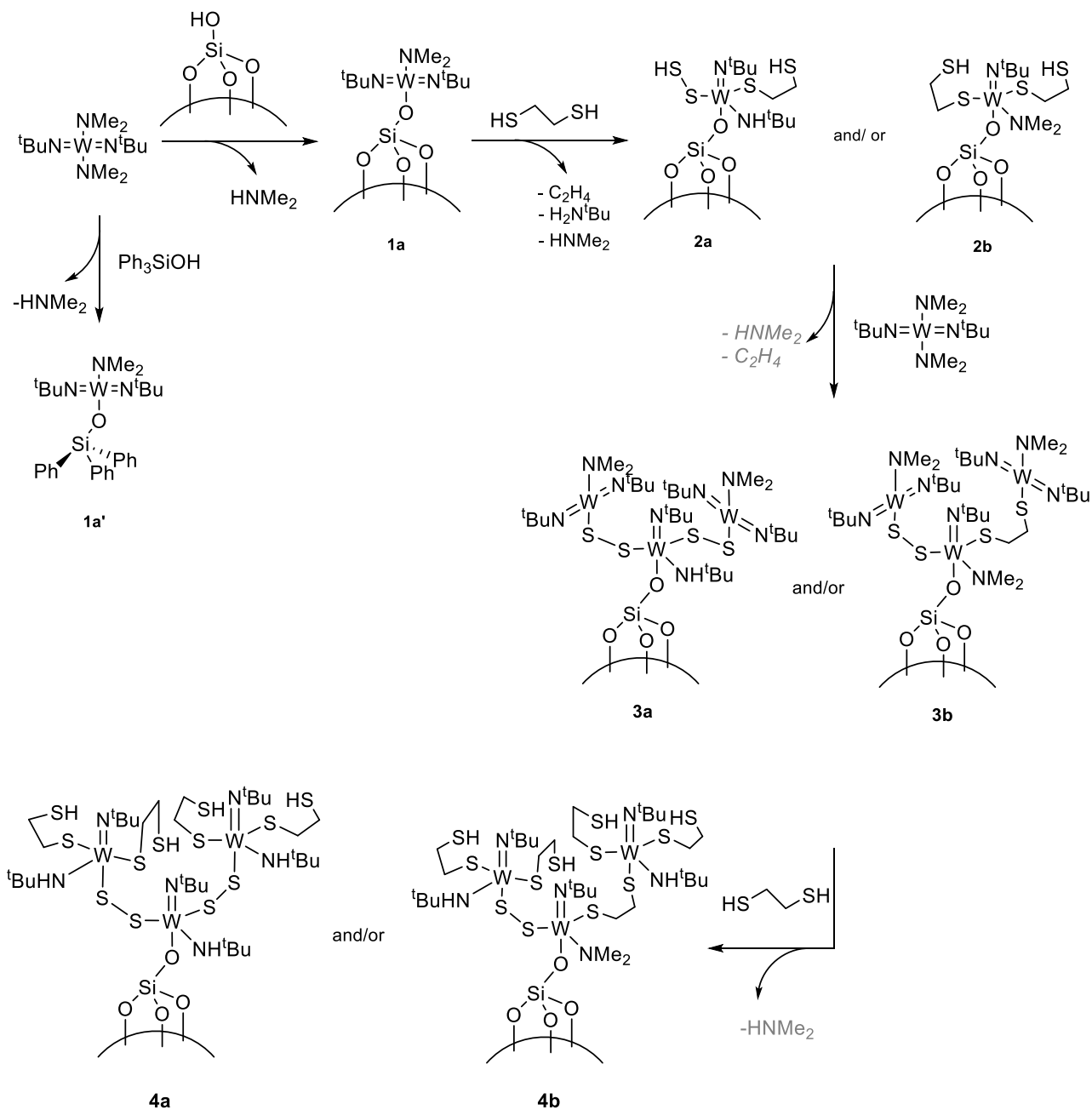
In sintesi, l'evidenza molecolare ottenuta dalla reazione di  $\text{W}(=\text{N}^t\text{Bu})_2(\text{NMe}_2)_2$  – BTBMW con trifenilsilanololo seguita da reazione con 1,2-etanditiolo suggerisce, in primo luogo, che la reazione superficiale desiderata tra il silanololo superficiale del substrato e il precursore metallico in ingresso è fattibile e, in secondo luogo, che l'etanditiolo reagisce con silossi W(VI) ammido, immido, legandosi in modo idoneo per il processo ALD che si desidera effettuare. Complesse reazioni collaterali legate alla perdita di etilene dai ponti tiolati per formare specie di persolfuro e/o la presenza di forme zwitterioniche che coinvolgono il tiolo e i residui amminici potrebbero complicare questa chimica.

Il secondo livello di modellazione è stato ottenuto utilizzando una silice solida e porosa ad alta area superficiale, invece della molecola trifenilsilanololo appena discusso, come miglior modello per il substrato finale 2D da funzionalizzare. Questo secondo livello di modellazione ci permette di indagare la reazione all'interfaccia gas-solido, come è usuale nei processi ALD, piuttosto che in soluzione, come fatto con il trifenilsilanololo. Nel corso dei 4 impulsi ALD modellati sulla silice, lo studio per trasformata di Fourier a infrarossi a riflessione diffusa (DRIFT) ha mostrato una ripetibilità periodica. Il primo impulso della deposizione di vapore di BTBMW ha consumato tutti i

gruppi idrossilici di superficie,  $\equiv\text{Si-OH}$ , come mostrato dalla scomparsa della banda di assorbimento a  $3747\text{ cm}^{-1}$  e ha portato nuove bande attribuite alle vibrazioni del legame alchilico C-H nell'intervallo tra  $2700$  e  $3000\text{ cm}^{-1}$ .

Lo spettro Raman del complesso impregnato su silice ha mostrato una buona corrispondenza con le bande Raman di BTBMW. I sottoprodotti volatili dell'impregnazione sono stati analizzati mediante NMR che ha mostrato ca. 98 mol. % di  $\text{HNMe}_2$  e 2 mol. % di  $\text{H}_2^t\text{Bu}$ . Lo spettro NMR  $^{13}\text{C}$  allo stato solido del prodotto solido ha confermato gli atomi di carbonio primario (32.6 ppm) e quaternario (66.0 ppm) del gruppo ter-butile, nonché gli atomi di carbonio primario (53.9 ppm) dei ligandi dimetilamminici. L'analisi elementare di quel prodotto del primo impulso è stata coerente con le altre osservazioni spettroscopiche e ha portato alla formula media seguente:  $\equiv\text{SiO-WC}_{10}\text{N}_3\text{H}_{25}$ . Questo ha permesso di proporre la struttura dei siti greffati **1a** (che corrisponde alla composizione atomica appena menzionata) come illustrato nello Schema 2.

L'ulteriore reazione del prodotto del primo impulso con EDT permette di modellare la 2° reazione a metà ciclo dell'ALD. L'analisi spettrale ha mostrato che il BTBMW supportato da silice reagisce prontamente con l'EDT, come è possibile vedere anche dal cambiamento di colore dal giallo al rosso. Lo spettro DRIFT registrato per il prodotto rosso mostra la scomparsa delle bande precedentemente assegnate al ligando  $-\text{NMe}_2$  e  $=\text{N}^t\text{Bu}$  e la comparsa di tiolo ( $2572\text{ cm}^{-1}$ ) e di nuovi gruppi di idrossile di superficie ( $3747\text{ cm}^{-1}$ ). Ciò conferma la riuscita della reazione superficiale dell'EDT e la presenza del gruppo funzionale disponibile per il seguente impulso al tungsteno. Un ampio picco tra  $2500$  e  $3500\text{ cm}^{-1}$  rappresenta un segno di interazione intramolecolare di tipo legame ad idrogeno. Tale interazione potrebbe essere prodotta dalla produzione di dimetilammina o ter-butilammina che può ancora essere coordinata al centro del metallo. Gli atomi di idrogeno legati all'azoto e allo zolfo possono creare un legame a idrogeno con lo zolfo ditiolato, l'azoto ammido e gli atomi di ossigeno di superficie (in ponti  $\equiv\text{Si-O-Si}\equiv$ ). I precedenti rapporti sulle reazioni dei complessi alchilammidici di tungsteno e molibdeno con tioli e alcoli voluminosi hanno mostrato che la sostituzione dei gruppi alchilammidici può essere incompleta.<sup>28-30</sup> Inoltre, i sottoprodotti volatili intrappolati nel tubo NMR hanno rivelato la presenza di etilene,  $\text{HNMe}_2$ , e  $\text{H}_2\text{N}^t\text{Bu}$ . L'eliminazione dell'etilene potrebbe essere una parte del percorso verso la formazione di  $\text{S}_2^{2-}$  che è stato prima proposto sulla base dei dati XPS relativi al prodotto molecolare analogo. Il modello molecolare e il prodotto legato al wafer hanno anche mostrato una parziale riduzione formale di  $\text{W}^{6+}$  a  $\text{W}^{5+}$  sull'impulso EDT. Come nel caso molecolare, dove sono stati osservati segnali XPS simili, la riduzione formale si spiega con la presenza del ligando  $\text{S}_2^{2-}$ .



Schema 2. Reazioni semplificate proposte per la modellazione ALD della crescita di WS<sub>2</sub> sulla superficie di SiO<sub>2-700</sub> e in soluzione con il modello molecolare Ph<sub>3</sub>SiOH, utilizzando BTBMW e EDT come precursori. Ad esempio, la parziale (ri)coordinazione parziale dell'ammina eliminata sui centri di tungsteno così come la coesistenza di diverse specie di superficie, sopra le principali specie disegnate, non sono mostrate.

La rigenerazione dell'idrossile superficiale potrebbe essere una prova indiretta dell'accoppiamento di gruppi tiolici (di siti vicini o di molecole EDT libere in eccesso) per formare un legame –S–S–.

Infatti tale accoppiamento ossidativo può produrre due elettroni e due protoni capaci di ridurre il  $W^{6+}$  e generare nuovi gruppi Si–OH aprendo ponti  $\equiv Si-O-Si\equiv$ . Sebbene questa proposta sia ancora incompleta e debba essere confermata sperimentalmente, essa ha il potenziale interessante di spiegare la ricomparsa del silanolo di superficie osservato nello studio IR.

L'analisi elementare del prodotto solido in polvere dopo il 1° impulso di EDT (2° semiciclo) ha permesso di definire la formula molecolare come  $\equiv SiO-WC_{10}N_2S_4H_{25}$ . Inoltre ha permesso di proporre le seguenti formule estese  $\equiv SiO-W(=N^tBu)(NH^tBu)(SCH_2CH_2SH)(SSH)$  (**2a**) e  $\equiv SiO-W(=N^tBu)(NMe_2)(SCH_2CH_2SH)_2$  (**2b**) come due possibili strutture principali. La riduzione del tungsteno è stata omessa in questa fase nelle strutture principali proposte, poiché l'XPS non è stato effettuato per i campioni supportati da silice. Allo stesso tempo, ciò è in accordo con i dati analitici disponibili per i composti legati al silicio e con le prove XPS acquisite sulle specie di trifenilsilanolo molecolare. La prima opzione (**2a**) può contenere persolfuro  $S_2^{2-}$  che lega entrambi gli atomi di zolfo al centro di tungsteno. Questo deve ancora essere confermato mediante una caratterizzazione più approfondita (ad esempio tramite EPR). Una nuova banda di assorbimento nello spettro Raman compare a  $463,3\text{ cm}^{-1}$  durante secondo impulso. Questa banda è in accordo con alcuni rapporti di letteratura sull'identificazione del legame S–S nei polisolfuri.<sup>31</sup> Nello Schema 2 sono state proposte due strutture per i prodotti di reazione.

Il terzo impulso, cioè la seconda reazione di BTBMW, reagisce con i prodotti del secondo impulso (rappresentati da **2a** e **2b** come specie di superficie principale) così come con i silanoli di superficie rigenerati discussi sopra. Di conseguenza, lo spettro DRIFT mostra il consumo di tiolo e di gruppi ossidrilici di superficie e la comparsa di bande di ligandi  $-NMe_2$  e  $=N^tBu$ . Complessivamente lo spettro IR e lo spettro Raman assomigliano a quelli che sono stati acquisiti al 1° impulso di BTBMW. L'analisi elementare mostra un aumento del carico di tungsteno di 2.7 volte dando una formula media  $\equiv SiO-W_3C_{28}N_8S_4H_{67}$ . Questo ci ha permesso di proporre i prodotti di reazione **3a** e **3b** come illustrato nello Schema 2. Le nuove strutture sono coerenti con gli spettri IR, Raman e con lo stato solido  $^{13}C$  NMR.

Il 4° impulso sembra procedere in modo simile al percorso del 2° impulso in cui il centro W era legato a 2 equivalenti di EDT. Gli spettri ss  $^{13}C$  NMR, IR, e Raman sono in effetti quasi identici a quelli visti dopo il 2° impulso, mostrando una sorta di periodicità con ogni ciclo ALD. L'analisi elementare del prodotto del 4° impulso ha mostrato un aumento del rapporto S/W a 4 e ha definito

la formula come  $\equiv\text{SiO}-\text{W}_3\text{C}_{32}\text{N}_6\text{S}_{12}\text{H}_{75}$ . Seguendo le due opzioni del 3° impulso, le strutture **4a** e **4b** sono state proposte per il 4° impulso nello Schema 2.

I nano-grani di silice dopo 4 impulsi mediante modellazione ALD sono stati poi riscaldati a 500 °C in flusso di elio, che è stato monitorato mediante DRIFT in *operando* accoppiato con la spettrometria GC-MS. La diminuzione delle bande di assorbimento assegnate alla vibrazione dei legami C–H inizia da 110 °C e scompare completamente al di sopra dei 450 °C. I grafici GC-MS hanno mostrato che il rilascio di etilene, isobutene, etantiolo, tiofene e tiirano inizia nell'intervallo 200-250 °C. Questi sono tutti i possibili frammenti e prodotti che potrebbero formarsi in seguito alla decomposizione delle strutture proposte per il 4° impulso. La calcinazione *ex-situ* (sia in argon a 800 °C che in idrogeno a 450 °C) della polvere ha rivelato la formazione di edifici lamellar e nano-cristalli ben strutturati. Quest'ultima ha permesso di stimare i parametri della cella unitaria tramite il calcolo FFT, che è risultato in accordo con i valori teorici di  $\text{WS}_2$  nella fase 2H (esagonale). Pertanto, si propone che durante la calcinazione il tungsteno si riduce al solfuro di  $\text{W}^{4+}$  desiderato.

Sulla base di questo risultato di modellazione, sia a livello molecolare che di COMS, il processo ALD è stato eseguito su un wafer di silicio 2D ricoperto di ossido termico, e ogni semi-ciclo è stato studiato mediante analisi XPS *in situ*. Più precisamente, l'analisi XPS del prodotto del primo impulso su  $\text{SiO}_2$ @Siwafer ha permesso di confermare lo stato di ossidazione  $\text{W}^{6+}$  e di legami SiO–W. Il livello del nucleo N 1s ha dimostrato la presenza non solo di atomi di azoto di tipo immido e ammido, ma anche di azoto compatibile con un gruppo amminico, suggerendo così che alcuni sottoprodotti amminici della reazione a metà ciclo possano rimanere coordinati al tungsteno e/o idrolisi avventizia. La formazione di ammina coordinata potrebbe anche suggerire l'esistenza di zwitterioni dovuti al trasferimento di protoni dai residui tiolo all'ammina. Quest'ultima ipotesi dovrebbe essere verificata con altri mezzi. In generale, i risultati restano in gran parte molto vicini alle prove raccolte sui modelli descritti sopra, mentre rivelano alcuni eventi minori inattesi (ad esempio la formazione di siliciuro di tungsteno).

L'annealing (ricottura) *ex-situ* dei tiolati di tungsteno ottenuti è stata danneggiata dall'esposizione accidentale all'aria e dalla formazione di uno strato superiore di ossido di tungsteno. Tuttavia, dopo l'attacco superficiale con  $\text{Ar}^+$ , la firma XPS per il  $\text{WS}_2$  è stata individuata. Per ottenere una migliore comprensione delle conversioni del tiolato molecolare al  $\text{WS}_2$  finale, l'annealing è stata ripetuta *in operando* direttamente all'interno della camera XPS (in condizioni di vuoto spinto), che ha rivelato l'abbassamento dell'energia di legame del picco W 4f<sub>7/2</sub> (BE) a partire da 300 °C. Questa

diminuzione del BE indicava la riduzione fino al  $W^{4+}$  che è arrivata in parallelo con la perdita del carbonio, dell'azoto e dell'eccesso di contenuto di zolfo. La formazione spuria di  $CuS_x$ , probabilmente dovuta alla contaminazione del portacampioni, ha impedito di osservare la completa trasformazione alla fase finale prevista.

Mediante annealing *in situ* nel microscopio elettronico a trasmissione ambientale (E-TEM), le forme lamellar sono state individuate a 400 °C. Un diverso rivestimento di silice del wafer e della griglia TEM potrebbe influire sulla facilità di cristallizzazione del  $WS_2$ . La FFT raggiunta delle immagini ha mostrato che i parametri delle cellule unitarie corrispondono ai parametri teorici della fase 2H del  $WS_2$ .

Infine, il metodo di crescita ALD sviluppato è stato applicato sui dischi TNT@Ti per indagare ulteriormente le prestazioni fotocatalitiche. I campioni di dischi di TNT@Ti modificati con ALD e incontaminati sono stati confrontati nei test di generazione di fotocorrenti. La crescita di TNT tramite anodizzazione dei dischi Ti e i test fotocatalitici dei campioni sono stati effettuati durante la mobilità nell'Università di Messina. A causa dei vincoli temporali e delle restrizioni pandemiche, l'elenco dei campioni studiati è stato limitato. Non è stato possibile migliorare la generazione di fotocatalisi rispetto al TNT incontaminato. Sebbene siano state provate varie condizioni, tra cui un diverso numero di cicli di ALD (3 e 5), una diversa temperatura di deposizione di BTBMW (temperatura ambiente e 60 °C), e diversa purezza del disco di Ti (99,96 e 99,8 %), è necessario investigare ulteriormente.

La riduzione elettrocatalitica di  $CO_2$  è stata effettuata in collaborazione con l'Università Humboldt di Berlino. Diversi campioni di film sottile  $WS_2$  cresciuti via ALD su nanotubi di carbonio a parete multipla (MWCNTs) sono stati preparati utilizzando BTBMW e  $H_2S$  dal gruppo di ricerca del Prof. N. Pinna di Berlino. Le polveri risultanti sono state spruzzate sull'elettrodo di carbonio e testate in riduzione elettrocatalitica della  $CO_2$  come catodo in modalità cronoamperometrica. Come prodotti principali sono stati osservati acido formico, monossido di carbonio e idrogeno gassoso. L'efficienza faradaica verso la formazione di prodotti a base di carbonio da  $CO_2$  è stata bassa, anche se i compositi  $WS_2@CNT$  sono riportati essere interessanti nella elettrocatalisi in precedenti lavori di letteratura. Sono necessari ulteriori studi.

In conclusione, questa tesi ha contribuito a valutare ulteriormente la COMS come un valido strumento per l'indagine, la comprensione e la progettazione di un nuovo processo ALD che mira ad una chimica precisa a partire già dal primo mezzo impulso e ad uno spessore finale di solo un monostrato. Oltre alla capacità di gettare le basi per una promettente crescita ultrasottile del WS<sub>2</sub>, questo lavoro ha anche esplorato il potente contributo che XPS *in situ* e *in operando* può dare comprendendo sia a livello molecolare tramite molecole modello, che tramite COMS su grani 3D ad alta area superficiale e supporti 2D come i wafer. È stato anche riportato il primo studio che utilizza la microscopia ambientale per testimoniare la trasformazione del livello atomico durante la fase di ricottura. Questa combinazione unica di chimica molecolare, tecniche analitiche *in operando* in vuoto spinto e chimica all'interfaccia gas-solido sulle polveri ad alta superficie è quindi molto promettente circa l'avanzamento della nostra capacità di modificare substrati 2D nanostrutturati verso la deposizione di film sottili, che possono essere cruciali per lo sviluppo di dispositivi efficienti per la conversione dell'energia.

## RIFERIMENTI :

1. Molaei, M. J. The optical properties and solar energy conversion applications of carbon quantum dots: A review. *Solar Energy* **196**, 549–566 (2020).
2. Ismael, M. Ferrites as solar photocatalytic materials and their activities in solar energy conversion and environmental protection: A review. *Solar Energy Materials and Solar Cells* **219**, 110786 (2021).
3. Dong, C. R., Wang, Y., Zhang, K. & Zeng, H. Halide perovskite materials as light harvesters for solar energy conversion. *EnergyChem* **2**, 100026 (2020).
4. Yu, X. & Sivula, K. Layered 2D semiconducting transition metal dichalcogenides for solar energy conversion. *Current Opinion in Electrochemistry* **2**, 97–103 (2017).
5. Yu, X. & Sivula, K. Toward Large-Area Solar Energy Conversion with Semiconducting 2D Transition Metal Dichalcogenides. *ACS Energy Letters* **1**, 315–322 (2016).
6. Iqbal, M. Z., Alam, S., Faisal, M. M. & Khan, S. Recent advancement in the performance of solar cells by incorporating transition metal dichalcogenides as counter electrode and photoabsorber. *International Journal of Energy Research* **43**, 3058–3079 (2019).
7. Tsai, M. L. *et al.* Monolayer MoS<sub>2</sub> heterojunction solar cells. *ACS Nano* **8**, 8317–8322 (2014).
8. Yin, Z. *et al.* Single-layer MoS<sub>2</sub> phototransistors. *ACS Nano* **6**, 74–80 (2012).
9. Krasnozhan, D., Lembke, D., Nyffeler, C., Leblebici, Y. & Kis, A. MoS<sub>2</sub> transistors operating at gigahertz frequencies. *Nano Lett.* **14**, 5905–5911 (2014).
10. Bertolazzi, S., Krasnozhan, D. & Kis, A. Nonvolatile Memory Cells Based on MoS<sub>2</sub>/Graphene Heterostructures. *Am. Chem. Soc. Nano* **7**, 3246–3252 (2013).
11. Sun, P., Zhang, W., Hu, X., Yuan, L. & Huang, Y. Synthesis of hierarchical MoS<sub>2</sub> and its electrochemical performance as an anode material for lithium-ion batteries. *J. Mater. Chem. A* **2**, 3498–3504 (2014).
12. Xiang, Q., Yu, J. & Jaroniec, M. Synergetic effect of MoS<sub>2</sub> and graphene as cocatalysts for enhanced photocatalytic H<sub>2</sub> production activity of TiO<sub>2</sub> nanoparticles. *J. Am. Chem. Soc.* **134**, 6575–6578 (2012).
13. Yan, Y., Xia, B., Xu, Z. & Wang, X. Recent development of molybdenum sulfides as advanced electrocatalysts for hydrogen evolution reaction. *ACS Catal.* **4**, 1693–1705 (2014).
14. Sobczynski, A. *et al.* Tungsten Disulfide: A Novel Hydrogen Evolution Catalyst for Water Decomposition. *J. Phys. Chem* **92**, 2311–2315 (1988).
15. Wu, Y. *et al.* A Self-Limited Atomic Layer Deposition of WS<sub>2</sub> Based on the Chemisorption and Reduction of Bis(t-butylimino)bis(dimethylamino) Complexes. *Chem. Mater.* **31**, 1881–1890 (2019).
16. Scharf, T. W., Prasad, S. V., Mayer, T. M., Goeke, R. S. & Dugger, M. T. Atomic layer deposition of tungsten disulfide solid lubricant thin films. *J. Mater. Res.* **19**, 3443–3446 (2004).
17. Nandi, D. K., Sen, U. K., Dhara, A., Mitra, S. & Sarkar, S. K. Intercalation based tungsten disulfide (WS<sub>2</sub>) Li-ion battery anode grown by atomic layer deposition. *RSC Adv.* **6**, 38024–

- 38032 (2016).
18. Copéret, C. *et al.* Surface Organometallic and Coordination Chemistry toward Single-Site Heterogeneous Catalysts: Strategies, Methods, Structures, and Activities. *Chem. Rev.* **116**, 323–421 (2016).
  19. Cadot, S. *et al.* A novel 2-step ALD route to ultra-thin MoS<sub>2</sub> films on SiO<sub>2</sub> through a surface organometallic intermediate. *Nanoscale* **9**, 538–546 (2017).
  20. Dezelah IV, C. L. *et al.* Atomic layer deposition of tungsten(III) oxide thin films from W<sub>2</sub>(NMe<sub>2</sub>)<sub>6</sub> and water: Precursor-based control of oxidation state in the thin film material. *J. Am. Chem. Soc.* **128**, 9638–9639 (2006).
  21. Dezelah IV, C. L. *et al.* A low valent metalorganic precursor for the growth of tungsten nitride thin films by atomic layer deposition. *J. Mater. Chem.* **17**, 1109–1116 (2007).
  22. Koch, V. M. *et al.* A solution-based ALD route towards (CH<sub>3</sub>NH<sub>3</sub>)(PbI<sub>3</sub>) perovskite: Via lead sulfide films. *J. Mater. Chem. A* **7**, 25112–25119 (2019).
  23. Wu, Y. *et al.* Atomic Layer Deposition from Dissolved Precursors. *Nano Lett.* **15**, 6379–6385 (2015).
  24. Dupin, J.C., Gonbeau, D., Martin-Litas, I., Vinatier, P. & Levasseur, A. Amorphous oxysulfide thin films MO<sub>y</sub>S<sub>z</sub> (M=W, Mo, Ti) XPS characterization: structural and electronic peculiarities. *Appl. Surf. Sci.* **173**, 140–150 (2001).
  25. Mukherjee, A., Sengupta, S. K., Steeves, D. M., Soares, J. W. & Whitten, J. E. Mechanism of thiol-induced color change of tungsten oxide nanoparticles. *Chem. Phys. Lett.* **752**, (2020).
  26. Bachrach, S. M., Nguyen, T. T. & Demoin, D. W. Microsolvation of cysteine: A density functional theory study. *J. Phys. Chem. A* **113**, 6172–6181 (2009).
  27. Ataman, E., Isvoranu, C., Andersen, J. N., Schnadt, J. & Schulte, K. Unconventional zwitterionic state of l-cysteine. *J. Phys. Chem. Lett.* **2**, 1677–1681 (2011).
  28. Coutelier, O. *et al.* A new donor-stabilized ditungsten amido alkoxido species: Synthesis, crystal structure, fluxionality, and grafting onto silica. *Eur. J. Inorg. Chem.* 5541–5547 (2007). doi:10.1002/ejic.200700732
  29. Chisholm, M. H., Corning, J. F. & Huffman, J. C. Bis(dimethylamine)tetrakis(tert-butyl mercaprido)di-μ-sulfido-dimolybdenum(IV). *Inorg. Chem.* **21**, 286–289 (1982).
  30. Chisholm, M. H., Corning, J. F. & Huffman, J. C. The molybdenum-molybdenum triple bond. 14.<sup>1</sup> preparation and characterization of mixed alkoxy-thiolate compounds of formula Mo<sub>2</sub>(OR)<sub>2</sub>(SAr)<sub>4</sub> (M≡M). *Inorg. Chem.* **23**, 754–757 (1984).
  31. Yu, X. G. *et al.* Lithium storage in conductive sulfur-containing polymers. *J. Electroanal. Chem.* **573**, 121–128 (2004).

Chapter 1 - **GENERAL**  
**INTRODUCTION**

## 1.1 PART 1 Energy conversion devices and the relevance of ALD

### 1.1.1. General considerations

Rates of growing CO<sub>2</sub> concentration are unprecedented over the last century. Starting from the mid of the 18<sup>th</sup> century, the emissions rate of anthropogenic greenhouse gases reached about 5 billion tons annually in the mid of the 20<sup>th</sup> century, and then grew to 35 billion tons with a nearly exponential growth since until 2019 (see Figure 1. 1)<sup>32</sup>. Activities that involve the use of fossil fuel energy are the main cause. The energy of fossils has undoubtedly been essential for industrial development until today and still is. Notwithstanding that the various fossil resources are not necessarily very close to depletion<sup>33–35</sup>, it is time now to massively investigate strategy towards renewable sources harnessing and integration in the production systems.

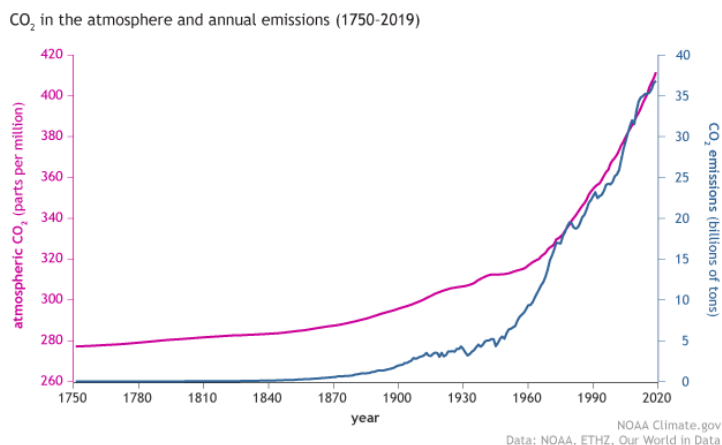


Figure 1. 1. The growing concentration of carbon dioxide in the atmosphere (purple line) along with anthropogenic CO<sub>2</sub> emissions (blue line) between 1750 and 2019. (no permission for reuse is required by the author)<sup>35</sup>

One of the sustainable energy long-term plans includes the conversion of solar energy to fuels.<sup>36,37</sup> This can be done by using the energy of solar irradiation to generate electricity,<sup>38,39</sup> to form H<sub>2</sub> fuel from water protons,<sup>40</sup> or to convert other energy carriers (such as CO<sub>2</sub>, CH<sub>4</sub>, or N<sub>2</sub>) to fuels.<sup>41–44</sup> There are of course other potential applications of solar energy that have been investigated for the last decades. Photochemical biomass transformation to produce chemical feedstock or degradation of organic pollutants being two examples of research fields in photo-assisted green chemistry. Different types of energy conversion devices<sup>1–6</sup> such as photovoltaics (solar to electrical), photo(electro)chemical cells for water splitting, photodegradation, CO<sub>2</sub> reduction and many others are therefore under development.

All of these approaches require materials with a high capability of absorbing light, coupled to the effective channeling of the ensuing photogenerated electrons and/or holes to the desired chemical reaction. The material structure engineering aims to direct the photogenerated electrons and holes into desired reactions while avoiding their recombination. For example, absorption of solar irradiation by solar cells can be maximized not only by locating panels at open spots seeing the sun more frequently or tracking it from sunrise to sunset, but also by enlarging the active surface area of the material able to absorb and convert the light. Interconversion between other energy forms (chemical, electrical) can also be increased by increasing the geometric surface area of the interface. However, at some moment the geometric surface area will reach the point at which the conversion is limited by charge carriers' diffusion. Therefore, a balance must be achieved between the elongation of the interface and maintaining short pathways.<sup>45</sup>

Transport of charge carriers at the interface and away from it plays a crucial role in the conversion of energy from light to electrical forms (solar cells), from light to chemical forms (photosynthesis), and from chemical to electrical forms (batteries, fuel cells). These charge carriers differ depending on the reaction involved in the conversion. For instance, solar cells produce electrons and holes at the interface of two solid semiconductors, lithium-ion batteries exchange electrons and  $\text{Li}^+$  ions at the interface of a solid electrode and liquid electrolyte, and photosynthetic reactions involve the production of molecules and ions between two liquids separated by a membrane.

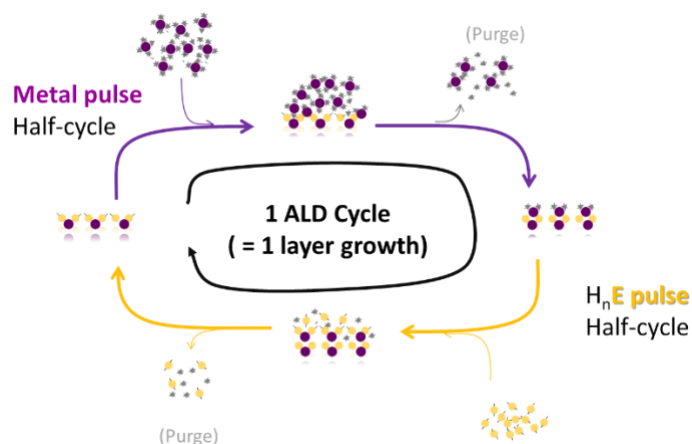
Therefore, the wise design of the geometry of the top surface material in energy conversion applications is highly important.

### 1.1.2. Relevance of ALD

Nanostructured materials, which present elongated structures with very large aspect ratios, can strike the desired balance between large interface areas and short transport paths of charge carriers, two properties simultaneously necessary for efficient energy conversion devices, as described above.<sup>45-47</sup> At the same time, the “bare” nanostructured materials might require further surface functionalization to add a further component to the device (such as a catalytic layer for example).<sup>48,49</sup> Classical surface modification approaches, such as wet impregnation techniques, might be inefficient for such substrates due to the high aspect ratios of the nanostructures. For example, initial (easier)

functionalization of the easily accessible areas might become a physical impediment for the subsequent functionalization of the full surface.

One method enabling functionalization of non-planar nanostructured support, forming a uniform thin layer even on substrates with a large surface with a thickness control down to a monolayer was discovered at the end of the last century and later termed Atomic Layer Deposition (ALD).<sup>50</sup> ALD is a unique technique executed in two (or more) main steps based on the succession of two different self-limiting surface reactions (see Scheme 1. 1).



Scheme 1. 1. Simplified representation of material growth by atomic layer deposition (ALD), that is a succession of two self-limiting surface reactions at the gas-solid interphase: (above) the half-cycle based on the gaseous metal precursor and the surface followed by (below) the second half cycle pulse (e.g. with  $\text{H}_2\text{O}$ ,  $\text{NH}_3$ ,  $\text{H}_2\text{S}$ , etc.), which through the second self-limiting reactions ideally leads to the desired materials (e.g. metal oxide, nitride or sulfide, respectively).

Ideally, in the first step, the substrate retains a single monolayer upon reaction with the first reactive gas in low pressure. The gas pulse is followed by evacuation or purging of the chamber with inert gas to remove unreacted excess precursor and volatile byproducts. A self-limiting monolayer is formed on the substrate through chemical bonds between the incoming gaseous reactant and the functional groups available on the surface of the substrate. In the next step, always ideally, the second gaseous reactive is injected in the chamber that leads to a further chemical reaction with the functional groups of the just formed top layer. Unreacted reactant and byproducts are removed by evacuating in a dynamic vacuum or purging with inert gas. These steps make one full cycle of ALD, which is repeated until the desired film thickness is achieved.

An ideal ALD process is robust with respect to several chemical physics and process engineering parameters; within a certain temperature window (called an ALD window), some fluctuations in temperature or flow dynamics do not strongly disrupt the quality of the film.

The ALD method also makes it possible to achieve extremely conformal ultrathin films. Nowadays, with the pressure to reduce the cost of production of microelectronic and nanotechnology devices in the semiconductor industry, the film features such as uniform topography and nanometer thickness become more important than quick deposition rates. Therefore, the ALD processes are more probable for the eventual use of such applications. The ALD processes demonstrate high beneficial use in the following fields: microelectromechanical and nanoelectromechanical systems (MEMS/NEMS), thin-film magnetic heads for reading and writing hard disc drives, coating nanomaterials and porous objects, catalysis, optical coatings, thin-film electroluminescent displays, anti-corrosion layers, and solar cells.<sup>50</sup>

### 1.1.3. Interest in WS<sub>2</sub> monolayer and ultrathin deposit

Since the early 1960's MoS<sub>2</sub> and WS<sub>2</sub> transition metal dichalcogenides (TMDs) have received growing interest as lubricants<sup>51,52</sup> and heterogeneous catalysts<sup>53</sup>. These MX<sub>2</sub> compounds (M = transition metal like Mo or W, X = S) form structurally and chemically well-defined layered structure, where the transition metal atomic layer is located between two chalcogen atomic layers. Bonds are strong within each X-M-X layer, while they are bound by weak electrostatic interactions between layers. Due to such properties of the crystal structure and high thermal stability, few of these TMDs have been utilized as lubricant materials. The low friction feature of these materials originates inter alia from weak van der Waals interactions between the planes that causes the low shear strength between neighboring layers. Besides lubricant properties, molybdenum and tungsten disulfides are crucial catalysts in hydrodesulfurization (HDS), hydrodenitrogenation (HDN) and other key reactions in the hydro treating process of oil fractions.<sup>53,54</sup>

Very recently new properties emerged when the TMDs are exfoliated down to a monolayer or to atomically thin layers (i.e. 2 or 3 layers), which we will collectively call *ultrathin* deposits. For example, a monolayer of MoS<sub>2</sub> becomes a direct bandgap semiconductor, while thicker deposit (still called *thin* in the current literature because they can be at the nanometric level) are not. The ultrathin layers display strong photoluminescence (PL) in the visible light which can be suitable for photovoltaic devices,<sup>7</sup> photodetectors,<sup>8</sup> transistors<sup>9</sup>, or memory devices<sup>10</sup>. Few layers of MoS<sub>2</sub> and

WS<sub>2</sub> can be applied as an electrode in Li-ion batteries<sup>11,55</sup> and as a catalyst for Hydrogen Evolution Reaction (HER)<sup>12-14</sup>. Figure 1. 2 displays the most studied applications of the 2D TMDs in various fields from electronic devices to sensors.

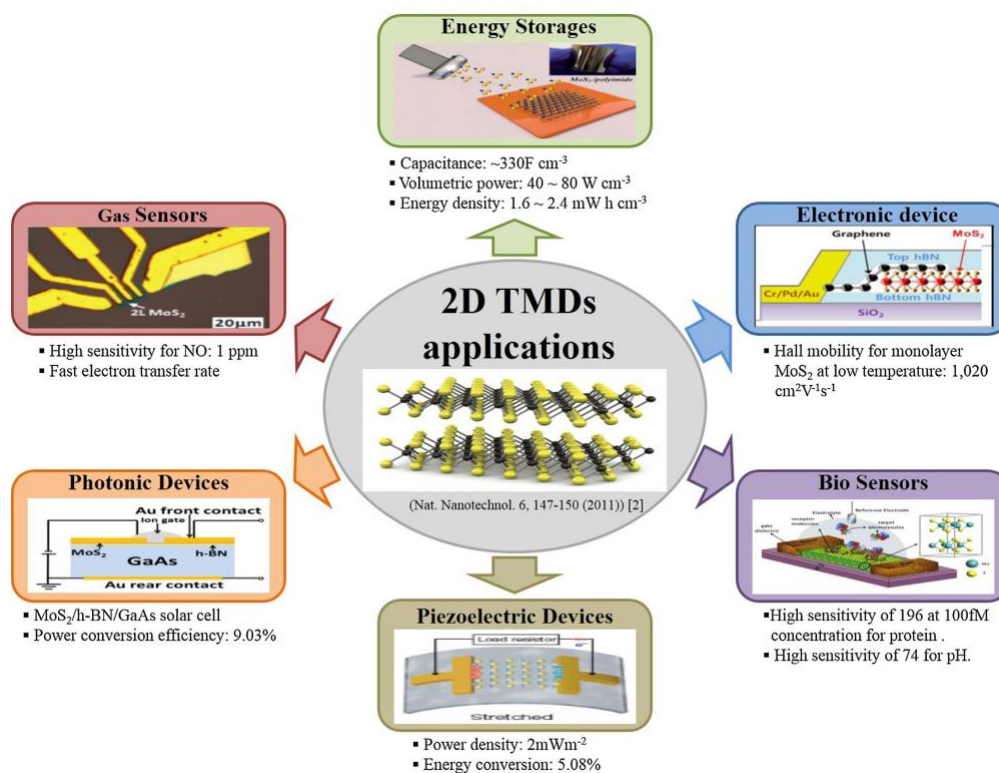


Figure 1. 2. 2D TMDs application fields. The image was reproduced with permission from ref<sup>56</sup>.

Unlike graphene, many 2D TMDs are semiconductors in nature and possess the potential to be made into ultra-small and low power transistors fighting to cope with ever-shrinking devices. Besides sharing the similarities of a bandgap in the visible to near-infrared (IR) range, high carrier mobility, and on/off ratio with ubiquitous silicon, TMDs can be deposited onto flexible substrates and survive the stress and strain compliance of flexible supports.<sup>56</sup>

The majority of the recent work on ultrathin TMD layers has dealt with MoS<sub>2</sub>. Our recent contribution on the ALD-based route to its monolayer growth<sup>19</sup> is lengthily discussed below. The studies relating to WS<sub>2</sub> are less common, which has inflected the choice of this material as the goal of this thesis (see the scope of the thesis at the end of the chapter). Bulk WS<sub>2</sub> is an indirect gap semiconductor and becomes a 2D direct bandgap semiconductor when the thickness reaches the single layer, as shown by DFT calculations of band structures (Figure 1. 3).<sup>57</sup> The calculations yield 1.9 eV for the direct bandgap and 1.3 eV for the indirect bandgap. These investigations confirmed

the potential application based on the unique optical properties of ultrathin layers of 2D WS<sub>2</sub> structures. Gutiérrez H. R. *et al.*<sup>58</sup> observed strong room-temperature photoluminescence (PL) in WS<sub>2</sub> monolayers, while the PL decreases dramatically for a larger number of layers.

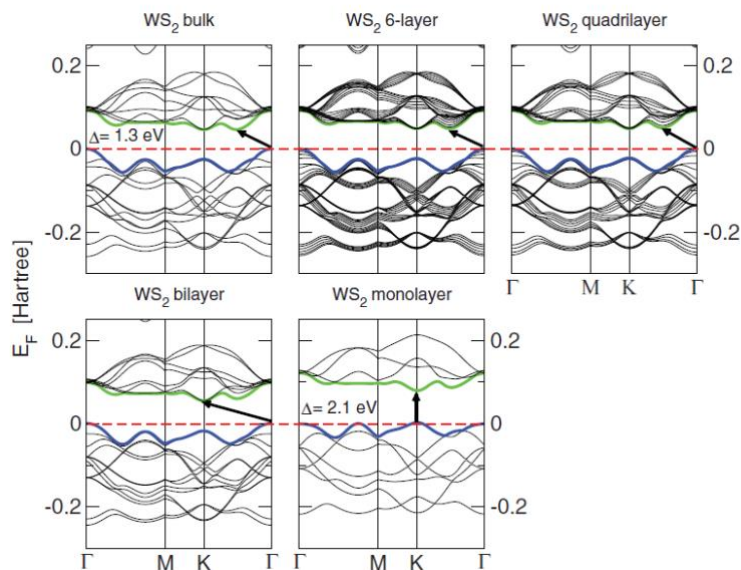


Figure 1. 3. Band structures of bulk WS<sub>2</sub>, its monolayer, and polylayers calculated at the DFT/PBE level. Reproduced with permission from ref.<sup>57</sup>

Photocatalytic applications of two-dimensional monolayer and ultrathin deposits MoS<sub>2</sub> and WS<sub>2</sub> have attracted many scientists with high performance in various energy conversion scenarios.<sup>59–61</sup> Despite a few studies on the ALD chemistry of these TMDs were reported in the literature,<sup>15,19</sup> there are still open questions on their growth mechanism. Especially, surface chemistry was not comprehensively explored for the initial deposition cycles. Therefore, the main interest of this dissertation is around studying the growth of WS<sub>2</sub> by ALD on 3D as well as 2D substrates, and its performance assay in photo(electro)catalysis.

#### 1.1.4. Growth of WS<sub>2</sub> and other transition metal dichalcogenides (TMD) thin films by Atomic Layer Deposition (ALD)

##### 1.1.4.1. State of the art on ALD growth of WS<sub>2</sub>

High-performance applications require these materials to be grown with control of layers number and degree of crystallinity. Several synthetic routes to obtain 2D TMDs have been developed which

can be classified as top-down (e.g. mechanical cleavage,<sup>62</sup> chemical exfoliation<sup>58</sup>) and bottom-up methods (e.g. chemical vapor deposition (CVD)<sup>58,63</sup>, hydrothermal method). However, these methods do not perform equally with respect to thickness control down to the monolayer, conformality, or degree of crystallinity. Despite exfoliation does not require a high-temperature and valves-controlling reactor, it can be a slow and low-yield method with challenges in the selection of a suitable solvent or solvents' mixture and isolation of the monolayer.<sup>64,65</sup> A solvent environment, in some cases assisted by sonication, is supposed to facilitate the exfoliation of layers without structural damaging.<sup>66,67</sup> In contrast, colloidal synthesis is a quick and simple method to prepare nanoparticles of TMDs of various morphologies (nanosheets, nanoflowers, microspheres, etc.).<sup>68-70</sup> However, it seems impossible to scale these methods up for a direct coating of large-area 2D substrates by TMDs and are therefore not adapted to industrial transfer.

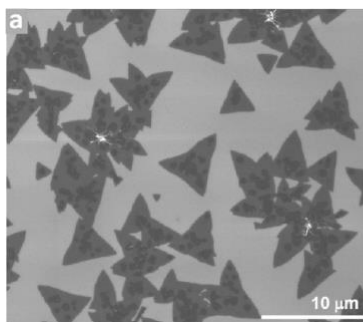
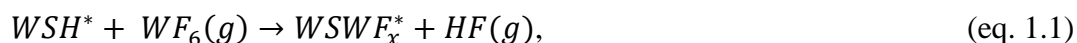


Figure 1. 4. SEM image of small triangular WS<sub>2</sub> monolayers. The dark contrast spots inside the triangles correspond to the early-stage formation of second-layer clusters. Reproduced with permission from ref.<sup>58</sup>

Among these techniques, the CVD overcomes issues with scalability and rapidity. It can also afford thin deposits on supports with a high aspect ratio. However, the uniformity of the film over large surfaces significantly depends on the uniformity of the fluid flow of precursors and temperature in the whole reactor.<sup>50</sup> While mono- to few-layer deposits are not the common target of CVD, precise control of the process parameters allowed to reach an ultrathin deposit of 2D WS<sub>2</sub>. Evaporation of tungsten oxide powder onto a SiO<sub>2</sub>/Si substrate followed by sulfurization at about 800 °C led to the formation of triangular ultrathin WS<sub>2</sub> clusters<sup>58</sup> (see SEM image in Figure 1. 4), but suffered from the presence of dislocations and grain boundaries of grown crystals.<sup>71</sup> Besides that, the CVD technique suffers from required harsh conditions (e.g. high temperature, high pressure) and poor control of chemistry reaction leading to contamination with side elements.

Atomic layer deposition (ALD), a subset of CVD ultrathin film growth techniques where chemical control is the key process parameter (as described above), allows at least ideally control over the number of layers. The quality of the ALD-grown film is homogeneous all over the substrate area irrespective of the uniformity of vapor flow and local temperature in the reactor. The method is possible to extend to the industrial level, and it is nowadays applied in the micro and nanoelectronics field.<sup>9,72</sup>

T.W. Scharf *et al.* (2004) was one of the first research groups to grow WS<sub>2</sub> thin film by ALD. They used WF<sub>6</sub> as a precursor of tungsten and H<sub>2</sub>S as a precursor of sulfur. The deposition temperature was 300 °C, while the *ex-situ* annealing was performed at 500 °C for 1 hour. The proposed surface reactions involved in two half-cycles of ALD are given below:



However, the surface species were not well-defined, and the authors provided their first hypothesis based on the analogous reaction in the CVD of WS<sub>2</sub>. The Raman and energy-dispersive X-ray (EDX) spectroscopies and scanning electron microscopy (SEM) images could determine the WS<sub>2</sub> phase after 200 ALD cycles on the Si substrate. Quartz crystal microbalance (QCM) measurements showed that the initial growth of WS<sub>2</sub> directly on the Si surface was not successful, while the pre-coating Si with ZnS by ALD (using ZnEt<sub>2</sub> and H<sub>2</sub>S) shortened the nucleation and resulted in a steady growth of WS<sub>2</sub> (see Figure 1. 5). This precedent has therefore achieved ALD growth of thin WS<sub>2</sub> layers but has failed to prove its applicability at the ultrathin level and has used halogen-containing precursor which are generally not recommended in the microelectronics-tailored process.<sup>73,74</sup>

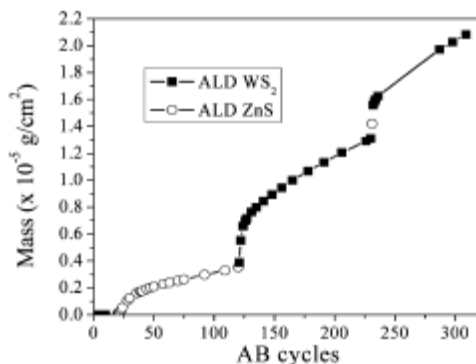


Figure 1. 5. QCM plot during ALD of ZnS and WS<sub>2</sub> on Si substrate. Reproduced with permission from ref.<sup>16</sup>

WS<sub>2</sub> thin films were also obtained by ALD on a stainless steel coin using W(CO)<sub>6</sub> and H<sub>2</sub>S precursors by D. Nandi *et al* (2016).<sup>17</sup> The authors could demonstrate the self-limiting character of the W and S pulses by quantitative FTIR analysis using a KBr pellet as a substrate. The absorption peak at 2000 cm<sup>-1</sup> assigned to the C=O bond slowly reaches the maximum intensity with 15 consecutive doses of W(CO)<sub>6</sub>. For the saturation of H<sub>2</sub>S, 5 consecutive doses led the absorption band at 2000 cm<sup>-1</sup> to reach its minimum intensity. QCM measurements have confirmed the self-limiting behavior, but with a smaller number of doses. It was supposed that the KBr requires a larger amount of the precursors for its saturation. Although the authors did demonstrate the self-limiting character of each half-cycle, the control of atomically thin deposits was not mentioned.

Recent collaborative work between our research group in C2P2-LCOMS and the group of Dr. N. Pinna at the University of Humboldt (2019)<sup>15</sup> has shown that WS<sub>2</sub> can be grown by ALD using W(=N<sup>t</sup>Bu)<sub>2</sub>(NMe<sub>2</sub>)<sub>2</sub> and H<sub>2</sub>S. While genuine ALD growth was confirmed once the stationary growth process was reached, the scalability down to the atomically thin domain was not achieved. This work will be described in more detail in Chapter 2 of the present thesis.

The literature contains several reports of WS<sub>2</sub> ALD enhanced with plasma.<sup>75-78</sup> Plasma generates radicals or other energetic species that induce reactions that are not possible using just thermal energy.<sup>79</sup> Although it is known that plasma usually lowers the temperature of ALD,<sup>80</sup> it brings other limitations. Low-temperature plasma-enhanced ALD of WS<sub>2</sub> onto amorphous alumina has been approached by applying WF<sub>6</sub> and H<sub>2</sub>S precursors.<sup>78</sup> The deposition was done at temperatures between 300 and 450 °C. In this work, an ALD cycle was done in three reaction steps: WF<sub>6</sub>/ H<sub>2</sub> plasma/ H<sub>2</sub>S. They propose that the H<sub>2</sub> plasma enables the deposition of polycrystalline WS<sub>2</sub> via the reduction of surface-bound -W<sup>VI</sup>F<sub>x</sub> species to W<sup>IV</sup> species. However, XPS revealed F-impurities mainly at the interface of the substrate and deposition, which are present due to the use of the WF<sub>6</sub> halide precursor. Plasma-enhanced ALD was shown to produce non-conformal thin films on high-aspect-ratio substrates.<sup>81</sup> Thickness of ALD-grown Ta film differed significantly between the top (28 nm) and bottom (11 nm) of the trench on a substrate surface with a 40:1 aspect ratio. Such a difference in thickness with depth was attributed to the recombination of hydrogen radicals on the trench walls that contract their flux.<sup>82</sup> Plasma ALD, therefore, has limited utility on substrates with high-aspect-ratio surface topography. Since this thesis focuses on well-defined chemistry, the works involving plasma are not further discussed in this introduction.

The fundamentals and state-of-the-art works discussed above provide a basic understanding of the route of the WS<sub>2</sub> film. However, all methods involve nucleation delay upon the first 10-50 cycles that is observable by a non-proportional increase of mass gain or thickness versus the number of cycles at the early stages. In summary, to the best of our knowledge, no ALD process for building ultrathin WS<sub>2</sub> film is available so far in the open literature.

#### 1.1.4.2. The compounded issue of sulfidation of ALD grown WS<sub>x</sub> films

Low-temperature deposition methods of WS<sub>2</sub> including both ALD and CVD can lead to amorphous WS<sub>2</sub> or sulfur-rich WS<sub>x</sub> phases. Therefore, post-deposition annealing is necessary to obtain the WS<sub>2</sub> film with good stoichiometry. Phase diagram<sup>83</sup> given in Figure 1. 6 shows that the formation of WS<sub>2</sub> is the only thermodynamically favored phase between 800 and 1200 °C in case there is excess content of sulfur (66-99 at.%). This was also evidenced by the studies of J.C. Wildervanck *et al.*<sup>84</sup>, who monitored the thermal decomposition of MS<sub>3</sub> (M = Mo or W). Crystallization of MS<sub>2</sub> became slightly observable on powder XRD spectra starting from 400 °C. According to the W – S diagram, the phase with sulfur below 66 at.% may yield WS<sub>2</sub> and W up to 1500 °C.

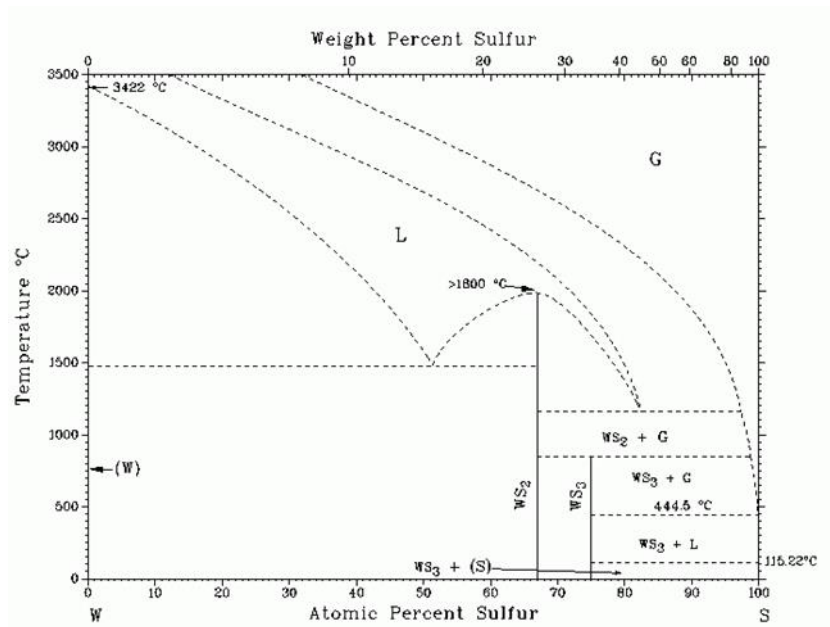


Figure 1. 6. Schematic phase diagram of W–S system<sup>83</sup>.

An analogous thermal transformation study was performed by heating  $(\text{NH}_4)_2\text{WS}_4$ . R. Voorhoeve and co-workers<sup>85</sup> found out that  $\text{WS}_3$  is formed in the temperature range of 120-200 °C depending on pressure. Then  $\text{WS}_2$  crystallization occurred from the decomposition of  $\text{WS}_3$  with long (5 hours) thermal treatment under vacuum starting from 330 °C or at a higher temperature in a shorter time. The authors could not observe any lowering of the crystallization temperature when annealing was carried out in the flow of  $\text{H}_2$ . Stoichiometric  $\text{WS}_2$  was acquired upon heating  $(\text{NH}_4)_2\text{WS}_4$  at 600 °C for 4 hours.

#### 1.1.4.3. *MoS<sub>2</sub> growth by ALD, a close system*

Besides being in the same group of the periodic table, molybdenum and tungsten share certain similarities. Both metal sulfides are transition metal dichalcogenides and semiconductors with close bandgap values (1.23 and 1.3 eV), possess similar M–S bond lengths in their crystal structures. Both metals have an oxidation state of 4+ in the final deposited film. That is why some selected review of  $\text{MoS}_2$  ALD was believed to be relevant to include in this subchapter to give a broader understanding of thin-film growth of the metal sulfides.

Our laboratory reported the first ALD route to ultrathin  $\text{MoS}_2$  film.<sup>19</sup> First, layer-by-layer growth of molybdenum (IV) ethanedithiolate was allowed with  $\text{Mo}(\text{NMe}_2)_4$  and 1,2-ethanedithiol (EDT) molecular precursors at 50 °C.  $\text{Mo}(\text{NMe}_2)_4$  is chosen as a well-suited metal source due to its adequate vapor pressure (0.1 Torr at 50 °C)<sup>86</sup> and expected good reactivity with hydroxyl groups (like homoleptic dialkylamides of other transition metals)<sup>87,88</sup>. EDT is a novel sulfur source, a relevant substitution for toxic  $\text{H}_2\text{S}$  and reactive gas for the intermediate hybrid organic-inorganic deposit, which is further turned to the  $\text{MoS}_2$  inorganic phase upon thermal annealing<sup>89</sup>. The use of an organic dithiol leads to an amorphous thiolate intermediate, which is converted to the final sulfide species only during the subsequent annealing step. The quality of the ALD-grown  $\text{MoS}_2$  layer thus obtained was confirmed by X-ray photoelectron spectroscopy (XPS), wavelength dispersive X-ray fluorescence (WDXRF), Raman spectroscopy, and high-resolution transmission electron microscopy (HRTEM) with remarkably the first in-plane micrograph of the monolayer after the polymer-aided transfer (see Figure 1. 7).<sup>19</sup>

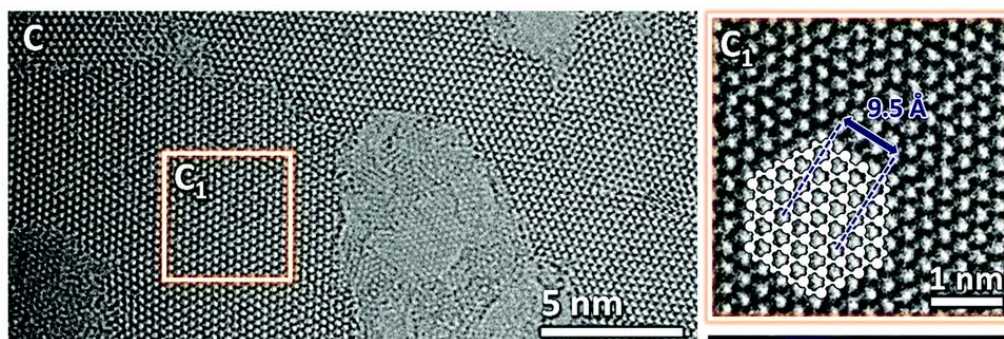


Figure 1. 7. In-plane HRTEM image of MoS<sub>2</sub> grown by ALD and transferred with polymer aide (with enlargement of area C1). Reproduced with permission from ref.<sup>19</sup>

Further ALD routes to thin layers – but no *ultrathin* layers - of MoS<sub>2</sub> with different precursors and substrates have been also reported in the literature.<sup>90–93</sup> Later in April 2017, Jurca, T. *et al.*<sup>93</sup> published a similar ALD methodology to MoS<sub>2</sub> film growth on the SiO<sub>2</sub>/Si substrate using the same Mo precursor as Cadot, S. *et al.*<sup>19</sup> (Mo(NMe<sub>2</sub>)<sub>4</sub>), but different sulfur precursor (H<sub>2</sub>S). Carrying the ALD cycles afforded the formation of amorphous MoS<sub>2</sub> with no strict thickness control – the minimum reported thickness was 10 nm, while post-ALD thermal annealing at 1000 °C produced highly crystalline films.

In parallel, another ALD route of MoS<sub>2</sub> growth on native oxide terminated silicon has been demonstrated by using Mo(thd)<sub>3</sub> (thd = 2,2,6,6-tetramethylheptane-3,5-dionato) as molybdenum source and H<sub>2</sub>S as a sulfur source.<sup>92</sup> The MoS<sub>2</sub> film was grown up to 4000 ALD cycles with a deposition rate of  $\sim 0.025 \text{ \AA} \cdot \text{cycle}^{-1}$  at 300 °C. Images obtained by SEM and AFM showed smooth and featureless surface until 250 ALD cycles.

The MoS<sub>2</sub> film could also be grown on SiO<sub>2</sub>/Si substrate using molybdenum hexacarbonyl and dimethyldisulfide at 100 °C.<sup>91</sup> In the first half-reaction of the ALD, physisorbed Mo(CO)<sub>6</sub> pass through allegedly self-terminating chemisorption yielding Mo(CO)<sub>n</sub> (where  $n \leq 5$ ). Before the second half-reaction starts, the CH<sub>3</sub>S<sub>2</sub>CH<sub>3</sub> turns into reactive CH<sub>3</sub>S– species making the Mo–S bond. After the chemisorption, methylthiolates release gaseous byproducts such as (CH<sub>3</sub>)<sub>2</sub>S and CH<sub>3</sub>CH<sub>3</sub> through cleavage C–S bonds.

The molybdenum (V) chloride and hydrogen disulfide were proven as good Mo and S precursors for ALD of MoS<sub>2</sub> on sapphire at 300 °C.<sup>90</sup> Self-limiting reactions of vapors afforded precise thickness control of MoS<sub>2</sub> film from mono-layer to fifty-layer thickness though a complete monolayer of

MoS<sub>2</sub> was achieved by performing 10 ALD cycles. PL emission of the monolayer has significantly increased after a post-annealing step at 800 °C that can be explained by improving the crystallinity of the as-deposited film.

## 1.2 PART 2 SOMC and its connection to ALD

### 1.2.1. Molecular level understanding of ALD film growth

Understanding the molecular level mechanism in ALD has been well identified key to the development of a successful thin-film process.<sup>94-97</sup> To this end, a major contribution is constituted by the use of *in situ* techniques in an ALD reactor such as mass spectrometry (MS), microbalance and Infrared Spectroscopy (IR) mainly, followed by optical techniques (surface photo absorption, incremental dielectric reflection, and surface photointerference, reflectance difference spectroscopy, optical emission spectrometry, and spectroscopic ellipsometry) and more recently synchrotron techniques (such as X-ray fluorescence and X-ray absorption spectroscopies).<sup>94</sup>

The planar supports of interest for the thin film growth application are generally used negatively affecting the signal to noise ratio of the measurement, due to the low surface area of the starting substrates. In some cases, modeling studies have been reported on porous substrates showing the potential relevance of porous powder supports to gain insight into ALD processes.<sup>98,99</sup>

At the same time this analogy building with high-surface-area powders has been criticized for example, because, when porous substrates are used in regular ALD reactor developed for planar substrate, the purge time between half-cycles becomes prohibitively long. And this line of research – on porous substrates has been dismissed by some.<sup>94</sup>

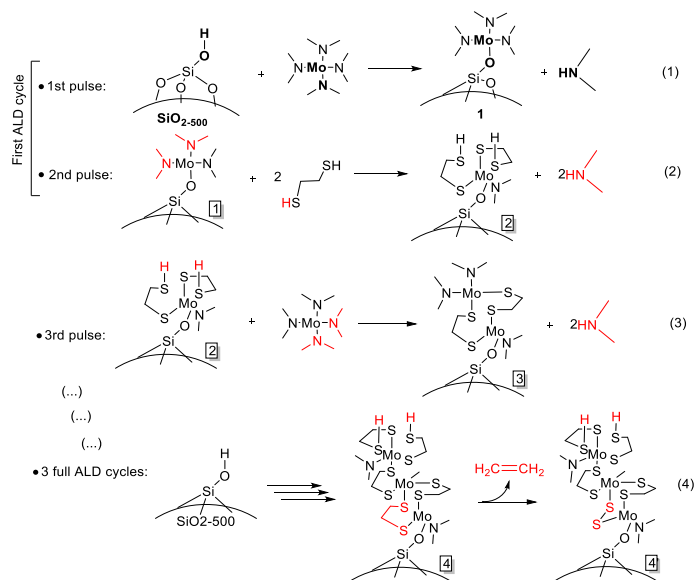
So if some precedents were drawn between “2D” substrates for ALD (like silicon or sapphire) and large surface area “3D” powders (like silica and alumina) these lines of research remain a small niche and mostly limited to model the first half-cycle or the final phase but never, to the best of our knowledge, the whole ALD growth.

The second aspect in which the ALD process towards MoS<sub>2</sub> monolayer on a silicon wafer developed in our group was noticeable in our eyes is that we designed it based on preliminary results acquired on silica nanobeads<sup>19</sup> for each of the half cycles up to 3 full ALD cycles and following annealing.

The silica beads used in SOMC typically display an area of about  $200 \text{ m}^2 \text{ g}^{-1}$ . Having the surface area with  $\sim 2 \cdot 10^5$  times larger than that of a silicon wafer, silica beads allow the characterization by IR, elemental analysis, nuclear magnetic resonance (NMR), and extended X-ray absorption fine structure (EXAFS). SOMC is capable of contributing to the field by bringing new tools to explore surface chemistry occurring within ALD cycles.

The IR spectroscopy and elemental analysis could help to define atomic ratio in as-deposited Mo thiolates using  $\text{Mo}(\text{NMe}_2)_4$  and EDT, which resulted in structural identification of grafted species on  $\text{SiO}_2$  nanobeads.

The mechanism of each deposition step (see Scheme 1. 2) was proposed via studying the reactions by diffuse reflectance infrared Fourier transform (DRIFT), elemental analyses and DRIFT coupled with GC-MS on 3D silica beads (dehydroxylated at  $500\text{ }^\circ\text{C}$  that provides the  $-\text{OH}$  density of ca.  $1.8\text{ OH nm}^{-2}$ ).



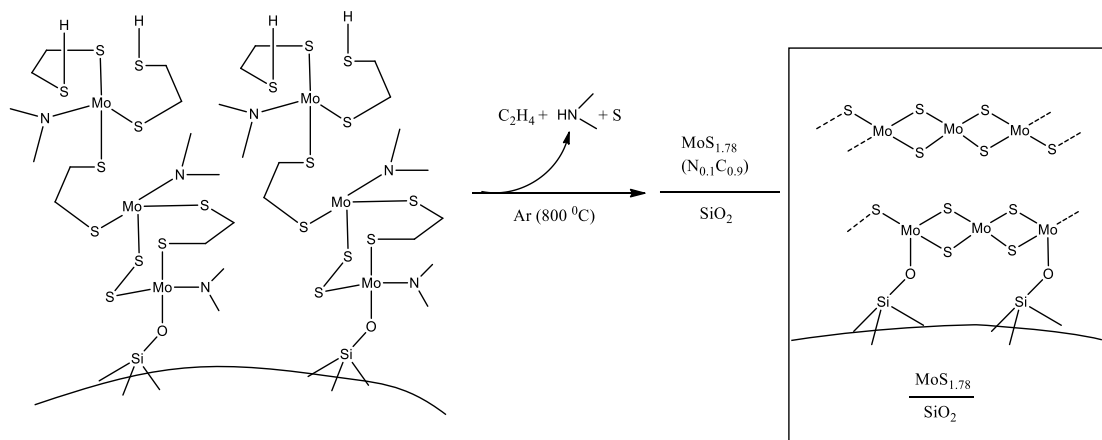
Scheme 1. 2. Proposed scheme for sequential grafting of  $\text{Mo}(\text{NMe}_2)_4$  and 1,2-ethanedithiol on the silica at  $50\text{ }^\circ\text{C}$  (reproduced with permission from ref<sup>19</sup>)

After the first pulse of  $\text{Mo}(\text{NMe}_2)_4$ , full coverage of the silica surface by Mo precursor and removal of the by-product,  $\text{HNMe}_2$ , were confirmed by observation of complete consumption of the isolated silanols and presence of C–H bonds on the surface on the DRIFT spectra. Besides, elemental analysis results supported a good ratio of the C/Mo and N/Mo. Similarly, after the EDT pulse, the IR and elemental analysis results corresponded to Mo (IV) thiolate species on the surface. Each ALD step brought one equivalent of Mo per  $\text{Mo}(\text{NMe}_2)_4$  pulse and two equivalents of sulfur per 1,2-ethanedithiol pulse.

It was clarified on the molecular level that these two precursors perform self-limiting surface reactions and lead to successful ALD of the ultrathin film. Mo(IV) ethanedithiolates in obtained

layers are transformed into a monolayer of crystalline nanodomains of MoS<sub>2</sub> by thermal annealing at 800 °C under Ar (see Scheme 1. 3).

The post-deposition thermal annealing was monitored *in-operando* by DRIFT and GC-MS spectroscopies to understand transformation occurring on the solid's surface and to detect released volatile products of the thermal decomposition, respectively. This smart analysis allowed authors to determine the temperature at which loss of organic moieties happens. Heating was analyzed in two different atmospheres, inert argon and H<sub>2</sub>, which showed that H<sub>2</sub> gas facilitates the cleavage of bonds. In argon flow, the C–H and S–H bond vibrations were disappearing in the range of 100-350 °C, while in H<sub>2</sub>, they vanished above 300 °C. Parallel probing of released gases by GC-MS confirmed that lost organic moieties were intermediates constituting the grown dithiolates structure such as C<sub>2</sub>H<sub>4</sub> and H<sub>2</sub>S (formed in H<sub>2</sub> flow). Electron microscopy revealed the formation of worm-like layered shapes around silica nanobeads after annealing. The results obtained using silica nanobeads as a model provided insights into the mechanism of initial pulses of MoS<sub>2</sub> growth and were consistent with results obtained from ALD on SiO<sub>2</sub>-coated Si wafer. The S/Mo atomic ratio was in good agreement for two supports (2D wafer and 3D beads) defined as ca. 1.8 after 3 ALD cycles.



Scheme 1. 3. Thermal annealing Mo(IV) thiolate layers at 800 °C under Ar (reproduced with permission from ref<sup>19</sup>).

First, annealing removes ethylene and dimethylamine as main products as evidenced by elemental analysis results like 0.21% of N and 1.21% of C, converting the thiolate to intermediate disulfide bridge. Then, it is converted into a well-structured MoS<sub>2</sub> hexagonal phase. It is in good agreement

with the reports in the literature, where annealing of sulfur-rich compounds of molybdenum ending up with the formation of MoS<sub>2</sub> as it is the most thermodynamically stable form<sup>84</sup>.

The accomplishment of every second ALD pulse accommodates sulfur atoms in excess with respect to the molybdenum atoms on the surface. Following the annealing step converts MoS<sub>2+x</sub> sulfur-rich molybdenum sulfide to its more stable form, molybdenum disulfide, MoS<sub>2</sub>. The Mo–S phase diagram demonstrates that the thermal treatment of sulfur-rich sulfides (Mo<33.3%, S>66.7%) will yield a more stable molybdenum disulfide form.

In summary, the surface chemistry of initial deposition cycles was well-defined on a model 3D support and help identify the successful conditions for an efficient ALD process on a 2D wafer.

Non-ALD-related work issued from others in our group helped lay the foundation between this 2D ↔ 3D relationship. The work demonstrates interesting similarities between surface chemistry on both SiO<sub>2</sub>@Si wafer and the silica nanobeads. Laurent Mathey et al.<sup>100</sup>, for instance, observed a similar density of incorporated boron atoms after functionalization of the two substrates with B-containing molecular precursors illustrated in Figure 1. 8 as C<sub>2</sub> and C<sub>3v</sub>. Upon functionalization with the C<sub>2</sub>, the boron content was found at 1.39·10<sup>14</sup> and 2.78·10<sup>14</sup> B atom·cm<sup>-2</sup> from silica nanobeads and silica-coated silicon wafer, when both were dehydroxylated at 500 °C prior to exposure to the boron-based reagent. These values were also close when functionalization was performed with C<sub>3v</sub> precursor, which were 0.81·10<sup>14</sup> and 2.55·10<sup>14</sup> B atom·cm<sup>-2</sup>. Possessing high surface area and well-defined surface functional groups, spectroscopic studies (e.g. NMR, IR), and elemental analysis of the grafted material on the silica nanobeads provided reliable insights into its structure and helped devise a successful implanting strategy.

Another related work<sup>101</sup> communicates a two-step well-controlled process for n-doping the silicon substrate with phosphorus. The first was the grafting of a phosphorus molecular precursor containing hepta-isobutyl-polyhedral oligomeric silsesquioxane triester. The second was annealing to induce diffusion of dopant P into Si substrate and to form a protective layer from its volatilization.

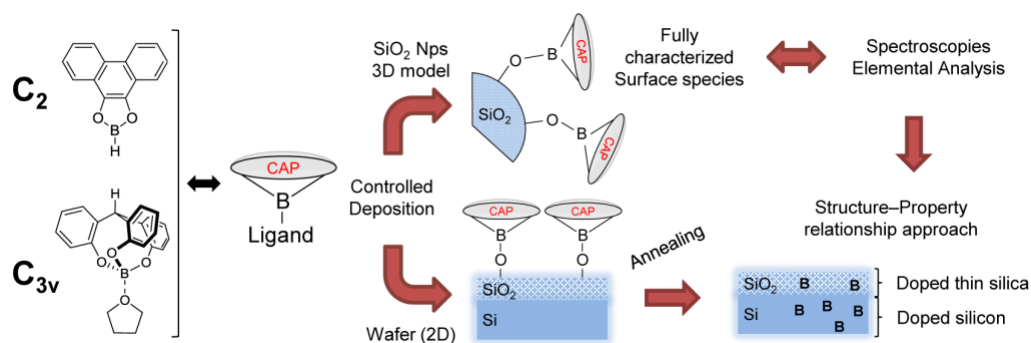


Figure 1. 8. Two-step doping process for 3D and 2D substrates (Reproduced with permission from ref<sup>100</sup>)

Comprehensive molecular understanding of the phosphorus embedding was achieved by conducting spectroscopic characterization of the surface species grafted on the silica nanoparticles.

Roussey, A. *et al.*<sup>102</sup> attained optimal conditions for anchoring molecular copper (I) complex on the 3D silica particles dehydroxylated at 700 °C and then reducing the grafted material to Cu nanoparticles under  $H_2$  at 200 °C. This methodology was successfully transposed to a thermally oxidized silicon wafer that has a 10 nm thick layer of silica. Besides, the authors pre-treated 3D silica and 2D wafer supports under varying temperatures between 135 and 700 °C in high vacuum and observed similar densities of the silanol groups on both substrates by deposition of Cu nanoparticles onto them. Figure 1. 9 illustrates close results for Cu loading over both supports that suggests comparable densities of grafting site in agreement with pre-treatment temperature was applied.

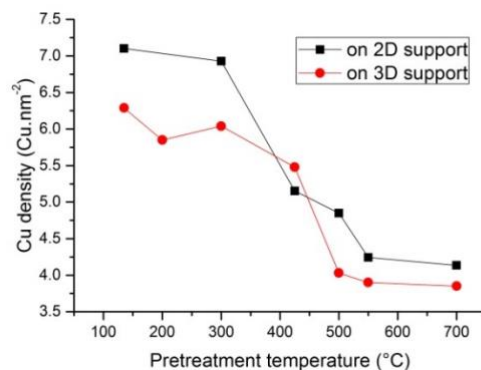


Figure 1. 9. Comparison of Cu loading densities obtained on the 3D silica beads and the 2D silicon wafer. Reproduced with permission from ref<sup>102</sup>.

These previous works indicated that the deposition of molecular precursors on a 2D substrate covered with silica layer and silica beads follows similar surface chemistry.

### 1.2.2. Surface organometallic chemistry and its utility for ALD

Surface organometallic chemistry (SOMC), developed since the 1970's,<sup>103</sup> and still vigorously present in the literature<sup>18</sup>, is a surface modification technique of (mostly) oxide supports with organometallic precursors, whose principal target is to develop heterogeneous catalysts.

In SOMC, a solid surface is considered as a collection of molecularly well-defined ligands, where, the grafted species are studied aiming at a molecular-level definition. The surface sites with well-defined structure can be further modified by thermal treatment in a vacuum, in the flow of inert or reactive gas to yield altered properties. It is essential to characterize the coordination sphere of surface sites to build a structure-activity relationship. Before impregnation of a metal complex, the support can be analyzed by the gas absorption technique to define its surface area. Quantification of released gas upon titration of the surface reactive groups with a titrant can provide information about maximum accommodating capacity and average density of the surface-active groups. Elemental analysis can confirm the theoretically expected loading of the substrate. These above-mentioned tools give a general bulk description, while vibrational and solid-state NMR (ss NMR) spectroscopies are powerful techniques to assign grafted structure in more detail. The IR is useful for monitoring the consumption of surface reactive bonds and a concomitant increase of intensity of new-arrived bonds upon a surface reaction. The ss NMR can provide distinctive information on atoms and surrounding functional groups, though it may suffer from common low loading of the samples. X-ray photoelectron spectroscopy is a complementary analysis carried to confirm the oxidation states of atoms present on the top surface. There are also other characterization means such as X-ray absorption near-edge spectroscopy (XANES), X-ray absorption fine structure (XAFS), electron paramagnetic resonance, Auger spectroscopies that are applicable for powder-supported compounds to describe the geometry, metal-ligand distances, oxidation states, etc.

To achieve foreseen interaction between metal complexes and substrate, the surface has to be treated so that the type and density of the functional groups are defined. For example, with increasing treatment temperature from 200 to 700 °C under vacuum ( $10^{-5}$  atm.) density of  $\equiv\text{Si}-\text{OH}$  groups on silica (Aerosol-200) surface drops from ca. 3 OH nm<sup>-2</sup> to 0.8 OH nm<sup>-2</sup>.<sup>18</sup> Besides, the treatment temperature has also an influence on the types of silanol groups dangling on the surface.

The silica dehydroxylated at 700 °C, SiO<sub>2-700</sub>, has mostly the isolated silanols with 5 to 10 % of geminal, whereas dehydroxylation at lower temperatures leads to the formation of vicinal and bis-grafted surface complexes. The illustration of different silanol groups is shown in Figure 1. 10.

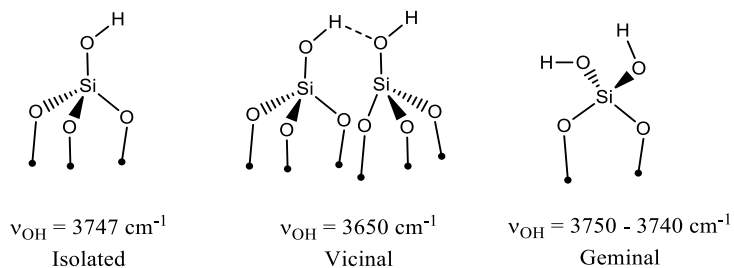


Figure 1. 10. Isolated, vicinal, and geminal silanols on the silica surface <sup>18</sup>.

L.T. Zhuravlev built a model that determines types and distribution of surface functional groups as a function of preliminary treatment temperature in a vacuum (see Figure 1. 11).<sup>104</sup> Total number of surface –OH groups decreases with increasing temperature of the treatment (curve 1), while free isolated silanol groups increase in the range from 200 to about 400 °C and start to decrease again above 400 °C (curve 2). Data agreement for the densities of the isolated silanols and total concentration of hydroxyl groups at about 400 °C as shown in Figure 1. 11 means that hydroxyl groups treated in vacuum at 400 °C are all isolated on the silica surface. Vicinal hydroxyl groups disappear at a temperature above 400 °C (curve 3). Correspondingly, the removal of hydroxyl groups from the surface that is illustrated by curve 4, generates ≡Si–O–Si≡ siloxane bridges.

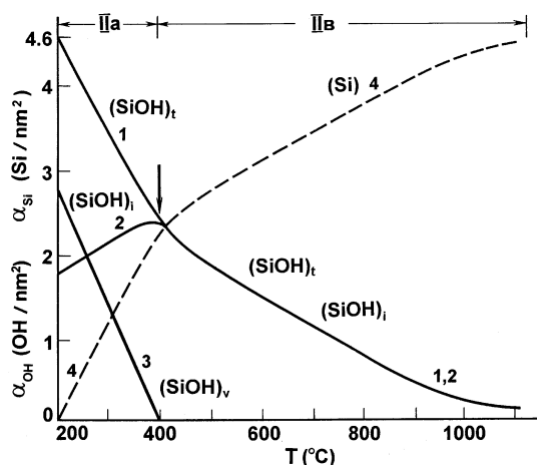
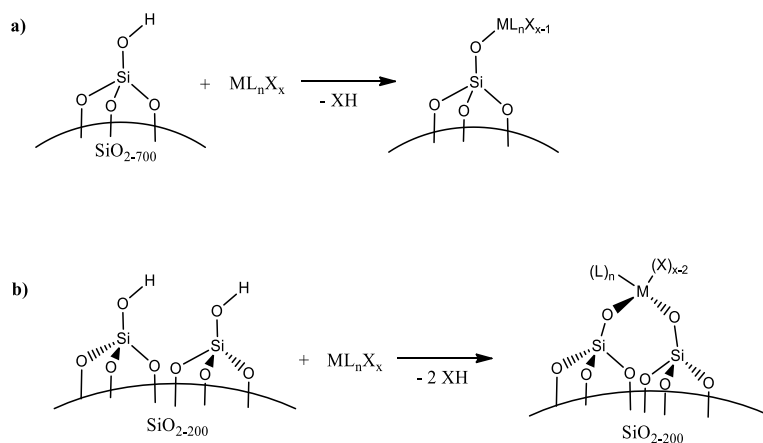


Figure 1. 11. Zhuravlev model-1: Distribution of the surface groups as a function of the temperature of pretreatment in a vacuum. Reproduced with permission from ref<sup>104</sup>.

Once the silica is dehydroxylated at the desired temperature and the surface functional groups are defined, the molecular precursors can be grafted on its surface. Depending on the silanol type, the metal complexes interact with the SiO<sub>2</sub> surface differently (see Scheme 1. 4). Isolated silanols and molecular precursors in the form of ML<sub>n</sub>X<sub>x</sub> follow the general reaction path releasing HX to form (≡SiO)ML<sub>n</sub>X<sub>x-1</sub> surface species (Scheme 1. 4a). Vicinal silanols react with metal complexes yielding bis-grafted species with corresponding reaction stoichiometry (Scheme 1. 4b).<sup>18</sup>



Scheme 1. 4. Grafting of ML<sub>n</sub>X<sub>x</sub> molecular precursor on SiO<sub>2-700</sub> (a) and SiO<sub>2-200</sub> (b) <sup>18</sup>.

The formation of the ≡SiO–M bonds chain is assured by the high reactivity of the metal-ligand bond towards the elimination of the ligand and hydrogen of the silanol. The SOMC supports can be analyzed by several analytical techniques (e.g. IR, NMR, elemental analysis, EXAFS), which is combined with theoretical modeling (e.g. DFT) can offer a well-defined and in-depth knowledge of surface molecular species on support.

The original twist in the line of research explained in this thesis is the connection of these bodies of work with ALD. To define the surface chemistry of ALD, the substrate's surface must be well-defined. Thermally grown SiO<sub>2</sub> can display hydroxyl surface densities as low as 0.42 (± 0.06) OH·nm<sup>-2</sup>. Such low loading was measured for example on a dry substrate grown at 1000°C. The analysis was based on temperature-programmed desorption (TPD) analysis of methanol covered surface, which enabled Si–OH species quantitative titration.<sup>105</sup> A silanol coverage as high as 3,9 OH·nm<sup>-2</sup> was measured elsewhere<sup>106</sup> when Si/SiO<sub>2</sub> rehydroxylated at 300°C was studied. The quantitative techniques were total X-ray reflection fluorescence (TXRF) and/or Rutherford backscattering spectroscopy (RBS) of chemisorbed hafnium content after one pulse reaction of the pristine substrate with HfCl<sub>4</sub>.<sup>106</sup>

Noticeably, one of these works<sup>105</sup> already drew a close comparison between surface silanols of “a planar silica surface” (what we call in this thesis 2D supports) and “high surface area silica powders” (what we call in this thesis 3D supports). The figure 10 of the original paper (reproduced here below in Figure 1. 12) shows the reflectance of this analogy.

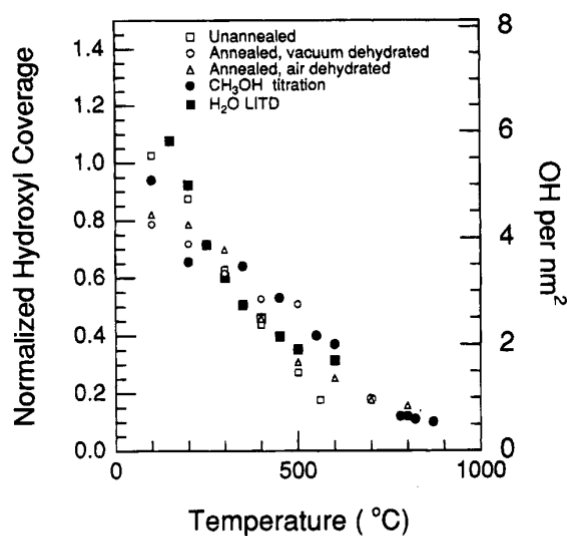


**Figure 10.** Comparison between the thermal stabilities of hydroxyl groups on the well-defined, planar silica surface and previous results obtained from high surface area silica powders.<sup>6,64–68</sup> The data for hydroxyl thermal stabilities on high surface area silica powders are taken from refs 64–68 (open squares), refs 64 and 65 (open circles), and ref 65 (open triangles).

Figure 1. 12. Original figure provided in ref<sup>105</sup> drawing quantitative parallels between 2D and 3D supports

Therefore, the foundational studies allowing to compare the 3D surface’s to 2D surface in terms of silanol density and pretreatment temperature are well over 25 years old. At the same time, to the best of our knowledge, the further step in the analogy that allows using SOMC on the high surface area for ALD on 2D support has no precedents beside the work issued from our group.<sup>19</sup>

Common tools of SOMC such as FTIR, liquid and solid-state NMR, and elemental analysis have proven their efficiency to define well surface-grafted sites at the molecular level on 3D supports. The 2D substrates of interest for ALD with much lower loading generally require the use of highly sensitive techniques such as X-ray Photoelectron Spectroscopy (XPS), Vapor Phase Decomposition (VPD), Secondary Ion Mass Spectrometry (SIMS) and Inductively Coupled Plasma Mass Spectrometry (ICP-MS), etc. The connection with 3D SOMC analytical suits opens new powerful investigation opportunities.

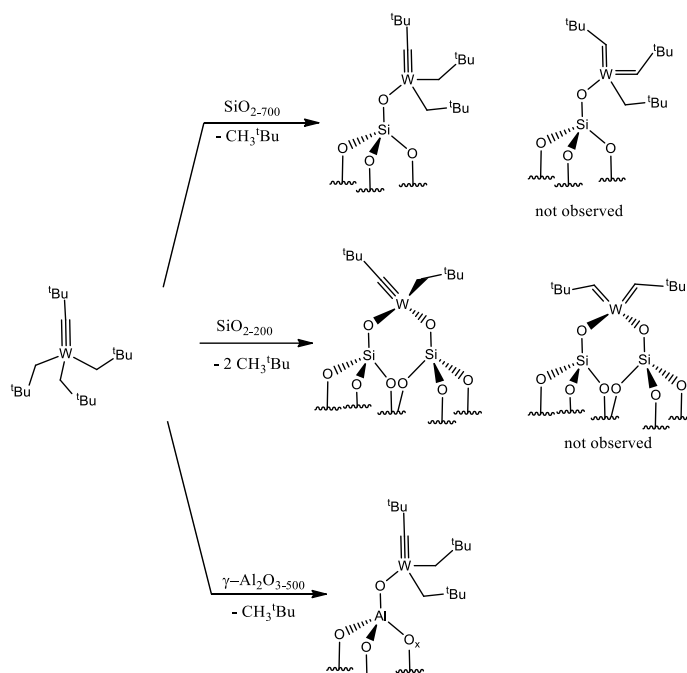
There are few challenges that one may face in devising deposition processes on a 2D support (e.g. Si wafer). The main challenges originate from the small surface area of the 2D wafer, which is at the value of  $8.5 \text{ cm}^2 \text{ g}^{-1}$  only (silica surface of the Si wafer). The quantity of the ultrathin deposit per unit surface area of the 2D silicon wafer remains quite sufficient for many applications and yet approachable for some of the surface characterization microscopy/spectroscopy techniques (XPS, SEM, AFM, QCM). However, due to weak sensitivity, insufficient mass loading makes use of some characterization tools impossible (e.g. IR, NMR, elemental analysis). After the same dehydroxylation conditions, the surface of both silica beads and flat silicon wafer with silica layer above will have the same distribution of the silanols and siloxane bridges.

### 1.2.3. SOMC of tungsten-based catalyst

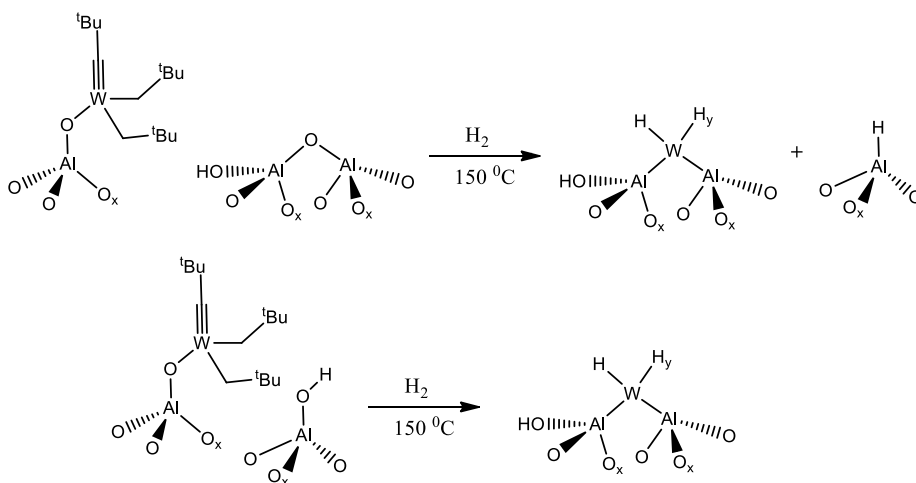
Tungsten has already been grafted on silica surfaces by SOMC. Gauvin, R. M. *et al.*<sup>107</sup> performed the selective synthesis of a silica-supported well-defined ditungsten pentaamide by the reaction of the silica-700 with hexakis(dimethylamido)ditungsten, which will be discussed in more detail in Chapter 2.

Tungsten neopentyl-neopentylidyne complex (*w6*) is a suitable precursor to load onto the surface of alumina and silica due to its selective reactivity with surface hydroxyl groups (see Scheme 1. 5). SOMC approach affords not only the well-defined grafting reaction of the molecular precursor onto the metal oxide, but also for a subsequent alteration of the coordination sphere of the metal center at the surface.

As such tungsten hydrides grafted on alumina-500 were synthesized by treatment of  $[(\text{AlO})\text{W}(\equiv\text{C}-{}^t\text{Bu})(\text{CH}_2-{}^t\text{Bu})_2]$  with  $\text{H}_2$  at  $150 \text{ }^\circ\text{C}$  (see Scheme 1. 6).<sup>108</sup> In contrast to alumina-supported tungsten hydride, tungsten atoms partially sinter on silica upon hydrogenation as evidenced by TEM and reappearance of surface hydroxyl IR band at  $3747 \text{ cm}^{-1}$ <sup>109</sup>. In addition,  $[\text{W}]\text{-H}/\text{Al}_2\text{O}_3$  demonstrated two times better efficiency as a catalyst for propane metathesis than the common  $[\text{Ta}]\text{-H}/\text{SiO}_2$  catalyst (120 vs. 55  $\text{mol}_{\text{propane}}/\text{mol}_{\text{W}}$  of TON, respectively). Such kind of post-treatment is another way to achieve tungsten-based metal oxide catalyst with desired properties.



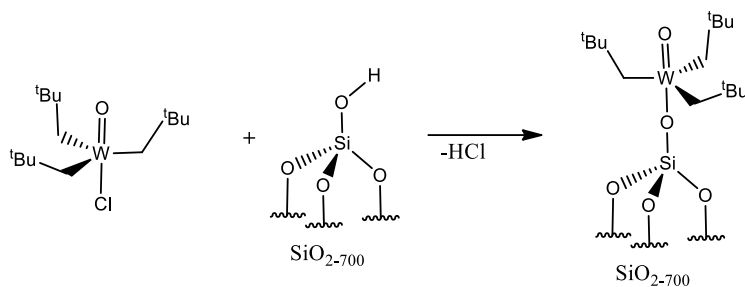
Scheme 1. 5. Grafting of tungsten neopentyl-neopentylidyne onto  $\text{SiO}_2\text{-700}$ ,  $\text{SiO}_2\text{-200}$  and  $\text{Al}_2\text{O}_3\text{-500}$  surfaces



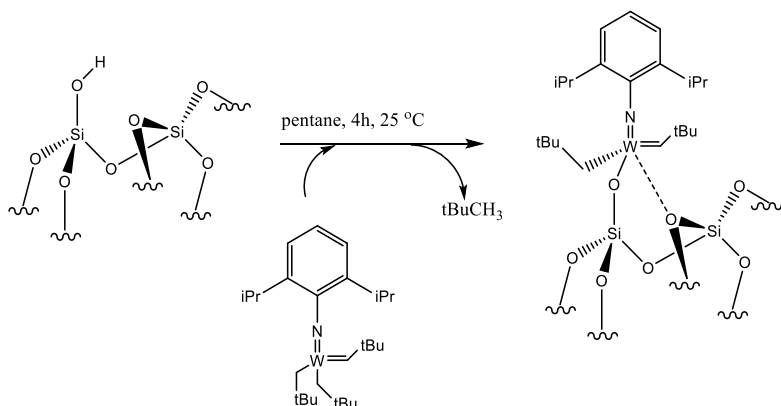
Scheme 1. 6. Alumina-supported tungsten neopentyl-neopentylidyne complexes treated with  $\text{H}_2$  at  $150\text{ }^\circ\text{C}$ .

Selectivity in the protonation of tungsten-ligand bond  $\text{W-CH}_2^t\text{Bu}$  was also compared with some other bonds such as  $\text{W-Cl}$  and  $\text{W=O}$  and reported in the literature.<sup>110</sup>  $\text{W-Cl}$  bond is selectively broken in the reaction of  $\text{W(=O)(CH}_2^t\text{Bu)}_3\text{Cl}$  with  $\text{SiO}_2\text{-700}$  to form  $(\equiv\text{SiO})\text{W(=O)(CH}_2^t\text{Bu)}_3$  (see

Scheme 1. 7). Nevertheless, the marginal release of neopentane was observed and quantified by GC that defined the major selection of the tungsten-chlorine bond.



Scheme 1. 7. Reaction of  $W(=O)(CH_2^tBu)_3Cl$  with silica dehydroxylated at 700 °C.<sup>110</sup>



Scheme 1. 8. Reaction of  $W(=NAr)(=CH_2^tBu)(CH_2^tBu)_2$  with  $SiO_{2-700}$ . Reproduced with permission from ref<sup>111</sup>.

Rhers B. *et al.*<sup>111</sup> provided evidence for the formation of  $(\equiv SiO)W(=NAr)(=CH_2tBu)(CH_2tBu)$  (where  $Ar=2,6-iPrC_6H_3$ ) and cleavage of one neopentyl group per W, when  $W(=NAr)(=CH_2tBu)(CH_2tBu)_2$  grafts on silica dehydroxylated at 700 °C (see the reaction in Scheme 1. 8). Alkylidene ligands remain more stable against protonation than alkyl groups, though the size of the alkoxy ligand does play a role.

All the studies performed on the surface chemistry of tungsten organometallic complexes provide insights into the reactivity of different ligands of tungsten complexes towards metal oxide surfaces and contribute to the future proper selection of a suitable tungsten precursor for ALD.

## 1.3 PART 3 Aim and scope of the thesis

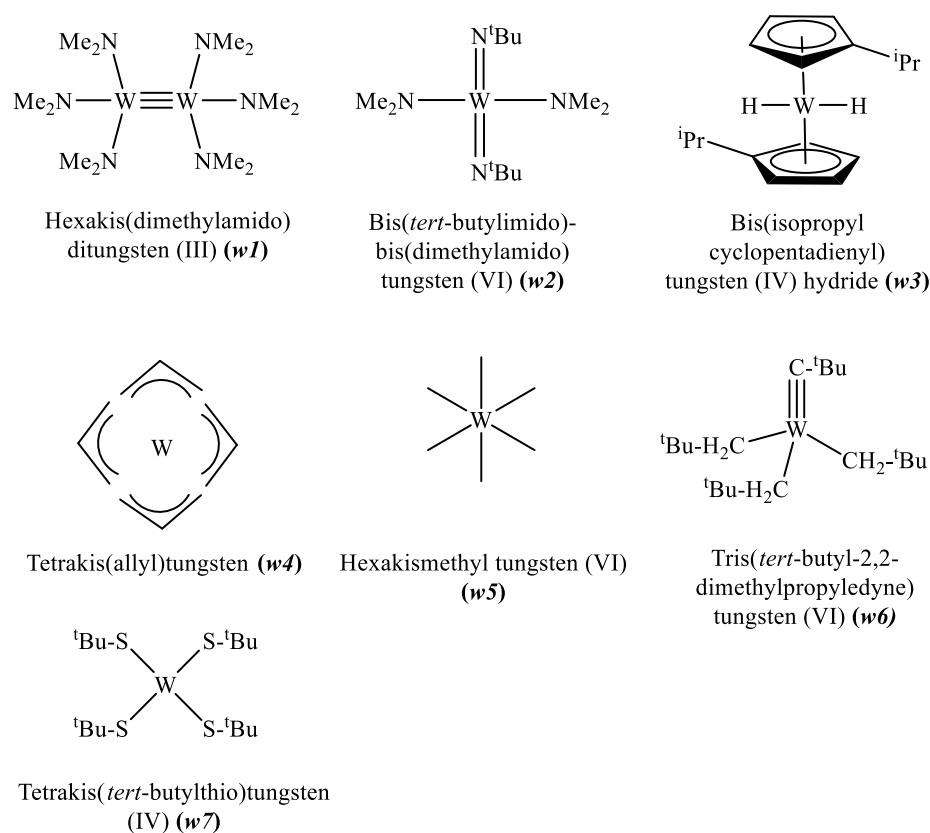
### 1.3.1. Aim of the present work

The general goal of the thesis is to continue to investigate the usefulness of SOMC on large surface areas of silica to develop relevant ALD processes on nanostructured 2D supports. The specific objective is an ALD route to molecularly thin WS<sub>2</sub> layers. We plan to develop the ALD route on dehydroxylated silica nanobeads, study the mechanism of surface reactions occurring in initial ALD cycles of the growth of WS<sub>2</sub> thin film on silica nanobeads and then transfer this methodology onto 2D substrates. As the first step, potential tungsten precursors will be first tested in solution reactions with molecular models of silica and EDT. The promising precursors will then be transferred to silica nanobeads by SOMC (see chapters 2 and 3). We aim to utilize the SOMC approach to explore the mechanism of the interaction between the surface species and deposited reactants. The third step will be the attempt to transfer the system onto 2D substrates such as SiO<sub>2</sub>@Si<sub>wafers</sub> and TiO<sub>2</sub>@Ti<sub>disk</sub>. The 2D substrates will be characterized by *in situ* and *operando* spectroscopy (XPS) and microscopy (TEM, SEM, EDS) techniques to see if this approach can help compare and contrast the 2D and 3D chemistry developed so far (see chapter 4). The 2D TiO<sub>2</sub>@Ti<sub>disk</sub> substrate will serve in energy conversion tests. We also provided initial studies on the electrocatalytic performance of carbon nanotubes samples functionalized by WS<sub>2</sub> ALD, which were prepared by a collaborating research group of N.Pinna *et al.* using BTBMW and H<sub>2</sub>S (ALD process was reported in ref<sup>15</sup>)

### 1.3.2. Scope of suitable ALD/CVD molecular precursors for growth of WS<sub>2</sub> and other W-containing phases

To perform the ALD of WS<sub>2</sub>, we need to define suitable molecular precursors of tungsten and sulfur. For tungsten, we first tried to consider W(IV) complexes to avoid the reduction of the metal to acquire good stoichiometry in the final film. As the second plan, complexes of W (III) and W(VI) were also inspected. The reductive and oxidative transformations of tungsten were already seen for the W (VI) and (III) complexes in the literature.<sup>112</sup> Of course, not all W complexes can enter that list of the potential precursors. An ALD precursor must satisfy several requirements: (i) to be chemically reactive towards both surface functional groups of a substrate and functional groups of the second ALD precursor; (ii) to be thermally stable in the ALD temperature window; (iii) to be enough volatile at the deposition temperature;<sup>113</sup> (iii) to produce volatile and easy removable by-

products upon the surface reactions. Unlike CVD, the ALD is based on a self-limiting reaction on the surface that requires only a sufficient amount of the precursor's vapor to cover all adsorption sites. The excess will be removed by a purge of inert gas. Therefore, the molecular compound must have fairly good reactivity towards chemical bonds of the support's surface as well as those of the second precursor, which is an essential feature of the precursor in its design. Also, the metal-containing precursor has to be thermally stable against decomposition at high temperatures within a typical ALD window, which is usually between 150 and 500 °C. Otherwise, it may lead to uncontrolled reactions followed by decomposition. Furthermore, because of the high chance to leave halogen impurities, the halide precursors of W were not considered in this thesis. By taking such preferable features into account, several potential tungsten complexes of different valences have been considered for this work (Scheme 1. 9).



Scheme 1. 9. Organometallic precursors of tungsten for ALD <sup>114–120</sup>

Among all these precursors, the ones used by the ALD community are hexakis(dimethylamido)ditungsten (III) (HDMDW, *w1*),<sup>20,21,121</sup> bis(*tert*-butylimido)-bis(dimethylamido)tungsten (VI) (BTBMW, *w2*),<sup>15,77,122–127</sup> and bis-(isopropylcyclopentadienyl)

tungsten (IV) dihydride (*w3*).<sup>114</sup> Other tungsten complexes shown in Scheme 1. 9 were used for the functionalization of metal oxide surfaces and studied from a surface organometallic chemistry point of view. There were reservations about the reactivity of the *w5*, *w6* and *w7* complexes with both the ALD substrates and sulfur precursors, because they were less investigated in ALD than the first four complexes. This thesis has thus initially identified *w1-w4* as promising candidates for ALD in this work. The *w1* precursor was previously utilized as a W precursor for ALD of WN, W<sub>2</sub>O<sub>3</sub>, and WS<sub>2</sub>. The latter needed oxidation of W that was achieved by annealing at 400 °C in the atmosphere of H<sub>2</sub>S, whereas the nitride and oxide forms did not require that in paring with NH<sub>3</sub> and H<sub>2</sub>O, respectively. The *w2* complex was already been seen in vapor deposition routes for thin films of WS<sub>2</sub>, WN, and WO<sub>3</sub>. It was coupled with H<sub>2</sub>S gas (or plasma), <sup>t</sup>BuSS<sup>t</sup>Bu, H<sub>2</sub> plasma, O<sub>2</sub> plasma, H<sub>2</sub>O, ammonia to yield a final thin film with the desired valency of tungsten in the temperature range of 200-400 °C. The literature of the *w1* and *w2* complexes will be discussed in more detail in chapters 2 and 3, respectively. The molecular compound *w3* together with oxygen plasma was applied in the plasma-enhanced ALD (PE-ALD) for WO<sub>3</sub> growth on silica/ silicon substrate, which is then sulfurized to WS<sub>2</sub> nanosheets in Ar and H<sub>2</sub>S ambient. The *w4* is appealing because it is already in a W<sup>4+</sup> oxidation state and a byproduct of the H-transfer reaction with incoming ligand should produce easy-to-remove propylene. Our preliminary tests (not shown here) between *w3* and *w4* and molecular models of surface silanols (like polyhedral oligomeric silsesquioxane (POSS)) in solution did not show any reaction up to 80 °C and therefore these precursors were not investigated further.

The top priority was given to *w1*, given its successful implementation in the ALD process and on our previous success in using amido densities for ALD of TMD. Chapter 2 will report the molecular and SOMC studies with this molecule. Secondly, complex *w2* was chosen given the literature precedents both in ALD-centred and in SOMC literature. The molecular and SOMC studies with these molecules are reported in Chapter 3.

The literature of metal sulfides ALD knows several sulfur precursors such as H<sub>2</sub>S,<sup>48,128,129</sup> dimethyldisulfide,<sup>91,130</sup> diethylsulfide<sup>131</sup>, di-tert-butylsulfide<sup>125</sup> and 1,2-ethanedithiol<sup>19</sup>. We selected to investigate the ALD route using 1,2-ethanedithiol (EDT). EDT was shown as a good alternative to common sulfur precursor H<sub>2</sub>S that is a toxic and flammable gas. Although EDT may lead to carbon impurities after annealing, it provides reactive SH groups enabling layer-by-layer growth. Two thiol groups on two sides of the carbon chain can link two metallic layers in consecutive pulses.

The organothiolate intermediate allows to circumvent the apparently ALD-incompatible fundamental characteristic of 2D materials: their unique properties are derived from the very fact that each sheet is isolated from its environment from an electronic point of view and in only weak (van der Waals) contact with the next. The intermediacy of an organometallic thiolate thus circumvents the apparent paradox of sturdy ALD growth by strong chemical reactions at the gas-solid interphase still ultimately leading to weakly stacking layers of chemically and electronically isolated MoS<sub>2</sub> single layer.<sup>19</sup>

**Chapter 2 - ELABORATION of ALD  
GROWTH of WS<sub>2</sub> USING W<sub>2</sub>(NMe<sub>2</sub>)<sub>6</sub>  
and EDT**

## 2.1 INTRODUCTION

### 2.1.1. Use of $[\text{W}_2(\text{NMe}_2)_6]$ as an ALD precursor

A successful precursor for tungsten based-materials by ALD necessitates, as already stated, a volatile tungsten complex with stable yet reactive ligands upon addition of the second ALD reactive. The dimer hexakis(dimethylamido)ditungsten (III),  $[\text{W}(\text{NMe}_2)_3]_2$  fits such requirement. This tungsten(III) complex, reported over forty years ago in the quest around obtaining new metal-metal multiple bonds,<sup>132</sup> was already noted for its easy sublimation (lower than 100°C at 10<sup>-3</sup> Torr). The sublimate can result in a mixture of the desired dimeric and the monomeric W(VI) peramido species  $\text{W}(\text{NMe}_2)_6$ . Both are characterized by terminal tungsten-amido bonds and the dimer is characterized by a triple  $\text{W}\equiv\text{W}$  bond.

$[\text{W}_2(\text{NMe}_2)_6]$  (later referred as HDMDW) was successfully combined with ammonia for the ALD growth of thin WN film.<sup>21</sup> Ch. H. Winter *et al.* states that almost all the nitrogen in the final WN originates from the ammonia via transamination reaction. The substrate temperature was optimized between 180-210 °C, while the W precursor was pre-heated to 120-122 °C. Interestingly, an increase of carbon impurities with increasing temperature of deposition is observed which may signify concurrent undesired thermal decomposition of the HDMDW precursor.

Similarly to the previous work, Ch. H. Winter *et al.* used HDMDW in ALD growth not involving redox reactions, but in that case for the production of  $\text{W}_2\text{O}_3$ , where oxygen was delivered by  $\text{H}_2\text{O}$  precursor.<sup>20</sup> The authors reported deposition temperature (180 °C), XPS measurement results, atomic fractions analyzed by time-of-flight elastic recoil detection analysis (TOF-ERDA) that were consistent with the expectations.

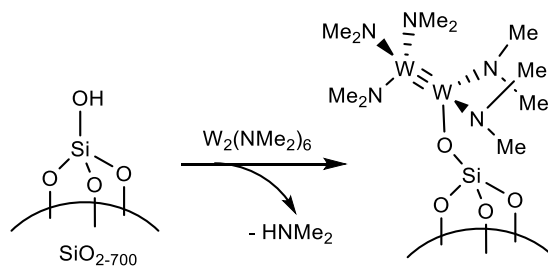
Hexakis(dimethylamido)ditungsten (III) was also reported as a working precursor of tungsten in the ALD growth of a tungsten-containing film necessitating a redox reaction from the starting W(III) center. Most appropriately for this thesis work, such film is tungsten sulfide. Amorphous layers of sulfur deficient disulfide ( $\text{WS}_x$ , where  $x < 2$ ) were obtained by the ALD process at 150 °C by combining HDMDW with  $\text{H}_2\text{S}$ .<sup>121</sup> The most relevant point for this PhD work here is that the amido  $\text{W}-\text{NMe}_2$  bond can be replaced by  $\text{W}-\text{S}$  through the reaction with  $-\text{SH}$  bonds. The worrisome point is the observed sulfur deficiency (S/W ratio of 1.11) in as-deposited film, not only in comparison with the desired  $\text{WS}_2$  but also with the possible  $\text{W}_2\text{S}_3$  stoichiometry for the  $\text{W}^{3+}$  oxidation state. The S/W ratio increased to 1.82 after annealing in the flow of  $\text{H}_2\text{S}/\text{N}_2$ . During optimization of the

deposition temperature, the authors observed the formation of the uniform metallic film in the range 200-300 °C. It was stated that at higher deposition temperature the growth follows CVD of the tungsten metal. XPS measurements revealed oxidation of 51% of W to WO<sub>3</sub> in as-deposited film and 17% in the annealed film that can likely happen in the air. The content of the sulfur bound to WS<sub>2</sub> increased from 47% (in the as-deposited film) to 71% only after annealing. While such precedent abodes well for the possibility to obtain WS<sub>x</sub> from HDMDW by ALD, this mismatch in stoichiometry suggests that the process, and more pointedly the redox aspect, might not be trivial.

### 2.1.2. SOMC of [W<sub>2</sub>(NMe<sub>2</sub>)<sub>6</sub>] complex on silica

The capacity of surface organometallic chemistry (SOMC) to model and offer useful information on an ALD process to be developed on a silicon wafer has been discussed in the previous chapter. As anticipated there, the complex HDMDW has already been investigated by SOMC, independently from ALD applications.

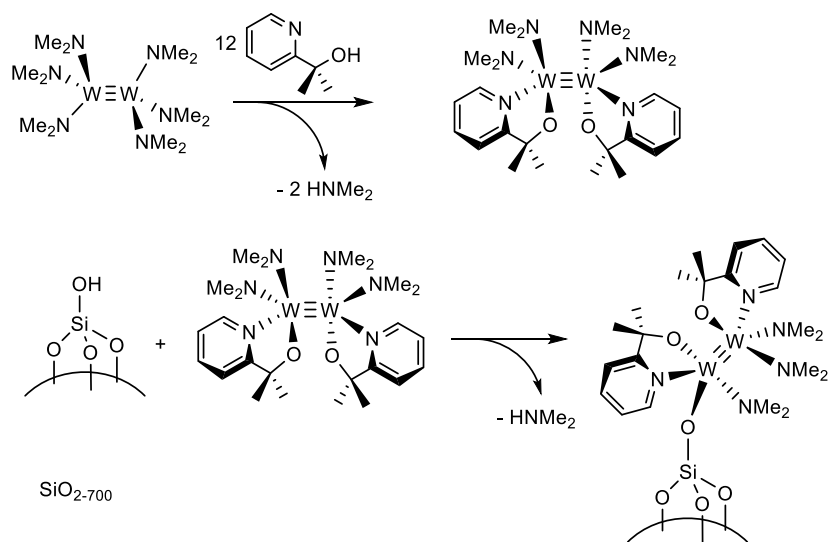
In a quest for a tungsten-based heterogeneous alkyne metathesis catalyst, Gauvin, R. M. *et al.*<sup>133</sup> synthesized the silica-supported well-defined ditungsten pentaamide by a reaction of highly dehydroxylated silica (silica-700) with hexakis(dimethylamido)ditungsten in pentane at room temperature (see Scheme 2. 1). The solution reactivity of tungsten amides with alcohols was a relevant molecular antecedent.<sup>112</sup> Indeed, the reaction between the isolated silanols on the silica support and the tungsten complex yielded a metal-oxygen bond towards ≡SiO–W<sub>2</sub>(NMe<sub>2</sub>)<sub>5</sub> keeping the tungsten-tungsten triple bond and its oxidation state (III) intact.



Scheme 2. 1. Formation of a silica-supported ditungsten pentaamide (adapted from ref.<sup>133</sup>)

Gauvin and co-workers<sup>28</sup> have also shown that a similar grafting reaction by silanolysis of one M-NMe<sub>2</sub> bond can be obtained from a related W≡W dimer, [W<sub>2</sub>{(2-pyr)C(Me<sub>2</sub>)<sub>2</sub>O}<sub>2</sub>(NMe<sub>2</sub>)<sub>4</sub>] (3), (see Scheme 2. 2). Compound 3 was synthesized upon reaction of HDMDW with 12 equivalents of 2-(2-

pyridyl)propan-2-ol pointing to an incomplete substitution of  $\text{-NMe}_2$  ligands (despite the longer reaction time and higher temperature). These literature precedents, therefore, suggest that (at least in solution) the reaction between the precursor and the surface should be well behaved and should be able to react with ALD substrates.



Scheme 2. 2. Synthesis of  $[\text{W}_2\{(2\text{-pyr})\text{C}(\text{Me}_2)_2\text{O}\}_2(\text{NMe}_2)_4]$  and its grafting on  $\text{SiO}_{2-700}$  (adapted from ref.<sup>28</sup>)

### 2.1.3. The goal of this chapter

The goal of this chapter is to test the possibility of using HDMDW and EDT as suitable precursors for ALD growth of ultrathin film of  $\text{WS}_2$ . Good reactivity between the precursors and the silica surface functional is expected based on the prior art just exposed, but the reactivity with EDT is uncharted. In addition to testing whether  $\text{WS}_2$  can be obtained, the aim is to provide insights on the mechanism of occurring surface reactions during the initial ALD pulses using spectroscopic (NMR, IR, elemental analysis) and microscopy (TEM, EDX, STEM) tools.

## 2.2 EXPERIMENTAL SECTION

### 2.2.1. General procedures

All reactions were carried out under a controlled atmosphere using schlenk glassware and glovebox. The synthesis and ALD-modelling reactions on the surface of silica nanobeads were conducted using ultra high-vacuum lines providing the vacuum in the range of  $8 \cdot 10^{-6}$ – $5 \cdot 10^{-5}$  mbar and glovebox containing traces of H<sub>2</sub>O below 0.1 ppm and O<sub>2</sub> below 0.8 ppm. Surface reactions with silica were carried in a homemade glass reactor that is, called double-schlenk, where two glass chambers are joined via frit and equipped with a stopcock and two necks. Inside the glovebox, one chamber is loaded with dehydroxylated silica, and the other chamber is loaded with the solution of depositing reactant. WCl<sub>4</sub> (ass. >95%), LiNMe<sub>2</sub> (ass. 95%) and tris(tert-butoxy) silanol were ordered from Sigma-Aldrich. Pentane, diethyl ether, benzene-D<sub>6</sub> and THF were dried by benzophenone/Na followed by degassing by freeze-pump-thaw cycles.

1,2-ethanedithiol (EDT) (assay > 98%), was ordered from Alfa Aesar, dried on activated 3Å molecular sieves before use. The activation of the molecular sieves was heated to 270 °C at a 5 °C/min ramp under a dynamic UHV of  $10^{-5}$  mbar overnight. Further transferring of EDT for characterization or to reaction vessels was carried in an argon-filled plastic glove bag.

<sup>1</sup>H NMR of EDT (300.16 MHz, C<sub>6</sub>D<sub>6</sub>, 298 K): δ 1.29 ppm (m, 2H of 2×SH), 2.18 ppm (m, 4H of 2×CH<sub>2</sub>).

<sup>13</sup>C NMR of EDT (75.43 MHz, C<sub>6</sub>D<sub>6</sub>, 298 K): δ 28.5 ppm.

Raman of EDT (cm<sup>-1</sup>) with tentative assignments: 304s (CCS bending), 402vw, 509vw, 639s (C–S str.), 668w (C–S str.), 724s (CH<sub>2</sub> rocking), 742s (CH<sub>2</sub> rocking), 819m, 899w, 980vw (C–C str.), 1029w, 1199w, 1287m (CH<sub>2</sub> wagging), 1421w (CH<sub>2</sub> deformation), 2561s (S–H str.), 2840w, 2926s (C–H sym str.), 2956m (C–H asym str.).

<sup>1</sup>H NMR of (tBuO)<sub>3</sub>SiOH (300.16 MHz, C<sub>6</sub>D<sub>6</sub>, 298 K): δ 1.41 ppm (s, 27H of 3×tBu), 3.12 ppm (s, 1H of SiOH).

<sup>13</sup>C NMR of (tBuO)<sub>3</sub>SiOH (75.43 MHz, C<sub>6</sub>D<sub>6</sub>, 298 K): 31.4 ppm (s, 9 primary-C), 72.8 ppm (s, 3 quaternary-C).

### 2.2.2. Synthesis of [W<sub>2</sub>(NMe<sub>2</sub>)<sub>6</sub>]

The synthesis discussed hereafter reproduces a report in the literature.<sup>134</sup> Schlenk reaction flask of ca. 200-mL equipped with a stirring bar was loaded with 8.25 g (25.33 mmol) of WCl<sub>4</sub> inside the glovebox. About 50 mL of Et<sub>2</sub>O was transferred by cannula from a storage flask equipped with Rotaflo® stopcock. Gray suspension was stirred and cooled to 0 °C in the ice bath. 5.82 g of LiNMe<sub>2</sub> (114 mmol) was loaded into the second Schlenk of the same volume inside the glovebox. About 70 mL of THF was added via cannula under argon flow. White slurry was stirred and added dropwise to the first Schlenk via cannula under the argon flow during 3-5 minutes. After the addition of LiNMe<sub>2</sub>, the reaction mixture was stirred for 3 hours at 0 °C, then 20 hours at room

temperature, and 2 more hours under reflux. The reaction mixture was cooled to room temperature and filtered through celite. Solvent from the filtrate was removed under dynamic vacuum (ca.  $10^{-2}$  mbar), and the remaining solid was redissolved in n-pentane. The mixture was filtered again to remove insoluble residues, and the new filtrate was left in the freezer at  $-25$  °C overnight. The next day, the supernatant was removed by a syringe, and orange-brown crystals were rinsed with a new portion of n-pentane. The crystals underwent redissolving in n-pentane, filtration, and recrystallization until bright yellow crystals were obtained. Repeating these steps more times led to the formation of a mixture of yellow and red crystals. Another way of purification was attempted by sublimation of the first solid residue isolated from the filtrate at  $90$ - $100$  °C under the UHV, dissolving the sublimed powder in n-pentane, filtration, and recrystallization. This way also required several recrystallization steps to start isolating yellow and red crystals.

*$^1\text{H}$  NMR of yellow crystals in  $\text{C}_6\text{D}_6$ :*  $\delta$  3.44 ppm (broad s, Me of  $-\text{NMe}_2$ )

*$^1\text{H}$  NMR of red crystals in  $\text{C}_6\text{D}_6$ :*  $\delta$  3.45 ppm (s, Me of  $-\text{NMe}_2$ ),  $\delta$  3.46 ppm (s, Me of  $-\text{NMe}_2$ )

*IR of yellow crystals:* 2976.6m, 2920.7s, 2855.1s, 2809.8s, 2767.4s, 1436.7m, 1243.9s, 1149.4s, 1125.3m, 1044.3m, 964.2s, 941.1s  $\text{cm}^{-1}$ .

### 2.2.3. Reaction of HDMDW with tris(tert-butoxy)silanol

35.3 mg (55.8  $\mu\text{mol}$ ) of yellow crystals of the tungsten complex were dissolved in ca. 0.3 mL of  $\text{C}_6\text{D}_6$  in an NMR tube inside the glovebox. 14.3 mg (54.1  $\mu\text{mol}$ ) of  $(^t\text{BuO})_3\text{SiOH}$  powder were dissolved in a separate vial in ca. 0.4 mL of  $\text{C}_6\text{D}_6$ . The second solution was poured into the tube, and quickly closed with the *Young* cap. The tube was shaken for better mixing and analyzed by NMR. The first  $^1\text{H}$  NMR record confirmed complete reaction with the disappearance of OH group proton of  $(^t\text{BuO})_3\text{SiOH}$ . Then, the deuterated solvent was removed in a dynamic vacuum via a connected pump to the glovebox. Fresh deuterated benzene was added into the tube to re-dissolve the yellow residue and measured by NMR spectroscopy.

*$^1\text{H}$  NMR before the evaporation step in  $\text{C}_6\text{D}_6$ :*  $\delta$  1.48 ppm (s, 27 H of three  $^t\text{Bu}$ ), 2.20 ppm (s, 6 H of  $\text{HNMe}_2$ ), 2.72 ppm (m, 6 H of  $\text{W}-\text{NMe}_2$ ), 3.43 ppm (br s, 18 H of  $\text{W}-\text{NMe}_2$ ), 4.32 ppm (m, 6 H of  $\text{W}-\text{NMe}_2$ ).

*$^{13}\text{C}$  NMR before the evaporation step in  $\text{C}_6\text{D}_6$ :*  $\delta$  31.7 ppm (s, p-C of  $^t\text{Bu}$ ), 31.9 ppm (s, p-C of  $^t\text{Bu}$ ), 38.8 ppm (s,  $\text{CH}_3$  of  $\text{HNMe}_2$ ), 71.9 ppm (s, t-C of  $^t\text{Bu}$ ), 72.1 ppm (s, t-C of  $^t\text{Bu}$ ).

*$^1\text{H}$  NMR of after the evaporation step in  $\text{C}_6\text{D}_6$ :*  $\delta$  1.49 ppm (s, 27 H of three  $^t\text{Bu}$ ), 2.72 ppm (m, 6 H of  $\text{W}-\text{NMe}_2$ ), 3.43 ppm (s, 18 H of  $\text{W}-\text{NMe}_2$ ), 4.32 ppm (m, 6 H of  $-\text{NMe}_2$ ).

### 2.2.4. Reaction of HDMDW with EDT

300 mg (474.6  $\mu\text{mol}$ ) of HDMDW was placed in the male-joint side of the double schlenk. Ca. 10 mL of n-pentane and 300  $\mu\text{L}$  (3505  $\mu\text{mol}$ ) of EDT were introduced to the female-joint side. The liquid part was frozen in liquid  $\text{N}_2$  to establish a vacuum. This made it easier to transfer the EDT

liquid from the other side of the double schlenk over the frozen side. Immediate precipitation was observed when the EDT solution reacted. The mixture was stirred to react for three hours. After five washing steps, the liquids were transferred into the intermediate trap. The solid part was dried for about three hours. Attempts to dissolve the solid in toluene, hexane, and THF failed. The solid was analyzed by  $^1\text{H}$ ,  $^{13}\text{C}$  solid-state (ss) NMR, IR, and elemental analysis.

$^1\text{H}$  ss NMR (300.16 MHz, 298 K):  $\delta$  0.01 ppm (s), 0.81 ppm (s), 1.24 ppm (s), 2.68 ppm (br).

$^{13}\text{C}$  ss NMR (75.43 MHz, 298 K):  $\delta$  28.8 ppm (s), 36.5 ppm (s) with a shoulder at 41.2 ppm.

IR: 3064.4br, 3014.2m, 2950.6s, 2898.5s, 2815.6m, 2750.0m, 2491.6w, 2406.8m  $\text{cm}^{-1}$ .

Elemental analysis results are given in Table 2. 1 together with calculated atomic ratios.

### 2.2.5. ALD-modelling surface reactions using the $\text{W}_2(\text{NMe}_2)_6$ and EDT on silica-700 in solution

**The 1<sup>st</sup> pulse:** the reaction between 800.0 mg of  $\text{SiO}_2\text{-700}$  ((0.23 mmol OH/g) and 140.0 mg (1.2 eq.) of  $[\text{W}_2(\text{NMe}_2)_6]$  complex in 15 mL of n-pentane was initiated by transferring the solution of  $[\text{W}_2(\text{NMe}_2)_6]$  to the compartment with  $\text{SiO}_2$  under reduced pressure. After 2 hours of stirring, the silica was washed three times with clean pentane to remove any excess of the  $[\text{W}_2(\text{NMe}_2)_6]$ . Vapors produced upon the reaction were attempted to analyze by  $^1\text{H}$  NMR by condensing them into the NMR tube containing  $\text{C}_6\text{D}_6$ , but the spectrum did not show different chemical shifts from those of benzene and n-pentane. The yellow powder was dried under dynamic UHV and studied by DRIFT, (ss) NMR spectroscopies, and elemental analysis (Table 2. 1).

IR: 2983w, 2931m, 2868s, 2821s, 2777s, 1867s.

$^{13}\text{C}$  ss NMR (75.43 MHz, 298 K):  $\delta$  36.5 ppm (s, distal  $\text{CH}_3$ ), 46.1 ppm (s, vicinal  $\text{CH}_3$ ), 56.5 ppm (s, proximal  $\text{CH}_3$ )

**Hydrolysis of the 1<sup>st</sup> pulse product:** 300 mg of the yellow powder obtained upon the 1<sup>st</sup> pulse was exposed to water vapors (40  $\mu\text{L}$ ) and the resulting volatiles were condensed into the NMR Tube containing about 0.7 mL of  $\text{D}_2\text{O}$  and 15  $\mu\text{L}$  of methanol (Sigma Aldrich, ass. 99.8%) as an internal reference. Attempts to quantify the dimethylamido by the use of methanol-based internal standard lead to finding half of  $\text{HNMe}_2$  with respect to the amount of total expected tungsten-bound ( $\text{W}\equiv\text{W}$ )  $-\text{NMe}_2$ . Comparing integrations (3.00 vs 1.08) of methyl protons of the reference methanol (15  $\mu\text{L}$ ) and detected methyl groups of the dimethylamine defines 84.3  $\mu\text{mol}$  of this gas (see Figure 2. 1). It is 1.9 times smaller than the largest possible amount of the dimethylamine present in case the grafting followed the mono-substitution. This points either to incomplete hydrolysis and/or equilibrium between the dissolved part in deuterated water and gaseous head-space.

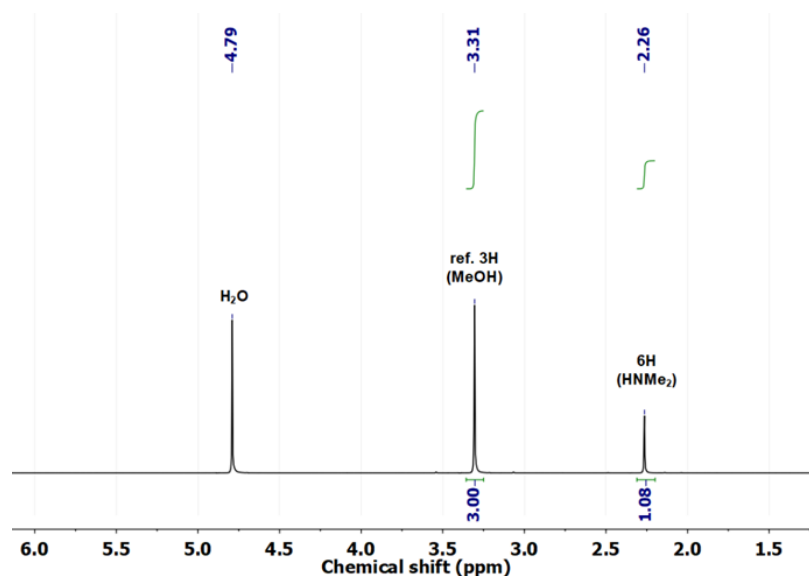


Figure 2. 1. <sup>1</sup>H NMR of trapped volatile products of hydrolysis of silica-supported HDMDW in the presence of reference MeOH

IR spectrum of the white powder after hydrolysis showed, besides large features above 3500 cm<sup>-1</sup> assigned to water-based moieties, residual NH stretches, confirming that the hydrolysis of W-NMe<sub>2</sub> bonds is partial. IR spectra of the solids before and after hydrolysis were compared in Figure 2. 2. The blue spectrum (B) shows that after hydrolysis small fraction of absorption bands assigned to C-H bond stretching are retained. It approves incomplete elimination of the dimethylamido ligands by hydrolysis though an excess of water vapors was injected.

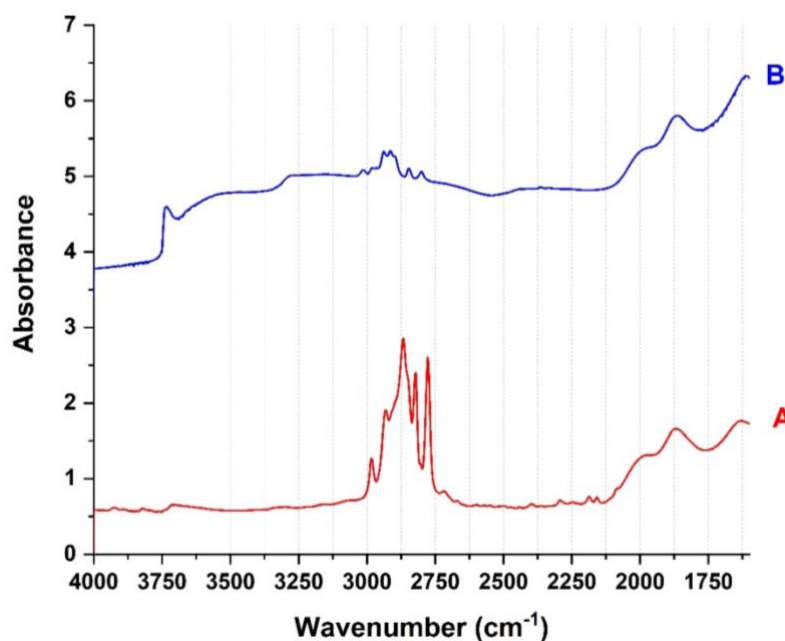


Figure 2. 2. IR spectra recorded for silica-supported HDMDW before (A, red spectrum) and after hydrolysis (B, blue spectrum)

**The 2<sup>nd</sup> pulse:** inside the glovebox, 800.0 mg of the pale-yellow powder and 15 mL of n-pentane were placed respectively in male and female-joint sides of the double-schlenk. 130  $\mu$ L of EDT is added to the side of the double-schlenk containing pentane inside a plastic glove bag filled with argon. The reaction is initiated by transferring the solution to the powder side and left for 2 hours to stir at room temperature. The color has instantaneously turned to brown. Then, the liquids were removed to an intermediate trap under reduced pressure and the residue solid was dried under dynamic UHV overnight. The solid was examined by DRIFT, ss NMR spectroscopies, and elemental analysis (Table 2. 1) in an inert atmosphere.

IR: 3747m, 3082br, 3012m, 2953m, 2902s, 2817w, 2752s, 2391m, 1864s.

<sup>13</sup>C ss NMR (75.43 MHz, 298K):  $\delta$  37.9 ppm (br. s) with a shoulder at ca. 42.0 ppm

**The 3<sup>rd</sup> pulse:** 700.0 mg of dried solid silica-supported tungsten thiolates were mixed with 165.0 mg of  $W_2(NMe_2)_6$  complex in the solution of n-pentane and stirred at room temperature for 2 hours. The reaction has been carried in the same way as the 1<sup>st</sup> pulse in the double-schlenk. Solid obtained upon the 3<sup>rd</sup> pulse was analyzed by ss NMR, DRIFT spectroscopies and elemental analysis.

IR: 3077br, 3009m, 2982m, 2900s, 2868s, 2822s, 2777s, 2393vw, 1870s.

<sup>13</sup>C ss NMR (75.43 MHz, 298K):  $\delta$  38.2 ppm (br. s) with a shoulder at 43.7 ppm, 57.7 ppm (s)

**The 4<sup>th</sup> pulse:** 700.0 mg of the solid of the 3<sup>rd</sup> pulse was reacted with 150  $\mu$ L of EDT in pentane at rt for 2 hours. The reaction procedure was analogous to the 2<sup>nd</sup> pulse. Acquired solid after drying was analyzed by DRIFT spectroscopy.

IR: 3747w, 3072br, 3009m, 2952m, 2901s, 2817w, 2751m, 2398m, 1869s.

<sup>13</sup>C ss NMR (75.43 MHz, 298K):  $\delta$  37.78 ppm (br. s) with a shoulder at ca. 41.8 ppm

**Attempts to deposit  $W_2(NMe_2)_6$  vapors onto silica-700:** About 62 mg of compacted and sieved silica has been pressed into a pellet under 15 tone pressure outside the glovebox. The silica pellet was dehydroxylated under vacuum at 700 °C in a quartz reactor. The silica pellet held in a quartz by a special holder and  $W_2(NMe_2)_6$  crystals were placed in a tube reactor equipped with a special glass arm connected perpendicularly to the tube and quartz window for IR measurements. The deposition was carried out by heating the crystals in the arm at various temperatures 70, 90, 110 °C for 20 minutes (40 minutes at 90 °C) under a static UHV. Fourier-Transform Infrared (FTIR) spectroscopy has been recorded after each deposition temperature. Besides, in order to check whether the adsorption was chemical or physical, only the pellet was heated to 110 °C for 20 minutes and analyzed by FTIR.

**The 2<sup>nd</sup> and 4<sup>th</sup> pulses carried out in gas-solid reaction:** the double schlenk was connected to the glass ALD reactor equipped with two bulbs and young caps via an adapter with a big-pore frit in the

middle. One of the bulbs contained 300  $\mu\text{L}$  of degassed ethanedithiol. After assembling the complete reactor in the glovebox, it was evacuated and the sulfur pulse is done under a static UHV ( $10^{-6}$  mbar) while stirring the silica powder. Evacuation and the EDT pulse were repeated alternately 4 times. The powder has changed its color from bright yellow to dark brown in the 2<sup>nd</sup> pulse. The solid product was dried in the same setup under dynamic UHV overnight at room temperature. The 4<sup>th</sup> pulse was repeated in the same way after the 3<sup>rd</sup> pulse was carried out in solution.

*IR of the 2<sup>nd</sup>-pulse product:* 3747s, 3082br, 3012m, 2956m, 2906s, 2821w, 2751s, 2398m, 1869m.

*IR of the 4<sup>th</sup>-pulse product:* 3747s, 3072br, 3010m, 2952w, 2902s, 2818w, 2748s, 2398m, 1869m.

#### 2.2.5.1. Annealing procedure of silica bound tungsten thiolates

The solid sample obtained after the fourth pulse was annealed in the furnace (shown in Figure 2. 3) of 700 W power in a horizontally placed quartz tube. Annealing atmosphere can be argon or argon/hydrogen mixture. The argon flow passed through copper/zeolite catalyst for gas purification. The powder samples were loaded into a ceramic boat, which was introduced into a quartz tube reactor inside the glovebox. The tube reactor was closed after a brief exposure to air. The tube reactor was connected to the outlet of continuous gas (Ar or H<sub>2</sub> diluted to 20 % in Ar) flow at 60 sccm and placed horizontally into the tubular furnace. Heating was carried at a 10 °C/minute ramp to 800 °C (in Ar flow) or to 450 °C (in H<sub>2</sub>/Ar flow) that was followed by an isotherm for 40 minutes and cooling to room temperature at a 20 °C/minute ramp. Annealed powder samples were characterized by HRTEM, STEM, SEM, and EDX. Elemental analysis was carried out for the argon-annealed sample (Table 3. 1)

*Elemental analysis of the argon-annealed sample (% wt.):* W = 12.6; S = 4.57; C = 0.95; N = 0.2; H < 0.1



Figure 2. 3. A photograph of the oven for annealing on the gas lines of the CVD/ALD reactor. Reproduced from the thesis of S. Cadot.<sup>135</sup>

Table 2. 1. Elemental analysis results on the products obtained in the following reactions: HDMDW+EDT, first 4 ALD-modelling pulses on SiO<sub>2-700</sub> using HDMDW and EDT in solution (starting from the HDMDW pulse), and following annealing step.

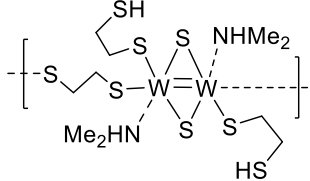
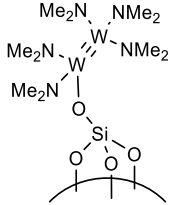
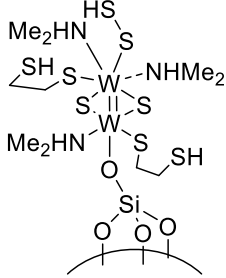
	Elemental analysis (wt. %) (expected)*					Atomic ratios (expected)*			Proposed structures or molecular formulas
	W	C	N	S	H	S/W	N/W	C/W	
<b>HDMDW+EDT</b>	44.10 (45.93)	15.15 (15.00)	3.92 (3.50)	29.5 (32.04)	3.33 (3.53)	3.8 (4.0)	1.2 (1.0)	5.3 (5.0)	
<b>1<sup>st</sup> pulse</b>	7.81 (7.73) <sup>+</sup>	2.66	1.67	0	0.61	0 (0)	2.8 (2.5)	5.2 (5)	
<b>2<sup>nd</sup> pulse</b>	7.51 (7.38) <sup>+</sup>	2.67	0.86	5.59	0.65	4.3 (4)	1.5 (1.5)	5.4 (5)	
<b>3<sup>rd</sup> pulse</b>	16.1 (13.4) <sup>+</sup>	3.97	1.77	4.74	0.91	1.7 (2)	1.4 (1.5)	3.8 (4)	≡SiO-W <sub>4</sub> C <sub>16</sub> N <sub>6</sub> S <sub>8</sub> H <sub>47</sub> with a tentative extension of formula: ≡SiO-W <sub>4</sub> (NMe <sub>2</sub> ) <sub>3</sub> (NHMe <sub>2</sub> ) <sub>3</sub> (-SS) <sub>2</sub> (S(CH <sub>2</sub> ) <sub>2</sub> S) <sub>2</sub>
<b>4<sup>th</sup> pulse</b>	11.5 (12.8) <sup>+</sup>	3.42	0.91	7.63	0.78	3.8 (4)	1.0 (1.0)	4.5 (4.5)	≡SiO-W <sub>4</sub> C <sub>18</sub> N <sub>4</sub> S <sub>15</sub> H <sub>49</sub>

Table 2.2. (continued)

	Elemental analysis (wt. %) (expected)*					Atomic ratios (expected)*			Proposed structures or molecular formulas
	W	C	N	S	H	S/W	N/W	C/W	
<b>Annealed at 800 °C</b>	12.6 (14.2) <sup>+</sup>	0.95	<0.2	4.57	<0.1	2.1 (2)	<0.21 (0)	1.2 (0)	<b>WS<sub>2.1</sub>C<sub>1.2</sub>N<sub>y</sub>H<sub>z</sub></b> (where x<0.21, y<1.5)

\*The expected fractions were estimated according to the proposed structure in the last column

<sup>+</sup> expected loadings were calculated based on the surface silanols concentration (defined by titration) on SiO<sub>2-700</sub> of 0.24 mmol·OH/g and proposed formulas

## 2.2.6. Characterization instruments

### 2.2.6.1. Infrared spectroscopy

Infrared analysis of powder samples was conducted on Diffuse Reflectance Infrared Fourier Transform (DRIFT) Spectroscopy. The DRIFT spectroscope is a Nicolet 6700-FT spectrometer using a cell equipped with CaF<sub>2</sub> or KBr window. In a typical measurement, 64 scans were accumulated for each spectrum (resolution 4 cm<sup>-1</sup>).

### 2.2.6.1. Solution and solid-state Nuclear Magnetic Resonance Spectroscopy

Solution NMR spectra were recorded on BRUKER AVANCE 300 spectrometer (<sup>1</sup>H: 300.1 MHz, <sup>13</sup>C: 75.4 MHz). Chemical shifts are given in ppm (h) relative to tetramethylsilane (TMS). Spectra were recorded using the residual peak of the deuterated solvent as the internal standard.

Solid-state NMR spectra were collected on BRUKER AVANCE III 500 (<sup>1</sup>H: 500.16 MHz, <sup>13</sup>C: 125.72 MHz) and BRUKER AVANCE II 300 (<sup>1</sup>H: 300.13 MHz, <sup>13</sup>C: 75.43 MHz) spectrometers. The zirconia impeller of 4 mm diameter is filled and rammed with the desired product inside the glovebox under Argon and sealed with a kel-f stopper. It was then transferred into the probe Bruker CP 4 mm spectrometer allowing rotation of the rotor at a speed of 10 kHz. The D1 time for <sup>1</sup>H acquisition in MAS recordings was set to 5/10 s. In CP-MAS recordings, the D1 time (of <sup>1</sup>H) and contact time were set to 2 (or 5) s and 2 ms, respectively. The time between two acquisitions was always optimized to allow complete relaxation of the protons.

### 2.2.6.1. Elemental analysis

The powder samples were sent to the Mikoanalytisches Labor Pascher in Remagen-Bandorf, (Germany) to conduct an elemental analysis of silica-supported and non-supported organometallic compounds on a Heraeus/Mannertz/Pascher C-H-N analyzer and iCap 6500 (Thermo Fisher Scientific).

### 2.2.6.1. In-operando thermal decomposition of W thiolates monitored by DRIFT and GC-MS

Thermal decomposition of powder samples was analyzed on an integrated setup consisted of mass flow controllers (Brooks), FT-IR adapted to the high-temperature reaction chamber (Harrick Scientific), and online GC-MS (Agilent GC 6850 MS 5975C). The reaction chamber was equipped with ZnSe windows and fitted into the Praying Mantis optical unit also provided by Harrick. In the glove box, about 25 mg of powder sample was placed onto a porous stainless-steel frit in the reaction chamber. Once the cell was inserted into the spectrophotometer, a controlled mass flow of

helium ( $5 \text{ ml}\cdot\text{min}^{-1}$ ) was introduced into the reaction chamber at 1 bar. Heating was programmed from  $20^\circ\text{C}$  to  $500^\circ\text{C}$  temperature, using a heating rate of  $2^\circ\text{C}\cdot\text{min}^{-1}$ . Released gases were analyzed in the GC-MS. The DRIFT spectrum was recorded by accumulating 64 scans every 20 minutes. FT-IR spectra were recorded in a Nicolet 6700 spectrophotometer with an MCT detector and  $4 \text{ cm}^{-1}$  resolution.

#### *2.2.6.1. (Scanning) Transmission Electron Microscopy (STEM and HRTEM)*

A JEOL 2100F (FEG) electron microscope at the “Centre Technologique des Microstructures”, CT $\mu$  UCBL, Villeurbanne, (France) was used to acquire conventional (HR)TEM and STEM micrographs. The acceleration voltage was 200 kV. The samples were prepared by drop-casting from the ethanol suspension of a ground sample on a Cu grid covered by a carbon film.

#### *2.2.6.1. Scanning Electron Microscopy and Energy Dispersive X-ray spectroscopy*

The morphological characterization of the powder samples was performed by a Scanning Electron Microscope (SEM) equipped with Quanta 250 FEG FEI high-resolution field emission gun, and with Energy Dispersive X-ray (EDX) analyzer, at the “Centre Technologique des Microstructures” (CT $\mu$ , Villeurbanne, France).

## 2.3 RESULTS AND DISCUSSION

### 2.3.1. The precursor

#### 2.3.1.1. *Synthesis and purification of $W_2(NMe_2)_6$*

The synthesis of dimeric hexakis(dimethylamido)ditungsten (III)  $[W(NMe_2)_3]_2$  (HDMDW) was adapted from Chisholm *et al.*<sup>134</sup> Its formation co-produces monomeric  $W(NMe_2)_6$  (HDMW, as opposed to HDMDW). Due to the similar physical and chemical properties of the two complexes, the purification was challenging. When the reaction is over, the mixture was filtered, the solid residue was washed with THF, and the filtrate was evaporated to leave brown powder. Starting from this, the pure dimer could be isolated via two routes. The first way included dissolving the crude brown powder in a minimum amount of n-pentane, filtration, and recrystallization from that solution at -25 °C. After removal of the supernatant, the resulting orange-red crystals contained impurities as shown by  $^1H$  NMR (see spectrum A, black, in Figure 2. 4). The black spectrum A clearly shows a sharp proton peak of  $W(NMe_2)_6$  at 3.45 ppm and a broad peak of  $[W(NMe_2)_3]_2$  at 3.44 ppm overlapping with each other. These crystals were then dissolved in a new portion of n-pentane and recrystallization was repeated. The second time, crystals of two different colors, yellow and red, were isolated from the supernatant. The red crystals were picked with a tweezer and studied by NMR (see the red spectrum B in Figure 2. 4) and powder XRD. NMR spectrum of the red crystals demonstrated two sharp peaks at 3.45 and 3.46 ppm attributed to methyl group protons of HDMW. The yellow crystals were isolated by picking them with a tweezer and dissolved in another portion of n-pentane. The third recrystallization from that solution yielded pure bright yellow crystals of HDMDW showing a broad proton peak at 3.44 ppm (see blue spectrum C in Figure 2. 4).

The second successful way of purification was sublimation from the initial brown powder, dissolution of the resulting yellow powder in the minimum amount of n-pentane, filtering, and recrystallization. The second method also resulted in producing bright yellow crystals that showed the single broad proton peak at 3.44 ppm in the  $^1H$ -NMR solution spectrum. Even though HDMDW and HDMW have some similarities, their application in ALD may lead to different chemical reactions on the surface of a substrate. Having W (III) in one and W (VI) in another complex, either oxidation or reduction will be required to W(IV) to obtain  $WS_2$  film.

Both forms of the W complex feature protons of  $N(CH_3)_2$  at 3.45 ppm. Filtration of the sublimed powder reduced the concentration of impurities. Nevertheless, the main peak at 3.45 ppm was still

combined with two overlapping peaks of HDMDW (broad peak) and its monomer form  $W(NMe_2)_6$  (sharp peak). After several steps of recrystallization from the same solution, bright and large yellow crystals have been mainly obtained in the initial recrystallization attempts, while small and red crystals were formed in the later attempts. In such a way, the ditungsten complex (HDMDW) has been isolated by recrystallizing it from a sublimed powder's solution.

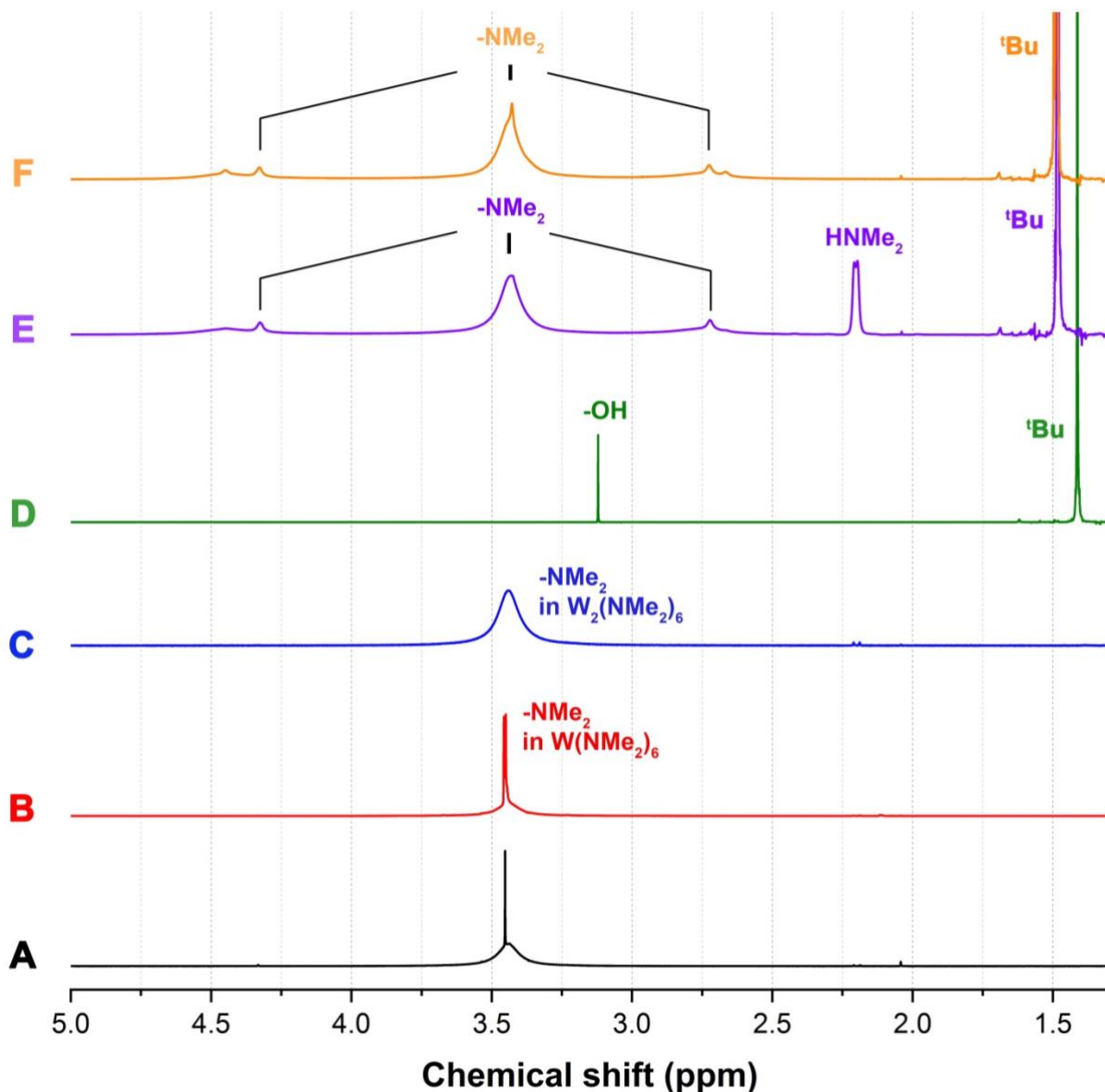


Figure 2. 4. NMR spectra recorded in  $C_6D_6$  for the following samples: A – 1st fraction of crystals isolated by a single crystallization; B – red crystals of  $W(NMe_2)_6$  isolated by manual separation from a mixture of yellow and red crystals after double crystallization; C – yellow crystals of HDMDW obtained after three recrystallizations; D –  $(tBuO)_3SiOH$  only; E – a mixture of  $(tBuO)_3SiOH$  and HDMDW in 1:1 mol. ratio in NMR tube; F – redissolved reaction products in new  $C_6D_6$  after evaporation of the mixture of  $(tBuO)_3SiOH$  and HDMDW;

The NMR spectroscopy alone cannot confirm the complete removal of  $W(NMe_2)_6$  from  $W_2(NMe_2)_6$  especially in the case of overlapping of the two corresponding chemical shifts. Therefore, XRD measurements were carried out to complement the characterization of the expected HDMDW complex.

Powder XRD measurements carried out on isolated yellow and red crystals confirmed their correspondence to the dimer HDMDW and monomer HDMW complexes, respectively (XRD patterns are collected in Figure 2. 5 along with the spectra of HDMDW and HDMW mixed with HDMDW (in 1:2 ratio) complexes found in the database of the International Center for Diffraction Data (ICDD)). Highlighted bands in dashed rectangles (at 9.3, 20.3, 28.9, 39.7, and 48.2 °) signified the presence of the monomer in the isolated red crystals and its absence in the yellow crystals.

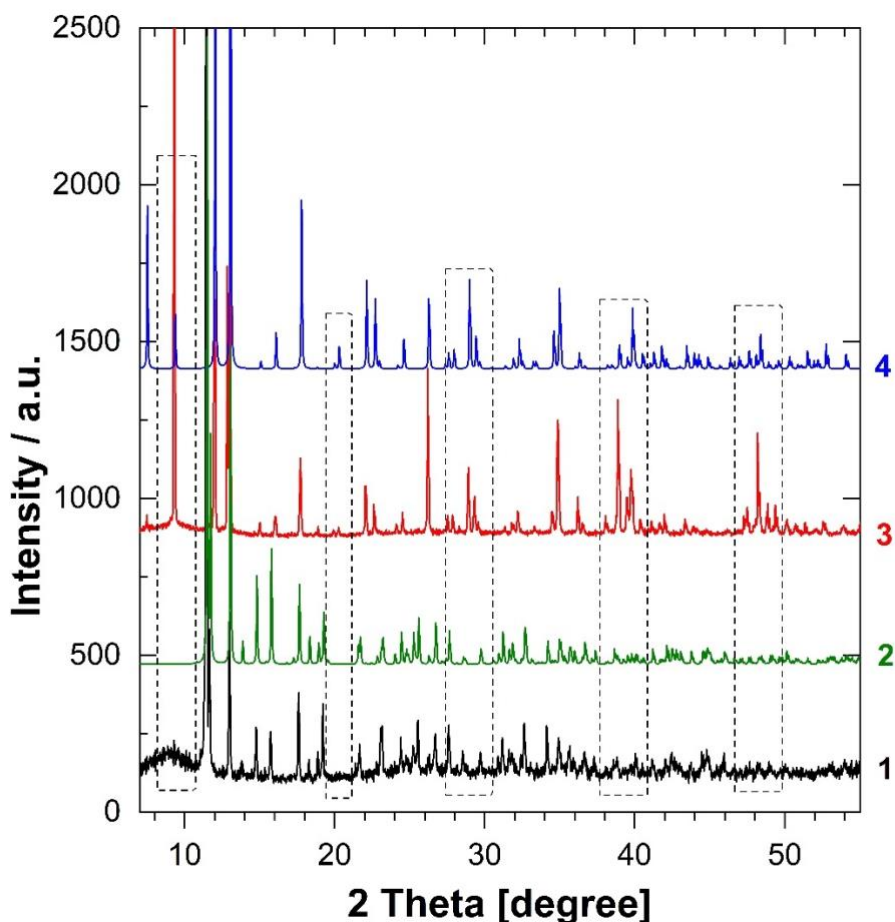


Figure 2. 5. XRD spectrum of isolated yellow crystals of HDMDW complex (1, black line), ICDD reference of HDMDW (2, green line), isolated red crystals HDMW (3, red line), and the ICDD reference of HDMW mixed with HDMDW (4, blue line).

### 2.3.1.2. Thermal stability of complex $W_2(NMe_2)_6$

Since ALD requires the evaporation of the precursors, it is important to define the temperature window of the HDMDW. Thermogravimetric analysis (TGA) has been conducted to study a weight loss in the range of 25 to 600 °C (see TGA plot in Figure 2. 6). Here, the loss of weight indicates the thermal decomposition of the complex. A sharp decrease in weight is observed between 230 and 290 °C. However, the first slight losses begin from 144 °C, which defines the highest temperature limit for the use of HDMDW in ALD. Therefore, it is essential to keep the deposition temperature below 150 °C to avoid impurities originating from the decomposition of HDMDW. This data is in agreement with the ALD processes and the SOMC studies presented in the chapter's introduction.

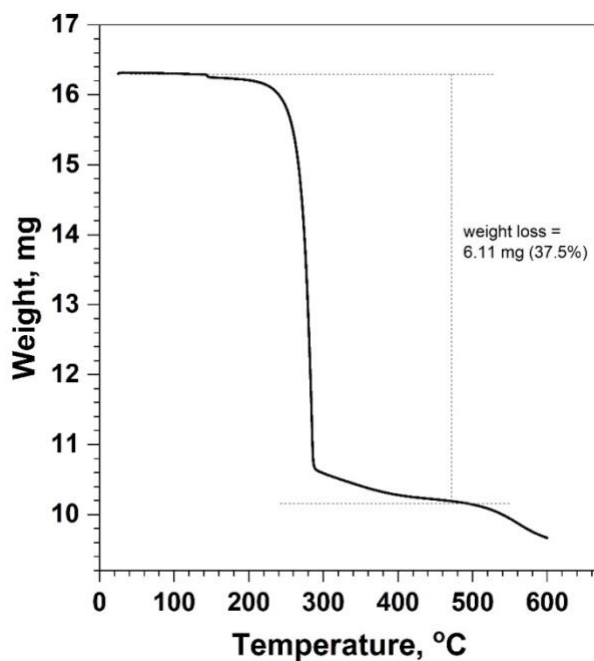


Figure 2. 6. Thermogravimetric profile of obtained yellow crystals of HDMDW

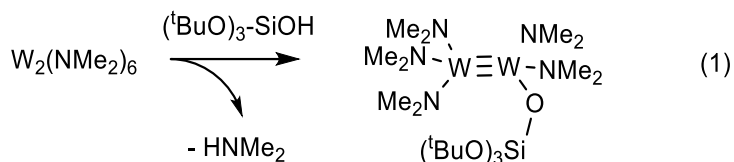
## 2.3.2. Preliminary study with molecular chemistry

### 2.3.2.1. Reaction of HDMDW with tris-(tert-butoxy)silanol in solution

Having a large cone angle and Si–OH functional group, tris-(tert-butoxy)silanol can be used to molecularly model silica surface silanols via homogeneous reactions.<sup>136</sup> We, therefore, investigated the reaction between tris-(tert-butoxy)silanol and HDMDW to gain preliminary insights on the

reactions that can occur on the surface of silica particles when exposed to HDMDW. A deuterated benzene solution of tris-(tert-butoxy)silanol was added to a deuterated-benzene solution of stoichiometric HDMDW in order to avoid local excess of tris-(tert-butoxy)silanol around HDMDW. Figure 2. 4 shows the  $^1\text{H}$  NMR spectra of the resulting reaction mixture (purple spectrum E) and tris-(tert-butoxy)silanol alone (green spectrum D) for easier comparison. Mono-substitution and production of dimethylamine  $\text{HNMe}_2$  as a side product are observed. To confirm the presence of dimethylamine, the same solution was evaporated directly from the NMR tube under a dynamic vacuum, and the residue was redissolved in new deuterated benzene. The spectrum F shows no peak at 2.20 ppm corresponding to the amine.

So, HDMDW has a well-defined reactivity towards  $\text{SiO-H}$  at room temperature, and the solution reaction proceeds via mono-substitution in case of reacting in the equimolar ratio (see Scheme 2. 3). This should contribute to understanding a reaction mechanism during the deposition of HDMDW on silica nanobeads and even on 2D substrates possessing surface hydroxyl groups.



Scheme 2. 3. Reaction of HDMDW with the molecular model of silica, tris(tert-butoxy)silanol

#### 2.3.2.2. Reactivity of HDMDW complex with EDT in solution

A desirable property for steady film growth is a quick chemical reaction between ALD precursors. The reactivity of HDMDW with EDT was first tested in solution (that is in the absence of solid support, also called substrate in the ALD community) to ascertain the mutual reactivity of the two ALD reagents. When HDMDW, previously dissolved in n-pentane is added dropwise to a solution of EDT in the same solvent, a red-brown solid precipitate, **B**, is produced instantaneously. Elemental analysis of solid **B** yields the following average formula  $\text{W}_2\text{C}_{10}\text{N}_2\text{S}_8\text{H}_{27}$  which is in good agreement with structure  $[\text{W}(\text{NMe}_2)(\text{SCH}_2\text{CH}_2\text{SH})_2]_2$  (for which the expected formula is  $\text{W}_2\text{C}_{12}\text{N}_2\text{S}_8\text{H}_{28}$ ), thus suggesting that four amido ligands in HDMDW can be replaced by thiolates upon reaction at room temperature with EDT. As already observed elsewhere on molybdenum thiolate systems,<sup>19,137</sup> the

loss of ethylene from one of the ethylenedithiolate bridge can explain the low carbon content observed in solid **B**.

The DRIFT spectrum of **B** displays several absorption bands in common with precursor HDMDW and some distinct bands (see Figure 2. 7). Both structures share common C–H stretching in the range of 3000-2700  $\text{cm}^{-1}$ , to  $\text{CH}_3$  rocking in the range of 1200-1100  $\text{cm}^{-1}$ ,  $\text{CH}_3$  deformation between 1450 and 1350  $\text{cm}^{-1}$ , and CNC stretching vibrations at 1300-1200  $\text{cm}^{-1}$ , due to dimethylamido groups present in both structures. Solid **B** exhibits a distinguishable S–H stretching vibration peak at 2407  $\text{cm}^{-1}$ . However, other bonds, that are inherent only to W thiolates such as C–S and W–S, could not be observed due to the limitation of the applied IR window (transparency of KBr between 4000 and 800  $\text{cm}^{-1}$ ).

The solid-state  $^1\text{H}$  NMR spectrum of that precipitate **B** is not informative (see experimental section) but confirms that the reaction between HDMDW and EDT does occur since several resonance peaks instead of the observed single proton peak of the dimethylamido group are observed.

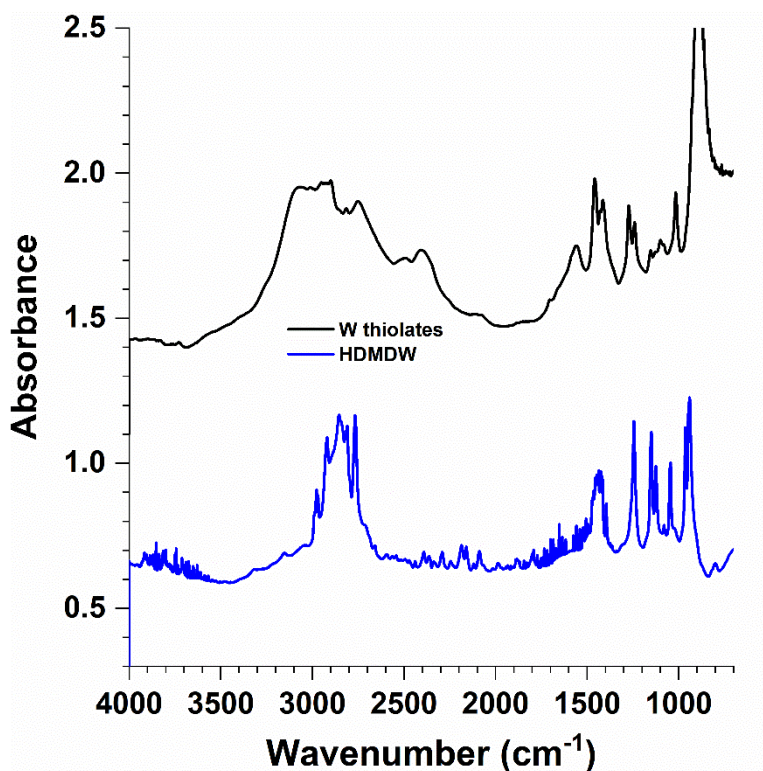
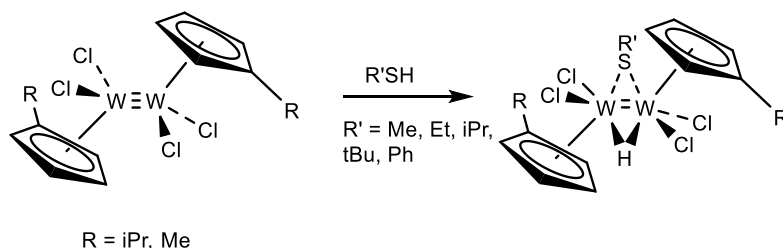


Figure 2. 7. DRIFT of HDMDW and the solid product obtained in its reaction with EDT

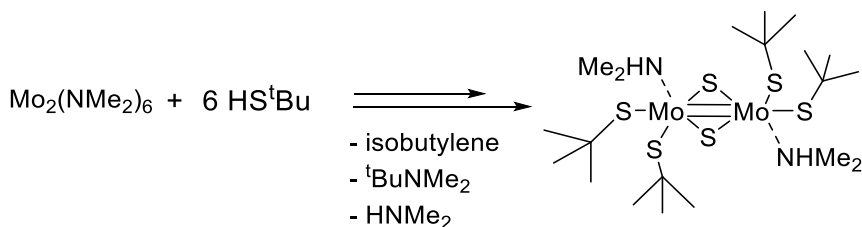
In summary, the combined elemental analysis and the IR data point to the existence of a fast reaction between the two reagents that could lead to a (dimethylamido)tungsten dithiolate product that retains some of the dimethylamido ligands as well as bound to dithiolate groups.

A relevant precedent in the literature, the molecular W(III) dimer complex,  $[W_2(\eta-C_5H_4R)_2Cl_4]$ , was reported to react with thiol,  $R'SH$ , involving oxidative addition across the  $W\equiv W$  triple bond to yield W(IV) (see Scheme 2. 4). Q. Feng *et al.* demonstrated the formation of analogous red-brown  $\mu$ -thiolato derivatives,  $[W_2(\eta-C_5H_4R)_2Cl_4(\mu-H)(\mu-SR')]$  using alkylthiols with the different alkyl groups involving oxidation of W(III) to W(IV).



Scheme 2. 4. Oxidative addition of  $R'SH$  across  $W\equiv W$  triple bond (reproduced from ref<sup>138</sup> with permission, copyright by RSC)

Even more fittingly for this thesis work, literature also shows precedents of the incomplete substitution of the dimethylamido ligands by thiols in the  $M\equiv M$  ( $M = Mo$  or  $W$ ) triple bond-containing alkyl amido dimer.<sup>29,139</sup> Authors failed to produce target  $Mo_2(SR)_6$ -type molecule and ended up with  $Mo_2(\mu-S)_2(^tBuS)_4(HNMe_2)_2$  when reacted  $Mo_2(NMe_2)_6$  with 6 equivalents of  $^tBuSH$ . (see Scheme 2. 5) Isobutylene, *tert*-butyldimethylamine, and dimethylamine were found as volatile by-products of the reaction. Such side reaction shows that thiol reaction with amido leads to W(III) to W(IV) clear oxidation with the concurrent formation of bridging sulfido group (see structure in Figure 2. 8).



Scheme 2. 5. Incomplete substitution of dimethyl amido ligands in the reaction between hexakis(dimethylamido)dimolybdenum (III) with excess  $HS^tBu$ . Adapted from ref.<sup>29</sup>

These literature precedents are suggesting that the EDT is able to partially substitute the dimethylamido ligands, to bridge across tungsten-tungsten triple bond via oxidative-addition to W (IV) and possibly evolve to bridging sulfido groups with proton transfer from the thiol to the amido ligand to yield W(IV) mixed thiolate/sulfide with coordinated amines.

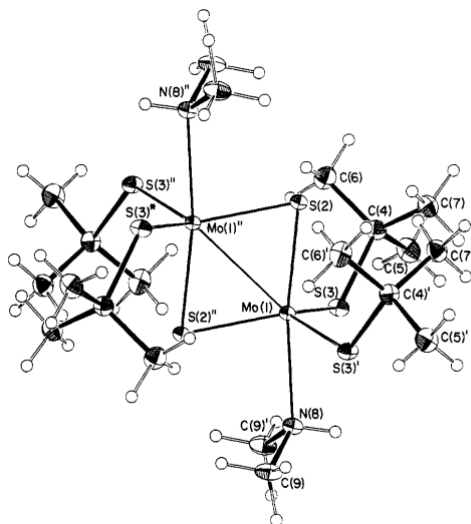
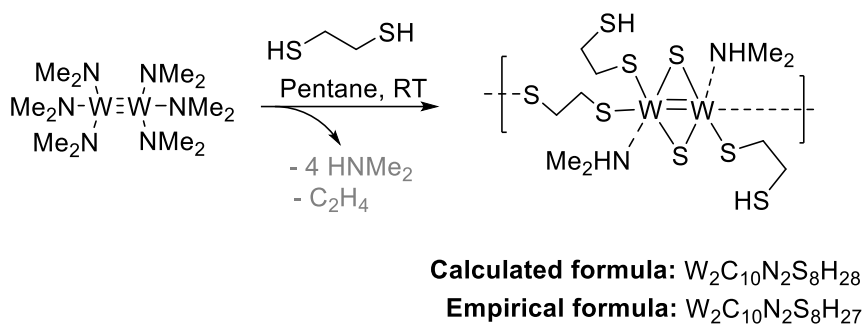


Figure 2. 8. Molecular structure of  $\text{Mo}_2(\mu\text{-S})_2(\text{tBuS})_4(\text{HNMe}_2)_2$  prepared in the reaction of excess  $\text{tBuSH}$  with  $\text{Mo}_2(\text{NMe}_2)_6$ . (reproduced with permission from ref<sup>29</sup>)

To come back to our understanding the reaction of HDMDW with EDT, while we have no information on the nuclearity of the several species formed, the relative ratio between tungsten, amido and ethylenethiolate seems to suggest a 2:2:4 ratio (see Scheme 2. 6 for a possible formulation). Bridging isomers and fluxionality are among the reasons why several isomers could occur. Further, thiol/amido systems are known to be in equilibrium with thiolate/amine due to a facile protonation of amido ligands. The chosen isomer in Scheme 2. 6 among all these possibilities, is the one that best matches the structure reported in a close molecular analogue shown in Figure 2. 8 and discussed above. Some further direct evidence of W (IV) oxidation state as well as the sulfido bridging system is required. Some formulation based on the discussed precedent can be tentatively proposed.



Scheme 2. 6. Proposed simplified reaction scheme of HDMDW and EDT. Only one possible isomer shown for clarity among the several possible products (see text for discussion)

### 2.3.3. Modeling ALD via impregnation of $W_2(NMe_2)_6$ on silica-700 and reaction with EDT

#### 2.3.3.1. Grafting of $W_2(NMe_2)_6$ on silica-700 nanobeads

Dehydroxylated silica,  $SiO_{2-700}$ , reacts instantaneously with HDMDW in pentane solution (where the ratio between HDMDW and surface hydroxyl groups was set to 1:1), leading to a color change of the powder from white to yellow. After washing and drying, the DRIFT spectrum of the powder demonstrates complete consumption of surface  $-OH$  groups and the appearance of new absorption peaks in the  $3000$  and  $2700\text{ cm}^{-1}$  range (see Figure 2. 9). The bands at  $2983$ ,  $2931\text{ cm}^{-1}$  are assigned to asymmetric stretching  $C-H$  in  $-NMe_2$  ligands, while bands at  $2868$ ,  $2821$ , and  $2777\text{ cm}^{-1}$  correspond to symmetric stretching of the  $C-H$  bonds, thus suggesting successful chemical grafting of the complex on silica. The band at  $1850\text{ cm}^{-1}$  caused absorption of combinational vibrations of  $Si-O$  bond was used for normalization of intensities of the IR spectra. Spectra at lower wavenumbers were not analyzed because the strong vibration bands originating from the substrate do not allow observe any other signal.

Elemental analysis (see Table 2. 1) of the yellow solid reveals the empirical formula  $[W_2C_{10}N_5H_{27}]$  for the metallated fragment which is in good agreement with the structure proposed in Scheme 2. 7. The metal loading obtained (7.8 wt.%) agrees with a 2:1 ratio with all the starting surface silanol, therefore suggesting that the main surface species should be close to  $[\equiv SiO-W_2(NMe_2)_5]$ , as already reported before us (see Scheme 2. 1).<sup>133</sup>

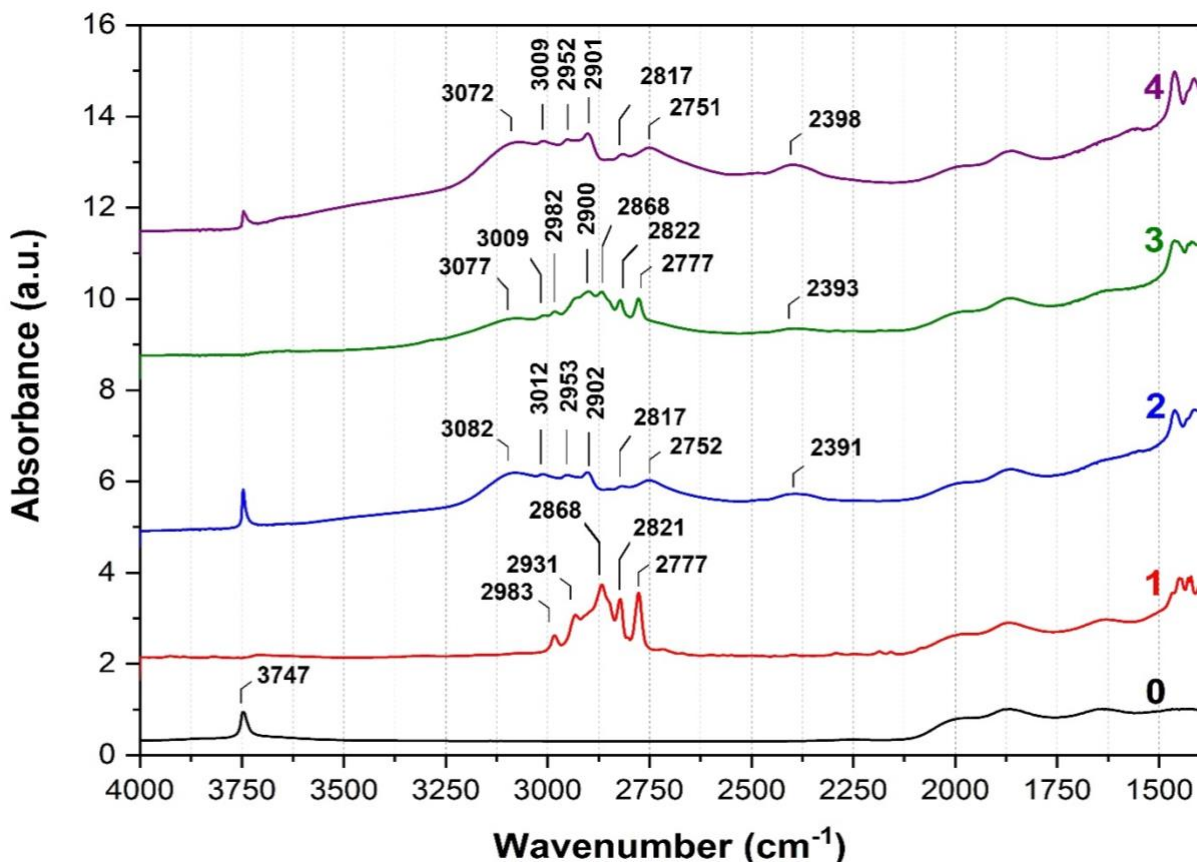
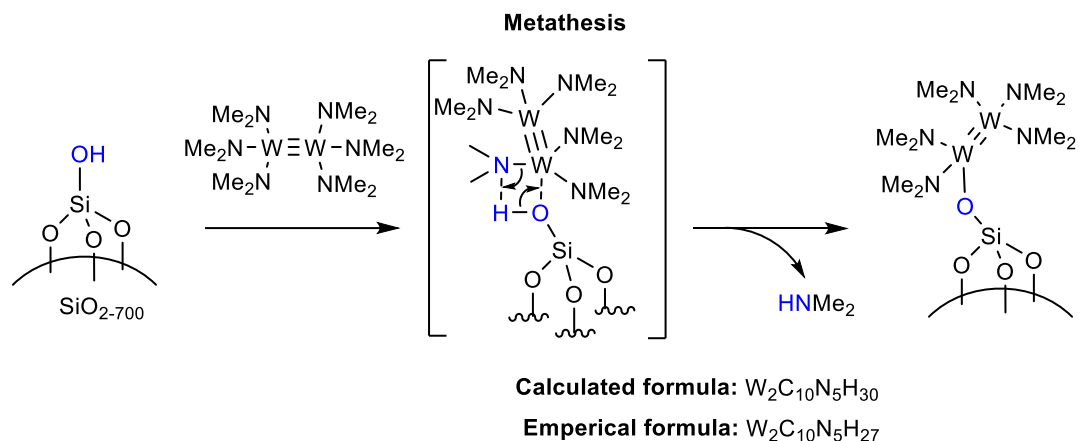


Figure 2. 9. IR spectra recorded between 1400 and 4000  $\text{cm}^{-1}$  for the sample of  $\text{SiO}_{2-700}$  before deposition (spectrum 0, black); after the 1<sup>st</sup> pulse of HDMDW precursor (spectrum 1, red) in solution; after the first pulse of EDT (spectrum 2, blue) in solution; after the second pulse of HDMDW (spectrum 3, green) in solution; after the second pulse of EDT (spectrum 4, purple) in solution;

The  $^1\text{H}$  NMR spectra did not provide informative data, given the broadness of the peaks. The  $^{13}\text{C}$  solid-state NMR spectrum (see the red spectrum 1, Figure 2. 10) displays three peaks at 56.5, 46.1, and 36.5 ppm, which are assigned to different orientations/distances of methyl groups from the silica surface. According to R. Gauvin *et al.*,<sup>133</sup> they are attributed to distal, vicinal ( $\text{W}(\text{NMe}_2)_3$ ) and proximal methyl groups, respectively.

In summary, based on the elemental analysis and the infrared and NMR spectroscopy data of the solid as well as analysis of the volatile by-products after hydrolysis, the first grafting step of complex HDMDW on silica nanobeads proceeds with a proton exchange between surface  $\equiv\text{Si}-\text{OH}$  and one of the dimethylamido ligands to yield as main surface species  $[\equiv\text{SiO}-\text{W}_2(\text{NMe}_2)_5]$  (see

Scheme 2. 7, which displays the proposed mechanism of  $\sigma$ -bonds metathesis). The proposed reaction scheme is in good agreement with the reference<sup>133</sup>.



Scheme 2. 7. Proposed reaction scheme for deposition of HDMDW on silica-700.

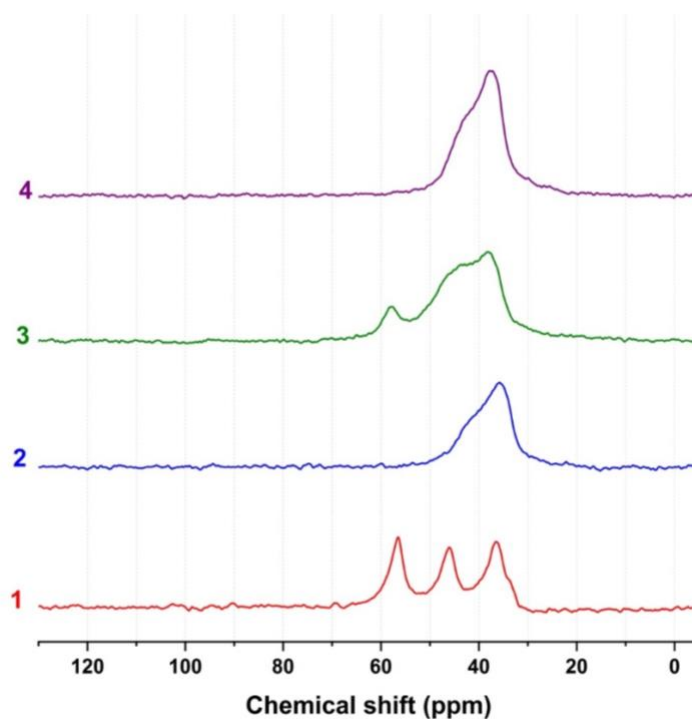


Figure 2. 10. Solid-state  $^{13}C$  NMR recorded for the products obtained in the ALD-modelling pulses  $SiO_{2-700}$  using HDMDW and EDT: the 1<sup>st</sup> pulse of HDMDW precursor (spectrum 1, red) in solution; after the first pulse of EDT (spectrum 2, blue) in solution; after the second pulse of HDMDW (spectrum 3, green) in solution; after the second pulse of EDT (spectrum 4, purple) in solution;

To understand whether HDMDW can be used in automated common ALD reactors, we studied the reactivity of HDMDW vapors with silica-700. In Figure 2. 11, DRIFT spectroscopy recorded all the changes upon adsorption of the  $W_2(NMe_2)_6$  on the surface of  $SiO_{2-700}$  pellet. The first heating step of  $W_2(NMe_2)_6$  (red curve) at 70 °C for 20 minutes under a high static vacuum did not lead to significant changes comparing with bare  $SiO_{2-700}$  (black curve). There is a barely noticeable increase in the region between 3000-2700  $cm^{-1}$  (C–H stretching vibrations) that supports the adsorption of a negligible amount of  $W_2(NMe_2)_6$ . Besides, the sharp band of surface hydroxyl groups (3747  $cm^{-1}$ ) has not changed its intensity pointing to no chemical reaction with HDMDW. Since the first step was unsuccessful, the temperature and time of exposure was increased to 90 °C and 40 minutes.

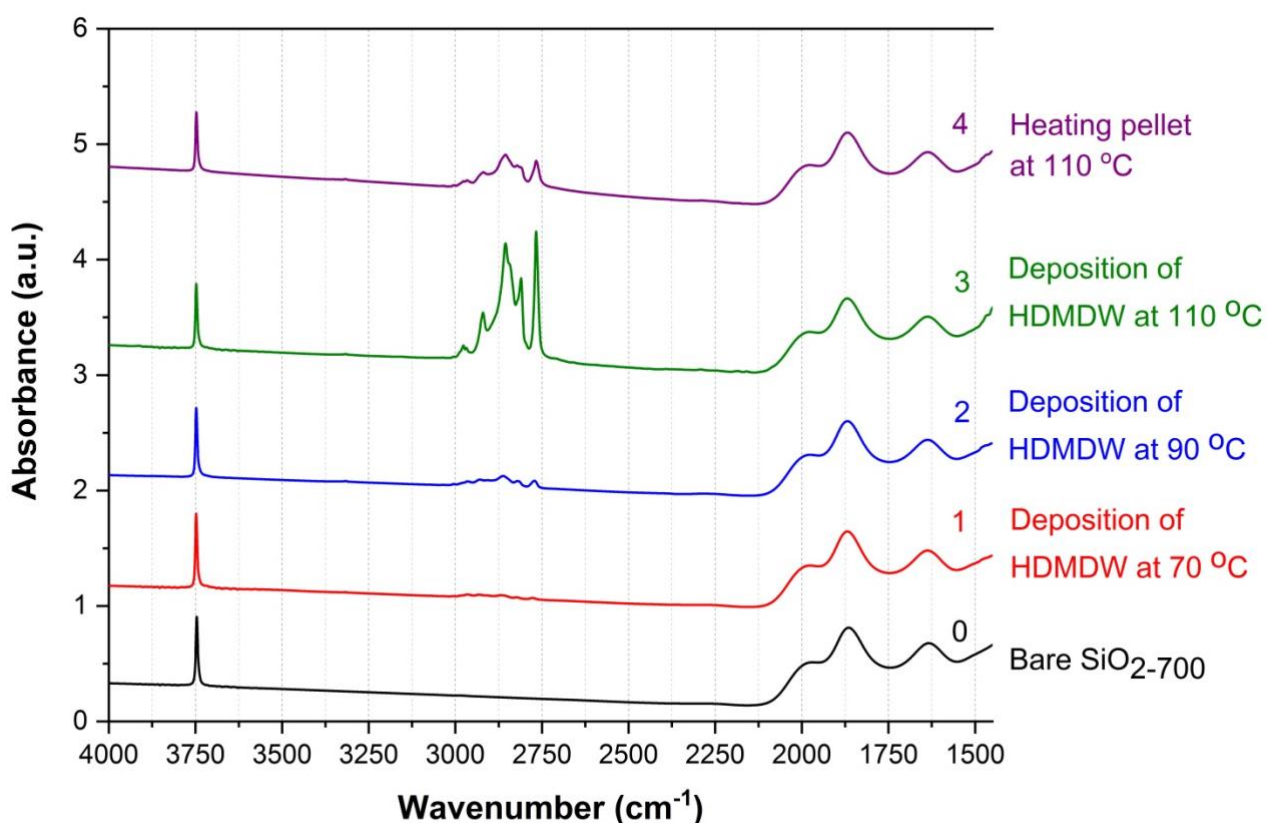


Figure 2. 11. IR absorption of silica-700 pellet during deposition of HDMDW vapors onto pellet in static UHV. 0: pristine  $SiO_{2-700}$  pellet; 1: after heating HDMDW complex at 70 °C; 2: after heating HDMDW complex at 90 °C; 3: after heating HDMDW complex at 110 °C; 4: after heating the pellet at 110 °C to check back sublimation;

The second heating step (blue curve) has resulted in a slightly greater increase of the bands between 3000 and 2700  $cm^{-1}$  that supports the effect of higher temperatures for deposition. However, despite

better deposition, there still seems no significant change of the OH band at  $3747\text{ cm}^{-1}$ . In the next step (green curve), the temperature was increased to  $110\text{ }^{\circ}\text{C}$  and heating time remained at 20 minutes. Adsorption of HDMDW brought a much more important amount onto the surface, see strong bands between  $3000$  and  $2700\text{ cm}^{-1}$ , but the band at  $3747\text{ cm}^{-1}$  remained substantially unchanged. The big increase of the HDMDW amount on the surface was coherent because the temperature exceeded its sublimation point. The persistence of OH peak suggests that adsorption of the HDMDW onto silica was only physical and without any chemical reaction (or with negligible yield). Indeed, the adsorbed  $\text{W}_2(\text{NMe}_2)_6$  could be sublimed off by heating the powder at  $110\text{ }^{\circ}\text{C}$  for 20 minutes.

These observations show that the  $\text{W}_2(\text{NMe}_2)_6$  vapors are not reactive with silica at moderately high temperatures and mainly adsorb on silica just physically. Therefore, surprisingly, while the reaction appears facile when the tungsten dimer is dissolved in solution but kinetically inert when the tungsten precursor is in the gas phase.

In reality, the chemical role of solvent in otherwise kinetically inert reaction at the gas-solid interphase has already been noted in the ALD community.<sup>23</sup>

#### *2.3.3.2. The reaction of EDT on silica-supported [ $\equiv\text{SiO}-\text{W}_2(\text{NMe}_2)_5$ ] as a modeling reaction of the 2<sup>nd</sup> half cycle*

The pale yellow powder of [ $\equiv\text{SiO}-\text{W}_2(\text{NMe}_2)_5$ ] obtained from solution reaction and dried was exposed to the vapor of 1,2-ethanedithiol,  $\text{HSCH}_2\text{CH}_2\text{SH}$  (EDT).

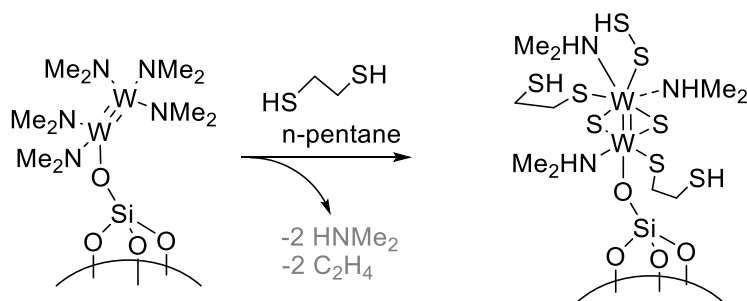
To gain insight into the structure of the surface site, the infrared spectrum of the brown powder was collected (see Figure 2. 9). A new broad peak at  $2391\text{ cm}^{-1}$  is among the most significant new features. In analogy with our previous similar observation and assignments<sup>19</sup>, the band assigned to the stretching vibration of the S–H bond was observed. This points to that at least one of the tungsten coordinated-thiolate ligands bind in a terminal  $\eta^1$  fashion, thus leaving availability of free –SH groups enabling deposition of HDMDW in the next pulse, which are crucial in the quest efficient ALD process based on repeating reactions of thiol moieties with tungsten amido ones.

The broad peak at  $3078\text{ cm}^{-1}$  can signify hydrogen bonding present in the new structure(s). There are several options for possible hydrogen bonding involving protons of dimethylamine, hydroxyl and thiol groups.<sup>140,141</sup> The hydrogen atoms of free thiol groups can also have hydrogen bonding with the

surface oxygen atoms of adjacent surface Si–O–Si moieties. In the spectrum, it was also observed the appearance of –OH groups at 3747 cm<sup>-1</sup>. In our experience, the appearance of the surface –OH bands after the addition of EDT precursor to a silica-supported metal complex previously took place.<sup>19</sup> This aspect cannot be settled at this point. An intriguing further possibility that will not be discussed further at this point in view of current lack of direct experimental evidence (such as EPR data that we have not been able to acquire yet) is the tendency of SSH to protonate adjacent bases in order to yield stable persulfide ligands as shown in eq. 2.1 below.<sup>142,143</sup> This possibility will nevertheless be better discussed in Chapter 4 reporting XPS evidence acquired on the wafer.



The solid-state <sup>13</sup>C NMR spectrum (see the blue spectrum 2 in Figure 2. 10) records a single peak at 37.9 ppm with a shoulder at ca. 42.0 ppm. Comparing with the 1<sup>st</sup> pulse product spectrum, peaks at 56.5 and 46.1 ppm have disappeared. This may be linked to symmetry simplification ensuing from the elimination of some of the dimethylamido groups. After binding the ethylenedithiolate ligands, there are now two carbon atom types, which are methyl bound to nitrogen and methylene bound to sulfur. The main peak at 35.6 ppm is assigned to the carbon atoms of the methylene moieties though it may also have a contribution from one of the dimethylamido carbons. The shoulder can then originate from methyl groups of the unsubstituted –NMe<sub>2</sub> ligands.



**Calculated formula:** W<sub>2</sub>C<sub>10</sub>N<sub>3</sub>S<sub>8</sub>H<sub>30</sub>

**Empirical formula:** W<sub>1.8</sub>C<sub>10</sub>N<sub>2.8</sub>S<sub>7.9</sub>H<sub>29</sub>

Scheme 2. 8. Proposed reaction scheme of the 2<sup>nd</sup> pulse. Only one of the possible isomers is shown (see text for discussion on several other possible isomers). The bridging possibility as well as the fluxional character of thiolate are omitted for clarity.

Elemental analysis of the ensuing brown powder (see Table 2. 1) shows the partial replacement of the dimethyl amido ligands by ethylenedithiolate and yielding the empirical formula

( $\equiv\text{SiO}-\text{W}_2\text{C}_{10}\text{N}_3\text{S}_8\text{H}_{29}$ ). The S:N:W atomic ratio was estimated at 8:3:2 suggesting that resulting structure bonded to four EDT-originating moieties and lost two amido groups. Therefore, the formula can be extended to  $[\equiv\text{SiO}-\text{W}_2(\text{NMe}_2)_3(\text{SCH}_2\text{CH}_2\text{SH})_2\text{S}_4]$ , where some sulfur groups were added without their carbon atoms to match the estimated C/W and S/W ratios and taking into account how subjected are the ethylenedithiol groups to liberate ethylene molecule. The loss of ethylene has already been observed from the silica-supported transition molybdenum ethylenedithiolate complex.<sup>19</sup> Elimination of 2 equivalents of  $\text{C}_2\text{H}_4$  adjusts the number of carbon atoms to 10. As it was discussed for the structure of molecular product of the reaction between HDMDW and EDT (see section 2.2.4), some closely related literature precedents reported the bridging possibility of sulfido groups that occurred via oxidative addition of M(III) to M(IV).<sup>29,138</sup>

In summary, the evidence collected so far on the reaction of EDT with  $[\equiv\text{SiO}-\text{W}_2(\text{NMe}_2)_5]$  shows partial substitution of dimethylamido by terminal ethylenedithiolate. Although the surface product(s) can (co)exist as numerous different conformations and isomers, we have tried to illustrate one of the potential structures in Scheme 2. 8 in analogy with the molecular proposal made before. Last two literature remarks and our results support the following extended formula  $[\equiv\text{SiO}-\text{W}_2(\text{HNMe}_2)_3(\text{SS})(\text{S}(\text{CH}_2)_2\text{SH})_2(\text{SSH})]$  that we will refer to hereafter.

### 2.3.3.3. Modeling the 2<sup>nd</sup> ALD cycle

The further reaction of the solid containing (*inter alia*, see above) surface species  $[\equiv\text{SiO}-\text{W}_2(\text{HNMe}_2)_3(\text{SS})(\text{S}(\text{CH}_2)_2\text{SH})_2(\text{SSH})]$  with HDMDW represents the modeling of the 3<sup>rd</sup> pulse of the targeted ALD process. As indicated by in-situ IR monitoring, the incoming tungsten dimer consumes the available surface hydroxyl  $-\text{OH}$  groups and decreases the intensity of SH groups (spectrum 3 in Figure 2. 9). It signifies that the second tungsten pulse reacts with both groups increasing the density of the first layer as well as adding more tungsten atoms on this sublayer. In addition, it leads to a similar pattern of IR absorption bands in the region of  $2750\text{-}2950\text{ cm}^{-1}$  as on the spectrum after the 1<sup>st</sup> pulse. The same absorption bands for asymmetric stretching of the C–H at  $2982\text{ cm}^{-1}$  (m) as well as symmetric stretching at  $2868$  (s),  $2822$  (m), and  $2777$  (s)  $\text{cm}^{-1}$  were observed as for the 1<sup>st</sup> pulse. These identical features between the 1<sup>st</sup> and 3<sup>rd</sup> pulse products corroborate successful deposition of HDMDW at this later stage of the ALD process.

Elemental analysis of the 3<sup>rd</sup> pulse product shows a tungsten loading of 16.1 %<sub>w</sub> that is 2.1 times higher than in the 1<sup>st</sup> or 2<sup>nd</sup> pulse products. This result is consistent with an addition of about 1

equivalent of the complex to the 2<sup>nd</sup> pulse product. The analysis results help to define the formula as  $\equiv\text{SiO}-\text{W}_4\text{C}_{16}\text{N}_6\text{S}_7\text{H}_{44}$ , therefore, three dimethylamido have been replaced upon this deposition. The elimination of the dimethylamido groups is consistent with the full reaction of the three S–H thiol bonds present in the starting structure. Taking into account that the structure of the 2<sup>nd</sup> pulse product can have various isomers, no structure was proposed for the 3<sup>rd</sup> pulse product, where tungsten dimer is added to the surface species through partial substitution of amido with thiolate. Nevertheless, the formula of the 3<sup>rd</sup> pulse product can be tentatively hypothesized as  $[\equiv\text{SiO}-\text{W}_4(\text{NHMe}_2)_3(\text{NMe}_2)_3(\text{SS})_2(\text{S}(\text{CH}_2)_2\text{S})_2]$ . The general formula of this configuration gives  $\equiv\text{SiO}-\text{W}_4\text{C}_{16}\text{N}_6\text{S}_8\text{H}_{47}$ , which matches well the experimental formula and loading (see Table 2. 1).

The solid-state NMR spectrum has supported the successful deposition as well as the on the proposed reaction stoichiometry. Solid-state <sup>13</sup>C NMR spectroscopy (see green spectrum 3 in Figure 2. 10) provided the spectrum showing a large peak with a chemical shift at 38.2 ppm having a shoulder at 43.7 ppm and another small peak at 57.7 ppm. This has similar features as does the 1<sup>st</sup> pulse product though the 3<sup>rd</sup> pulse product exhibits the methylene carbon atoms. Intensities of the newly added carbon atoms ( $\delta$  57.7 and 43.7 ppm) have increased with respect to the 2<sup>nd</sup> pulse. Therefore, the results suggest that only dimethylamido carbon atoms were added upon the 3<sup>rd</sup> pulse deposition while preserving already-existing methylene carbon atoms.

The resulting solid was then exposed to EDT, that models the 4<sup>th</sup> ALD pulse (and the end of the second full ALD cycle). *In situ* monitoring by IR spectroscopy shows an increase of already present IR absorption bands at 3747 (w), 3072 (br), 3009 (m), 2952 (s), 2901 (s) and 2391 (br)  $\text{cm}^{-1}$  that were observed after the 2<sup>nd</sup> pulse in Figure 2. 9 (see the purple spectrum 4). The second pulse of EDT leads to the appearance of some surface –OH group and new –SH groups. The broad peak at 3072  $\text{cm}^{-1}$  signifies intramolecular hydrogen bonding that can occur between thiol and dimethylamine groups, and oxygen of the surface siloxy (Si–O–Si) groups. The absorption bands at 3009 (m) and 2952 (s)  $\text{cm}^{-1}$  can be assigned to the asymmetric stretching vibration of C–H bonds, whereas the bands at 2901(s), 2817 (m), and 2751 (s)  $\text{cm}^{-1}$  are assigned to the symmetric stretching vibration of C–H bonds. As it can be noticed, some of the absorption bands appear with each EDT pulse and disappear or at least diminishes with each HDMDW pulse. For instance, the hydrogen bonding band (3072  $\text{cm}^{-1}$ ) always increased upon the 2<sup>nd</sup> and 4<sup>th</sup> pulses (pulses of EDT) and decreased well upon the 3<sup>rd</sup> pulse. Another alternating peak was observed at 2952 (s)  $\text{cm}^{-1}$ , which is seen after each EDT pulse, but disappeared after the 3<sup>rd</sup> pulse. The repeatability with each ALD

cycle is thus illustrated by the DRIFT spectroscopy featuring continuous pulse-by-pulse growth of the tungsten thiolates.

Elemental analysis of the 4<sup>th</sup> pulse product estimated that the C/W, N/W, and S/W ratios equal to 4.5, 1.0, and 3.8, respectively (see Table 2. 1 in experimental section). It defined the empirical formula as  $\equiv\text{SiO}-\text{W}_4\text{C}_{18}\text{N}_4\text{S}_{15}\text{H}_{49}$  showing that successful thiol/thiolate incorporation was achieved suggesting that two dimethylamido ligands are replaced by 2 ethylenedithiolate ligands.

The solid-state  $^{13}\text{C}$  NMR spectroscopy recorded for the 4<sup>th</sup> pulse product has revealed the spectrum identical to that of the 2<sup>nd</sup> pulse. It exhibits a single peak at  $\delta$  37.9 ppm having a shoulder at ca. 41.8 ppm. Similarly, these peaks can be assigned to the methylene carbon (of ethylenedithiolate) and methyl carbon atoms, respectively.

ALD-modelling surface reactions using  $\text{W}_2(\text{NMe}_2)_6$  and EDT on silica-700 were attempted to be conducted in alternating phases. The 1<sup>st</sup> and 3<sup>rd</sup> pulses of HDMDW deposition were carried in solution in the same way as previously described, while the pulses of EDT (2<sup>nd</sup> and 4<sup>th</sup>) were carried by diffusing EDT vapors over the solid under static vacuum.

#### 2.3.3.4. Study of the annealing step

The target is to test whether the silica-supported tungsten thiolates do evolve to  $\text{WS}_2$  by thermal treatment in analogy to what was observed for the  $\text{MoS}_2$  system.<sup>19</sup>

The first experiment was an *operando* GC-MS-coupled DRIFT analysis of the thermal treatment of the silica-supported tungsten thiolates after two full ALD cycles (or four pulses) up to 500 °C with 2 °C/min rate under helium flow. The DRIFT spectra (see Figure 2. 12) show a slow decrease of absorption bands ascribed to alkyl C–H stretching in the region of 3100-2700  $\text{cm}^{-1}$  starting from 110 °C and diminishing until 350 °C. The organic part of the structure remains stable up to 110 °C (see Figure 2. 13). It starts to decompose above this temperature and appears complete around 350 °C. Meanwhile, there is an increase in surface –OH bands at 3747  $\text{cm}^{-1}$  that can not be precisely attributed. Densification of silica at higher temperatures and traces of moisture could lead to its formation.

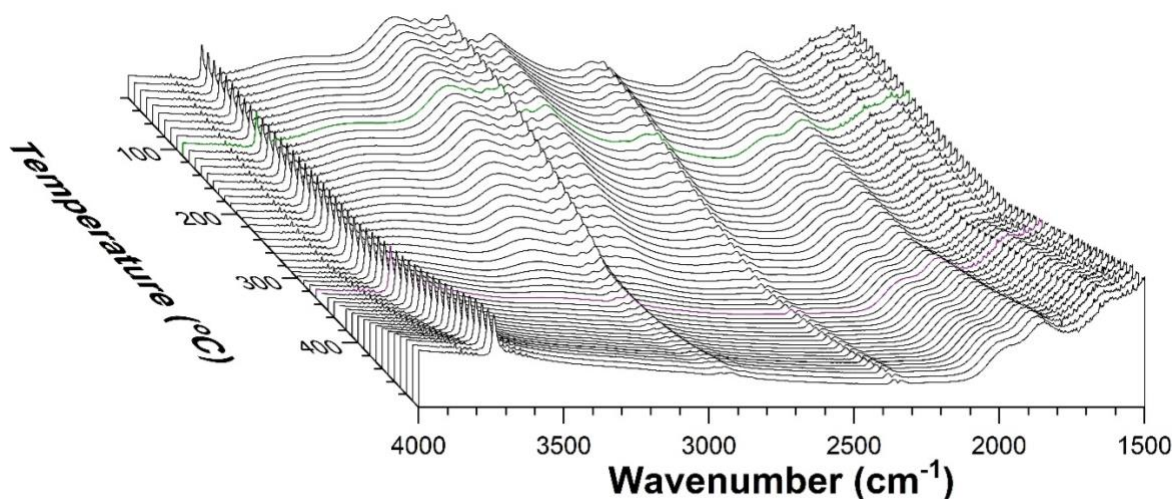


Figure 2. 12. Evolution of the DRIFT spectra with heating the W thiolates

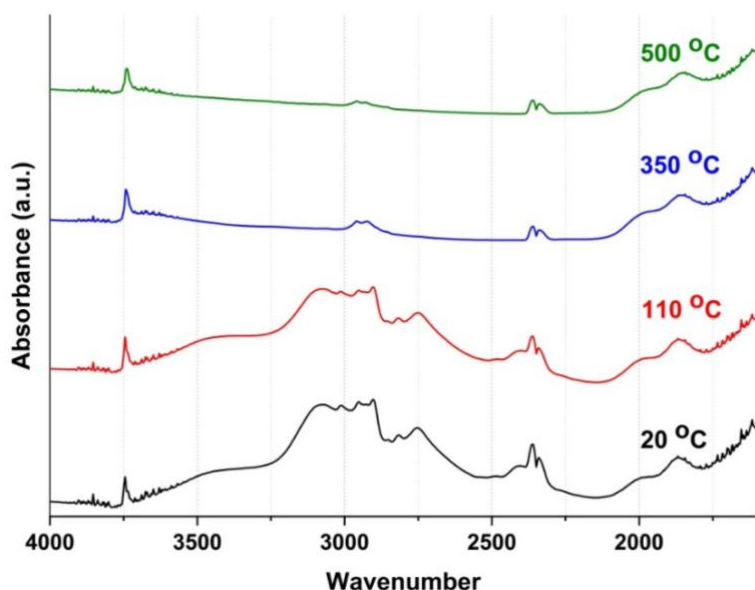


Figure 2. 13. Selected DRIFT spectra recorded at different temperature of thermal decomposition of the W thiolates

Released gaseous molecules were analyzed by GC-MS. The main fractions that we expected to observe upon heating were ethylene, nitrogen- and sulfur-containing compounds. Indeed, these molecules did show up in GC spectra along with argon, water and thiophene as can be seen in Figure 2. 14. Ethylene was attributed to the elimination from the ethylenedithiolate moiety as it was seen from the ALD grown W thiolates with BTBMW and EDT in Chapter 3, and from Mo thiolates.<sup>19</sup> Isocyanomethane could be produced upon elimination of remaining unsubstituted

dimethylamido groups through previously reported  $\beta$ -hydrogen elimination.<sup>144–146</sup> Water was detected over all along the measurement and thus identified as contamination of the GC column.

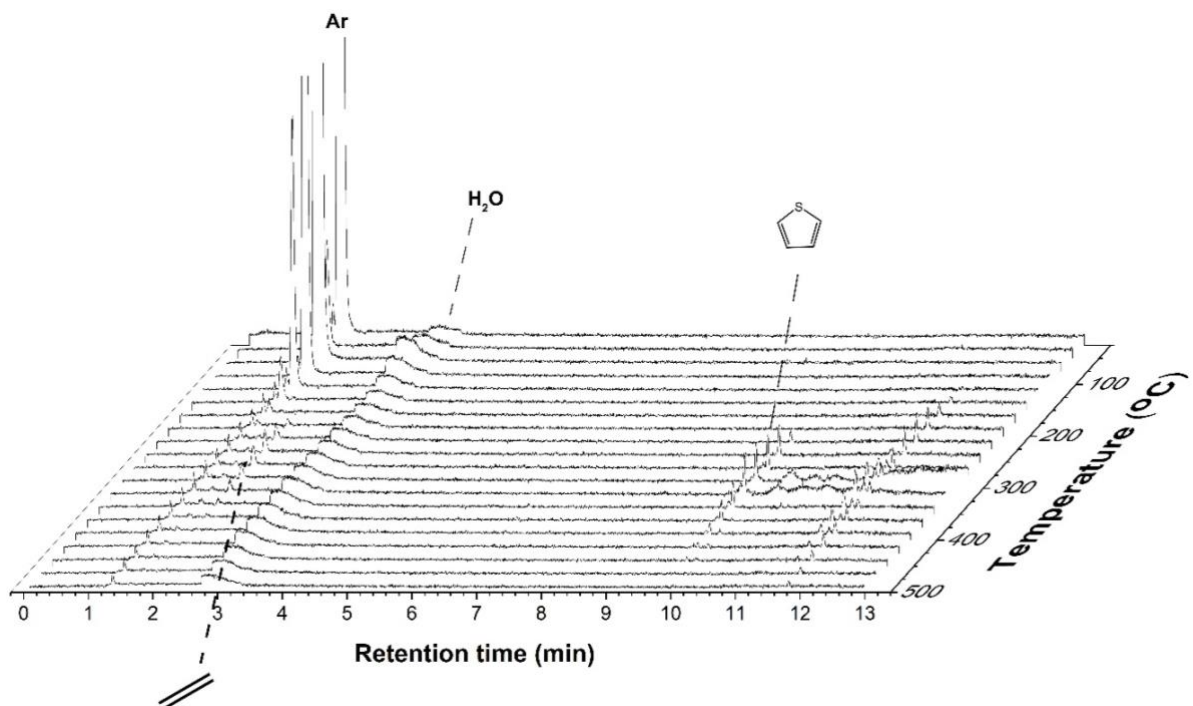


Figure 2. 14. GC spectra recorded for the headspace of DRIFT cell every 25 °C of thermal decomposition of the W thiolates

In summary, this *operando* study showed that the thiolates evolve to mineralized solid and that such mineralization is already substantial at 350 °C. The *in situ* monitoring of the gaseous byproducts and of the solid shows that the main organic byproduct is ethylene. At a temperature close to 275 °C, more complex chemistry starts. The evolution of thiophene starting at 250 °C might suggest desulfurization of the solid,

This *operando* study is technically capped at 500 °C. The second set of experiments was carried out to characterize the solid after a more important thermal treatment. The ALD-grown W thiolates were annealed under the argon flow at 800 °C *ex situ*. The (HR)TEM images of the annealed solids on 10 and 2 nm scale are reported below in Figure 2. 15 A and B. Figure A illustrates the layered structures grown mostly on the edges of the ca. 20 nm silica nanobeads. Image B shows a closer view of that layered pattern, from which the average distance between layers was measured to be 0.64 nm. this value comes in good agreement with computationally calculated distances between two layers in bilayer WS<sub>2</sub>.<sup>147</sup> As authors state, the best method was random phase approximation

yielding several values between 6.24 and 6.84 Å for the various crystal phases (2H and 3R). The experimental value obtained on the samples, 0.64 nm, lies within these values and may stem from any of these phases. The STEM image (Figure 2. 15C) shows a homogeneous distribution of the WS<sub>2</sub> all over the silica. The brightest area in the STEM image identifies patterns of WS<sub>2</sub> which have mostly elongated curved shapes around silica nanobeads. The D and E images represent the selected area on the SEM images for further analysis by EDX (image F) spectroscopy. In the EDX, atomic fractions of S / W were determined as 3.60 / 2.68 on the “Spectre 1”, and as 7.53 / 2.83 on the “Spectre 2”. This provides the S/W ratio in average of about 2 (±0.7) that matches well with the expected WS<sub>2</sub> formula.

The work reported by S. Cadot *et al.*<sup>19</sup> also showed that hydrogen gas facilitates annealing of the ALD-grown Mo thiolates transforming the amorphous phase to crystalline at a lower temperature (450 °C). Silica-supported W thiolates prepared by solution ALD in this work were annealed at the same temperature under hydrogen flow (diluted in argon). STEM and HRTEM micrographs display layered patterns curved and distributed around spherical silica nanobeads (images A and B in Figure 2. 16) that is coherent with expected deposition on the surface of the non-porous beads. The interlayer distance was calculated from the high-resolution image (image C,  $d = 0.64$  nm), which came in good agreement with the value calculated from the sample annealed at 800 °C as well as with that of the mentioned report. Nanocrystalline domains were also found all over the analyzed surface (Figure 2. 16 D). The E and F SEM images illustrate the selected areas of *Spectre 1* and *Spectre 2* for further EDX analysis. The atomic fractions of sulfur and tungsten were determined in the area of the spectre 1 as 4.06 and 3.68 %, while in the spectre 2 area as 2.62 and 1.73 %. The ratio of the latter zone (1.51:1) is closer to the expected stoichiometric ratio than that of the first zone (1.10:1). This provides an average S/W ratio of about 1.3 (±0.2).

In summary annealing at 800 °C (under argon) as well as at 450 °C (under hydrogen) of silica-supported tungsten thiolates obtained in our solution ALD process appear to yield the targeted WS<sub>2</sub> phase.

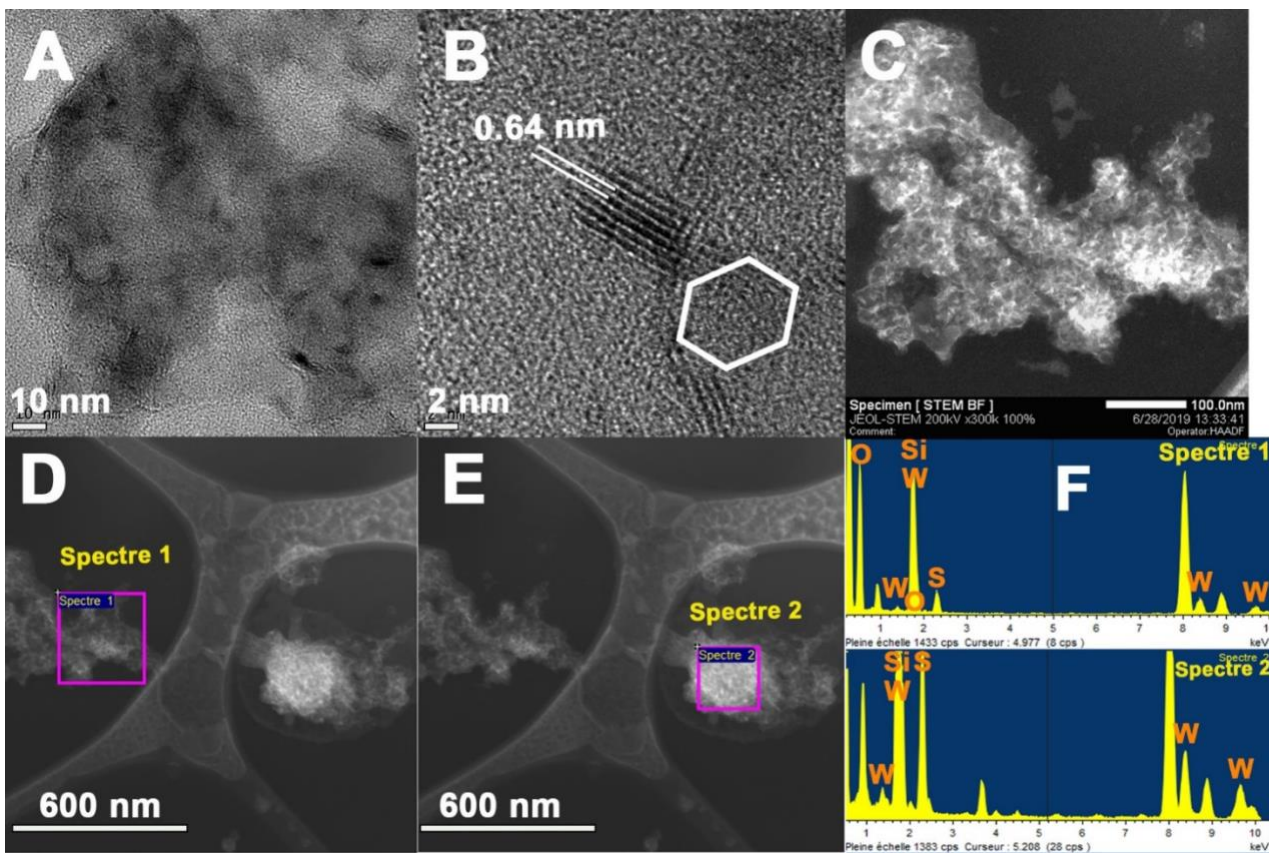


Figure 2. 15. Electron microscopy images: A and C - (HR)TEM images on 10 and 2 nm scales, respectively, of the argon-annealed powder; B - STEM image on 100 nm scale, D and E - SEM images of analyzed areas by EDX; F - EDX analyses on the corresponding spots.

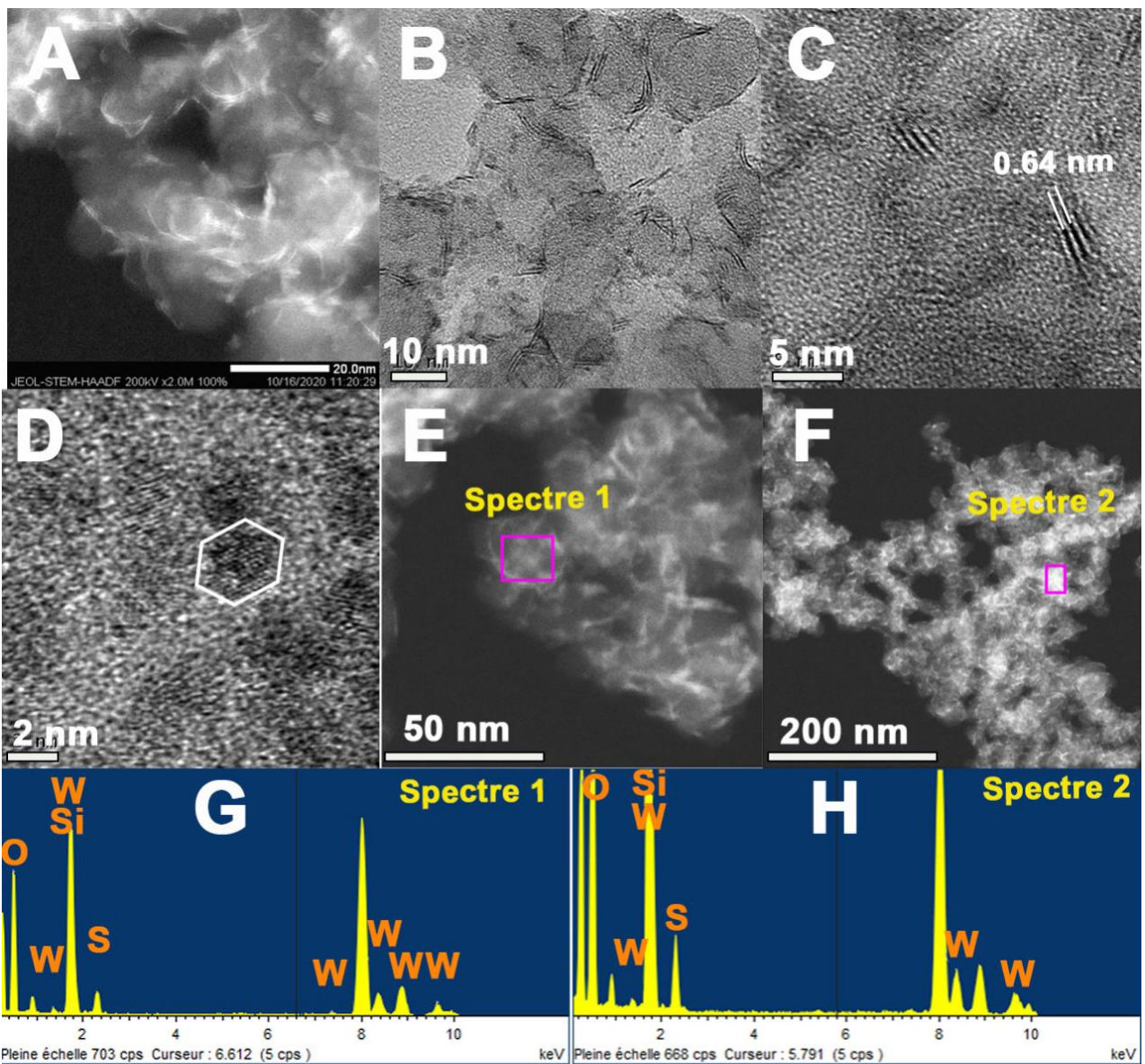


Figure 2. 16. Electron micrographs and EDX results of hydrogen-annealed silica-supported W thiolates on silica: A - STEM image on 20 nm scale showing WS<sub>2</sub> film as bright lines; B, C and D - (HR)TEM images at 10, 5 and 2 nm scale magnification, respectively, E and F – SEM images of the zones of *Spectre 1* and *2* analyzed by EDX, respectively; G and H – EDX graphs recorded from the *spectre 1* and *spectre 2* zones, respectively. Atom labels were reproduced for better visibility

## 2.4 CONCLUSION

In this chapter, complex hexakis(dimethylamido)ditungsten (III),  $[W_2(NMe_2)_6]$  (HDMDW) is an interesting potential precursor to provide a well-defined solution ALD process aiming at a tungsten-based phase on silica-terminated surfaces. Although there are some challenges in its preparation and purification steps, the main hurdle remains the partially unsolved inertness at the gas-solid interphase of the very first pulse (inertness which can be circumvented by operating at liquid-solid interphase through the dispersion of the metal precursor via solution chemistry). As studied by others,<sup>22</sup> solution-based ALD can be an interesting alternative to the full gas phase.

SOMC convergent surface analysis such as IR, solid-state NMR spectroscopies, and elemental analysis, inter alia, have also allowed investigating the reaction of tungsten-based surface moieties with 1,2-ethanedithiol (EDT). The main insight that such modeling has offered is the fact that reaction indeed occurs and yet only partially consumes the available thiols, thus permitting the instauration of a truly alternating chemically controlled ALD growth process. Mechanistically, the hypothesis of oxidative-addition across W(III)-W(III) multiple bonds at this, which is backed by molecular precedents discussed above, can be an entry for reaching the W(IV) oxidation state of the final desired phase  $WS_2$ . Likewise, the presence of persulfide moieties ( $(S-SH)^-$  or  $(S-S)^{2-}$ ) formed at this step, as suggested by the elemental analysis and in particular, the low carbon content which is the known tendency of ethylene dithiolate core ( $S-CH_2CH_2-S$ ) to lose ethylene, leads to a proposal that persulfide bond can act as an oxidant.

The formation of  $WS_2$  from this tungsten thiolates-decorated solid was observed. Namely, electron microscopy tools confirmed the formation of the layered structure upon the annealing powder.

In conclusion, all these results qualify HDMDW and EDT as a good couple of ALD precursors toward  $WS_2$  on silica terminated surfaces as well as deliver an understanding on the growth mechanism. More broadly, this further example shows how molecular chemistry, as well as SOMC on high surface area model surfaces, can lay an interesting foundation for the identification of reasonable starting parameters for the development of novel ALD processes.

**Chapter 3 - ELABORATION of ALD  
GROWTH of WS<sub>2</sub> USING  
W(NMe<sub>2</sub>)<sub>2</sub>(=N<sup>t</sup>Bu)<sub>2</sub> and EDT**

### 3.1 INTRODUCTION

#### 3.1.1. Details of bis(*tert*-butylimido)bis(dimethylamido) tungsten (VI) utilization in ALD (and known molecular characteristics)

ALD growth of WS<sub>2</sub>,<sup>15,125,148</sup> WN<sup>124</sup> and WO<sub>3</sub><sup>126</sup> were all successfully achieved using Bis(*tert*-butylimido)bis(dimethylamido)tungsten (VI) (BTBMW) as the metal precursor. The sulfide is a W(IV) compound, nitride a W(III), and the oxide a W(VI). The metallic d<sup>0</sup> type heteroleptic transition metal complex BTBMW is therefore amenable to various redox reactions. It is a moisture and air-sensitive, yellow, non-viscous, and volatile liquid. To the best of our knowledge, a thermal stability study was not reported for this complex. However, BTBMW was successfully applied as a tungsten precursor in ALD of WN in the range of temperatures 250-350 °C, where thermal decomposition of *tert*-butyl ligands was proposed by authors.<sup>124</sup> Other reports on the growth of WS<sub>2</sub> carried the tungsten pulse with BTBMW at a lower temperature of 80 °C.<sup>15,125</sup> BTBMW provides sufficient vapor pressure of ca. 2.3 Pa at 80 °C, it is therefore well suited for moderate temperature ALD process.

BTBMW was reported as a suitable tungsten precursor for WS<sub>2</sub> film deposition in the case of pairing with di-*tert*-butyldisulfide, <sup>t</sup>Bu<sub>2</sub>S<sub>2</sub>, as a sulfur precursor.<sup>125</sup> Injection of the vaporized precursors was controlled by pneumatic valves, but each deposition cycle was composed of 4 steps in the following order: W pulse, S pulse, purging gas, and evacuation. The difference from the classic ALD method is the absence of a purging step between pulsing two precursors, which questions the existence of self-limiting reactions. The purging gas consisted of ~95% argon and ~5% hydrogen. The latter is presumably injected in order to form thiol groups allowing the next deposition cycle. The authors noticed that the SiO<sub>2</sub>/Si substrate could be coated with WS<sub>2</sub> film at 400 °C. They managed to lower the growth temperature to 350 °C yet obtaining the same crystallinity only by pre-coating the substrate's surface with a catalytic metal film of tungsten or gold. Pre-coated metal film was believed to promote the decomposition of the W complex.

Methods of forming 2D metal chalcogenide films using laser-assisted atomic layer deposition are disclosed<sup>149</sup> as well as area-selective atomic layer deposition (AS-ALD) using an ABC-type plasma-enhanced ALD process involving acetylacetone (Hacac) as inhibitor (A), bis(*tert*-butylimido)-bis-(dimethylamido)-tungsten as a precursor (B), and H<sub>2</sub>S plasma as the co-reactant (C) at a low deposition temperature of 250 °C.<sup>77</sup> The thus developed AS-ALD process results in the immediate growth of WS<sub>2</sub> on SiO<sub>2</sub> while effectively blocking growth on Al<sub>2</sub>O<sub>3</sub> as confirmed by *in situ*

spectroscopic ellipsometry and ex situ X-ray photoelectron spectroscopy measurements, upon annealing at temperatures within the thermal budget of semiconductor back-end-of-line processing ( $\leq 450$  °C).

Prof. N. Pinna at Humboldt University in collaboration with us has demonstrated the usefulness of BTBMW and H<sub>2</sub>S gas for the ALD growth of WS<sub>2</sub> on various substrates.<sup>15</sup> By optimizing various reaction parameters (temperatures of the reaction chamber and the precursor, pulse durations), a high growth per cycle (GPC) of 1.7 Å and high quality of the deposited thin films was achieved. HRTEM showed WS<sub>2</sub> platelets with a thickness of 6 to 10 nm and a diameter of 30 nm after 50 ALD cycles. Among other ALD-specific characteristics, the self-terminating nature of the surface reactions was evidenced by the lack of precursors' dose influence on the GPC. Our work at the LCOMS team was to elucidate the mechanism of the first deposition of BTBMW on silica as will be detailed later in the chapter.

### 3.1.2. The goal of the chapter

The goal of this chapter is to assess if 1,2-ethanedithiol, EDT, is an appropriate sulfiding candidate for well-behaved ALD growth of WS<sub>2</sub> with bis(tert-butyylimido)bis(dimethylamido)tungsten (VI) (BTBMW). This chapter covers all the exploratory modeling work preliminary to the thin-film growth which will be described in chapter 4. This chapter will therefore cover strictly solution chemistry (molecular chemistry among the two reagents and reaction of BTBMW with molecular silanol) as well as surface organometallic chemistry on high surface area silica. The first aim is to extend the potential of replacing frequently-used H<sub>2</sub>S by EDT by achieving ultrathin film growth of WS<sub>2</sub> with BTBMW. In light of the literature precedents stated above, the second advantage of this work is to gain an understanding of the mechanism(s) of the early ALD growth stage of the WS<sub>2</sub> by BTBMW reaction with silica terminated surfaces.

## 3.2 EXPERIMENTAL SECTION

### 3.2.1. General procedures

Synthesis and purification of products sensitive to air and/or moisture have been conducted using the usual Schlenk glassware (use of vacuum/argon ramps). Before using solvents, they were dried using the MBraun® purification system SPS-800 (for pentane and diethyl ether), dried with sodium benzophenone ketyl, distilled and degassed with 3 cycles of freeze-pump-thaw (freezing under argon – dynamic vacuum treatment – defrosting under static vacuum). Transfers and weighing were carried out under argon in a glove box containing less than 0.1 ppm of oxygen and water.

The dehydroxylation and desorption operations under UHV ( $10^{-6}$ - $10^{-4}$  mbar) were carried out using a ramp designed in the C2P2 laboratory for surface organometallic chemistry.<sup>18</sup> The system is composed of a pumping unit, a glass ramp (synthesis ramp type), and a trap cooled in liquid nitrogen. The pumping part is composed of a vane pump (primary vacuum) and a turbomolecular pump (secondary vacuum), whose start-up and connection to the ramp are automated by a Siemens SIMATIC controller connected to solenoid valves and pressure sensors.<sup>150</sup>

### 3.2.2. Precursors

*Bis(tert-butylimido)bis(dimethylamido)tungsten (VI)* (> 97%) was ordered from Strem Chemicals Inc. Before use, the orange liquid of BTBMW was distilled to liquid nitrogen-cooled finger schlenk at 80-90 °C in a dynamic vacuum ( $10^{-2}$ - $10^{-1}$  mbar). After the distillation, the liquid color turns to yellow.

<sup>1</sup>H NMR of BTBMW (300.16 MHz, C<sub>6</sub>D<sub>6</sub>, 298 K): δ 1.41 ppm (s, 18 H of 2×<sup>t</sup>Bu), 3.51 ppm (s, 12 H of 2×NMe<sub>2</sub>).

<sup>13</sup>C NMR of BTBMW (75.43 MHz, C<sub>6</sub>D<sub>6</sub>, 298 K): δ 33.8 ppm (primary-C of <sup>t</sup>Bu), 53.6 ppm (methyl C of NMe<sub>2</sub>), 66.1 ppm (quaternary-C of <sup>t</sup>Bu).

*Raman of BTBMW (cm<sup>-1</sup>) with tentative assignments:* 110m, 125m, 161m, 215w, 269s (CC<sub>3</sub> deformation), 324m (CC<sub>3</sub> deformation), 371w (CNC deformation), 542m (W–N str), 568w, 593m, 810m, 915w, 980m (NC<sub>2</sub> sym str.), 1154m, 1219w, 1257m (CH<sub>3</sub> rocking, CC<sub>3</sub> str), 1292vs (CC<sub>3</sub> str), 1407w (CH<sub>3</sub> deformation), 1473w (CH<sub>3</sub> deformation), 2696w, 2780s (C–H sym str.), 2825m (C–H sym str.), 2866s (C–H sym str.), 2921s (C–H sym str.), 2943m (C–H asym str.), 2968m (C–H asym str.).

*Triphenylsilanol* (98%) was purchased from Sigma-Aldrich and dried in a dynamic vacuum before use.

<sup>1</sup>H NMR of Ph<sub>3</sub>SiOH (300.16 MHz, C<sub>6</sub>D<sub>6</sub>, 298 K): δ 2.33 ppm (s, 1 H of OH), 7.21 ppm (m, 9 H<sub>ar</sub> on meta- and para- positions of 3×Ph), 7.67 ppm (m, 6 H on ortho- positions of 3×Ph).

$^{13}\text{C}$  NMR of  $\text{Ph}_3\text{SiOH}$  (75.43 MHz,  $\text{C}_6\text{D}_6$ , 298 K):  $\delta$  127.9 ppm (C at meta position of Ph), 129.9 ppm (C at the para position of Ph), 135.2 ppm (C at the ortho position of Ph), 135.7 ppm (phenyl C binding to Si).

Raman of  $\text{Ph}_3\text{SiOH}$  ( $\text{cm}^{-1}$ ) with tentative assignments: 184m, 240m, 620m (out-of-plane ring deformation), 676m (in-plane ring deformation), 1001vs (C–H out of plane deformation), 1029m, 1110m (=C–H in-plane deformation), 1160w (=C–H in-plane deformation), 1190w, 1569w (–C=C– str), 1590m (–C=C– str), 2963vw (C–H str), 3051s (C–H<sub>ar</sub> str).

**Starting silica nanobeads:** Non-porous silica (Aerosil® Degussa, 200  $\text{m}^2\text{g}^{-1}$ ) was compacted at 120 °C during 48 hours from aqueous suspension. Chunks of silica were carefully milled and sieved through a mesh of average size 250-400  $\mu\text{m}$ . The collected powder was placed in a quartz reactor and heated to 700 °C for 16 hours under a dynamic UHV at the heating rate of 5°/min to yield partially dehydroxylated silica,  $\text{SiO}_{2-700}$ . DRIFT spectroscopy showed the presence of an isolated hydroxyl group at 3747  $\text{cm}^{-1}$  ( $\nu_s$ ) assigned to its stretching vibration absorption. Nitrogen adsorption measurement by BET has confirmed the surface area of 194  $\text{m}^2/\text{g}$ . Titration of the surface –OH groups with tris(*tert*-butyl)aluminum and analysis of the released gases by GC defined the concentration of –OH at 0.24 mmol/g.

### 3.2.3. Preparation of molecular samples

#### 3.2.3.1. The reaction of BTBMW with EDT in solution

150  $\mu\text{L}$  (473  $\mu\text{mol}$ ) of BTBMW dissolved in ca. 15 mL of n-pentane was loaded into a Schlenk flask of 50 mL. Another Schlenk flask with 15 mL of n-pentane was introduced into the argon-filled glove bag to dissolve 180  $\mu\text{L}$  (2.10 mmol) of EDT in it. The solution of the BTBMW was added on top of the solution of EDT (not in reverse to avoid an excess of the metal complex around dithiol). Red precipitation was observed immediately. The solid was washed 3 times with 10-15 mL of n-pentane and filtered through a cannula. The red solid was dried under a dynamic vacuum ( $10^{-2}$  mbar) for 5 hours. IR absorption of the solid was analyzed by DRIFT spectroscopy. The solid-state  $^1\text{H}$  NMR spectrum gave one broad peak that was not informative. Elemental analysis results are also given in Table 3. 1.

IR ( $\text{cm}^{-1}$ ): 547m (W–N str.), 562m, 591m, 667m, 686m, 802m, 843s, 886m, 930m, 1019s (sym  $\text{NC}_2$ ), 1097m ( $\text{CH}_3$  rocking or asym  $\text{NC}_2$ ), 1156w ( $\text{CH}_3$  rocking or asym  $\text{NC}_2$ ), 1258vs ( $\text{CH}_3$  deform), 1357s, 1377w, 1413s, 1457s, 1577m, 2084w, 2413m, 2751m, 2816s, 2899m, 2921s, 2970s.

Solid-state  $^1\text{H}$  NMR (500.13 MHz, 298K):  $\delta$  1.65 ppm (br.)

Solid-state  $^{13}\text{C}$  NMR (125.72 MHz, 298K):  $\delta$  31.1 ppm, 37.1 ppm (primary C of  $^t\text{Bu}$ ), 43.4 ppm, 48.6 ppm, 54.7 ppm (C of – $\text{NMe}_2$ ), 69.2 ppm (quaternary C of  $^t\text{Bu}$ ).

Elemental analysis (% wt.): W = 32.30; C = 24.85; N 5.04; S = 31.90; H = 5.23;

### 3.2.3.2. The reaction of BTBMW with triphenylsilanol in solution

BTBMW (86 mg, 208  $\mu\text{mol}$ ) was dissolved in dry n-pentane (ca. 5 mL) in a Schlenk flask of ca. 50 mL.  $\text{Ph}_3\text{SiOH}$  (57.4 mg, 208  $\mu\text{mol}$ ) was dissolved in 10-15 mL of n-pentane/toluene mixture in another Schlenk. The  $\text{Ph}_3\text{SiOH}$  solution was added onto the stirred solution of the W complex dropwise using a syringe and a needle. The schlenk of the BTBMW was closed with a septum to limit diffusion of produced gases upon reaction with  $\text{Ph}_3\text{SiOH}$  in the glovebox. After 30 minutes of stirring at room temperature, the solvents were evaporated under a dynamic vacuum in the glovebox. The obtained pale yellow powder was characterized by liquid-state NMR and XPS (see Figure 3. 6, Figure 3. 7 and discussion section). The same reaction was repeated in an NMR tube equipped with a *Young* valve seeking to detect expected  $\text{HNMe}_2$  byproduct. In this small scale reaction, BTBMW (43.9 mg, 106  $\mu\text{mol}$ ) and  $\text{Ph}_3\text{SiOH}$  (29 mg, 103  $\mu\text{mol}$ ) were dissolved separately in ca. 0.5 mL of  $\text{C}_6\text{D}_6$  and mixed in the NMR tube. The tube was quickly closed and measured by liquid-state NMR.

$^1\text{H}$  NMR of redissolved yellow powder (300.16 MHz,  $\text{C}_6\text{D}_6$ , 298 K):  $\delta$  1.30 ppm (s, 18 H of  $2\times^t\text{Bu}$ ), 3.49 ppm (s, 6 H of  $-\text{NMe}_2$ ), 7.21 ppm (m, 9  $\text{H}_{\text{ar}}$  on meta- and para- positions of  $3\times\text{Ph}$ ), 7.88 ppm (m, 6 H on ortho- positions of  $3\times\text{Ph}$ ).

$^1\text{H}$  NMR of the small-scale reaction mixture (300.16 MHz,  $\text{C}_6\text{D}_6$ , 298 K):  $\delta$  1.30 ppm (s, 18 H of  $2\times^t\text{Bu}$  at  $\text{Ph}_3\text{SiO}-\text{W}(\text{NMe}_2)(=\text{N}^t\text{Bu})_2$ ), 1.41 ppm (s, 18 H of  $2\times^t\text{Bu}$  at unreacted  $\text{W}(\text{NMe}_2)_2(=\text{N}^t\text{Bu})_2$ ), 2.21 ppm (d, 6 H of byproduct  $\text{HNMe}_2$ ), 3.49 ppm (s, 6 H of  $-\text{NMe}_2$  at  $\text{Ph}_3\text{SiO}-\text{W}(\text{NMe}_2)(=\text{N}^t\text{Bu})_2$ ), 3.50 ppm (s, 12 H of  $-\text{NMe}_2$  at unreacted  $\text{W}(\text{NMe}_2)_2(=\text{N}^t\text{Bu})_2$ ), 6.94 ppm (m, 9  $\text{H}_{\text{ar}}$  on meta- and para- positions of  $3\times\text{Ph}$  at  $\text{Ph}_3\text{SiO}-\text{W}(\text{NMe}_2)(=\text{N}^t\text{Bu})_2$ ), 7.21 ppm (m, 9  $\text{H}_{\text{ar}}$  on meta- and para- positions of  $3\times\text{Ph}$  at unreacted  $\text{Ph}_3\text{SiOH}$ ), 7.59 ppm (m, 6 H on ortho- positions of  $3\times\text{Ph}$  at  $\text{Ph}_3\text{SiO}-\text{W}(\text{NMe}_2)(=\text{N}^t\text{Bu})_2$ ), 7.88 ppm (m, 6 H on ortho- positions of  $3\times\text{Ph}$  at unreacted  $\text{Ph}_3\text{SiOH}$ ). Traces: 0.29 ppm (s), 0.39 ppm (br), 0.99 ppm (s), 1.13 ppm (s).

$^{13}\text{C}$  NMR of the small-scale reaction mixture (75.43 MHz,  $\text{C}_6\text{D}_6$ , 298 K):  $\delta$  33.5 ppm (primary-C of  $^t\text{Bu}$  at  $\text{Ph}_3\text{SiO}-\text{W}(\text{NMe}_2)(=\text{N}^t\text{Bu})_2$ ), 33.8 ppm (primary-C of  $^t\text{Bu}$  at unreacted  $\text{W}(\text{NMe}_2)_2(=\text{N}^t\text{Bu})_2$ ), 38.9 ppm (C of byproduct  $\text{HNMe}_2$ ), 53.6 ppm (methyl C at unreacted  $\text{W}(\text{NMe}_2)_2(=\text{N}^t\text{Bu})_2$ ), 54.5 ppm (methyl C at  $\text{Ph}_3\text{SiO}-\text{W}(\text{NMe}_2)(=\text{N}^t\text{Bu})_2$ ), 66.1 ppm (quaternary C of  $^t\text{Bu}$  at unreacted  $\text{W}(\text{NMe}_2)_2(=\text{N}^t\text{Bu})_2$ ), 66.2 ppm (quaternary C of  $^t\text{Bu}$  at  $\text{Ph}_3\text{SiO}-\text{W}(\text{NMe}_2)(=\text{N}^t\text{Bu})_2$ ), 127.7 ppm (phenyl C), 129.2 ppm, 129.6 ppm, 135.4 ppm, 136.6 ppm, 137.4 ppm, 137.6 ppm.

Raman of yellow powder ( $\text{cm}^{-1}$ ): 202w, 236s, 263m ( $\text{CC}_3$  deformation), 278m ( $\text{CC}_3$  deformation), 326m ( $\text{CC}_3$  deformation), 340m (CNC deformation), 547m (W-N str), 576m, 601m, 622m (out-of-plane ring deformation), 681m (in-plane ring deformation), 710w, 812s, 919m, 978m ( $\text{NC}_2$  str), 1000vs (C-H out of plane deformation), 1032s, 1107m, 1158m ( $=\text{C}-\text{H}$  in-plane deformation), 1189w, 1220m, 1253m, 1293s, 1404w ( $\text{CH}_3$  deformation), 1442m ( $\text{CH}_3$  deformation), 1569m ( $-\text{C}=\text{C}-$  str), 1591s ( $-\text{C}=\text{C}-$  str), 2784m (C-H sym str), 2829m (C-H sym str), 2873m (C-H sym str), 2898m (C-H sym str), 2920s (C-H sym str in  $^t\text{Bu}$ ), 2943m (C-H asym str), 2970s (C-H asym str), 3052s (C- $\text{H}_{\text{ar}}$  str).

The reaction product between  $\text{Ph}_3\text{SiOH}$  and BTBMW was identified as  $\text{Ph}_3\text{SiO}-\text{W}(\text{NMe}_2)(=\text{N}^t\text{Bu})_2$  (see discussion).

### 3.2.3.3. Reactivity of EDT with $\text{Ph}_3\text{SiO}-\text{W}(\text{NMe}_2)(=\text{N}^t\text{Bu})_2$

The 124  $\mu\text{L}$  of EDT (1.48 mmol) was added into the schlenk containing 311.7 mg of  $\text{Ph}_3\text{SiO}-\text{W}(\text{NMe}_2)(=\text{N}^t\text{Bu})_2$  (0.483 mmol) in dry 20 mL of toluene inside the plastic bag filled with argon. Dark red precipitation was observed immediately after mixing. The stirring began in 2-3 minutes after the addition and was continued for 1 hour. Then, the reaction mixture with the solid precipitate in toluene was filtered through a frit and washed one time with 12 mL of toluene. Both the solid residue and filtrate were dried in UHV, and yielded 130 and 122 mg, respectively. The powder obtained from the filtrate was studied by XPS and Raman spectroscopies. Liquid-state  $^1\text{H}$  NMR spectrum was not informative, whose signals are listed below. This may need careful repetition of the reaction.

*Raman ( $\text{cm}^{-1}$ ) of solid recovered from the filtrate with tentative assignments:* 296m, 355s (CCS deformation,  $\text{CC}_3$  deformation), 416m, 463w (S-S str), 507w (W-N str), 656w (C-S str, ring deformation), 808w, 845w, 930w, 1152m ( $\text{CC}_3$  str,  $\text{CH}_x$  deformation), 1241m ( $\text{CH}_x$  deformation), 1262 ( $\text{CH}_x$  deformation), 1322m ( $\text{CH}_x$  deformation), 1415w ( $\text{CH}_x$  deformation), 2907s (C-H sym str), 2940m (C-H asym str).

*$^1\text{H}$  NMR (300.16 MHz,  $\text{C}_6\text{D}_6$ , 298 K):*  $\delta$  0.33 ppm (s), 1.31 ppm (s), 7.20 ppm (m, H-Ar), 7.69 ppm (m, H-Ar). Traces: 0.83 ppm, 1.60 ppm, 2.07 ppm, 2.10 ppm, 2.36 ppm, 2.40 ppm, 2.63 ppm, 2.68 ppm, 2.72 ppm, 2.74 ppm.

## 3.2.4. ALD-modeling reactions on the surface of silica nanobeads

### 3.2.4.1. ALD homemade glass reactor and its general use for deposition

ALD was carried out in a glass reactor equipped with two bulbs that are sealed with *young* valves and detachable tubular parts (see Figure 3. 1). Two bulbs are separately loaded with ALD precursors in the glovebox (for metal precursors) or argon-filled plastic glove bag (for sulfur precursors or other volatile, toxic, and compounds active towards glovebox's catalyst). Liquid ALD precursors are degassed by two freeze-pump-thaw cycles from these bulbs while the main tube is empty. Then, powder or 2D substrates are loaded into the tubular part of the reactor inside the glovebox.



Figure 3. 1. Picture of the homemade ALD glass reactor equipped with two bulbs and tubular part.

#### 3.2.4.2. Deposition of $(\text{NMe}_2)_2(=\text{N}^t\text{Bu})_2\text{W}$ (VI) on the silica nanobeads

Deposition of  $(\text{NMe}_2)_2(=\text{N}^t\text{Bu})_2\text{W}$  (VI) complex on silica nanobeads was conducted in the glass ALD reactor described above. 200  $\mu\text{L}$  of BTBMW and 200  $\mu\text{L}$  of EDT were loaded into the two bulbs and degassed. 708 mg of  $\text{SiO}_2\text{-700}$  was loaded into the tubular part inside the glovebox. The ALD reactor was connected to the ultra-high vacuum line via an additional intermediate trap cooled in liquid nitrogen. Evacuation of the reactor was done until the pressure decreases down to  $2 \cdot 10^{-5}$ - $4 \cdot 10^{-5}$  mbar. The reactor's valve was closed and placed in an oven at 80 °C for 6 hours. The reactor was gently shaken approximately every 10-20 minutes while it was in the oven. The silica powder changed its color from white to bright yellow. After 6 hours of the vapor deposition, the bulb was closed and volatile byproducts of the deposition were condensed into an NMR tube containing 0.8-0.1 mL of dry and degassed  $\text{C}_6\text{D}_6$  (see Figure 3. 11).

$^1\text{H}$  NMR (300.16 MHz,  $\text{C}_6\text{D}_6$ , 298 K) of condensed volatile byproducts:  $\delta$  2.20 ppm (s, Me in  $\text{HNMe}_2$ ). Trace: 0.99 ppm (s,  $^t\text{Bu}$  in  $\text{H}_2\text{N}^t\text{Bu}$ ).

The reactor was connected to a dynamic UHV to remove the excess BTBMW and reaction byproducts. Its tubular part was inserted into the tubular oven at 80 °C for 30 minutes. The thus obtained yellow powder was analyzed by DRIFT, ss NMR, Raman spectroscopies, and elemental analysis. All further manipulations with the obtained powder were carried inside the glovebox due to its sensitivity to air and moisture.

IR ( $\text{cm}^{-1}$ ): 1625m, 1862m, 1968m, 2787m, 2832m, 2868s, 2925s, 2900m, 2947s, 2970vs.

Raman ( $\text{cm}^{-1}$ ) of yellow powder with tentative assignments: 273m, 333w ( $\text{CC}_3$  rocking,  $\text{CC}_3$  deformation, CNC wagging), 550w (W-N str), 602m, 810s ( $\text{CC}_3$  sym str), 917m, 972m ( $\text{NC}_2$  str), 1156m ( $\text{CH}_3$  rocking,  $\text{NC}_2$  asym str,  $\text{CC}_3$  str), 1220m ( $\text{CH}_3$  rocking,  $\text{CC}_3$  asym str), 1248m, 1294vs (skeletal  $\text{CC}_3$  asym str,  $\text{CH}_3$  deformation), 1444m ( $\text{CH}_3$  deformation), 1474m ( $\text{CH}_3$  deformation),

2704w (C–H sym str), 2788w (C–H sym str), 2833w (C–H sym str), 2905s (C–H sym str), 2927vs (C–H asym str), 2948s (C–H asym str), 2972m (C–H asym str).

*ss*  $^1\text{H NMR}$  (300.16 MHz, 298K):  $\delta$  1.14 ppm (s, NMe<sub>2</sub>), 3.33 ppm (s, <sup>t</sup>Bu)

*ss*  $^{13}\text{C NMR}$  (75.43 MHz, 298K):  $\delta$  32.6 ppm (primary C of <sup>t</sup>Bu), 53.9 ppm (methyl C of –NMe<sub>2</sub>), 66.0 ppm (quaternary C of <sup>t</sup>Bu).

*Elemental analysis* (% wt.): W = 5.22; C = 3.48; N = 1.28; H = 0.74;

#### 3.2.4.3. Hydrolysis of silica-supported BTBMW

After the 1<sup>st</sup> pulse, 150 mg of yellow powder was placed in a schlenk tube. A rota-flo® flask of ca. volume 100 mL was filled with distilled 20  $\mu\text{L}$  water that was then degassed. The powder containing schlenk tube was connected to the UHV line and to the water-containing rota-flo® via a T-type connector. After evacuating the schlenk, water was transferred to it by freeze-trapping under a static vacuum. The mixture was warmed back to room temperature in the closed schlenk. The NMR tube was loaded with a deuterated solvent (~1.0 mL of C<sub>6</sub>D<sub>6</sub>) and 11.1 mg of Durene (82.7  $\mu\text{mol}$ ). Volatile products of the hydrolysis were then collected into a Young NMR tube also by freeze-trapping under a static UHV.

$^1\text{H NMR}$  (300.16 MHz, C<sub>6</sub>D<sub>6</sub>, 298 K) :  $\delta$  0.96 ppm (s, <sup>t</sup>Bu in H<sub>2</sub>N<sup>t</sup>Bu), 2.08 ppm (s, Me in Durene), 2.15 ppm (s, Me at HNMe<sub>2</sub>), 4.90 ppm (s, H<sub>2</sub>O), 6.86 ppm (s, H-Ar). Traces: 1.25 ppm, 5.01 ppm.

Analysis of the relative area of the peaks of HNMe<sub>2</sub>, H<sub>2</sub>N<sup>t</sup>Bu and durene let to estimate the following fractions: 83  $\mu\text{mol}$  of durene, 10  $\mu\text{mol}$  of HNMe<sub>2</sub> and 24  $\mu\text{mol}$  of H<sub>2</sub>N<sup>t</sup>Bu. Calculations based on the proposed structure (see Scheme 3. 3) and the weight of the hydrolyzed powder (150 mg) supposed to yield 69  $\mu\text{mol}$  of HNMe<sub>2</sub> and 138  $\mu\text{mol}$  of H<sub>2</sub>N<sup>t</sup>Bu.

#### 3.2.4.4. The reaction of EDT with silica-supported BTBMW

The yellow powder resulting from the reaction of SiO<sub>2-700</sub> with BTBMW was exposed to EDT vapors. Evacuation of the reactor was done till the pressure decreases down to  $2 \cdot 10^{-5}$ - $4 \cdot 10^{-5}$  mbar. The reactor's valve was closed and placed in an oven at 80 °C for 1 hour. The reactor was shaken approximately every 10 minutes while it was in the oven. The powder slowly turned from yellow to wine-red. Since the color change was observed mainly on the top layer of the powder, the shaking of the reactor was necessary to make the deposition uniform. After 1 hour of the vapor deposition, the bulb was closed, and volatile (by)products of the deposition were condensed into an NMR tube containing dry and degassed C<sub>6</sub>D<sub>6</sub>. The same NMR solution was diluted in toluene (5 times) and characterized by electrospray ionization mass spectrometry (ESI-MS) that identified two main peaks of dimethylamine (46 Da) and tert-butylamine (74 Da) besides solvents' fragments.

*Solution*  $^1\text{H NMR}$  (300.16 MHz, 298K) of trapped gaseous byproducts:  $\delta$  0.99 ppm (s, methyl H in H<sub>2</sub>N<sup>t</sup>Bu), 2.06 ppm (s, unassigned), 2.19 ppm (s, methyl H in HNMe<sub>2</sub>), 5.25 ppm (s, ethylene)

*Solution  $^{13}\text{C}$  NMR (75.43 MHz, 298K) of trapped gaseous byproducts:*  $\delta$  28.4 ppm (unassigned), 32.6 ppm (primary C of  $\text{H}_2\text{N}^t\text{Bu}$ ), 38.6 ppm (C of  $\text{HNMe}_2$ ), 46.8 ppm (quaternary C of  $^t\text{Bu}$ ).

To remove the excess of the EDT and reaction products, the tubular part of the reactor was heated to 80 °C for 30 minutes under a dynamic UHV. Completion of the reaction was monitored by studying DRIFT of the powder after 1-hour deposition and once again after 30 minutes more deposition. No change of the DRIFT spectrum suggested that 1 hour was enough to complete the surface reaction. The obtained powder was analyzed by DRIFT, solid-state NMR, Raman spectroscopies, and elemental analysis. All further manipulations with the obtained powder were carried inside the glovebox due to its sensitivity to air and moisture.

*IR ( $\text{cm}^{-1}$ ) of red powder:* 1587m, 1863m, 1968m, 2415w, 2572w, 2759w, 2821m, 2903s, 2922m, 2949w, 2976s.

*ss  $^1\text{H}$  NMR (300.16 MHz, 298K) of red powder:*  $\delta$  1.41 ppm (br. s)

*ss  $^{13}\text{C}$  NMR (75.43 MHz, 298K) of red powder:*  $\delta$  29.1 ppm (primary C of  $^t\text{Bu}$ ), 37.5 ppm (secondary C of  $-\text{SCH}_2\text{CH}_2\text{SH}$ ), 42.8 ppm (secondary C of  $-\text{SCH}_2\text{CH}_2\text{SH}$ ), 69.6 ppm (quaternary C of  $^t\text{Bu}$ ).

*Raman ( $\text{cm}^{-1}$ ) of the 2<sup>nd</sup> pulse with tentative assignments:* 351m (CCS bending), 413m ( $\text{CC}_3$  deformation), 463m (S–S str), 534w (W–N str), 654w (C–S str.), 1011vw ( $\text{CH}_x$  deformation), 1155vw ( $\text{CC}_3$  asym str,  $\text{CH}_x$  deformation), 1332br.w. ( $\text{CH}_x$  deformation), 1458br.w ( $\text{CH}_x$  deformation).

*Elemental analysis (% wt.):* W = 5.57; C = 4.06; N = 1.03; S = 4.15; H = 0.84;

#### 3.2.4.5. Surface reactions on silica nanobeads modelling the 2<sup>nd</sup> ALD cycle

Deposition of  $(\text{NMe}_2)_2(=\text{N}^t\text{Bu})_2\text{W}$  (VI) complex on silica nanobeads to model the 3<sup>rd</sup> pulse (1<sup>st</sup> half of the 2<sup>nd</sup> ALD cycle) was conducted in the same manner as for the 1<sup>st</sup> pulse described above. This surface reaction was done on powder obtained upon the reaction of EDT with silica-supported BTBMW. This time, upon exposure to BTBMW pulse no color change of the powder was observed except little darkening after the deposition.

*IR ( $\text{cm}^{-1}$ ):* 1628m, 1869m, 1968m, 2780m, 2825m, 2867s, 2921s, 2945w, 2970s, 3180w.

*Raman ( $\text{cm}^{-1}$ ) with tentative assignments:* 273m, 360br (deformation of CCS,  $\text{CC}_3$ , and/or CNC), 444w, 579m (W–N str.), 808s (CNC str.), 918w, 961w (C–C str), 1029br.w ( $\text{CH}_x$  deformation), 1156s ( $\text{CH}_x$  deformation,  $\text{CC}_3$  str), 1287s ( $\text{CH}_x$  deformation), 1450w ( $\text{CH}_3$  deformation), 1472w ( $\text{CH}_3$  deformation), 2926vs (C–H asym str), 2974m (C–H asym str), 3060 br (N–H str).

*ss  $^1\text{H}$  NMR (300.16 MHz, 298K):*  $\delta$  broad signal at 1.22 ppm with shoulder at 0.03 ppm

*ss  $^{13}\text{C}$  NMR (75.43 MHz, 298K):*  $\delta$  32.6 ppm (primary C of  $^t\text{Bu}$ ), 44.0 ppm (secondary C of  $-\text{SCH}_2\text{CH}_2\text{S}-$ ), 54.5 ppm (methyl C of  $-\text{NMe}_2$ ), 68.6 ppm (quaternary C of  $^t\text{Bu}$ ).

*Elemental analysis (% wt.):* W = 14.90; C = 8.49; N = 2.62; S = 2.91; H = 1.67;

The resulting powder was exposed to EDT for modeling the 4<sup>th</sup> pulse (i.e. 2<sup>nd</sup> half of the 2<sup>nd</sup> ALD cycle). A slight color change was observed towards dark red-brown. The obtained dark red-brown powders were analyzed by DRIFT, solid-state NMR, Raman spectroscopies, and elemental analysis.

*IR (cm<sup>-1</sup>):* 1587m, 1863m, 1979m, 2472vw, 2569w, 2759m, 2818m, 2911s, 2971s, 3057br, 3745sh. m.

*Raman (cm<sup>-1</sup>) with tentative assignments:* 288m, 327w, 365s (CCS bending), 463s (S–S str), 519w (W–N), 676w (C–S str), 1045vw (CH<sub>x</sub> deformation), 1151m (CC<sub>3</sub> str, CH<sub>x</sub> deformation), 1330s (CH<sub>x</sub> deformation), 1459br (CH<sub>x</sub> deformation), 2915br.w (C–H str).

*ss <sup>1</sup>H NMR (300.16 MHz, 298K):* δ broad signal at 1.36 ppm.

*ss <sup>13</sup>C NMR (75.43 MHz, 298K):* δ 30.4 ppm (primary C of 'Bu), 37.1 ppm (secondary C of –SCH<sub>2</sub>CH<sub>2</sub>SH), 44.0 ppm (secondary C of –SCH<sub>2</sub>CH<sub>2</sub>SH), 69.8 ppm (quaternary C of 'Bu).

*Elemental analysis (% wt.):* W = 10.65; C = 7.25; N = 1.54; S = 7.47; H = 1.42;

#### 3.2.4.6. *Annealing procedure of silica bound tungsten thiolates*

The solid obtained after the fourth pulse was annealed in the furnace described in the experimental section of previous chapter. Annealed powder samples were characterized by HRTEM, STEM and elemental analysis (Table 3. 1). Raman was collected for the Ar-annealed sample.

*Raman (cm<sup>-1</sup>) after annealing at 800 °C in Ar:* 147w, 172w, 229w, 295m, 332m, 351s (first-order in-plane phonon mode E<sub>12g</sub> (Γ)), 414s (first-order out-of-plane phonon mode A<sub>1g</sub> (Γ)).

*Elemental analysis of Ar-annealed solid (% wt.):* W = 16.90; S = 6.53; C = 1.22; N ≤ 0.20; H ≤ 0.1;

*Elemental analysis of H<sub>2</sub>-annealed solid (% wt.):* W = 17.00; S = 6.20; C = 0.70; N ≤ 0.20; H = 0.15;

### 3.2.5. **Characterization instruments**

#### 3.2.5.1. *Raman spectroscopy*

Raman spectra were collected in collaboration with Dr. Jules Galipaud from the Laboratory of Tribology and Dynamics of Systems (LTDS) at École centrale de Lyon. Renishaw InVia spectrometer was used for Raman spectroscopy measurements. Excitation was carried by a laser of wavelength 633 nm and the used power was 11 mW on the sample. However, since the powders were loaded in a quartz vessel filled with argon, the power on the powder was considerably less than 11 mW. The real power seen by the powder sample was not estimated. Data were treated with the

software Wire 5.0 for cosmic ray and baseline removal. All the tentative assignments were given according to a handbook<sup>151</sup> and several literature reports<sup>31,152–157</sup>.

### 3.2.5.2. ESI-MS spectroscopy

The Electrospray Ionization Source Mass Spectrometry (ESI-MS) measurements were conducted at the Centre Commun de Spectrométrie de Masse (CCSM) of University of Lyon 1. The system used was a high resolution hybrid quadrupole-time of flight mass spectrometer (Impact II, Bruker, Bremen, Germany) equipped with ESI. Instrument control and data collection were performed using DataAnalysis 5.0 software. The ESI interface was operated on full scan mode ( $m/z$  20-500) in positive ion mode. The parameters for the ESI ion source were as follows: capillary voltage, 4.5 kV; the source temperature, 200°C; the operating pressure of the nitrogen flow for the nebulizer gas, 0.3 bar. The calibration of the mass spectrometer was performed with a sodium formate cluster solution.

### 3.2.5.3. X-ray Photoelectron Spectroscopy

Characterization by XPS spectroscopy was performed in collaboration with Dr. Jules Galipaud at École centrale de Lyon. A ULVAC-PHI Versa Probe II apparatus was used to conduct the X-ray photoelectron spectroscopy (XPS) to characterize the chemical states of the elements of the molecular samples and those deposited by ALD on the SiO<sub>2</sub>@Si wafer (discussed in Chapter 4 - ). A specially designed airtight transfer box was used for transferring samples between the glovebox antechamber and the XPS antechamber. The samples were pressed into pellets and fixed by screws onto a metal circular holder of XPS. The holder with pellets is loaded onto the transfer box inside the glovebox and tightly closed maintaining the argon atmosphere. The transfer box is then opened to the antechamber of XPS under dynamic UHV ( $\sim 10^{-6}$  mbar). The sample holder is manually moved and to place under the X-ray located in a different chamber under stronger dynamic UHV ( $10^{-9}$  mbar).

The X-ray source is Al K $\alpha$  operating at 1486.6 eV, and the size of the X-ray spot is 200  $\mu\text{m}$ . The energy scale was calibrated using the C 1s binding energy located at 284.8 eV. First, a wide range survey between 0 and 1100 eV was conducted to define all chemical elements. Then, a narrow range survey of each chemical element was conducted to determine the different chemical states. Multipak software was used to perform the fitting of each peak and provide quantitative analysis. For *operando* annealing experiments, applied special sample holder was heated by resistive heaters, and the temperature was measured by a connected thermocouple (results of *operando* annealing are discussed in Chapter 4).

### 3.3 RESULTS AND DISCUSSION

#### 3.3.1. Preliminary study with molecular chemistry

##### 3.3.1.1. Reactivity of $(\text{NMe}_2)_2(=\text{N}^t\text{Bu})_2\text{W}$ complex with EDT in solution

Good reactivity of the sulfur precursor with the metal complex is a prerequisite for a successful ALD process. Hence, we have studied the reactivity of EDT with BTBMW to sulfides in a solution that led to the instantaneous precipitation of a red-brown solid **B**, which is insoluble in most solvents, thus suggesting the formation of a polymeric precipitate. This data alone already points towards the fact that (1) BTBMW and EDT react with each other and (2) the mutual reaction is not self-terminating to low nuclearity product but rather amenable to propagating systems. Both these aspects are positive in the quest for ALD-compatible reagents. At the same time, the insolubility of the precipitate makes its characterization complicated by standard molecular techniques. The solid residue was characterized by solid-state NMR and DRIFT spectroscopies as well as elemental analysis. The  $^1\text{H}$  solid-state NMR spectrum displays a wide peak at 1.65 ppm that is poorly informative. The solid-state  $^{13}\text{C}$  NMR spectra are shown in Figure 3. 2. The spectrum of the starting BTBMW tungsten complex (see Figure 3. 2A) resonances at 34.0 ppm and 66.3 ppm (assigned to primary and quaternary carbon atoms of the  $=\text{N}^t\text{Bu}$  ligand), and at 53.7 ppm (assigned to  $-\text{NMe}_2$ ). After the reaction with EDT, two resonances of the  $=\text{N}^t\text{Bu}$  are still present on the spectrum at 31.1 and 69.2 ppm, respectively. The third resonance at 54.7 ppm (assigned to  $-\text{NMe}_2$  also based on the experiments carried out on silica nanobeads (vide infra) decreased in relative intensity with respect to the other two points to the partial elimination of  $-\text{NMe}_2$  moieties upon reaction with EDT. New resonance at 37.1, 43.4, and 48.6 ppm appear in agreement with the substitution of  $-\text{NMe}_2$  by the ethylenedithiolate group. This comes in good agreement with DFT calculations on a similar complex by M. Shirazi et al.<sup>158</sup> determining that substitution of  $-\text{NMe}_2$  by thiol group is more favorable than that of  $=\text{N}^t\text{Bu}$  group. At the same time, the appearance of several resonances suggests chemistry more complex than simple substitution of  $\text{W}-\text{NMe}_2$  with  $\text{W}-\text{SCH}_2\text{CH}_2\text{SH}$ .

The DRIFT spectrum is reported in Figure 3. 3. Features between 3000 and 2700  $\text{cm}^{-1}$  are assigned to the symmetric and asymmetric stretching vibrations of the C–H bonds. The low wavenumber modes (1500-500  $\text{cm}^{-1}$ ) could be assigned to deformation and rocking of  $\text{CH}_x$  systems as well as to stretching of C–N,  $\text{CC}_3$ , C–S systems. The presence of thiol is an important achievement since for the ALD process to be effective, the addition of the sulfiding agent must leave sufficient unreacted thiols to allow binding of further tungsten complex during the subsequent metal pulse.

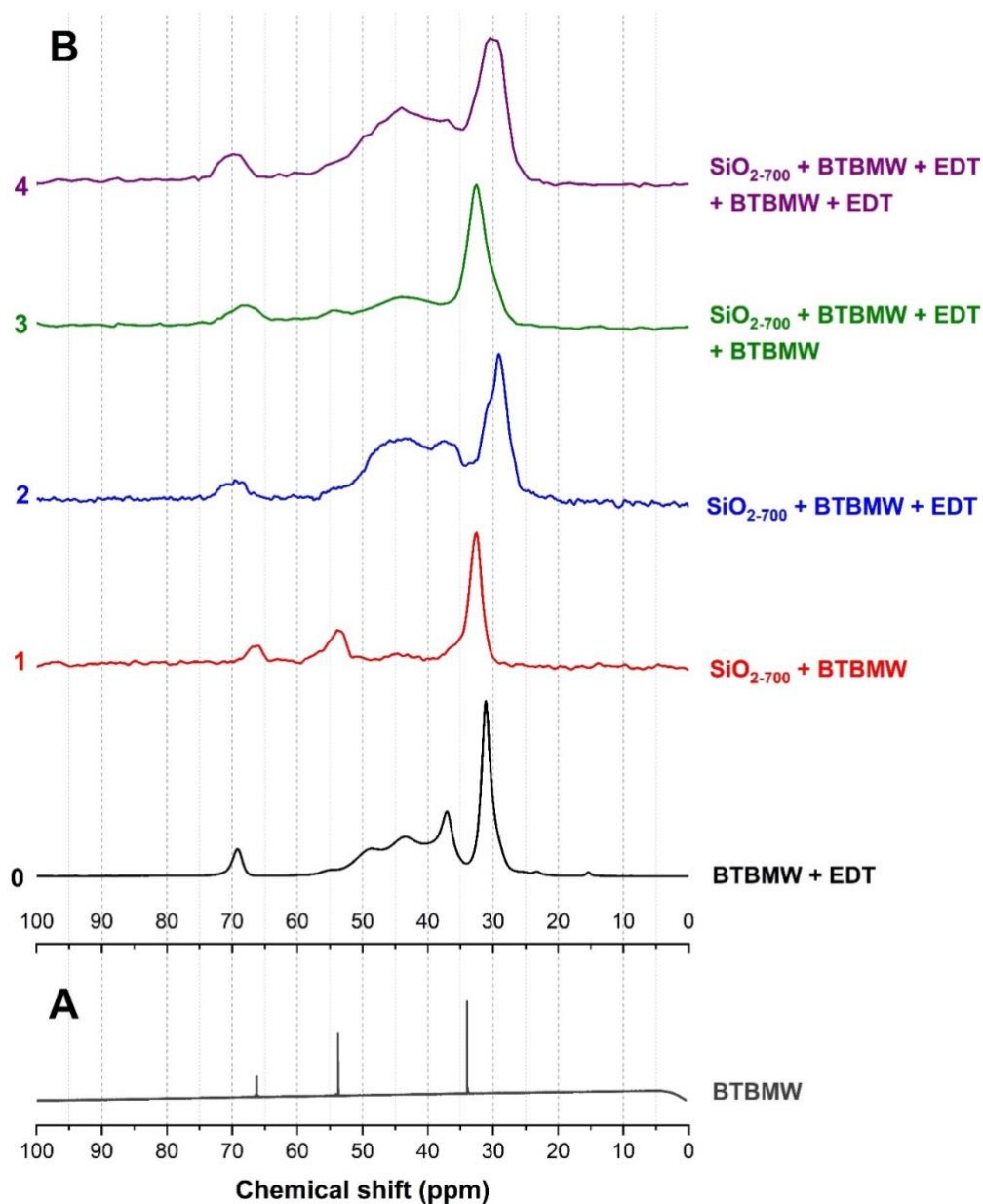


Figure 3. 2. **A:** liquid-state  $^{13}\text{C}$  NMR spectrum of BTBMW (in  $\text{C}_6\text{D}_6$ ) solution. **B:** solid-state  $^{13}\text{C}$  NMR spectra of the products of the following reactions, spectrum **0**: BTBMW + EDT (black line); spectrum **1**: the 1<sup>st</sup> pulse of BTBMW on silica-700 (red line); spectrum **2**: the 1<sup>st</sup> pulse of EDT on silica-700 (blue line); spectrum **3**: the 2<sup>nd</sup> pulse of BTBMW (green line); spectrum **4**: the 2<sup>nd</sup> pulse of EDT (purple line);

The modes at 2413 and 886  $\text{cm}^{-1}$  are tentatively assigned, respectively, to the stretching vibration and in-plane bending of the S–H moiety. A very broad feature from 3200 to 2500  $\text{cm}^{-1}$  suggests a strongly hydrogen bonded system between the thiol/thiolate and the =N/NH bonds present in the oligomer. Protonation of nitrogen atoms in intramolecular proton transfer from thiol group to

nitrogen was reported in the literature.<sup>159</sup> The mode linked to the W–S bond vibrations could not be viewed due to the cut-off range of the IR window.

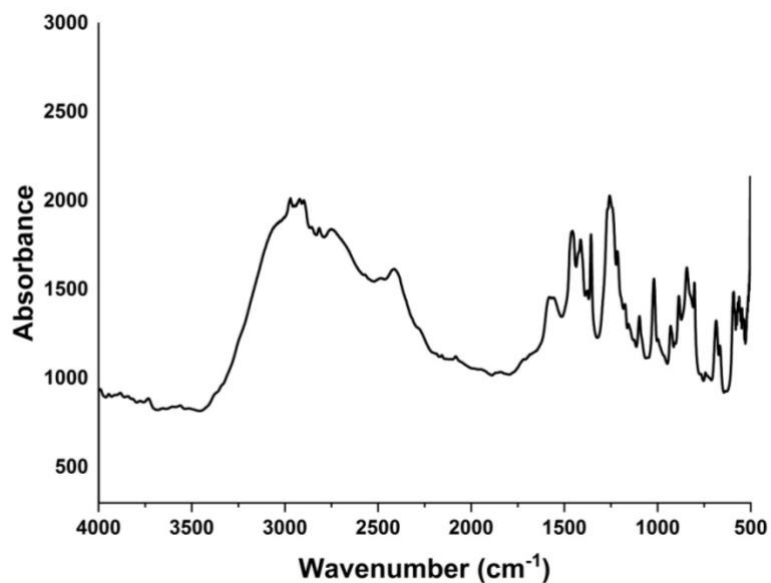
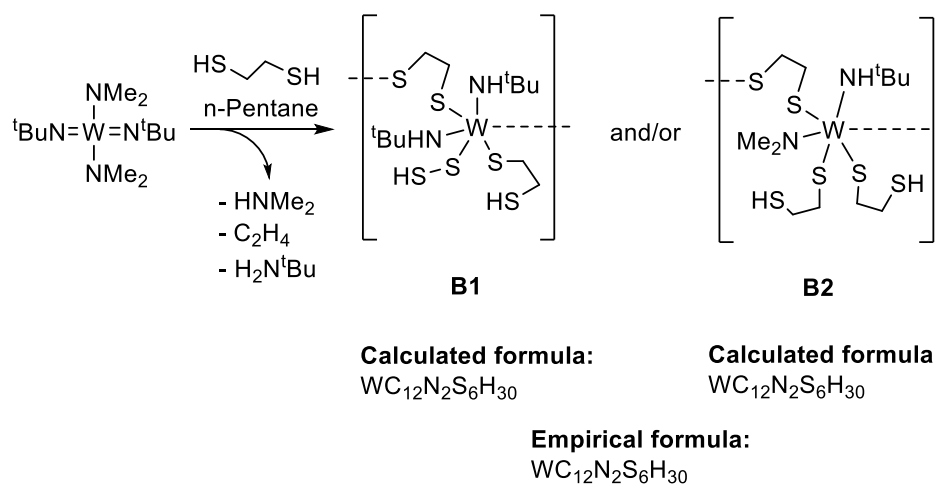


Figure 3. 3. DRIFT spectrum of the solid product B

Elemental analysis of the precipitate **B** leads to C/W, N/W and S/W ratios of 12, 2 and 6, respectively. The empirical formula,  $\equiv\text{SiO}-\text{WC}_{12}\text{N}_2\text{S}_6\text{H}_{30}$ , defined according to the elemental analysis results and other above-mentioned spectral data helped to build the first proposed structures (see Scheme 3. 1).

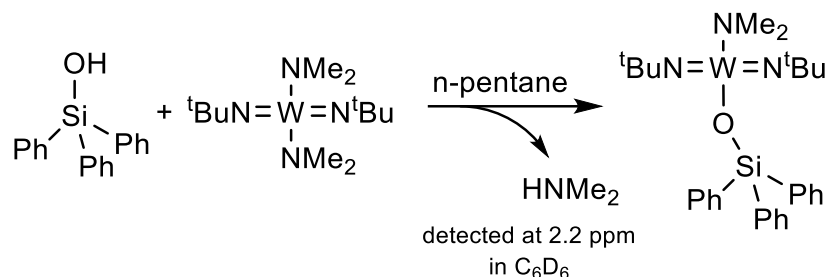


Scheme 3. 1. Working hypothesis on two of the possible coordination polymers resulting from BTBMW and EDT. Proposed scheme of the reaction between BTBMW and EDT in solution

### 3.3.1.2. Exploratory data on the reactivity of $(\text{NMe}_2)_2(=\text{N}^t\text{Bu})_2\text{W}$ (VI) complex with triphenylsilanol in solution

Triphenylsilanol,  $\text{Ph}_3\text{SiOH}$ , serves well for the initial molecular assessment of whether the metal complex precursor reacts with silanol or similar functional groups present on the final targeted surface of metal oxide substrates.<sup>136</sup> Here, we have carried exploratory studies on the reaction of BTBMW with  $\text{Ph}_3\text{SiOH}$  in solution. BTBMW and  $\text{Ph}_3\text{SiOH}$  were dissolved in equimolar amounts in n-pentane. The resulting yellow solid obtained after evaporation of the solvent was characterized by  $^1\text{H}$  NMR,  $^{13}\text{C}$  NMR, Raman, and XPS. These latter two techniques are informative in their own right. In the context of this work, they are also particularly insightful as a blueprint for the analogous data that will be acquired for the thin film on the wafer (see chapter 4), thus laying the foundation for a molecular-level understanding of the surface reaction in thin-film ALD growth.

Overall, as detailed here below, the reaction leads to the clear identification of a single product (see Scheme 3. 2).



Scheme 3. 2. Main reaction scheme between BTBMW and  $\text{Ph}_3\text{SiOH}$  in pentane. Elimination of the byproduct  $\text{HNMe}_2$  has been confirmed by carrying the reaction in a closed NMR tube.

Analysis of the  $^1\text{H}$  NMR of the  $\text{C}_6\text{D}_6$  solution of the isolated white product exhibits protons of the methyl groups assigned to dimethylamido (at 3.49 ppm) and *tert*-butylimido (1.30 ppm) groups (see Figure 3. 4C). These peaks have little shifts towards higher fields with respect to the initial resonances of the BTBMW (at 3.51 ppm and 1.41 ppm see Figure 3. 4A), respectively. The integration ratio of the peaks 6:18 on the spectrum C confirms substitution of only one of the dimethylamido groups by  $\text{Ph}_3\text{SiO}-$ . Aromatic protons of the phenyl groups yield resonances at 7.2 and 7.9 ppm in a 15:6 ratio with respect to the dimethylamido resonance. This ratio matches well with fifteen protons of the three phenyl groups and six protons of the dimethylamido group. Curiosity to observe  $\text{HNMe}_2$  expected in this reaction encouraged us to carry the same reaction on a

small scale inside an NMR tube. It was expected that mixing of the reactants in the NMR tube and its quick closing will keep gaseous byproducts inside. The spectrum D (Figure 3. 4), indeed, showed a peak at 2.21 ppm corresponding to the expected byproduct, HNMe<sub>2</sub>. In the spectrum D, resonances at 3.51 and 1.41 ppm in 12:18 relative ratio can be assigned to dimethylamido and *tert*-butylimido ligands of unreacted BTBMW complex. The other two singlets at 3.49 and 1.30 ppm correspond to dimethylamido and *tert*-butylimido groups of the reacted complex.

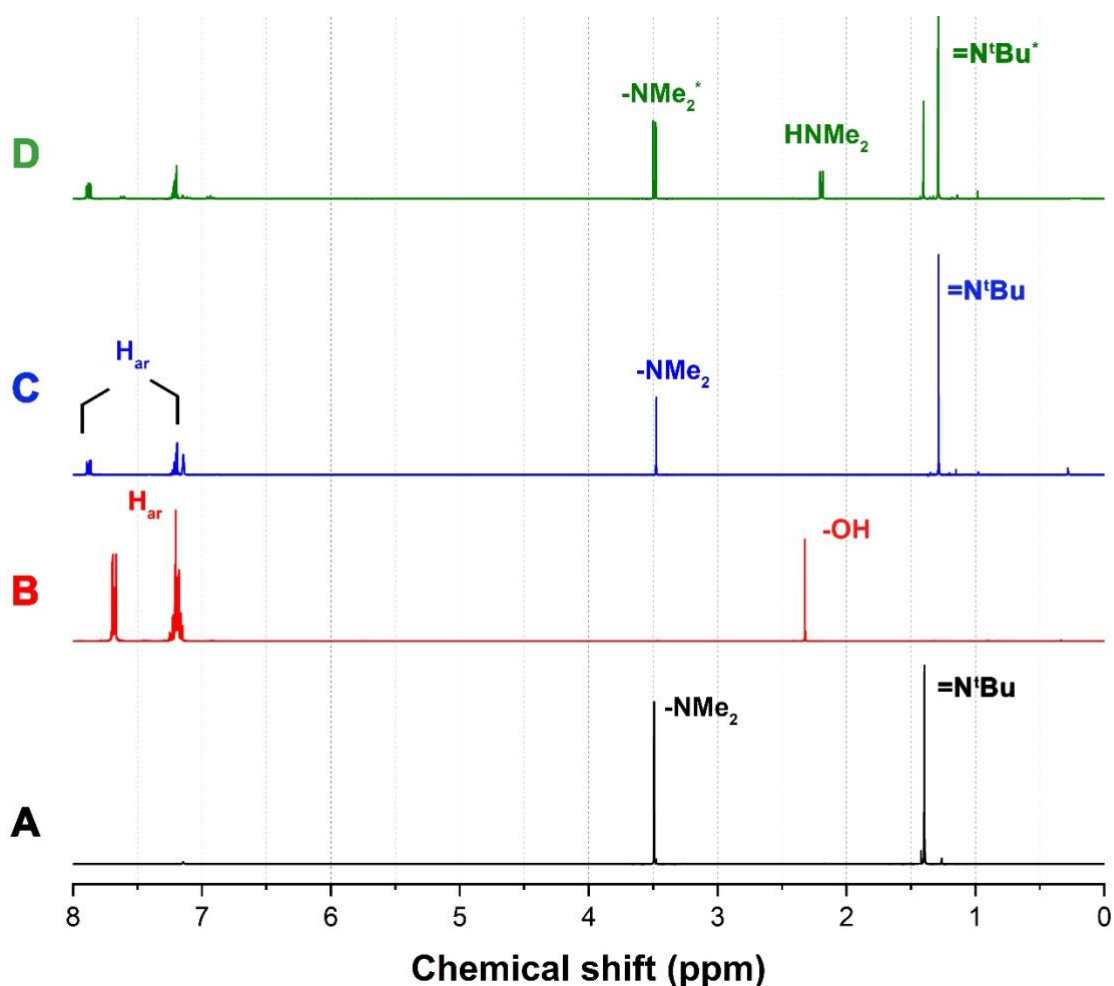


Figure 3. 4. <sup>1</sup>H NMR spectra recorded in C<sub>6</sub>D<sub>6</sub> of A – starting BTBMW complex; B – Ph<sub>3</sub>SiOH; C – product isolated from the reaction of BTBMW with Ph<sub>3</sub>SiOH in pentane; D – a mixture of a reaction carried in small scale directly in NMR tube between BTBMW and Ph<sub>3</sub>SiOH;

XPS measurement was carried on a pellet made of that yellow powder product. The first challenge in this *in situ* XPS study was to protect the series of samples (the starting activated pristine substrate and one for each half cycle up to two full ALD cycles ) from adventitious water and air exposure, given the redox sensitivity of the low valent tungsten precursor and the presence of hydrolysis prone

thiol and thiolate bonds. With this in mind, the series of experiments were carried on a specifically designed ALD batch reactor which could be introduced in an argon-filled glovebox with no exposure to air. This was coupled to a transfer box from inside of the glove box to inside of the XPS system with no to very little exposure to air in this second step too. This system gives us sufficient confidence that what we observe by XPS should be not too hydrolyzed and oxidized with respect to the sample prepared in the ALD reaction. First, survey spectra were recorded in the range of 0-1100 eV to determine the overall content (see Figure 3. 5), and then high-resolution spectra were acquired for the core-levels of W 4f, N 1s, S 2p, C 1s, O 1s, and Si 2p (see spectra 1, the blue line in Figure 3. 6). The deconvolution of the high-resolution XPS spectra was carried and identified peaks were fitted to calculate atomic fractions in Figure 3. 7.

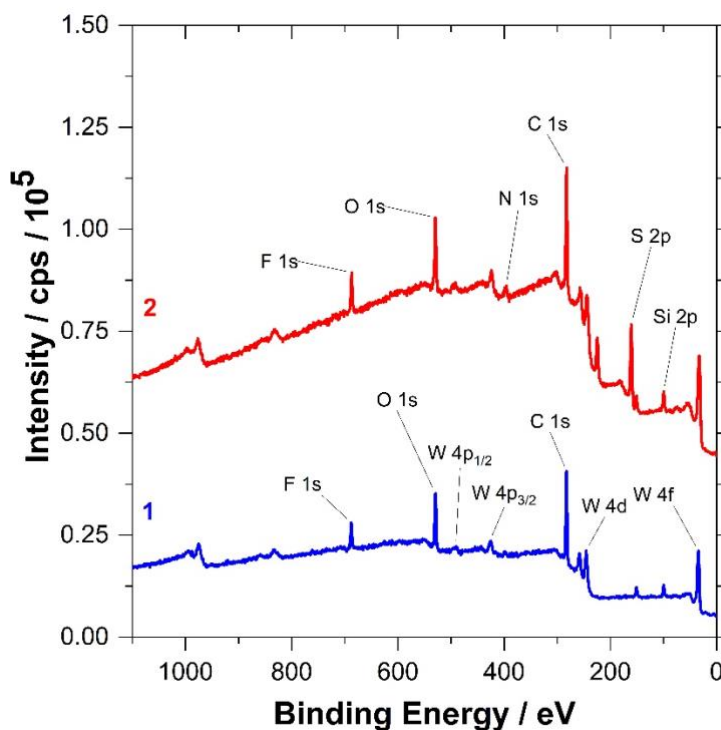


Figure 3. 5. Spectrum 1 (blue line) – XPS survey spectrum of the molecular product of the reaction between BTBMW and  $\text{Ph}_3\text{SiOH}$ ; Spectrum 2 (red line) – XPS survey spectrum the molecular product recovered from the filtrate that was obtained in the reaction between EDT and  $\text{Ph}_3\text{SiO-W}(\text{NMe}_2)(=\text{N}^t\text{Bu})_2$ ;

The survey spectrum of the yellow product found the presence of fluorine (689.5 eV) besides the expected elements. The presence of fluorine was ascribed to the contamination originating from the grease that was used for sealing the Schlenk flask. The W 4f band is found as a doublet with

contributions of the  $4f_{7/2}$  and  $4f_{5/2}$  spin orbitals. The third peak is observed in low intensity at higher binding energy (BE) and assigned to the W 5p level.

The narrow scan spectrum of the W 4f and its deconvolution revealed the  $W^{6+}$  state ( $4f_{7/2}$  peak at 35.75 eV). The N 1s level appeared in two major peaks at 398.12 and 401.93 eV. The deconvolution of the N 1s range (Figure 3. 7) shows a third contribution at 399.82 eV. According to J.-B. Wu et al,<sup>160</sup> BE of the N 1s shifts to lower values with a higher bond order of a metal-nitrogen bond. The three peaks are thus attributed to nitrogen atoms in imido (398.12 eV, W=NR), amido (399.82 eV, W-NR<sub>2</sub>) and amine (401.93 eV, W-NHR<sub>2</sub>) ligands. Formation of the amine group can originate from coordinated dimethylamine to tungsten after protonation of the metal-dimethylamido ligand bond. As tungsten (VI) complex exhibits an empty  $d^0$  orbital, it acts as an electron-withdrawing group, which can shift the N 1s peak of the coordinated amine towards higher BE. Attribution of the N 1s to amine was supported by works reporting the XPS study on the protonation of nitrogen-containing functional group<sup>27,161</sup> and organometallic study reporting an incomplete liberation of HNMe<sub>2</sub> upon protonolysis of the tungsten-dimethylamido bond.<sup>162,163</sup> Mechanistically, the already mentioned intramolecular proton transfer between thiol and amine to give zwitterionic ammonium thiolate<sup>27</sup> can also be at play. In this work, which studied intramolecular proton exchange in the L-cysteine amino acid, XPS characterization is also reported. The reported assignment<sup>27</sup> is in agreement with the assignment proposed here, in as much as the reported difference (1.98 eV) between ammonium and amine is of about the same magnitude as the one proposed here for tungsten-coordinated amine and tungsten amido peaks (2.11 eV). The absolute value differ by about 0.56 eV, which is expected given the presence of the transition metal in our case

The presence of amine in our sample suggests that the sample was hydrolyzed. Internal ratios between all elements corroborate this hypothesis. Especially, the high O/Si (2.9), O/W (4.4) and low N/W (0.71), C/W (14) ratios suggest hydrolysis of the product most probably occurred during transportation of the sample from the glovebox to the XPS chamber. Therefore, in our case, the specially designed transporting box ensure some protection from hydrolysis (tungsten imido and tungsten amido bonds can be observed) but this protection does not appear to be completely air-tight in our hands.

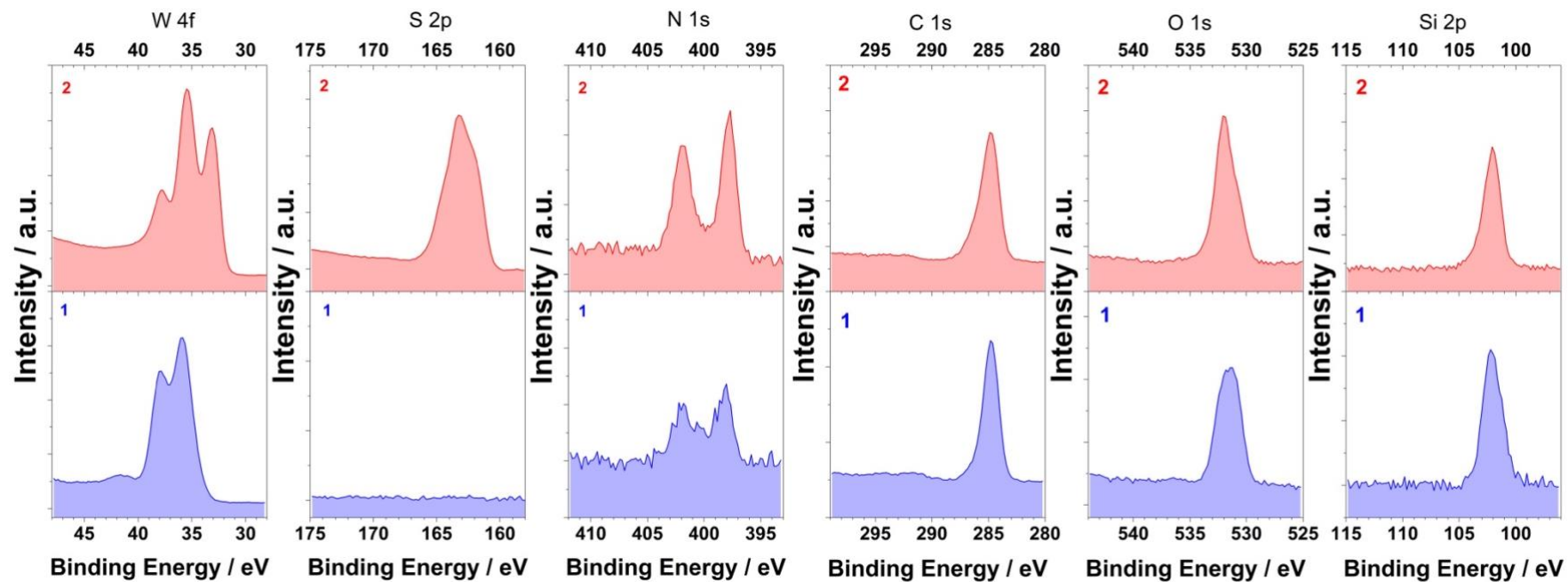


Figure 3. 6. High-resolution XPS spectra of the W 4f, S 2p, N 1s, C 1s, O 1s, and Si 2p levels of the molecular product of the reactions between BTBMW and  $\text{Ph}_3\text{SiOH}$  (spectra 1, blue line); the molecular product of the reaction between EDT and  $\text{Ph}_3\text{SiO-W}(\text{NMe}_2)(=\text{N}^t\text{Bu})_2$  (spectra 2, red line);

The C 1s peak was fitted into two components. The first component observed at a lower BE (284.77 eV) has a major fraction and was assigned to organic moieties composed of C–C bonds. As the survey spectra showed the presence of fluorine, the C–C bonds can also originate from contamination by grease. The second component (at 286.19 eV) having a minor fraction was assigned to the C–N bond containing moiety, which is supposed to be NMe<sub>2</sub>, NHMe<sub>2</sub>, N<sup>t</sup>Bu ligands. Two peaks defined from the deconvolution of the O 1s core-level were attributed to the bonded complex, W–O–Si (531.02 eV) and metal hydroxides (532.26 eV) in agreement with literature XPS assignment for tungsten hydroxides.<sup>164</sup> Ratio of their atomic fractions point to that about 40 % of the product underwent hydrolysis. However, hydrolysis could lead not only to the cleavage of Si–O–W bonds but also to the increased fraction of coordinated amine. Thus, the estimation of the fraction of the product that was subjected to hydrolysis remains complicated.

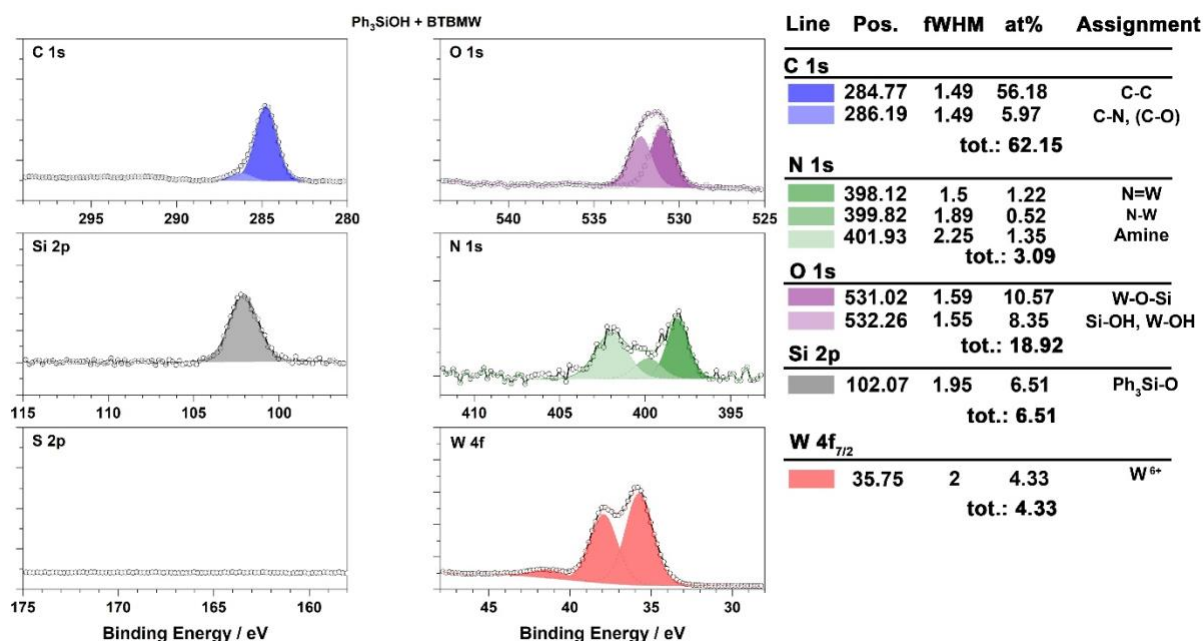


Figure 3. 7. Deconvolution of the high-resolution XPS spectra of the W 4f, N 1s, S 2p, C 1s, O 1s, and Si 2p levels of the molecular product of the reaction between BTBMW and Ph<sub>3</sub>SiOH, respective quantifications and assignments;

Nevertheless, observation of nitrogen in amido and imido forms, tungsten in W<sup>6+</sup> oxidation state, and oxygen in W–O–Si environment of the corresponding molecular model support the formation of the proposed structure in Scheme 3. 2.

The yellow powder product of this reaction was also studied by Raman spectroscopy (see red spectrum *m1* in Figure 3. 8A). While the precise assignment goes beyond the scope of this work, the Raman spectrum will serve as a fingerprint comparison for the subsequent silica and wafer-based species. The red spectrum *m1* shows the features observed on the Raman spectra of both pure BTBMW and Ph<sub>3</sub>SiOH in black *m0* and gray *m0'* spectra (Figure 3. 8A), respectively.

Overall, the reactivity observed here between Ph<sub>3</sub>SiOH and BTBMW is in very good agreement with the density functional theory (DFT) study recently published by M. Shirazi *et al.*<sup>158</sup> in the closely related system of SiO<sub>2</sub> and molybdenum analog of BTBMW. The outcome of the study can be summarized as silanolysis of the Mo–NMe<sub>2</sub> bond is more favorable than that of Mo=N<sup>t</sup>Bu. During the subsequent H<sub>2</sub>S pulse, dissociation of H<sub>2</sub>S on the partially protonated *tert*-butylimido ligand gives rise to *tert*-butylamine desorption, while this does not occur in the case of the non-protonated *tert*-butyl imido ligand.

The next step was the investigation of Ph<sub>3</sub>SiO–W(=N<sup>t</sup>Bu)<sub>2</sub>(NMe<sub>2</sub>) with EDT, which can provide some insights into the surface chemistry of the second half-cycle of ALD on a substrate. A solution of Ph<sub>3</sub>SiO–W(=N<sup>t</sup>Bu)<sub>2</sub>(NMe<sub>2</sub>) in toluene was added to the toluene solution of excess (1:5) EDT, which led to coloring the mixture to red and precipitation. The precipitate was filtered out and washed with toluene. A red solid product isolated after evaporating the solvent and excess EDT from the filtrate was characterized by solution NMR, Raman, and XPS that identified the formation of the W–S bond and partial reduction to the formal W<sup>5+</sup> state.

The survey XPS spectrum identifies the addition of sulfur atoms to the 1<sup>st</sup> molecular product (red spectrum 2 in Figure 3. 5). The W 4f range showed a partial reduction to the W<sup>5+</sup> state but still retaining the contribution of W<sup>6+</sup>. The research group of James E. Whitten has observed a reduction of W<sup>6+</sup> to W<sup>5+</sup> when WO<sub>3</sub> nanoparticles were treated with methanethiol. The authors state that coupling of thiol groups, forming the S–S bond, can induce the reduction of the metal.<sup>25</sup> At the same time, oxidative coupling of different types of mercaptans were reported in other works supporting the potential of EDT to induce a reduction of tungsten.<sup>165,166</sup> There can be several pathways for coupling of two thiol groups especially in the case of excess EDT (e.g. between individual free EDT molecules, ethylenedithiolate ligands of neighboring or same metal centers).

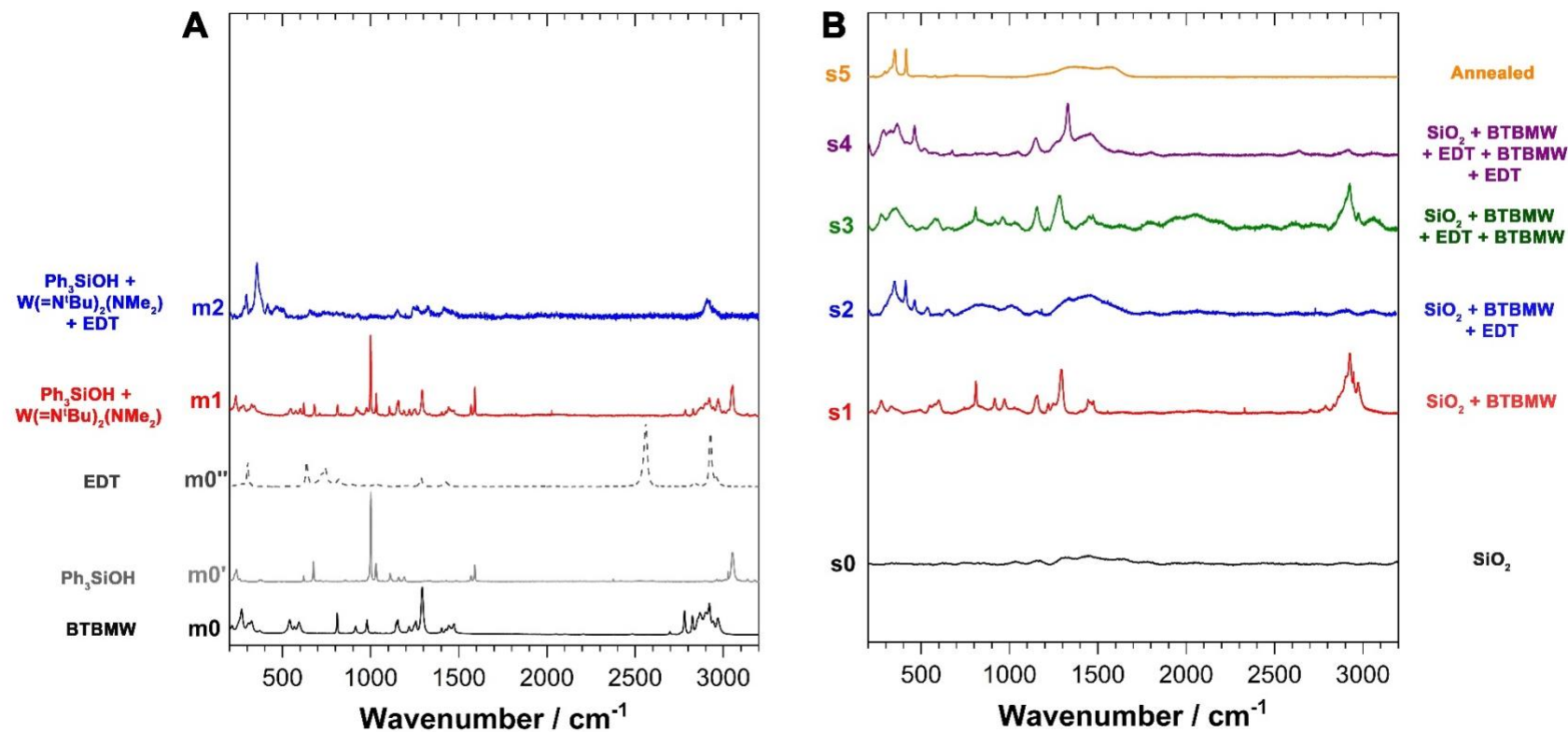


Figure 3. 8. **A** - Raman spectra of pure BTBMW (spectrum  $m_0$ , black line), pure  $\text{Ph}_3\text{SiOH}$  (spectrum  $m_0'$ , gray line), pure EDT (spectrum  $m_0''$ , green line), the molecular product of the reaction between BTBMW and  $\text{Ph}_3\text{SiOH}$  (spectrum  $m_1$ , red line), the molecular product of the reaction between EDT and  $\text{Ph}_3\text{SiO}-\text{W}(\text{NMe}_2)(=\text{N}^i\text{Bu})_2$  (spectrum  $m_2$ , blue line); **B** - Raman spectra of silica-based solids: dehydroxylated  $\text{SiO}_{2-500}$  before deposition (spectrum  $s_0$ , black line); the product of the 1<sup>st</sup> pulse of BTBMW (spectrum  $s_1$ , red line); the product the 1<sup>st</sup> pulse of EDT (spectrum  $s_2$ , blue line); the product of the 2<sup>nd</sup> pulse of BTBMW (spectrum  $s_3$ , green line); the product of the 2<sup>nd</sup> pulse of EDT (spectrum  $s_4$ , purple line); the product of annealing of silica nanobeads after 2 full ALD cycles (spectrum  $s_5$ , orange line).

Elimination of ethylene from the ethylenedithiolate ligand, as it was already mentioned earlier<sup>19,137</sup>, can also promote the S-S coupling. The thiol-induced formal reduction of tungsten appears to be substantial since the atomic fractions suggest a  $W^{5+}:W^{6+}$  ratio of about 2:1. The hydrolysis issue mentioned before actually suggests that this ratio might be even higher.

The narrow scan spectrum of the S 2p core-level (see Figure 3. 6) shows the main peak at 163.3 eV with a shoulder on the lower BE side. The deconvolution in Figure 3. 9 reveals the presence of two main contributions of sulfur. The first component is observed at a lower BE of S 2p<sub>3/2</sub> (161.79 eV) that was assigned to the sulfur atom in thiolate ( $-S^-$ ) form.<sup>24,27,167</sup> To assert the second contribution in S 2p core-level, we looked at the literature precedents reporting XPS study of oxysulfide system of tungsten and other transition metals. According to these references,<sup>24,167</sup> the second contribution at a higher BE of S 2p<sub>3/2</sub> (163.27 eV) was attributed to the presence of coupled sulfur atoms in  $S_2^{2-}$  form ( $-S-S-$ ). BE difference of the S 2p 3/2 peaks of mentioned  $S_2^{2-}$  and  $-S^-$  forms (1.48 eV) also comes in agreement with reported differences (1.5<sup>167</sup> and 1.7<sup>24</sup> eV) of BE between  $S_2^{2-}$  and  $-S^-$  peaks. According to these literature precedents, the presence of  $S_2^{2-}$  is coherent with the observed W 4f<sub>7/2</sub> peak at lower BE that was attributed to the formal  $W^{5+}$  oxidation state.

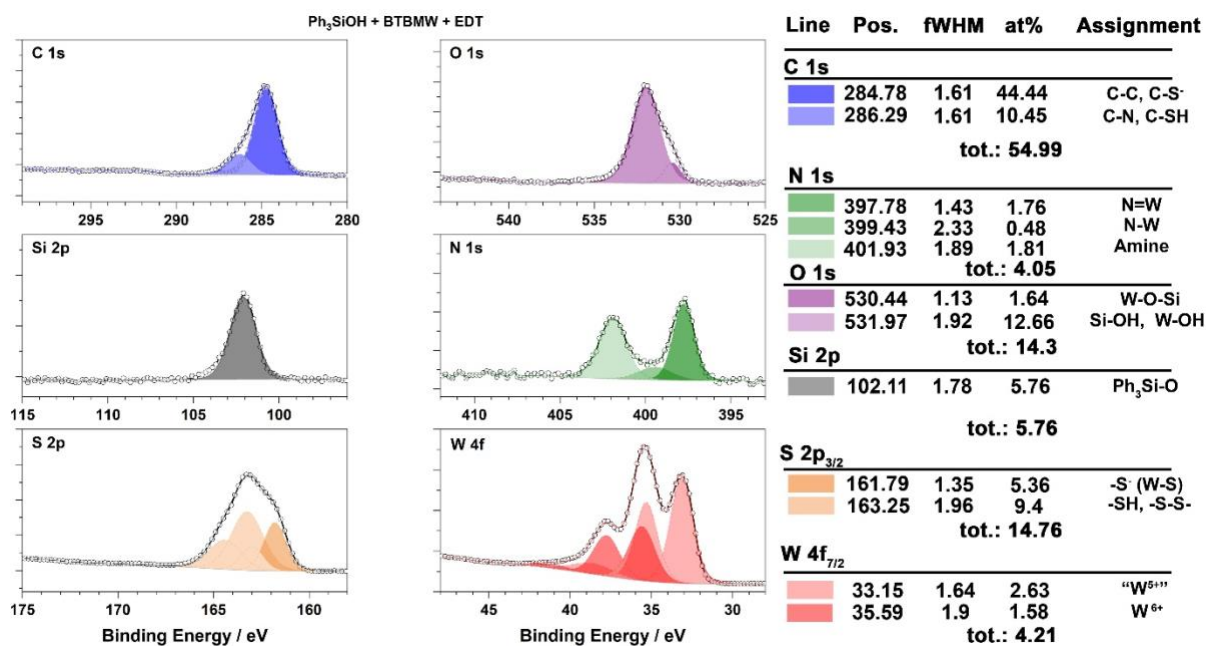


Figure 3. 9. Deconvolution of the high-resolution XPS spectra of the W 4f, N 1s, S 2p, C 1s, O 1s, and Si 2p levels of the molecular product recovered from the filtrate obtained in the reaction between EDT and Ph<sub>3</sub>SiO-W(NMe<sub>2</sub>)(=N<sup>t</sup>Bu)<sub>2</sub>, respective quantifications and assignments;

As monodentate ethylenedithiolate ligand ( $W-SCH_2CH_2SH$ ) is supposed to leave one of the thiol groups unreacted, the free  $-SH$  group's contribution could also be present in the XPS spectrum. E. Ataman *et al.*<sup>27</sup> discussed partial proton transfer from thiol to the amino group to form a zwitterion and reported deconvolution of the S 2p core-level. Authors of this work report that the thiol peak should appear at 2.34 eV apart from the thiolate ( $-S^-$ ) form towards higher BE. Therefore, given the lower energy resolution of our XPS instrument, and greater full width at half maximum (fWHM) of the second contribution, the  $-SH$  fraction could overlap with the  $S_2^{2-}$  form.

The C 1s core-level showed the increase of the full width at half maximum (fWHM) and the fraction of the component at higher BE. This suggests the addition of new moieties in the environment of carbon such as carbon-thiolate and carbon-thiol bonds (see Figure 3. 9). These assignments can also overlap with the previously identified organic carbon-carbon bonds and carbon-amino bonds, respectively, whose differences of BEs also come in-line with the literature.<sup>27</sup>

High-resolution XPS of the O 1s range demonstrated the sharpening of the peak. Deconvolution revealed that the atomic fraction of previously assigned tungsten siloxide ( $Si-O-W$ ) moiety significantly decreased, and that of hydroxides ( $Si-OH$ ,  $W-OH$ ) increased with respect to total oxygen content. This may originate from exposure to air leaks followed by hydrolysis.

The Raman spectrum (see spectrum *m2* in Figure 3. 8A) showed bands of lowered intensity with respect to that of  $Ph_3SiO-W(NMe_2)(=N^tBu)_2$ . Some literature precedents helped to tentatively propose attributions for a part of the Raman bands. Bradley *et al.*<sup>163</sup> reported a list of the IR bands for tungsten thiolates obtained in the reaction of similar  $W(NMe_2)_6$  complex with PhSH or MeSH, which match some of the Raman bands in our spectrum. Several other works provided more detailed attributions of Raman and IR bands for similar systems containing alkylthiolate,<sup>153</sup> thiol,<sup>153</sup> di<sup>31,154</sup>- and polysulfide<sup>155</sup> as well as dimethylamido<sup>157</sup> functional groups. Based on these literature precedents, bands observed at 355s, 463w and 656w  $cm^{-1}$  for the *m2* product suggest the existence of C-S and S-S bonds in the structure. While the first band can be contributed by the  $CCS$  and  $CC_3$  deformation vibrations, the second band (463w  $cm^{-1}$ ) originates from the S-S bond stretching. A weak signal of the second band is coherent with observed low intensity of alkyl disulfide Raman bands reported in the above-mentioned references.<sup>31,155</sup> Raman band of the S-S bond stretching also supports the S 2p deconvolution to the  $-S_2^{2-}$  component. The third band (at 656w  $cm^{-1}$ ) can originate from the C-S bond stretching and aromatic ring deformation vibration. Existence of the C-S bond points to the thiolate moiety bonded to tungsten,  $W-SCH_2CH_2SH$ . At the same time, the band

previously assigned to the W–N stretching in  $\text{Ph}_3\text{SiO–W}(\text{NMe}_2)(=\text{N}^t\text{Bu})_2$  seems to shift from 547 to  $507\text{ cm}^{-1}$  in the product after exposure to EDT. However, the Raman spectrum did not retain the high-intensity band previously assigned to the out-of-plane deformation vibration of aromatic  $=\text{C–H}$  at  $1000\text{ cm}^{-1}$ . This may be caused by the deactivation of the vibration mode in Raman. Also, it may point to the fact that the filtrate part of the reaction mixture does not provide a full image of the molecular product.

The solution NMR was not informative due to the low solubility of the product in tested solvents. This reaction should still be continued to investigate, therefore, no robust conclusions can be given at this moment so far. Nevertheless, the outcome of the reaction of EDT with the first molecular product demonstrated quick reactivity.

In summary, the exploratory data on the molecular chemistry between BTBMW and EDT and between BTBMW and  $\text{Ph}_3\text{SiOH}$  leads to two important and positive information in view of the targeted ALD process:

1. BTBMW reacts cleanly with silanols at room temperature, which is encouraging with respect to the outcome of the first pulse between gaseous BMBTW and surface silanols of the supports (next amorphous silica as a more sophisticated model and finally silica of a wafer surface).
2. BTBMW and EDT react with each other in a way, which is conducive to the growth by alternate pulses. Partial reduction of  $\text{W}^{6+}$  complex to formal  $\text{W}^{5+}$  oxidation state seems to happen by thiol addition.

### 3.3.2. Modeling the 1<sup>st</sup> pulse via deposition of $(\text{NMe}_2)_2(=\text{N}^t\text{Bu})_2\text{W}$ (VI) on nanobeads of silica-700

Our next step in our modeling strategy toward a well-defined ALD process is to test the process on a high surface area solid displaying the similar reactive moieties in a similar density as the targeted final ALD substrate (silica covered Silicon wafer in our case). Silica previously dehydroxylated at  $700^\circ\text{C}$  can be described as a collection of isolated silanols, therefore bearing some similarity with silica thermally grown on a silicon wafer in terms of chemical reactive synthons, as better described in Chapter 1. At the same time, amorphous silica used here displays, unlike silicon wafers, a very

large surface area that eases the characterization of the grafted species, in a typical SOMC approach, also better described in Chapter 1.

### 3.3.2.1. Grafting of $(\text{NMe}_2)_2(=\text{N}^t\text{Bu})_2\text{W}$ (VI) on silica-700

Upon surface reaction between BTBMW vapors and dehydroxylated silica-700, white powder has turned to pale yellow color. Total consumption of surface  $-\text{OH}$  hydroxyl groups observed on DRIFT spectrum (see the disappearance of the band at  $3747\text{ cm}^{-1}$  assigned to O-H stretching,  $\nu_s(\text{O}-\text{H})$ , in Figure 3. 10) has confirmed completed grafting of BTBMW on silica-700. New absorption peaks appeared in the range of  $2700\text{-}3000\text{ cm}^{-1}$ , concomitantly with this disappearance. We attempted to give approximate attributions of observed IR bands according to a handbook of IR spectroscopy<sup>151</sup> and some spectroscopic reports<sup>157</sup> on similar complexes. The red curve shows the absorption bands between  $2970$  and  $2787$  assigned to  $\text{CH}_x$  symmetric and asymmetric stretching vibrations in  $-\text{NMe}_2$  and in  $=\text{N}^t\text{Bu}$ .

The Raman spectrum of pure BTBMW served as a good fingerprint for the spectrum recorded for solid obtained in the 1<sup>st</sup> grafting of BTBMW on  $\text{SiO}_2\text{-}500$  (see red spectrum s1 in Figure 3. 8B). This way the chemisorption of the BTBMW on silica surface was well-confirmed. The assigned Raman peaks were collected and tentatively proposed in the experimental section of this chapter.

Gaseous byproducts produced upon deposition of BTBMW on silica-700 have been trapped in  $\text{C}_6\text{D}_6$  and analyzed by  $^1\text{H}$  NMR (see Figure 3. 11A). The main signal at  $2.20$  ppm was assigned to protons of the methyl groups of dimethylamine. A little peak was caused by methyl protons of *tert*-butylamine at  $0.99$  ppm with a ratio to the dimethylamine protons  $0.39:6.0$ . Considering the number of protons in two amines and the high volatility of dimethylamine, the volume fraction of dimethylamine was determined as high as  $96\%$ . This points to the BTBMW deposition on silica goes along with the substitution of dimethylamido groups as a major pathway. According to the previously mentioned DFT study<sup>158</sup>, the substitution of  $=\text{N}^t\text{Bu}$  ligand is less favorable than that of  $-\text{NMe}_2$  ligand.

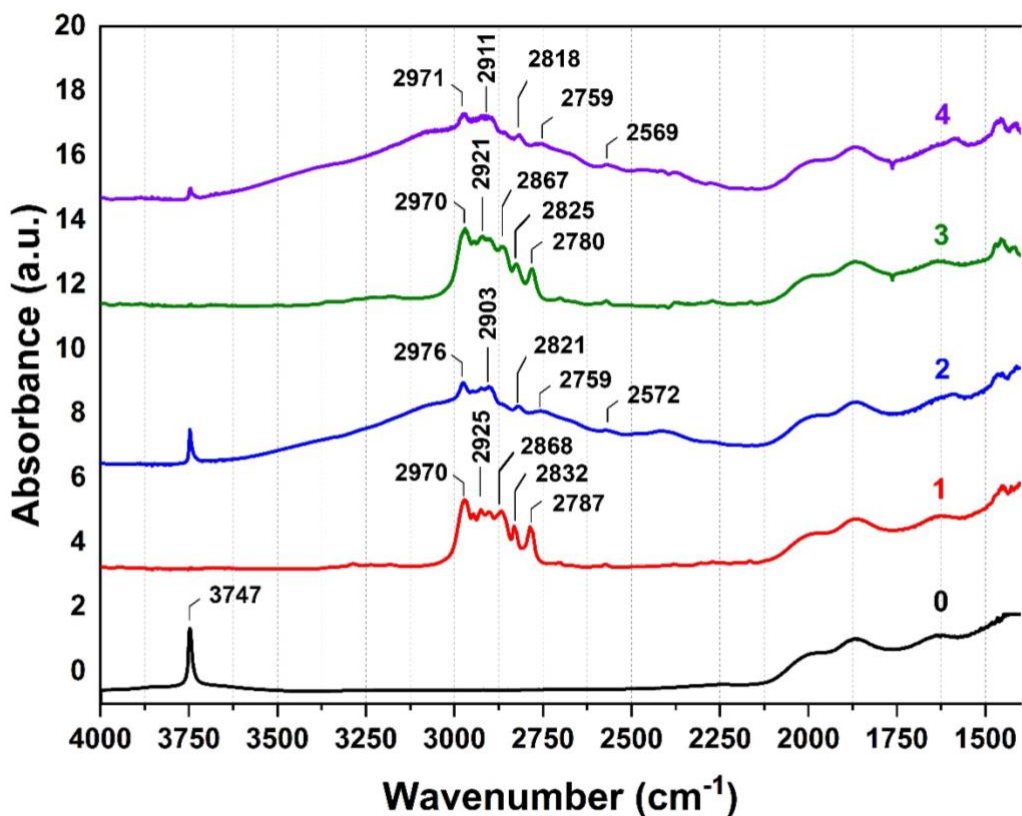


Figure 3. 10. IR spectra recorded between 1400 and 4000  $\text{cm}^{-1}$  for the sample of  $\text{SiO}_2\text{-700}$  before deposition (spectrum 0, black); after the 1<sup>st</sup> pulse of BTBMW precursor (spectrum 1, red); after the first pulse of EDT (spectrum 2, blue); after the second pulse of BTBMW (spectrum 3, green); after the second pulse of EDT (spectrum 4, purple)

The elemental analysis determined metal loading on silica at 5.22 % after the 1<sup>st</sup> pulse (see Table 3. 1). The resulted surface concentration of  $0.28 \text{ mmol W} \cdot \text{g}^{-1}$  is in good agreement with the usual range of metal loading in the case of the mono-grafted complex on  $\text{SiO}_2\text{-700}$ .<sup>168</sup> as well as with the concentration of surface hydroxyl groups estimated from our titration ( $0.24 \text{ mmol} \cdot \text{OH} \cdot \text{g}^{-1}$ ). Table 3. 1 together with theoretically calculated ratios from hypothesized formulas contains empirical atomic ratios defined by the elemental analysis results and proposed product structures. Calculated atomic ratios served to estimate the molecular formula of deposited W complex as  $\equiv\text{SiO-WC}_{10}\text{N}_3\text{H}_{26}$ , which is in good agreement with the molecular structure given in Scheme 3. 3.

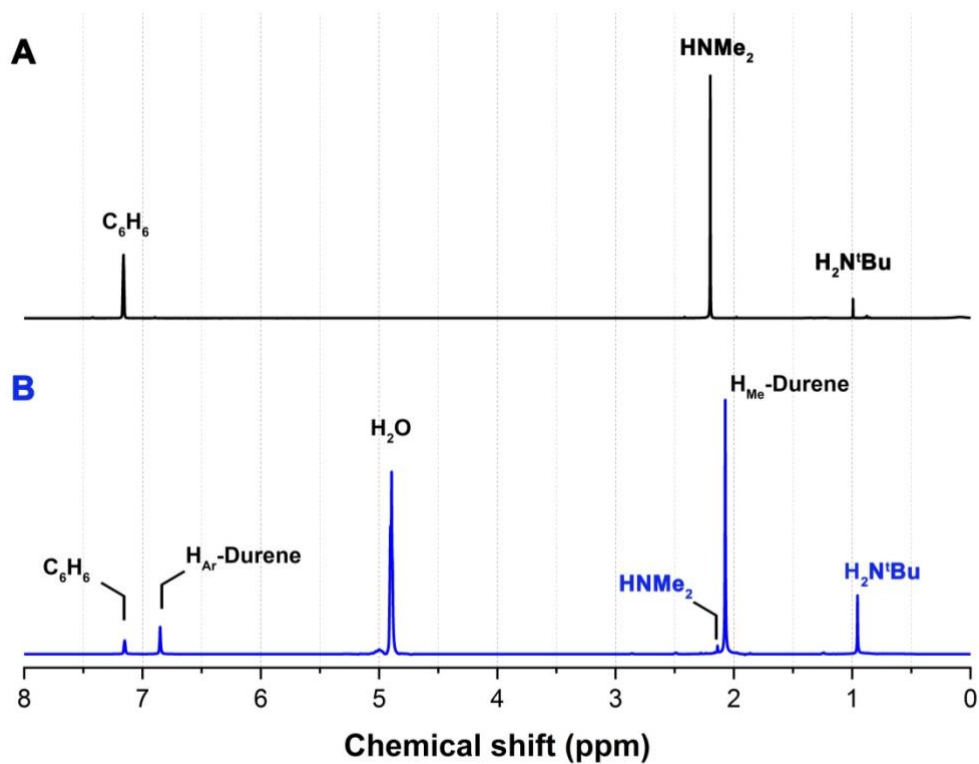


Figure 3. 11.  $^1\text{H}$  NMR spectra of condensed gaseous products released upon grafting of BTBMW (spectrum A, black) on silica-500 and after hydrolysis of the silica-supported BTBMW (spectrum B, blue)

Solid-state  $^{13}\text{C}$  NMR spectrum (see Figure 3. 2, spectrum 1, red line) of the solid product of the 1<sup>st</sup> deposition of BTBMW on  $\text{SiO}_2\text{-700}$  reveals three carbon atoms resonances at 32.6, 53.9, and 66.0 ppm. The peak in the middle, at 53.9 ppm, is assigned to two carbon atoms of the dimethylamido group. The signals at 32.6 and 66.0 ppm correspond to one primary and three tertiary carbon atoms of each *tert*-butylimido ligands. These assignments were based on comparison with the  $^{13}\text{C}$  NMR spectrum of BTBMW recorded in solution (see precursors section 3.2.2). No other carbon types were observed upon the 1<sup>st</sup> pulse of BTBMW.

Table 3. 1 Elemental analysis results of BTBMW grafted on silica-700 and calculated atomic ratios.

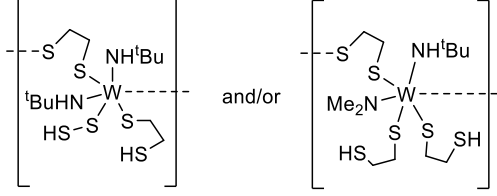
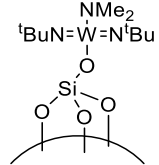
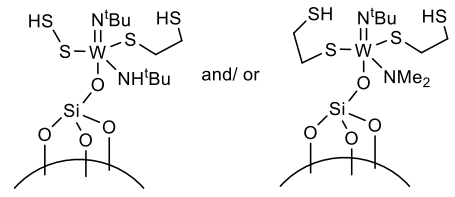
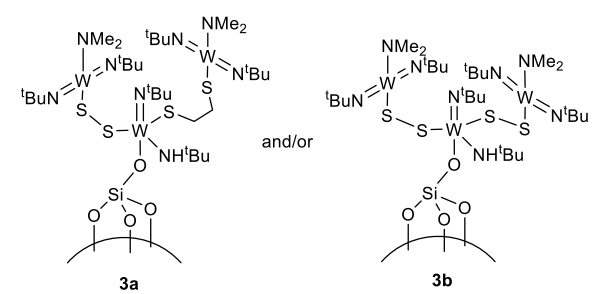
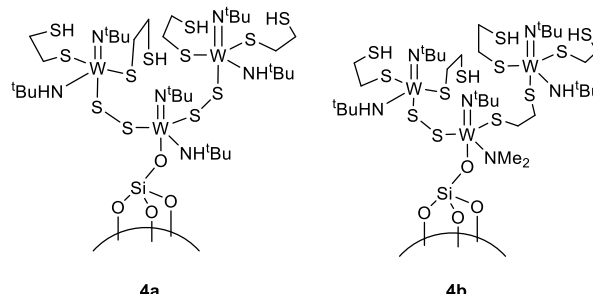
	Elemental analysis (wt. %) (expected)*					Empirical atomic ratios (expected)*			Proposed structures or molecular formulas
	W	C	N	S	H	S/W	N/W	C/W	
<b>BTBMW + EDT</b>	32.30 (31.8)*	24.85 (24.9)*	5.04 (4.84)*	31.90 (33.3)*	5.23 (5.23)*	5.7 (6)	2.0 (2)	12 (12)	 <p style="text-align: center;"><b>B1</b>                      <b>B2</b></p>
<b>1<sup>st</sup> pulse</b>	5.22 (4.05) <sup>+</sup>	3.48	1.28	0	0.74	0 (0)	3.2 (3)	10 (10)	
<b>2<sup>nd</sup> pulse</b>	5.57 (3.95) <sup>+</sup>	4.06	1.03	4.15	0.84	4.3 (4)	2.4 (2)	11 (10)	 <p style="text-align: center;"><b>2a</b>                      <b>2b</b></p>

Table 3.1 (continued)

	Elemental analysis (wt. %) (expected)*					Empirical atomic ratios (expected)*			Proposed structures or molecular formulas
	W	C	N	S	H	S/W	N/W	C/W	
<b>3<sup>rd</sup> pulse</b>	14.90 (10.29) <sup>+</sup>	8.49	2.62	2.91	1.67	1.1 (1.3)	2.3 (2.7)	8.7 (9.3)	 3a and/or 3b
<b>4<sup>th</sup> pulse</b>	10.65 (9.76) <sup>+</sup>	7.25	1.54	7.47	1.42	4.0 (4)	1.9 (2)	10 (10.7)	 4a and 4b
<b>Annealed at 800 °C in Ar</b>	16.90	1.22	≤ 0.20	6.53	≤ 0.1	2.2 (2)	≤ 0.15 (0)	1.1 (0)	$\equiv\text{SiO}-\text{WS}_{2.2}\text{C}_{1.1}\text{N}_x\text{H}_y$ ( $x < 0.15$ , $y < 1.1$ )
<b>Annealed at 450 °C in H<sub>2</sub></b>	17.00	0.70	≤ 0.20	6.20	0.15	2.1 (2)	≤ 0.15 (0)	0.63 (0)	$\equiv\text{SiO}-\text{WS}_{2.1}\text{C}_{0.63}\text{N}_x\text{H}_{1.6}$ ( $x < 0.15$ )

\*The expected fractions were estimated according to the proposed structure in the last column

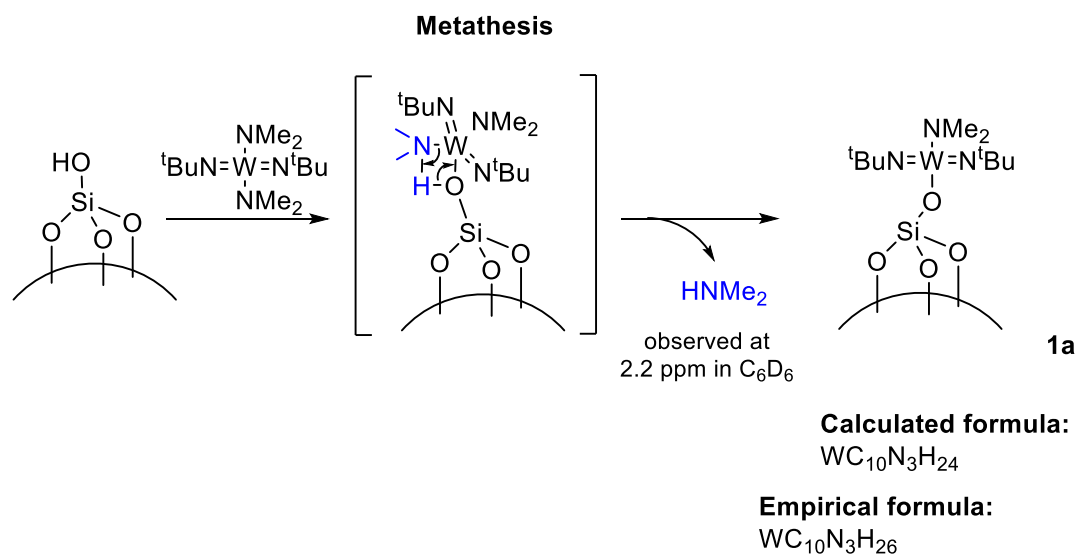
<sup>+</sup> Expected loadings were calculated based on the surface silanols concentration (defined by titration) on SiO<sub>2-700</sub> of 0.24 mmol·OH/g and proposed formulas

### 3.3.2.2. Hydrolysis of silica-supported BTBMW

The literature has precedents of alcoholysis of tungsten-amido bonds,<sup>163</sup> therefore, hydrolysis of BTBMW was also expected to cleave the W–N bonds and release volatile amines. Analysis of gaseous products released upon the hydrolysis was carried out by solution NMR in the presence of internal standard, durene (1,2,4,5-tetramethylbenzene), to verify the proposed structure of BTBMW after the 1<sup>st</sup> grafting. Durene gives two singlet peaks at 2.08 and 6.86 ppm for methyl protons and aromatic protons, respectively. The <sup>1</sup>H NMR spectrum in Figure 3. 11 (spectrum B) shows those peaks of durene as well as methyl protons of released *tert*-butylamine and dimethylamine at 0.96 and 2.15 ppm, respectively. Integration of the last two peaks in 9:2.75 ratio defines *tert*-butyl amine to be in about 2:1 ratio with respect to dimethylamine. However, estimation of relative areas of the peaks with respect to the known amount of durene and theoretically expected maximum amount of the amines, suggests that only a small fraction remained dissolved in deuterated benzene (see the experimental section of this chapter). The rest of the amines may stay either in the gas phase above the analyzed solution (in the headspace of the NMR tube) or in the aqueous phase that was separated from benzene and resonated at 4.90 ppm (instead of the common water proton resonance at 0.40 ppm in C<sub>6</sub>D<sub>6</sub>).

### 3.3.2.3. Proposed mechanism of the first pulse

Obtained results of DRIFT, NMR, GC-MS spectroscopies, and elemental analysis have allowed us to observe the formation of dimethylamine as a byproduct upon the grafting of BTBMW on the silica surface. Observed IR absorption of solid product exhibits bands inherent to the C–H bond stretching in alkyl-amido groups along with consumption of all surface hydroxyl groups. Elemental analysis confirms deposition of one tungsten atom per each surface –OH group and two *tert*-butylimido and one dimethylamido ligands per grafted W. The outcome of the hydrolysis conducted on silica-supported BTBMW supported the nature and estimated ratio ( $[=N^tBu]:[-NMe_2] = 2:1$ ) of the ligands by elemental analysis. All this collected information suggests the proposed reaction mechanism of the grafting of BTBMW on silica nanobeads as illustrated in Scheme 3. 3.



Scheme 3. 3. Proposed mechanism of the grafting reaction of the BTBMW on SiO<sub>2-700</sub> surface

According to I. Novak *et al.*<sup>169</sup>, a study of the electronic structure of BTBMW by UV photoelectron spectroscopy and DFT/outer-valence Green's function (OVGF) calculations reveals lower ionization energy for the -NMe<sub>2</sub> groups (7.9-8.35 eV) than that of =N<sup>t</sup>Bu (9.25 eV). It implies that metathesis with surface ≡SiO-H is more favorable for the tungsten-amido bond, which comes in good agreement with the above-discussed results.

### 3.3.3. Exploratory SOMC work toward ALD process with 1,2-ethanedithiol and [(=N<sup>t</sup>Bu)<sub>2</sub>(NMe<sub>2</sub>)<sub>2</sub>W]

#### 3.3.3.1. The reaction of 1,2-ethanedithiol with silica-supported [(=N<sup>t</sup>Bu)<sub>2</sub>(NMe<sub>2</sub>)<sub>2</sub>W] as a modeling reaction of the 2<sup>nd</sup> half cycle

The first pulse of EDT on the silica-supported BTBMW can model the second half-cycle of ALD. As already stated, the aim is two-fold: identify a facile reaction of the gaseous thiols on the metal-terminated surface while, at the same time preserving after reaction some unreacted thiols as to allow further reaction with new metal source in the next ALD cycle.

Exposure to EDT vapors induced a color change of the powder from pale yellow to red. Such a sharp color change can be consistent with the new oxidation state of tungsten,<sup>138</sup> as it was observed by XPS for analogous molecular product.

IR spectrum (blue spectrum 2 in Figure 3. 10) recorded for the solid after EDT pulse displays the significant decrease of the bands at 2786 and 2832  $\text{cm}^{-1}$  that were previously assigned to  $-\text{NMe}_2$  and/or  $\text{N}^t\text{Bu}$  ligands (in red spectrum 1), and the appearance of a new surface  $-\text{OH}$  groups at 3747  $\text{cm}^{-1}$ . A weak absorption band at 2572  $\text{cm}^{-1}$  can be attributed to stretching vibration of the  $\text{S}-\text{H}$  bond that confirms successful surface reaction of the EDT and presence of the available functional group for the following tungsten pulse. New bands at 2922, 2903 and 2759  $\text{cm}^{-1}$  could be due to symmetric and asymmetric stretching of  $\text{C}-\text{H}$  in sulfur-containing moieties like  $-\text{CH}_2\text{SH}$ . Hence, the decrease of the bands assigned to amido or imido and the appearance of new bands assigned to  $-\text{CH}_2\text{SH}$ -like groups let us expect successful substitution of the starting groups by EDT. The wide increase of peaks together with a baseline between 2500 and 3500  $\text{cm}^{-1}$  is a sign of intermolecular interaction like hydrogen bonding.<sup>140,141,151</sup> Such interaction can occur between the  $\text{NH}$  groups of protonated nitrogen atoms, thiol groups of bonded ethylenedithiolate moiety or excess EDT, and surface  $-\text{OH}$  group and  $\equiv\text{Si}-\text{O}-\text{Si}\equiv$  bridges (as already discussed in section 3.3.1). Evacuation after each pulse for 30 minutes under a dynamic ultra-high vacuum at 80  $^\circ\text{C}$  did not change this interaction with the surface. This drying duration was extended to 90 minutes, but no decrease of the wideband was observed.

The formation of the  $\text{W}-\text{S}$  bond is suggested by the observation the Raman bands at 351, 463 and 654  $\text{cm}^{-1}$  (see in Figure 3. 8B)<sup>170</sup>. As earlier discussed in section 3.2.3.3, these Raman bands may originate from the deformation vibration of  $\text{CCS}$  (351  $\text{cm}^{-1}$ ),  $\text{CC}_3$  (351  $\text{cm}^{-1}$ ), the stretching vibration of the  $\text{S}-\text{S}$  (463  $\text{cm}^{-1}$ ) and  $\text{C}-\text{S}$  bonds (654  $\text{cm}^{-1}$ ). A more detailed assignment of the Raman spectra is proposed in the experimental section. Incomplete substitution of the  $\text{N}$ -containing ligands is supported by the Raman band at 534  $\text{cm}^{-1}$  assigned to the stretching mode of the  $\text{W}-\text{N}$  bond.

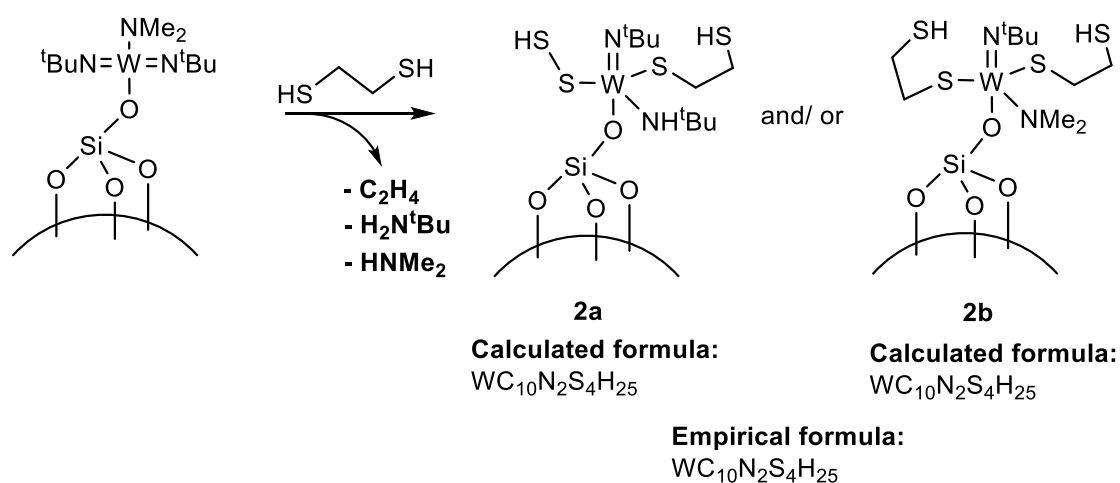
The volatile byproducts upon EDT addition were condensed into the NMR tube and analyzed by  $^1\text{H}$  and  $^{13}\text{C}$  NMR spectroscopy. The NMR spectra revealed proton and carbon signals of  $\text{H}_2\text{N}^t\text{Bu}$ ,  $\text{HNMe}_2$ , and  $\text{H}_2\text{C}=\text{CH}_2$ . The release of dimethylamine supported our expectations due to easier protonolysis of the dimethylamido ligand than *tert*-butylimido. However, the production of *tert*-butylamine was probably possible with the excess of EDT that delivers enough protonation source and high temperature. One of the resonances (at 2.06 ppm) could not be assigned. Therefore, ESI-MS analysis was complementary conducted in the attempt to elucidate unassigned resonance. However, it showed the presence of dimethylamine (46 Da) and *tert*-butylamine (74 Da) and was limited to detect fragments with molecular weight higher than 40 Da. Transition metal alkylamido complexes are known to undergo thermal decomposition<sup>146,171</sup> that is in couple with the presence of

excess EDT might lead to the generation of unassigned product. Two current hypotheses are methylamine and thiirane.

Elemental analysis of the solid product (Table 3. 1) after the surface reaction of EDT vapors with the silica-supported BTBMW yield the molecular formula as  $\equiv\text{SiO}-\text{WC}_{10}\text{N}_2\text{S}_4\text{H}_{25}$ . It is clearly seen that the surface reaction occurred between two molecules of EDT and one W center while two nitrogen-containing groups remained. Starting from the proposed structure after the 1<sup>st</sup> pulse ( $\equiv\text{SiO}-\text{WC}_{10}\text{N}_3\text{H}_{24}$ ), subtraction of one nitrogen atom can go either via eliminating one equivalent of dimethylamine or *tert*-butylamine, or both of them in partial fractions. The major substitution is expected to result in releasing  $\text{HNMe}_2$ .<sup>169</sup> Formation of the second W–S bond with another EDT molecule may proceed via the exchange of the S–H and one of the W=N bonds as well yielding W–NH<sup>t</sup>Bu by hydrogenation of nitrogen in the *tert*-butyl imido group. This way, each tungsten atom could retain 2 nitrogen atoms and acquire 4 sulfur atoms. However, in this pathway, the molecular formula would differ from the empirical formula for 2 carbon and 4 hydrogen atoms that matches with one equivalent of ethylene. Loss of ethylene from the dithiolate bridge is known to be relatively easy.<sup>19,137</sup> Therefore, the first proposed pathway suggests the substitution of one  $-\text{NMe}_2$ , binding two  $-\text{SCH}_2\text{CH}_2\text{SH}$  ligands, and elimination of one equivalent of ethylene. Another way to yield the same number of atoms is to substitute one of the  $=\text{N}^t\text{Bu}$  (by releasing  $\text{H}_2\text{N}^t\text{Bu}$ ) group by binding two ethylenedithiolate ligands instead. Based on these two pathways, two possible structures (**2a** and **2b**) of grafted species were proposed in Scheme 3. 4, which provide the same molecular formulas,  $\equiv\text{SiO}-\text{WC}_{12}\text{N}_2\text{S}_4\text{H}_{25}$ , excellent match with the empirical formula. Integration of the ethylene signal in the <sup>1</sup>H NMR spectrum of condensed byproducts was not reliable due to its only partial dissolution in the solvent. Nevertheless, the  $\text{H}_2\text{N}^t\text{Bu}$  to  $\text{HNMe}_2$  ratio equal to 2.4:1 points to that substitution of  $-\text{NMe}_2$  does not dominate over the substitution of  $=\text{N}^t\text{Bu}$ . One should note the low boiling point of dimethylamine (6.8 °C) suggests that it partially stay in the headspace (in the gaseous phase). Hence, the integration of liquid-state NMR peaks cannot provide a reliable comparison of yields of the proposed structures **2a** and **2b**.

Solid-state <sup>13</sup>C NMR spectrum (see Figure 3. 2, spectrum 2, blue line) of the solid product of the 1<sup>st</sup> pulse of EDT shows four peaks at 29.1, 37.5, 42.8, and 69.6 ppm. Two signals of the *tert*-butyl group (primary and secondary carbons) are found at 29.1 and 69.6 ppm though with little shifting. The upfield shift of the primary carbon signal from 32.6 to 29.1 ppm can originate from the protonation of N turning imido into a corresponding amido ligand (see the structure **2a** in Scheme 3. 4). However, the signal of primary carbon atoms of <sup>t</sup>Bu group still exhibits a signal at the former

chemical shift and is seen as a peak's left shoulder. This is coherent with the presence of both imido and amido forms of N<sup>t</sup>Bu ligand for the structure **2a**. The other two peaks in the middle, at 37.5 and 42.8 ppm, can be assigned to two carbon atoms of the EDT moiety. These assignments support the proposed reaction product given in Scheme 3. 4. The peak of dimethylamido carbon that was previously observed at 53.9 ppm almost disappeared after the EDT pulse. Therefore, it suggests that the substitution of the dimethylamido ligand by EDT is a more dominant pathway than the substitution of the *tert*-butylimido ligand. This comes in agreement with the above-mentioned electronic structure study<sup>169</sup> that reported a difference in ionization energies.



Scheme 3. 4. Proposed reaction route of the reaction of EDT with silica-supported BTBMW modeling the 2<sup>nd</sup> half-cycle. Ethylene, HNMe<sub>2</sub> and H<sub>2</sub>N<sup>t</sup>Bu were identified as gaseous byproducts of the reaction

### 3.3.3.2. 3<sup>rd</sup> and 4<sup>th</sup> pulses using [(=N<sup>t</sup>Bu)<sub>2</sub>(NMe<sub>2</sub>)<sub>2</sub>W] and 1,2-ethanedithiol to show periodicity of surface reactions

In the IR spectrum recorded after the 3<sup>rd</sup> pulse (see Figure 3. 10, spectrum 3, green line) that is an addition of BTBMW, one can observe the recovery of all bands that were present after the 1<sup>st</sup> pulse at 2780, 2825, 2867, and 2970 cm<sup>-1</sup> and the disappearance of the surface OH band at 3747 cm<sup>-1</sup>. Some of those bands (e.g. 2780 and 2825 cm<sup>-1</sup>) originating from symmetric C–H stretching modes have shifted to lower frequency vibration for about 7 cm<sup>-1</sup> probably due to the new environment around C–H bonds and longer distance from silica. The band at 2825 cm<sup>-1</sup> may also be contributed from the vibration of the C–H bonds in sulfur-containing moiety (e.g. –CH<sub>2</sub>SH). As in the product

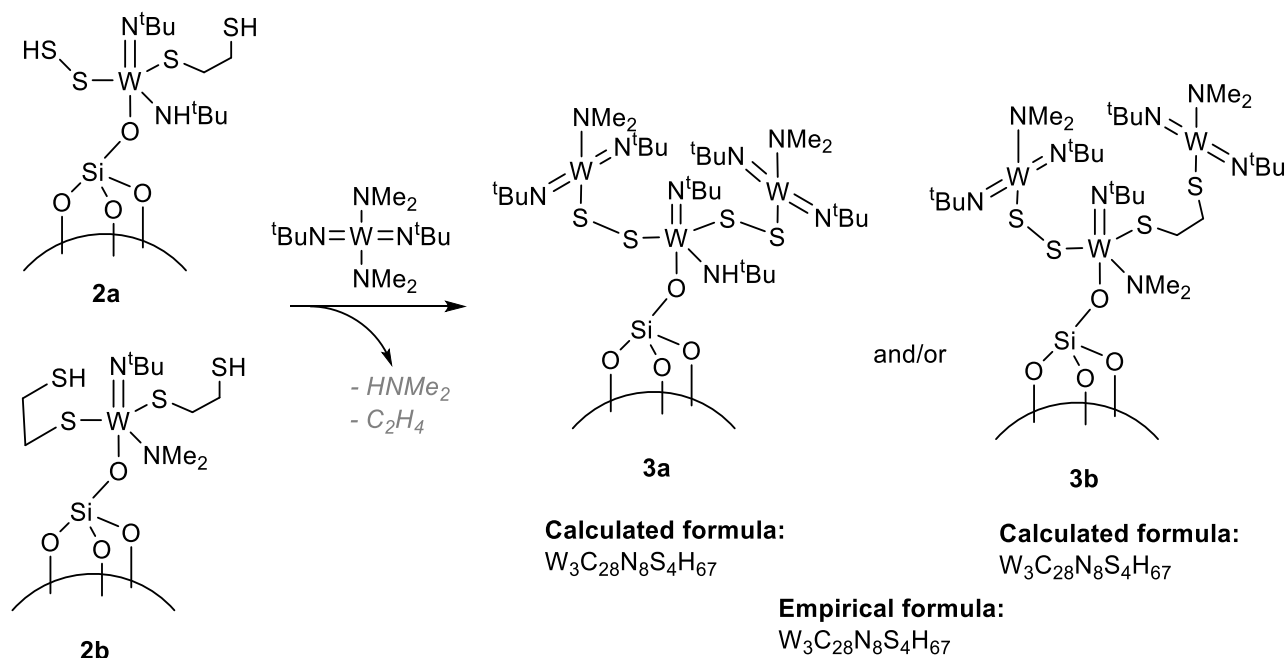
of the 1<sup>st</sup> pulse, band at 2970 and 2867 cm<sup>-1</sup> are respectively assigned to asymmetric and symmetric stretching of the C–H bonds in the *tert*-butyl and/or dimethylamido groups. Another important sign in this spectrum is the disappearance of the broad and weak signal of S–H at 2572 cm<sup>-1</sup>. This suggests the reaction of the thiols with ensuing W complex. Interestingly, the disappearance of the S–H stretching occurred along with shrinking the previously seen wide band between 2500 and 3500 cm<sup>-1</sup>. It supports the proposed hydrogen bonded system involving the thiol group in the 2<sup>nd</sup> pulse product structure.

Analysis of the 3<sup>rd</sup> pulse powder product by Raman spectroscopy (see the spectrum *s3*, green line, in Figure 3. 8B) was similar to the one obtained after the 1<sup>st</sup> pulse though still retaining some peaks associated with the 2<sup>nd</sup> pulse. These data confirm bringing new –NMe<sub>2</sub> and =N<sup>t</sup>Bu groups via observation of stretching and deformation vibrations of NC<sub>2</sub>, CH<sub>3</sub> and CC<sub>3</sub> systems. Besides, the increased intensity of the W–N stretching mode observed at 579 cm<sup>-1</sup> points to the addition of BTBMW. Complete list of the Raman bands and tentative assignment of some of them can be found in the experimental section.

Table 3. 1 contains the weight fractions analyzed after the 3<sup>rd</sup> pulse, using which it was possible to define the ratios S/W, N/W, and C/W as 1.1, 2.3, and 8.7, respectively. Considering that the 2<sup>nd</sup> pulse product bears 4 S atoms per each W and an almost 3-fold increase of the weight fraction of W (from 5.6 to 14.9 wt. %) in the 3<sup>rd</sup> pulse, it was proposed to attach two equivalents of BTBMW to 2 available thiol groups. This brings 3 tungsten atoms per each initial ≡Si–OH group. As the surface reaction of BTBMW with thiol proceeds via elimination of HNMe<sub>2</sub>, 2 equivalents of BTBMW would deliver 6 nitrogen and 20 carbon atoms. The number of added carbon atoms could be balanced to 18 if one takes into account the possible loss of 1 equivalent of ethylene. Based on these suggestions, the product formula was proposed as ≡SiO–W<sub>3</sub>C<sub>28</sub>N<sub>8</sub>S<sub>4</sub>H<sub>67</sub>, which matches the empirically defined formula, ≡SiO–W<sub>3</sub>C<sub>28</sub>N<sub>8</sub>S<sub>4</sub>H<sub>67</sub>. The composition of the product structure from two options in the 2<sup>nd</sup> pulse, 2a and 2b, leads to two different structures, **3a** and **3b**, with the same formulas. The **3a** and **3b** structures are illustrated in Scheme 3. 5.

The solid-state <sup>13</sup>C NMR spectrum (see spectrum 3, the green line in Figure 3. 2) of the solid product of the 3<sup>rd</sup> pulse shows four signals at 32.6, 44.0, 54.5, and 68.6 ppm. Like in the previous two pulses, the *tert*-butyl carbons are present at 32.6 and 68.6 ppm. The signal of the primary carbons shifted back downfield for 2-3 ppm, which signifies about an increased fraction of =N<sup>t</sup>Bu

form. The appearance of the dimethylamido carbons at 54.5 ppm is an indication of mono substitution of BTBMW grafting during the 3<sup>rd</sup> pulse. However, the resonance in the middle with a chemical shift of 44.0 ppm signifies the presence of the methylene moieties of the ethylenedithiolate (–SCH<sub>2</sub>CH<sub>2</sub>SH) ligand. These assignments come in good agreement with the proposed reaction product given in Scheme 3. 5.



Scheme 3. 5. Proposed reaction pathways in the reaction of the 3<sup>rd</sup> pulse

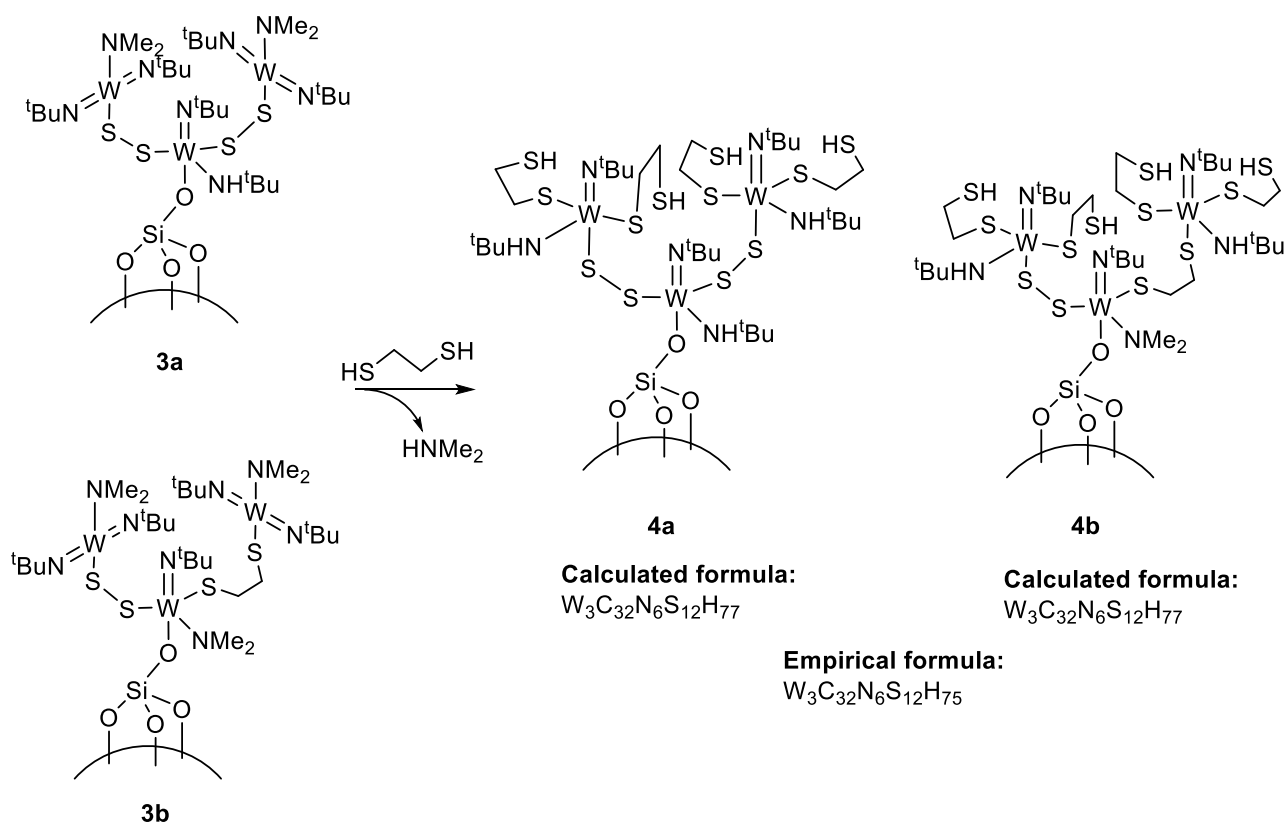
The 4<sup>th</sup> pulse is the second deposition of EDT that was expected to result in a similar reactivity as in the 2<sup>nd</sup> pulse. The DRIFT spectrum (purple spectrum 4) indeed, shows IR absorption bands either at the same wavenumber as of the 2<sup>nd</sup> pulse or with little shifts (2-10 cm<sup>-1</sup>). Four of them were easier to recognize, which are  $\nu_{\text{asym}}(\text{C-H})$  of the *tert*-butyl group at 2971 cm<sup>-1</sup>,  $\nu_{\text{sym}}(\text{C-H})$  of the –CH<sub>2</sub>SH moiety at 2818 and 2759 cm<sup>-1</sup> and  $\nu(\text{S-H})$  vibration at 2569 cm<sup>-1</sup>. Another band at 2911 cm<sup>-1</sup> could be brought by the contribution of  $\nu_{\text{asym}}(\text{C-H})$  in the –CH<sub>2</sub>SH and  $\nu_{\text{sym}}(\text{C-H})$  of the *tert*-butyl group.

After seeing all four DRIFT spectra, one can notice periodicity with each ALD cycle. Each pulse of BTBMW reacts with all surface –SH (and –OH) groups, while each following pulse of EDT brings new –SH groups enabling the next metal pulse. This is one of the features inherent to the chemistry of ALD.

The Raman spectrum (see spectrum 4, purple, in Figure 3. 8B) recorded after the 4<sup>th</sup> pulse, the powder product exhibits similar features as the 2<sup>nd</sup> pulse product. One of the main indications is the formation of the W–S bond that is confirmed by vibration absorbance at 418 and 365 cm<sup>-1</sup>, respectively. However, it was observed that Raman bands, like DRIFT bands, tend to shift with the number of pulses. It can probably be linked to increasing distance from the silica surface with each deposition reaction. All the Raman bands were listed in the experimental section and some of the were tentatively assigned.

The 4<sup>th</sup> pulse was expected to proceed similarly to the 2<sup>nd</sup> pulse path in which the W center was bound to 2 equivalents of EDT. The elemental analysis (see Table 3. 1) led to determine the empirical formula of the 4<sup>th</sup>-pulse product, W<sub>3</sub>C<sub>32</sub>N<sub>6</sub>S<sub>12</sub>H<sub>75</sub>, which shows an increased S/W ratio equal to 4. The deposition of new 4 equivalents of EDT (2 equivalents per each W) satisfies both last indications as well as make the number of carbon atoms to match the empirical number (32). In this case, the binding of ethylenedithiolate ligands was considered to occur at the expense of the elimination of only dimethylamido ligands. Starting from two proposed structures in the 3<sup>rd</sup> pulse, we came up with two new structures, **4a** and **4b**, for the 4<sup>th</sup> pulse products can be proposed (see in Scheme 3. 6). Both structures give the same molecular formula in good agreement with the experimental one.

Solid-state <sup>13</sup>C NMR of the 4<sup>th</sup> pulse product (see spectrum 4, purple line, in Figure 3. 2) repeats the chemical shift changes of the 2<sup>nd</sup> pulse. The disappearance of the dimethylamido carbons (from ca. 54 ppm) implies their elimination in the form of HNMe<sub>2</sub> upon the surface reaction with EDT. The *tert*-butyl groups remain unsubstituted and their primary and tertiary carbons are seen at 30.4 and 69.8 ppm, respectively. Similar to the previous EDT pulse, the primary carbon atoms' signal has again shifted upfield by broadening its peak. It suggests the presence of both =N<sup>t</sup>Bu and –NH<sup>t</sup>Bu ligands. A broad resonance in the middle at 44.0 ppm can originate from the dithiolate-bridging carbon atoms (methylene groups). These assignments agree with proposed structures, 4a and 4b, provided in Scheme 3. 6.



Scheme 3. 6. Proposed reaction pathways in the reaction of the 4th pulse

Summary of SOMC studies carried after each pulse confirms periodical behavior of observed features with each deposition cycle. This is especially noticeable from IR, Raman, and solid-state <sup>13</sup>C NMR spectra. Clear indications were provided for the availability of -SH groups after each sulfur pulse and their consumption with each tungsten pulse. Deposition of BTBMW was always seen by the increase of the =N<sup>t</sup>Bu and -NMe<sub>2</sub> signals, while the EDT pulse resulted in the replacement of -NMe<sub>2</sub> and protonation of =N<sup>t</sup>Bu to turn it to -NH<sup>t</sup>Bu (or even elimination as H<sub>2</sub>N<sup>t</sup>Bu).

### 3.3.4. Study of the annealing step

#### 3.3.4.1. Operando study of thermal decomposition of W thiolates up to 500 °C

Heating of the silica-supported tungsten thiolates after two full ALD cycles (or four single pulses) to 500 °C with 2 °C/min rate under helium flow was monitored with DRIFT and GC-MS. While the

ALD-grown structure can be broken down to blocks upon heating, this study was expected to complement to the understanding of surface sites.

The DRIFT spectrum was recorded at each increase of temperature for 2 °. Evolution of IR absorbance with temperature (see Figure 3. 12) showed that the wide band previously assigned to C–H stretching vibration (3000-2700  $\text{cm}^{-1}$ ) and intramolecular interaction like hydrogen bonding was first shrunk between 110 and 300 °C leaving a sharp band at 2974  $\text{cm}^{-1}$ . This peak was then diminished upon continued heating to 450 °C. Figure 3. 13 shows selected stages of transitions that is a slow decrease of absorption bands ascribed to alkyl C–H stretching starting from 300 °C till 450 °C. Disappearance of the S–H absorption band (2569  $\text{cm}^{-1}$ ) was observed starting from ca. 250 °C. The major organic part of the structure remains stable up to 300 °C. It starts to decompose above this temperature and vanishes around 450 °C. An increase of the surface OH bands at 3747  $\text{cm}^{-1}$  along with the increasing temperature was also seen. Generation of the surface hydroxyl groups can be caused by interactions between thermal decomposition fragments and the silica surface.

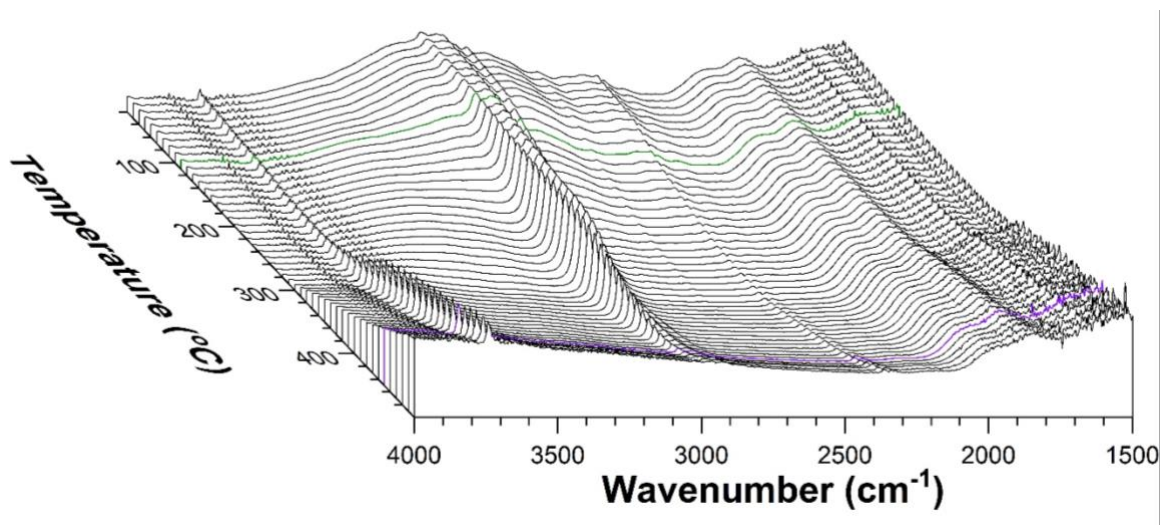


Figure 3. 12. Evolution of DRIFT spectra with heating the ALD-grown W thiolates

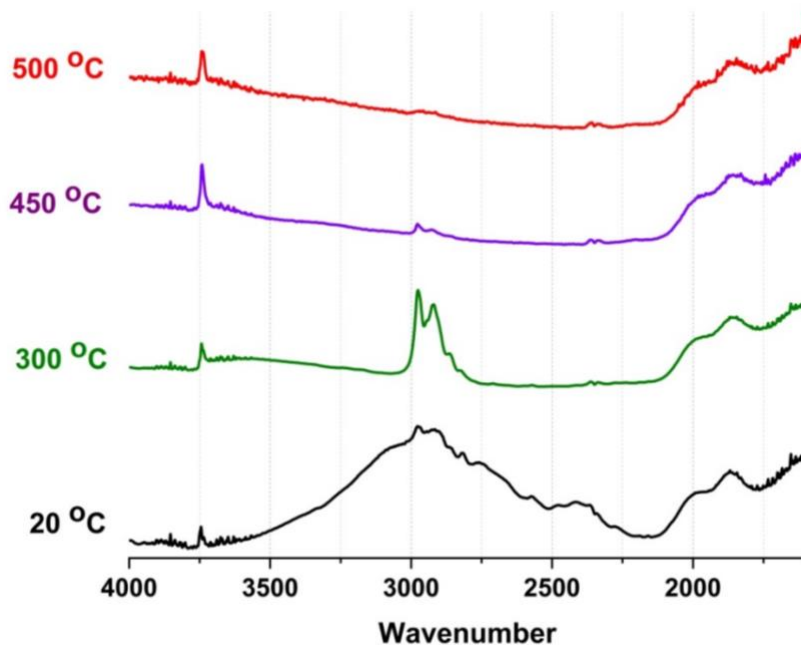


Figure 3. 13. IR spectra recorded during thermal decomposition of the 4th pulse product on SiO<sub>2</sub>-700

Volatile molecular fractions released upon the thermal decomposition were also analyzed by injecting the headspace above powder into a GC-MS spectrometer (see Figure 3. 14). Being based on the proposed structures in Scheme 3. 6, it was expected to observe ethylene, isobutene or *tert*-butylamine, and various modifications of ethylenedithiolate. Indeed, ethylene was observed at 1.9 minutes starting from about 200 °C and until 475 °C. At 6.1 minutes of retention time and between 250 and 475 °C, we can observe a large amount of isobutene. Isobutene originates from the decomposition of  $\text{-NH}^t\text{Bu}$  and  $\text{=N}^t\text{Bu}$  ligands<sup>172</sup> and seems to play significant role of the loss of absorbance at  $2974\text{ cm}^{-1}$  between 300 and 450 °C (Figure 3. 12). Ethanethiol ( $\text{C}_2\text{H}_5\text{SH}$ ) was detected at about 7.4 minutes that is ascribed to cleavage of the C–S bond in the ethylenedithiolate ligand. A minor peak at 6.8 minutes was assigned to methylisocyanide ( $\text{CH}_3\text{-N}\equiv\text{C}$ ) that was produced starting from 300 °C. Formation of methylisocyanide can be considered to occur via  $\beta$ -H subtraction from dimethylamido ligand and the W–N bond cleavage as reported for other supported transition metal alkylamido complexes.<sup>145,173</sup> However, the decomposition of *tert*-butyl group towards the formation of  $\text{CH}_3\text{-N}\equiv\text{C}$  can not be excluded too. Above 225 °C, we start to observe the formation of thiophene ( $\text{C}_4\text{H}_6\text{S}$ ) at 9.9 minutes. Thiophene, as well as other cyclic sulfur-containing byproducts (thiirane at 7.8 minutes between 125 and 250 °C, 2-methyl-1,3-dithiolane at 8 minutes above 400 °C), may originate from base-catalyzed thiol-ene reactions involving thiol and ethylene.<sup>174,175</sup> Among all

mentioned volatile products detected in GC-MS, ethylene, isobutene, ethanethiol, methylisocyanide, and thiirane correspond to building blocks of the proposed structures. Whereas, other volatiles (thiophene, and 2-methyl-1,3-dithiolane) could be produced upon further reactions between the decomposition fragments.

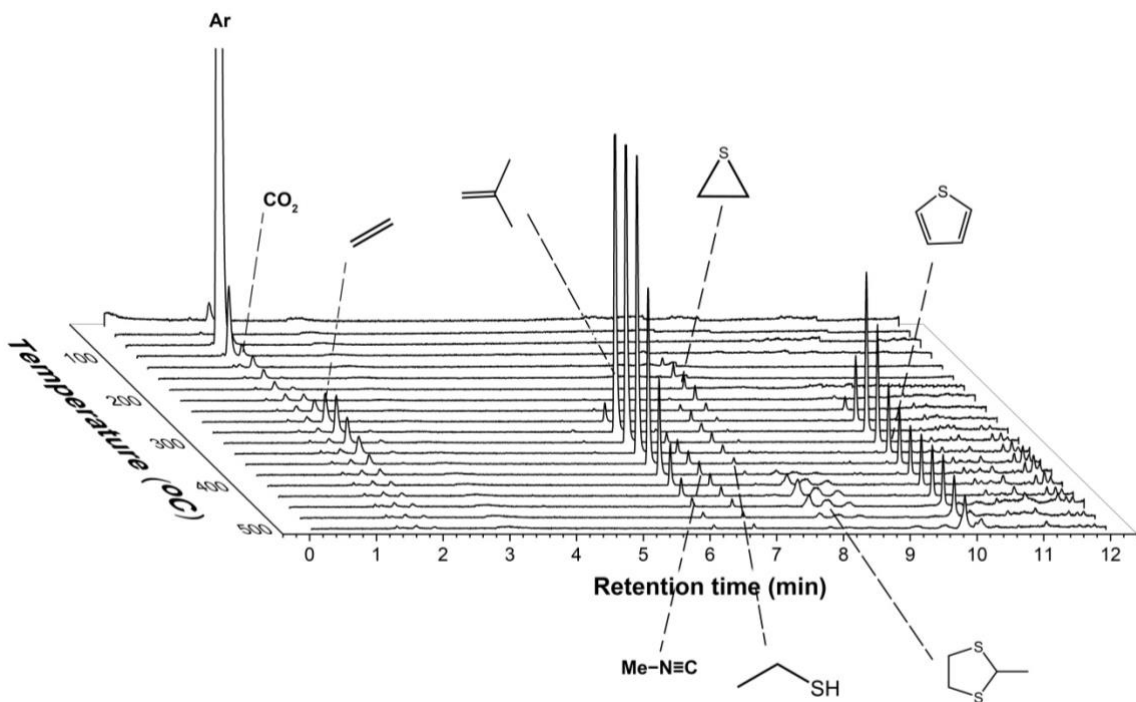


Figure 3. 14. GC-MS spectra of volatile products of the thermal decomposition of the 4th pulse product on SiO<sub>2-700</sub>

This experiment is limited to 500 °C, so no higher temperature was investigated. It, nevertheless, allowed us to observe that mineralization process occurs around 300 °C.

#### 3.3.4.2. *Ex-situ annealing in argon flow at 800 °C*

Since WS<sub>2</sub> becomes thermodynamically the most stable form among its sulfides starting from 800 °C (see the phase diagram in Chapter 1), it was decided to perform annealing at this temperature. The brown powder of the 4<sup>th</sup> pulse product turned black after the annealing in a quartz tube under argon flow. Elemental analysis of the annealed powder reveals the S/W atomic ratio to be equal to 2.2. The analysis also showed significant removal of the carbon content from 7.25 to 1.22 wt. % presence. Perhaps, complete removal of carbon may be achieved with a longer time of annealing.

The STEM and HRTEM images (see Figure 3. 15) of the powder annealed in argon flow at 800 °C reveal layered patterns that exhibit the homogenous distance between lines. On the images of a 10-nm scale (figures A and B), the layers curve around silica nanobeads' surface. It coincides with expected deposition on the outer surface because the silica substrate was non-porous. Besides, the STEM image displays small bright particles located out of silica. It may originate from the tungsten-rich phase that can not be elucidated at this moment, and requires more detailed characterization. Most of the layered patterns were composed of two layers. The average distance between layers was defined as 0.66 nm (see Figure 3. 15C), which is in very good agreement with computationally calculated distances between two layers in bilayer WS<sub>2</sub>.<sup>147</sup> According to the conclusion of the authors, the best results were provided by random phase approximation (RPA) calculation method and yielded 6.84, 6.24, 6.78, 6.24, 6.27 Å for various stacking modes of 2H and 3R crystal phases. Our value, 0.66 nm, lies between those results. Probably, the crystal phase produced upon annealing of our samples is a combination of both phases. Besides the worm-like curved shapes, there are observed well-ordered crystalline nanoparticles (see Figure 3. 15D). This kind of particle yields a fast Fourier transform (FFT) pattern of the single-cell parameters such as angles and distances between crystal planes that confirmed the crystal structure of WS<sub>2</sub> in a trigonal (2H) phase. The empirical and theoretical values are given in Table 3. 2. The theoretical parameters were calculated from the Joint Committee on Powder Diffraction Standards (JCPDS) file of WS<sub>2</sub> in a 2H (hexagonal) phase and P63/mmc (194) space group using CarIN Crystallography software.

Raman spectrum of the argon-annealed solid showed two strong bands at 351 and 414 cm<sup>-1</sup> (see spectrum 5, orange line, in Figure 3. 8B). They can be assigned to the first-order in-plane and out-of-plane optical phonon modes, E<sup>1</sup><sub>2g</sub> (Γ) and A<sub>1g</sub> (Γ), of WS<sub>2</sub>, respectively.<sup>176,177</sup> The in-plane phonon mode, E<sup>1</sup><sub>2g</sub> (Γ), in single-layer WS<sub>2</sub> is expected to display a shoulder originating from the doubled longitudinal acoustic second-order mode labeled as 2 LA(M).<sup>176</sup> Indeed, the E<sup>1</sup><sub>2g</sub> (Γ) band in our spectrum shows a small shoulder at 332 cm<sup>-1</sup> that may correspond to the mentioned second-order mode (2 LA(M)). Nevertheless, this is not yet solid proof for the formation of monolayer WS<sub>2</sub> film. Considering, the low surface density of the silanol groups of dehydroxylated silica before starting ALD (ca. 0.8 OH/nm<sup>2</sup>)<sup>18,178</sup>, a 3-fold increase of tungsten loading upon the 2<sup>nd</sup> ALD cycle and electron micrographs of non-uniformly coated silica suggest more complex crystallization and coalescence process than expected.

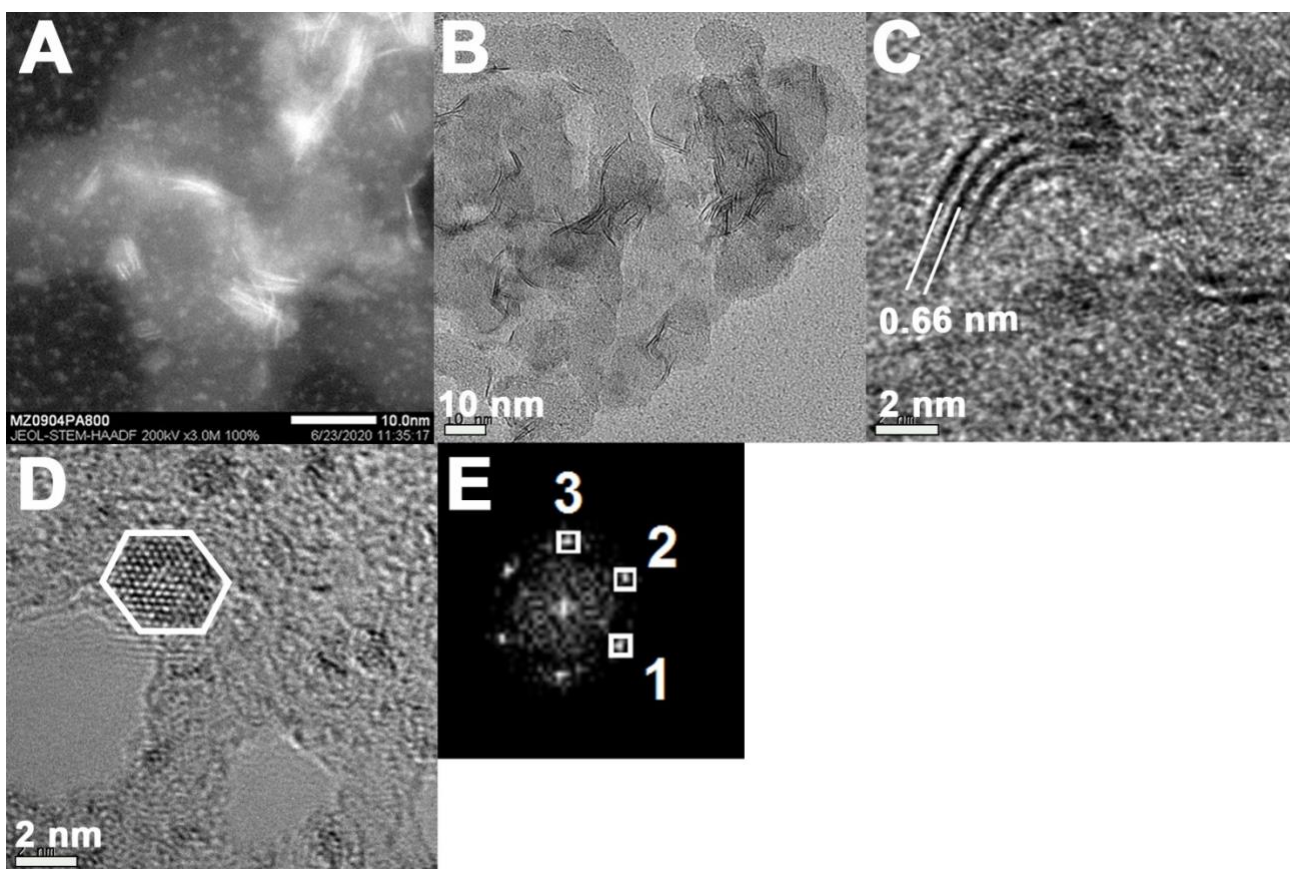


Figure 3. 15. STEM (A) and HRTEM (B-D) images of the 4th pulse product after annealing at 800 °C in Ar flow. FFT pattern (E) acquired from the crystalline nanoparticle in image D.

Table 3. 2. Comparison of distances and angles between planes acquired from the FFT patterns with corresponding cell parameters calculated from the JCPDS file of 2H WS<sub>2</sub> phase (P63/mmc space group) by CarIN Crystallography software.

	Plane	(h, k, l)	Empirical d-spacings, nm	Calculated d-spacings, nm	Empirical angles, °	Calculated angles, °
Annealed at 800 °C in Ar	1	(-1,1,1)	0.250	0.267	0	0
	2	(0,1,2)	0.245	0.249	58.6	57.7
	3	(1,0,1)	0.257	0.267	117.5	115.5
Annealed at 450 °C in Ar/H <sub>2</sub>	1	(-1,1,1)	0.255	0.267	0	0
	2	(0,1,2)	0.251	0.249	59.1	57.7
	3	(1,0,1)	0.264	0.267	118.8	115.5

### 3.3.4.3. *Ex-situ annealing in hydrogen flow at 450 °C*

Another annealing approach was to heat the powder of the 4<sup>th</sup> pulse product at 450 °C under the flow of argon/hydrogen mixture. The presence of H<sub>2</sub> was shown to facilitate the removal of organic moieties and crystallization of MoS<sub>2</sub>.<sup>19</sup> The brown powder was also turned to black after the annealing. Elemental analysis of the black powder revealed the sulfur to tungsten ratio at about 2.1 pointing to an expected stoichiometry of tungsten disulfide. The presence of hydrogen was shown to be more effective in the removal of carbon. It decreased carbon content from 7.25 (before annealing) to 0.70 wt.%, while argon annealing had calcined 1.22 wt.% of C. The STEM and HRTEM images (Figure 3. 16) show layered patterns having a homogeneous distance distribution between lines. The STEM image also displays bright particles in the area out of silica. As it was suggested for the argon-annealed sample, these particles may be composed of a tungsten-rich phase.

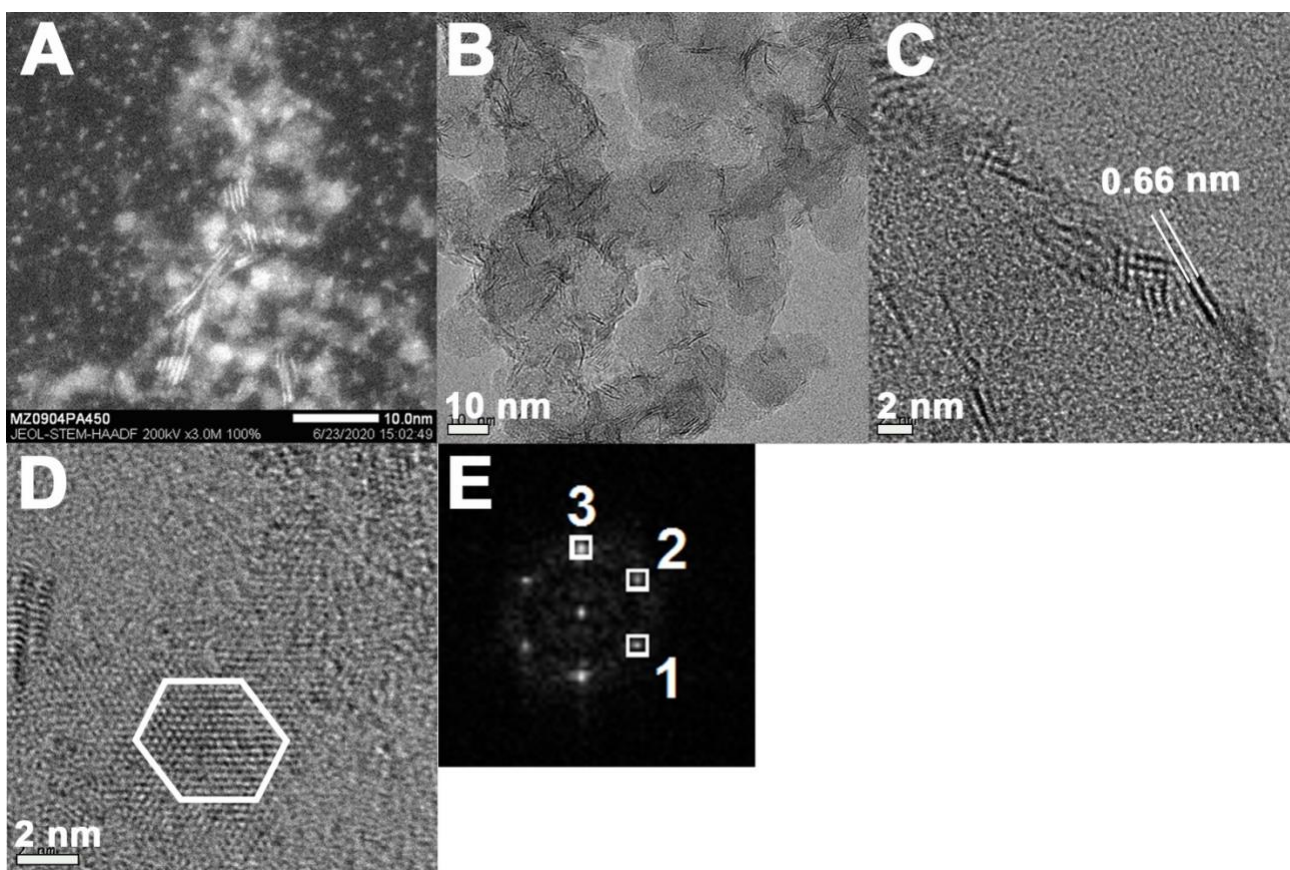


Figure 3. 16. STEM (A) and HRTEM (B-D) images of the 4th pulse product after annealing at 450 °C in Ar/H<sub>2</sub> flow. FFT pattern (E) acquired from the crystalline nanoparticle in image D

The TEM image of the 10-nm scale (Figure 3. 16B) shows that most of the layers curve around silica nanobeads' surface and they are composed of two layers. From the zoomed-in image at a 2-nm scale (Figure 3. 16C), the average distance between layers was found as 0.66 nm, which matches well with the acquired distance in the samples annealed at 800 °C. Apart from the worm-like layers, there were observed well-ordered nanocrystalline particles. FFT of such particles (see Figure 3. 16E) allowed us to estimate cell parameters that suggest the crystal to be 2H phase of WS<sub>2</sub>. The empirical values of d-spacing and angles between planes come in good agreement with the calculated ones (see Table 3. 2).

### 3.4 CONCLUSION

The ensemble of molecular and silica-based modeling reactions performed and the connected multi-technique analyses described in the chapter start to give a coherent picture of the probable surface reactions of the first 4 ALD pulses as illustrated in Scheme 3. 3-Scheme 3. 6. Each sulfur pulse substitutes alkylamido groups and leaves a functional group ( $-SH$ ) for grafting of tungsten complex in the next ALD cycle. Both annealing methods were shown to yield  $WS_2$  crystals in the hexagonal crystal phase (2H).

# Chapter 4 - **WS<sub>2</sub> GROWTH by ALD** **ON SILICON WAFERS**

## 4.1 INTRODUCTION

### 4.1.1. Silicon wafers as ALD substrate. What do we know of their ultimate surface?

To what extent our ALD-process proposal, mostly deduced from solution molecular chemistry and surface chemistry on high surface area silica powder, can be translated to self-standing 2D-supports? To answer this question, we selected silicon wafers as the appropriate 2D support to make the powder-to-self-standing structure transition, silanol-terminated silica at the solid-gas interphase being the connecting link, as discussed in Chapter 1 - .

A silicon wafer can be considered the archetypical 2D support, given its dominance in microelectronics. Silicon wafers (most commonly now p- or n-doped) are the most largely used support in micro-electro-mechanical systems (MEMS) as well as nano electric mechanical systems (NEMS), due in part to their semiconducting nature, the possibility to finely tune their resistivity, their large and cheap availability, inertness under normal conditions, mechanical stability and compatibility with the wide industrial process leading to functional devices.<sup>179,180</sup>

When exposed to air, the wafer grows a protective oxide layer, called native oxide. This native oxide layer, generally 1-2 nm thick, is usually noted as  $\text{SiO}_x/\text{Si}$ .  $\text{SiO}_x$  can be summarily described as non-stoichiometric silicon sub-oxides displaying mostly inert surface Si-O-Si and reactive Si-OH bonds on their ultimate surface. This hydrophilic top layer attracts further physisorbed water layers.<sup>181</sup>

Generally, three other ultimate surface surfaces can be conditioned before further processing:

- i) thermally grown oxide, generally from better controlled and more extensive reaction of the silicon layer with oxygen and water, and generally described as stoichiometric silica  $\text{SiO}_2@\text{Si}$  (v. infra),
- ii) hydrogen saturated silicon surfaces (which generally confer hydrophobic property to the wafer and are obtained by HF etching of the ‘native oxide top layer) noted Si/H. These Si-F and Si-H terminated surfaces slowly grow ( $<7 \text{ \AA} \cdot \text{week}^{-1}$ ) a thin sub-stoichiometric  $\text{SiO}_x$  layer in the air.<sup>182,183</sup>
- iii) only under UHV condition clean silicon surfaces, Si.<sup>184</sup>

Among all these options, silicon dioxide is the most common top layer in the field of silicon-based device fabrication.<sup>185</sup> While a basic 2-dimensional method of such silicon oxide layer exists, and the

presence of non-bridging oxygen (presumably there included surface silanols) is mentioned,<sup>185</sup> no particular mention of these reactive sites is generally made on work focusing on the wafer only.

The presence of the surface reactive sites comes specifically to the forefront when the oxide layer becomes the starting substrate for the growth of further functional layers. When the film growth technique is ALD on SiO<sub>2</sub>/Si, the presence of surface hydroxyl as the reactive sites is well established<sup>186</sup> and in some case specifically characterized, in particular when the attention is brought to the first cycles and how the growth begins on the substrate<sup>79,97,187</sup>

As discussed in the chapter 1, substantial evidence shows that nature and concentration of surface hydroxyls of SiO<sub>2</sub>/Si of planar wafers and surface hydroxylated porous silica are very similar in nature and in surface concentrations nature and concentration of surface hydroxyls in planar wafers of well-defined silicon oxide and porous silica.<sup>105</sup>

With this firm literature evidence on the chemical nature of silicon wafers, we now embark on testing if we can successfully transfer WS<sub>2</sub> thin film growth from the evidence we have acquired in the non-porous silica-based work.

The thesis has tested two substrates so far HDMDW and BTBMW. Since we showed that HDMDW does not readily reacts with SiO–H in the gas phase (see chapter 2), we have chosen BTBMW, described in chapter 3, as a tungsten source.

## 4.2 EXPERIMENTAL PART

### 4.2.1. XPS studies

#### 4.2.1.1. Preparation of the samples:

**Preparation of silicon wafer:** Circular Si wafers ( $\phi = 1$  inch, thickness = 300  $\mu\text{m}$ ) with 270-280 nm  $\text{SiO}_2$  coating (thermally oxidized) were ordered from *Neyco.s.a. Vacuum & Materials*. A wafer was split into smaller pieces of the nearly same area (about  $5 \times 5$  mm). The wafer pieces were calcined at 800 °C for 4 hours in the air, immersed into water for 48 hours, and then dehydroxylated at 200 °C for 30 minutes in a dynamic ultra-high vacuum (UHV) ( $10^{-5}$  mbar). One of them was stored in the glovebox and later measured by XPS as a blank sample. Further manipulation and characterization of the dehydroxylated wafers were performed either in a vacuum or argon atmosphere.

**In situ XPS study of sequentially the prepared tungsten thiolates on silicon wafers:** Two full ALD cycles of  $\text{WS}_2$  onto the wafers were carried using BTBMW as a tungsten source and EDT as a sulfur source. After each half-cycle, a piece of the wafer was separated and stored in the glovebox for later characterization. After degassing W and S precursors, five Si wafers were loaded into the main tube of the glass ALD reactor in the glove box. The first pulse of W was carried out by opening the W complex containing bulb for 30 minutes while the whole reactor was placed in the oven at 80 °C. The W pulse was followed by an evacuation step at 80 °C under a dynamic UHV. The second half-cycle, that is the S pulse, was performed by opening the EDT-containing bulb for 15 minutes while only the tubular part of the reactor was placed into the tubular oven preheated at 80 °C. The sulfur pulse was followed by the same evacuation. Two more ALD pulses have been repeated in the same manner. Pieces of the wafer were displaced from the reactor one by one after each pulse (4 wafer pieces after 4 pulses) and stored in the glovebox. Up to here, the experiment can be considered *in situ* since each step is sequentially applied to the very sample wafer and no exposure to air or water is experienced by the samples at any moment. The instrument and sample loading procedure were described in the experimental section of previous chapter. The energy scale was calibrated using the Si 2p binding energy located at 103.5 eV.

**Ex-situ annealing of the wafer-bound tungsten thiolates after the in situ experiments:** the last piece of the wafer described above was introduced under air in a tubular glass reactor prefilled with argon and annealed in argon flow (60 sccm) at 800 °C. After cooling back to room temperature, the wafer was transferred under short exposure to air to an argon-filled glove box, since no airtight transfer box was available between the annealing apparatus and the glove box.

**Operando annealing inside the XPS spectrometer:** For the *operando* annealing study, 2 full ALD cycles were performed on a wafer. The wafer was introduced in the XPS chamber with no air

exposure and its stepwise thermal treatment, from RT to the annealing final temperature of 500°C, was carried inside the spectrometer's chamber under dynamic UHV ( $10^{-9}$ - $10^{-8}$  mbar).

#### 4.2.1.2. XPS spectra

***In situ XPS study: survey scan spectra*** were first recorded in the range of 0 to 1100 eV on the SiO<sub>2</sub>/Si wafers (see Figure 4. 1) before ALD (black spectrum 0), after ALD pulses using BTBMW (1<sup>st</sup> and 3<sup>rd</sup> red and green spectra, respectively), and EDT (2<sup>nd</sup> and 4<sup>th</sup> blue and purple spectra, respectively), and after annealing (orange spectrum 5). All the XPS spectra were calibrated to a well observable signal of Si 2p level to 103.5 eV. The survey spectra show bands assigned to Si, O, and C atoms in the samples before as well as after the deposition pulses. The precise assignments will be discussed in the high-resolution spectra paragraphs below as well as in the discussion section.

***Survey scan of the pristine support:*** C 1s (280-290 eV), Si 2s (150-155 eV), 2p (100-105 eV), O 1s (530-535 eV), 2s (20-25 eV).

***Survey scan of the 1<sup>st</sup> pulse:*** W 4f (30-40 eV), 5s (75-80 eV), 4d (245-250), 4p (420-500 eV), 4s (595-600 eV), N 1s (395-405 eV), C 1s (280-290 eV), Si 2s (150-155 eV), 2p (100-105 eV), O 1s (530-535 eV), 2s (20-25 eV).

***Survey scan of 2<sup>nd</sup> pulse (first pulse of EDT):*** S 2s (222-227 eV), 2p (159-164 eV), W 4f (30-40 eV), 5s (75-80 eV), 4d (245-250), 4p (420-500 eV), 4s (595-600 eV), N 1s (395-405 eV), C 1s (280-290 eV), Si 2s (150-155 eV), 2p (100-105 eV), O 1s (530-535 eV), 2s (20-25 eV).

The third and fourth pulses have shown similar survey spectra as the second pulse. This is expected since neither loss nor addition of elements was expected upon deposition of BTBMW and EDT in the second ALD cycle.

***In situ study: high-resolution spectra*** at the W 4f, N 1s, S 2p, Si 2p, C 1s, and O 1s levels were recorded at each step within 2 full ALD cycles (see a synoptic view in Figure 4. 6). The high-resolution XPS spectra were then fitted and quantified after deconvolution for each step (see Figure 4. 7 - Figure 4. 11).

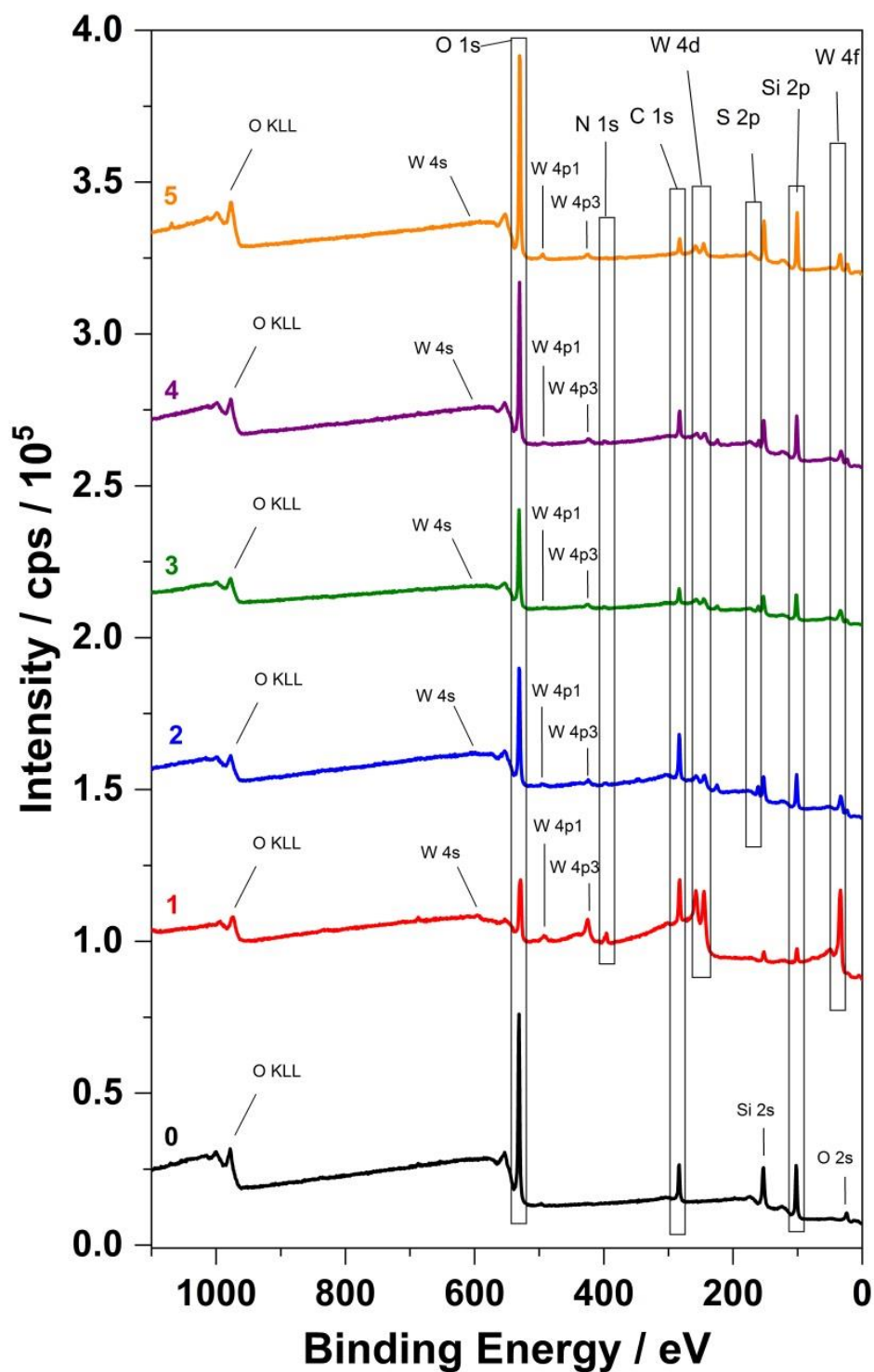


Figure 4. 1. Survey spectra of the *in situ* XPS study (spectra 0-4) and ex-situ annealing (spectrum 5). Spectra recorded before ALD (black spectrum 0), after the first pulse of BTBMW (red spectrum 1), the first pulse of EDT (blue spectrum 2), the second pulse of BTBMW (green spectrum 3), the second pulse of EDT (purple spectrum 4) and after annealing at 800 °C in argon flow (orange spectrum 5)

**High-resolution scan of pristine support:** Figure 4. 6 (gray spectra 0) collects the high-resolution XPS spectra of the starting blank support. The Si 2p BE (103.5 eV) corresponds to the silicon in its oxide form. This was confirmed by fitting the peaks in Figure 4. 7 that also defined a very minor shoulder at 101.44 eV attributed to silicon suboxide and subnitride ( $\text{SiO}_x$ ,  $\text{SiN}_x$ ) supporting the N 1s assignment. N-containing impurities were detected with a very weak peak in the N 1s range at 399.85 eV. Its fitting identified impurities in the  $\text{CN}_x$  and  $\text{SiN}_x$  forms. Carbon was seen at 284.8 eV that can originate from traces of organic impurities on the surface. Deconvoluted peaks of carbon were fitted to C–C, C–O, and C=O bonds composing the contamination (blue spectra). Most of these organics (89.3 at%) contained C–C bonds that may signify the presence of grease or other organic impurities. As expected, the blank wafer (black spectra 0 in Figure 4. 6) showed the presence of neither tungsten nor sulfur.

**High-resolution scan of the 1st pulse:** Figure 4. 6 (red spectra) collects the high-resolution XPS spectra of the wafer after the first pulse of BTBMW. The major component of the W 4f spectrum is a doublet (due to the spin-orbit ( $4f_{7/2}$ ,  $4f_{5/2}$ ) coupling of electrons. The third component at higher BE (40.9 eV) is assigned to the W 5p level.<sup>188</sup> Fitting in Figure 4. 8 reveals only one form of tungsten with its  $4f_{7/2}$  at 35.32 eV. The deconvolution of the N 1s peaks displayed three contributions at 397.97, 399.7, and 401.23 eV. The Si 2p forms a small new peak at 98.7 eV apart from the previously observed signal at 103.7 eV. The deconvolution of the Si 2p peaks has revealed three peaks at 103.66, 101.65, and 98.69 eV, where the middle peak shows a negligible fraction though. The O 1s peak was deconvoluted to two peaks (530.83 and 532.88 eV).

**High-resolution scan of the 2nd pulse:** High-resolution spectrum of the W 4f core-level shows a slight shift towards lower BE (see blue spectra 2 in Figure 4. 6). Fittings estimated the W  $4f_{7/2}$  at 2 positions at 34.96 and 33.06 eV (Figure 4. 9). The narrow scan XPS spectra found the S 2p signal as a doublet peak at 161.7 and 163.3 eV corresponding to its 3/2 and 1/2 spin-orbit components.<sup>188</sup> Apart from the two states, the third peak of sulfur was attributed to the higher oxidate state  $\text{SO}_x$ . The latter might originate from the reaction of EDT with the surface impurities and its low fraction supports this hypothesis. The maxima of N 1s core level is found at 397.8 and 401.7 eV, whereas the latter has shifted for 1.5 eV in comparison with the shoulder of the 1<sup>st</sup> half-cycle. The Si 2p orbital retained the high BE peaks (103.52 and 101.74 eV) and lost the low BE signal (at 98.69 eV). The high-resolution spectrum of the O 1s level showed a shortening of the peak's width and its fitting identified a significant decrease of the fraction of the peak at 530.84 eV.

**High-resolution scan of the 3rd pulse:** The second deposition of BTBMW records the W 4f doublet at 33.0 and 35.2 eV (positions of W  $4f_{7/2}$  peak), S 2p at 161.7 and 163.1 eV (positions of S  $2p_{3/2}$  peak), and N 1s at 397.8 and 401.7 eV (see green spectra 3 in Figure 4. 6). Deconvolution of the S 2p peaks reveals two doublets with their  $2p_{3/2}$  positions at 161.66 and 163.06 eV indicating the

$-S^-$  and  $-SH / S_2^{2-}$  forms of the sulfur, respectively (see Figure 4. 10). The N 1s, W 4f Si 2p, C 1s and O 1s core-levels retained the main BEs same as in the previous pulse (including their deconvolution).

***High-resolution scan of the 4th pulse:*** No significant modifications were observed for the above-mentioned core levels of all the six elements with respect to the previous pulse (see purple spectra 4 in Figure 4. 6).

***XPS study of ex-situ annealed sample:*** The annealed sample showed coverage with  $WO_3$  (W 4f peak) and absence of the S 2p and N peaks. This was an indication of the oxidation of the top layer. Therefore, the annealed wafer surface was etched by high-energy  $Ar^+$  for 6, 9, and 12 minutes. Monitoring it by XPS revealed the presence of peaks of not only W 4f with lower BE (34.8 eV) but also N 1s and S 2p (orange spectra 5 in Figure 4. 6), thus, the depth was analyzed by etching by  $Ar^+$  ions for 12 minutes.

**Survey spectrum after ex-situ annealing and etching:** S 2p (159-164 eV), W 4f (30-40 eV), 5s (75-80 eV), 4d (245-250), 4p (420-500 eV), 4s (595-600 eV), C 1s (280-290 eV), Si 2s (150-155 eV), 2p (100-105 eV), O 1s (530-535 eV), 2s (20-25 eV).

***High-resolution scan of the ex-situ annealed and etched sample:*** Orange plots 5 in Figure 4. 6 demonstrate high-resolution spectra of the annealed and etched sample. Deconvolution of the new W 4f peak revealed a merge of three doublets with the  $4f_{7/2}$  positions at 35.68, 33.63, and 32.28 eV (Figure 4. 12). The N 1s peak that was not observed immediately after annealing appeared in a high-resolution spectrum after etching the top layer. The high-resolution spectrum of the S 2p displayed a small peak at about 163.0 eV with  $2p_{3/2}$  positions at 161.72 and 162.64 eV. The main peaks of the Si 2p, C 1s, and O 1s retained their positions on the BE axis though the carbon fraction decreased significantly. The C 1s peak was present after annealing though its intensity was significantly lowered in respect to other peaks (e.g. to Si 2p peak).

**XPS study of operando annealing:**

Figure 4. 2 shows the survey spectra recorded between 0 and 1100 eV before and after *operando* annealing. A substantial decrease of the C 1s peak intensity and of the half intensity of the O 1s peak can be seen after the *in situ* annealing.

**Survey spectrum after operando annealing:** S 2p (160-164 eV), W 4f (30-40 eV), 5s (75-80 eV), 4d (242-250), 4s (593-598 eV), C 1s (280-290 eV), Si 2s (150-155 eV), 2p (100-105 eV), O 1s (530-535 eV), 2s (20-25 eV). Mo 3d (220-235 eV), 3s (505-510 eV), 3p (d, 390-415 eV), Cu 3p (73-78 eV), 2p (d, 930-955 eV).

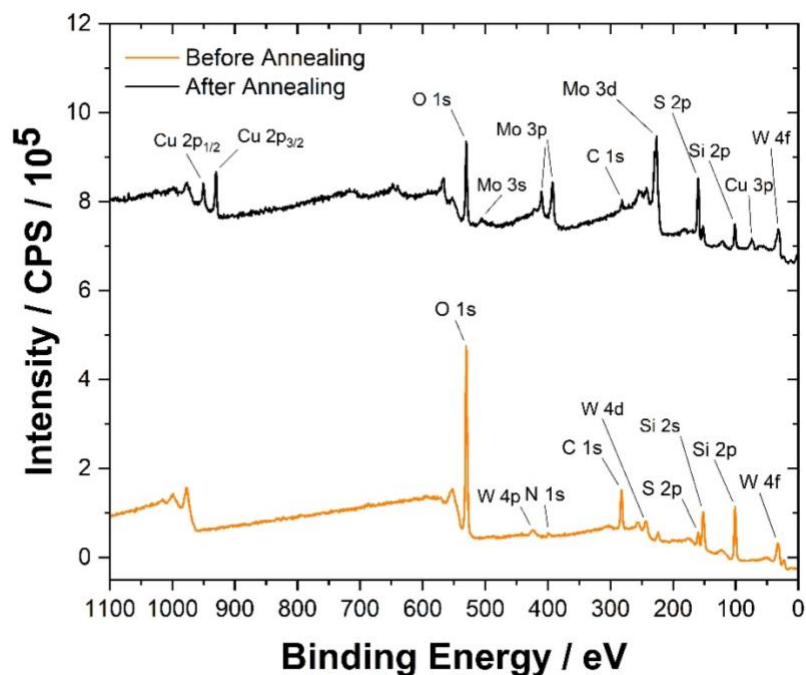


Figure 4. 2. Survey XPS analysis of the wafer after 4 ALD pulses before and after *in situ* annealing to 500 °C

The spectrum after annealing (black line) displays the appearance of Mo and Cu. Since neither wafer nor ALD precursors contained Mo or Cu compounds, they were considered as impurities that could originate from the outside. The sample holder contained Cu, whereas the metallic ring around the holder contained Mo. At as high temperature as 500 °C and dynamic UHV, released decomposition products from the sample (excess sulfur, ethylene, isobutene, etc.) could produce more volatile impurities rather than pure metals. The hypothesis of a possible reaction between copper and elemental sulfur finds support in the literature.<sup>189,190</sup> The sublimation of metal sulfides including cuprous and molybdenum sulfides is also possible in our experiment according to the doctoral dissertation work carried by C.-M. Hsiao.<sup>191</sup>

## 4.2.2. Environmental TEM studies

### 4.2.2.1. Sample holder

A special holder made of polyether ether ketone (PEEK) was designed for holding Cu grids during dehydroxylation in a dynamic UHV, ALD pulses as well as evacuation steps. The PEEK is a robust thermoplastic polymer having a melting point of 343 °C and compatible with ultra-high vacuum applications. The holder was composed of two parts whereas the thickness of each part is 5 mm. The bottom part has 6 circular recesses with a diameter of 3.2 mm (the grid's diameter = 3 mm), where the Cu grid was placed with a silica suboxide layer looking up. The upper part of the holder has six

holes across whole thickness with a diameter of 2.8 mm, so that the grids cannot be lost from the holes when the upper and bottom parts are put together by screwing in two corners. The position of the holes and recesses match with each other which allows interaction between the grid surface and the precursor vapors.

#### 4.2.2.2. Preparation of Mo thiolates-coated TEM grid

TEM grids (200 mesh Cu) with silicon oxide ( $\text{SiO}_x$ ) layer purchased from *SPI Supplies*® were placed in the holder, which then was placed in the tubular reactor for dehydroxylation at 200 °C (heating ramp = 10 °/min) for 30 minutes in a dynamic UHV ( $10^{-5}$  mbar). After dehydroxylation, two grids were placed into the above-mentioned holder with the silica coating layer facing up (to the hole) inside the glove box. First, three ALD cycles of Mo thiolates growth was carried by a method adapted from S. Cadot *et al.*<sup>19</sup> using  $\text{Mo}(\text{NMe}_2)_4$  and EDT at 50 °C in the glass ALD reactor (see Figure 3.1 in Chapter 3). Each ALD cycle consisted of the Mo and EDT pulses and each of the pulses was followed by an evacuation step. First, the reactor was evacuated down to UHV (static  $10^{-5}$  mbar), placed in an oven preheated to 50 °C and the valve of the Mo precursor was opened for 30 minutes. After the Mo pulse, the valve was closed, evacuation at RT and dynamic UHV was carried for 20 minutes. EDT pulse was started at a static UHV by opening the corresponding valve in the oven and lasted for 15 minutes. The evacuation of the reactor was carried for 30 minutes at RT under a dynamic vacuum. This ALD cycle was repeated three times, and one of the grids was recovered inside the glovebox. Second grid remained in the holder for three more ALD cycles to complete six cycles in total. The grid coated with 6 cycles was annealed *in situ* and monitored by environmental (HR)TEM (E-TEM) in hydrogen pressure (2 mbar). The second grid with 3 ALD cycles was annealed *in situ* in E-TEM in argon pressure (2 mbar).

#### 4.2.2.3. Preparation of W thiolates-coated TEM grid:

3 and 5 full ALD cycles were performed on the grids in the same way as on the Si wafers (though one more cycle was added). The grid coated with 5 cycles was analyzed by HRTEM and EDX at RT and UHV ( $10^{-6}$  mbar). Another grid with 5 cycles of W thiolates was annealed ex-situ in argon flow (60 sccm) at 800 °C for 40 minutes and analyzed by HRTEM and EDX. One of the grids with 3 cycles of W thiolates was annealed *in situ* and monitored E-TEM in dynamic UHV. The temperature was raised stepwise from 50 to 800 °C by an increment of 50 °C. TEM images were recorded at each step.

#### 4.2.2.4. Microscope:

The annular dark-field TEM measurements were performed with an FEI Titan E-TEM G2 electron microscope equipped with an imaging aberration corrector and an energy-dispersive X-ray (EDX) analyzer (SDD X-Max 80 mm<sup>2</sup> from Oxford Instruments™). The e-TEM experiments took place in

the Research Institute of Catalysis and Environment of Lyon (IRCELYON and were performed by Dr. Mimoun Aouine. A Gatan™ furnace-type holder allowed direct observation of the transformations (from thiolates to sulfides) at elevated temperature and controlled atmosphere (H<sub>2</sub>, Ar, vacuum). The holder could be tilted in two axes for changing an incident beam angle to the sample.

#### 4.2.2.5. EDX results collected after *in situ* annealing

EDX analysis was carried on a different grid holder specially designed for plane rotation possibility. Therefore, the annealed sample was recovered from the first holder and placed on the second in the air.

EDX data recorded after annealing in argon for the sample of Mo thiolates grown by 3 ALD cycles are collected in Table 4. 1, while for the sample of W thiolates annealed in UHV, EDX data are collected in Table 4. 2.

Table 4. 1. EDX data collected for annealed Mo sample grown by 3 ALD cycles. See spectral zones in Figure 4. 3.

	Atomic fraction on Spectre 1 (%)	Atomic fraction on Spectre 2 (%)	Atomic fraction on Spectre 3 (%)	Atomic fraction on Spectre 4 (%)
Mo	22.67	4.94	3.60	6.26
S	1.19	12.81	29.53	11.32
O	76.14	82.24	66.86	82.42

Table 4. 2. EDX data collected for annealed Mo sample grown by 3 ALD cycles. See spectral zones in Figure 4. 4. EDX data collected after *in situ* annealing in argon of W thiolates sample grown by 3 ALD cycles

	Atomic fraction on Spectre 1 (%)	Atomic fraction on Spectre 2 (%)	Atomic fraction on Spectre 3 (%)	Atomic fraction on Spectre 4 (%)
W	38.29	52.36	26.19	84.59
S	37.56	28.31	45.03	15.41
Mn	24.16	19.33	28.78	-

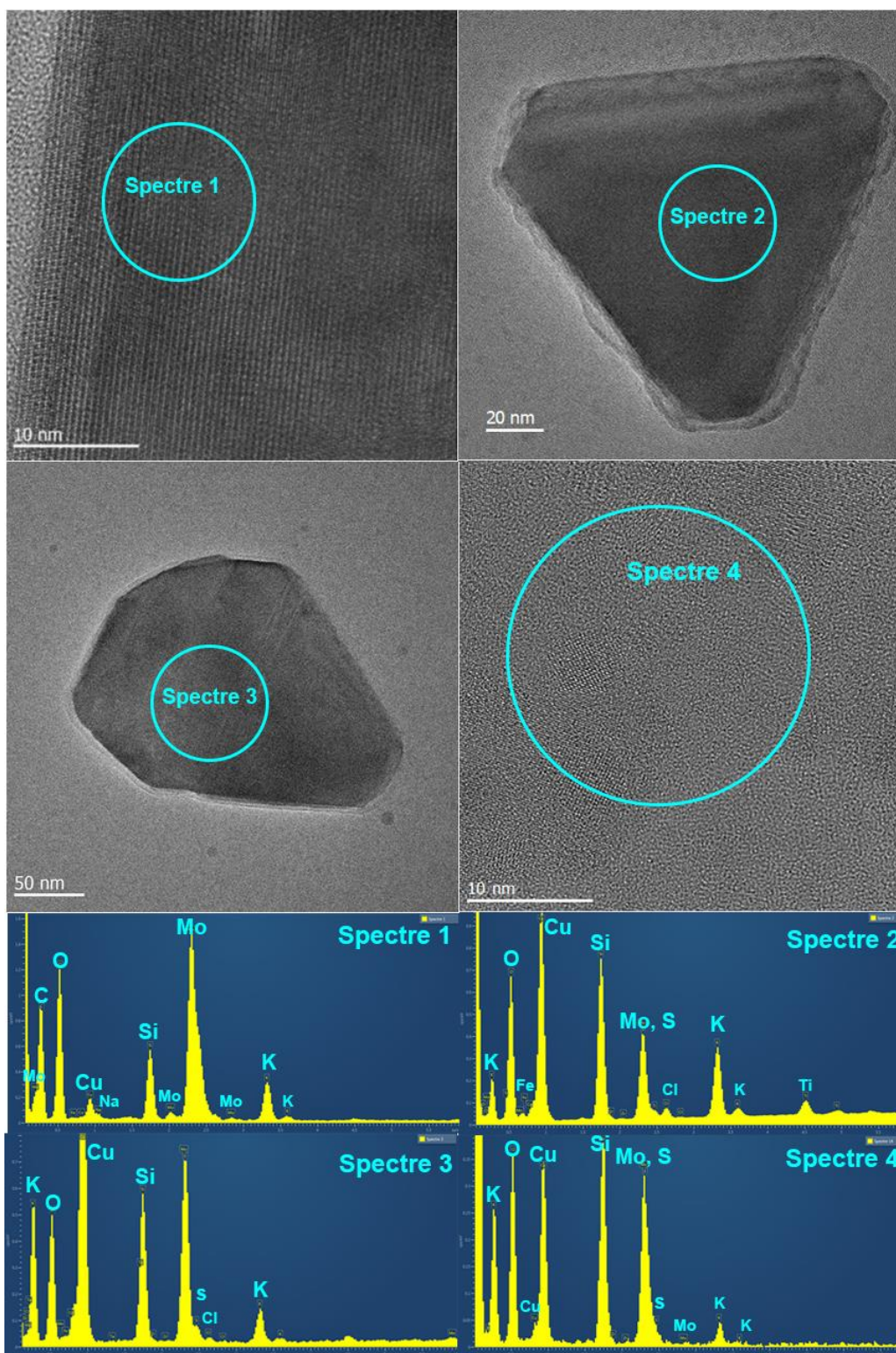


Figure 4. 3. EDX data collected after *in situ* annealing in argon of Mo thiolates sample grown by 3 ALD cycles



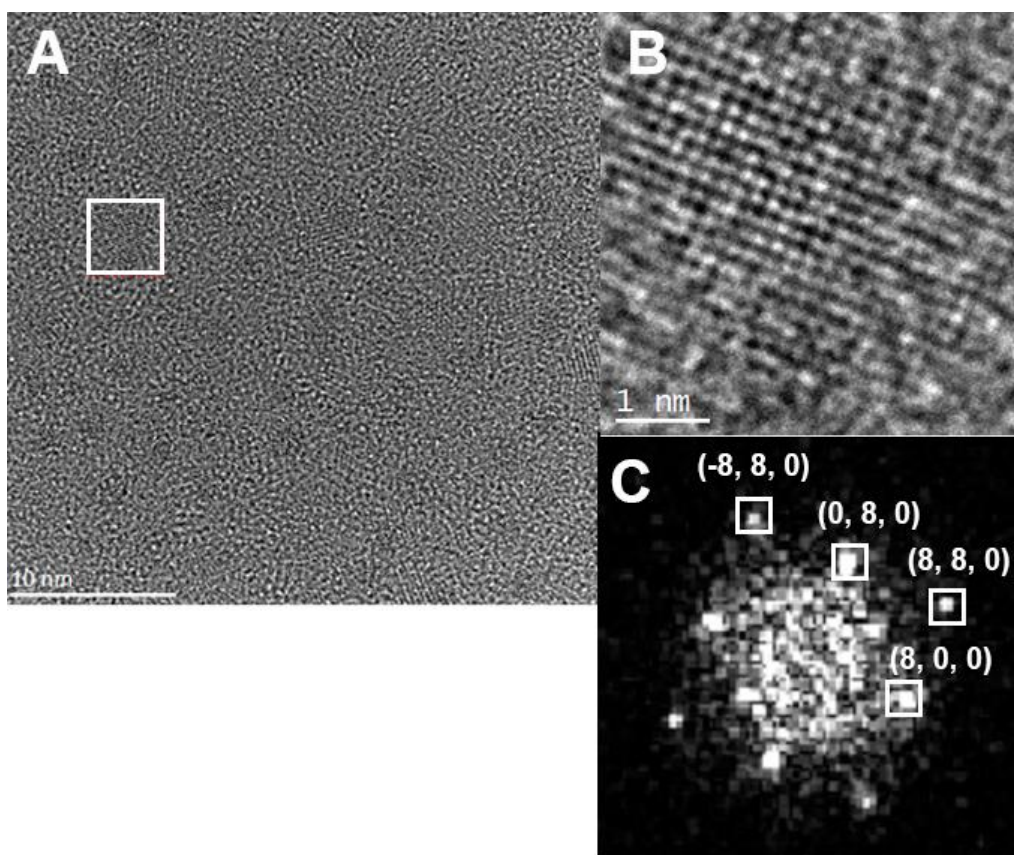


Figure 4. 5. FFT analysis of one of the crystalline nanodomains recorded at the *in situ* annealing step of 400 °C

Table 4. 3. Estimated unit cell parameters from the FFT pattern acquired at the *in situ* annealing step of W thiolates sample (see in Figure 4. 5). Theoretical values were calculated using JCPDS file of  $W_{21}S_8$  with a space group of I4/m (87).

(h, k, l)	d spacing (experimental), nm	Angle (experimental), °	d spacing (theoretical), nm	Angle (theoretical), °
(8, 0, 0)	0.190	0.00	0.2096	0.00
(8, 8, 0)	0.136	46.50	0.1482	45.00
(0, 8, 0)	0.193	91.30	0.2096	90.00
(-8, 8, 0)	0.133	135.90	0.1482	135.00

## 4.3 RESULTS AND DISCUSSION

### 4.3.1. XPS study

An ideal ALD process is a succession of self-limiting reactions at the gas-solid interphase between the incoming reactant and the existing substrate. The cycling occurs among the two half-reactions each involving separately the two reagents, the metal source, and the sulfur source as the incoming reagent in the gas phase. X-ray photoelectron spectroscopy is known to provide essential insights into the oxidation states and the environment of the atoms. *In situ* XPS studies have been reported also for ALD work included the study of the very first cycles in an ALD process.<sup>192,193</sup> We will describe hereafter the XPS studies performed by and analyzed in collaboration with Dr. Jules Galipaud from the Laboratory of Tribology and Dynamics of Systems (LTDS) of École centrale de Lyon on samples synthesized for this PhD work.

#### 4.3.1.1. *In situ* XPS monitoring of tungsten thiolates growth by ALD on silicon wafers

As shown in Figure 4. 6, the high-resolution XPS spectra indeed indicated that very substantial changes occurred during the first four half-cycles of the ALD process. Six wafer-based samples were studied by XPS. The pristine SiO<sub>2</sub>@Si wafer, each of the product of the four half ALD cycles, and the solid resulting from the annealing under argon at 800 °C.

The results detailed in chapter 3 show that some adventitious water can contaminate the sample between the ALD reactor and the XPS chamber. Nevertheless, in the molecular system, the tungsten amido and tungsten imido bonds could be observed. This gives us some confidence that we can observe the real chemistry occurred in the ALD reactor, alongside some decomposition.

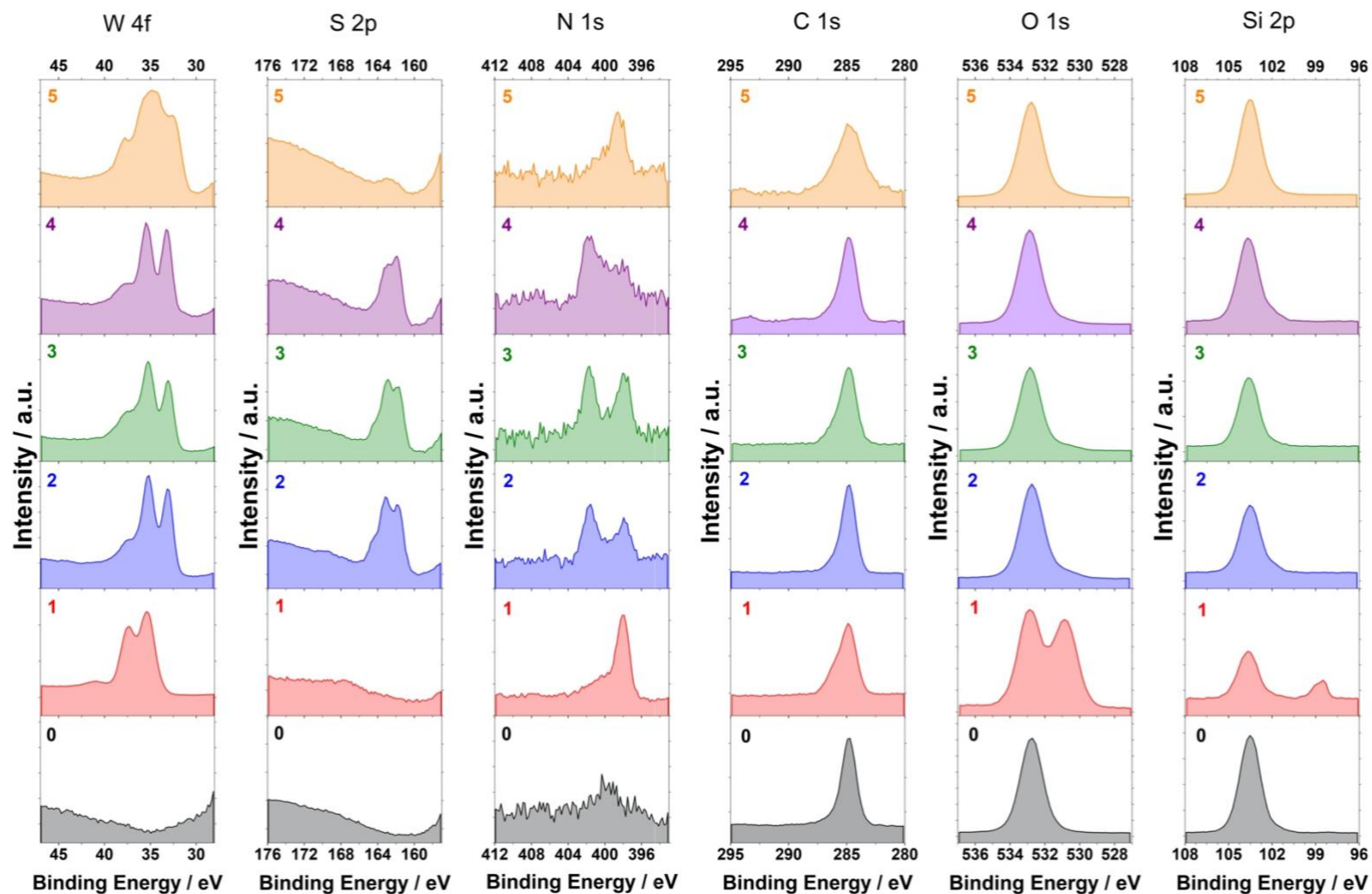


Figure 4. 6. High-resolution XPS spectra of W 4f, S 2p, N 1s, C 1s, O 1s, and Si 2p regions recorded at each step within 2 ALD cycles: **0** - blank wafer without deposition; **1** - after the 1<sup>st</sup> pulse of BTBMW; **2** - after the 1<sup>st</sup> of pulse EDT; **3** - after the 2<sup>nd</sup> pulse of BTBMW; **4** - the 2<sup>nd</sup> pulse of EDT (before annealing); **5** - 2 full ALD cycles after ex-situ annealing.

### 4.3.1.2. Pristine support

The blank wafer (see black spectra 0 in Figure 4. 6) displayed the expected characteristic peaks for the silicon oxide coating the silicon wafers. The Si 2p BE (103.5 eV) corresponds to the silicon in its oxide form. Since the top oxide layer exhibits  $\equiv\text{Si-OH}$  bonds and  $\equiv\text{Si-O-Si}\equiv$  siloxy bridges, and both these surface moieties are characterized by Si(IV) surrounded by four oxygen atoms, the observed peak at 103.5 eV is assigned to both. A little shoulder at 101.44 eV is attributed to silicon suboxide and subnitride ( $\text{SiO}_x$ ,  $\text{SiN}_x$ ). Consistently, N-containing impurities were also detected in the N 1s range as traces. The O 1s peak at 532.77 eV supports the top coating silicon dioxide layer. We also expect contribution due to the surface hydroxyl group. We expect this contribution minor with respect to the sum of the surface and bulk Si-O-Si sampled by the X-ray beam. This signal is therefore overlapping with the major peak or is a minor component elsewhere. Deconvolution of the O 1s range identifies a minor component (ca. hundredfold less at lower binding energy). Since this signal could also originate from traces of not better identified metallic oxide as an impurity within the silicon wafer, we do not assign oxygen peaks of Si-OH at this stage.

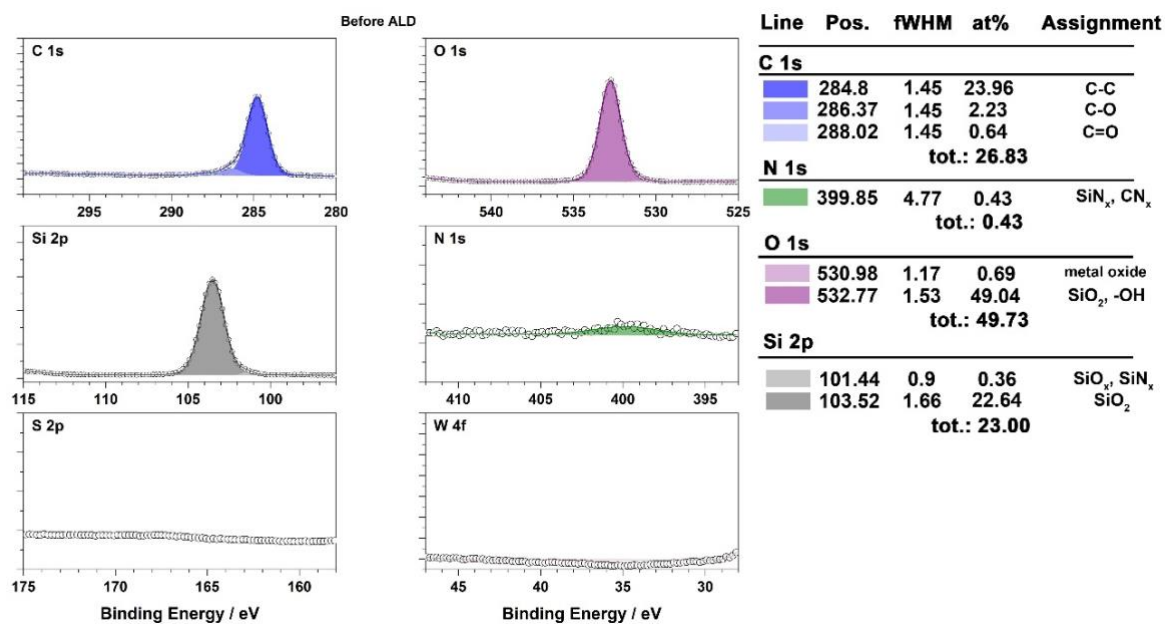


Figure 4. 7. Fitting of XPS data of the C 1s, O 1s, Si 2p, N 1s, S 2p, and W 4f regions for the pristine wafer with assignments

The C 1s region shows three contributions, fitted to C-C, C-O, and C=O bonds based on literature tables, which therefore suggest the presence of organics impurities (with mainly C-C bonds) (Figure 4. 7). This observation of C- (and N-impurities) shows that the  $\text{SiO}_2$ @Si surface could not be

completely cleaned from the contamination by the steps carried out (calcination at 800 °C, hydroxylation in distilled water, and dehydroxylation at 200 °C, handling).

#### 4.3.1.3. *The first metal pulse on the substrate, the 1<sup>st</sup> half-cycle*

Tungsten becomes observable after the 1<sup>st</sup> pulse (red spectra 1 in Figure 4. 6) corroborating the facile grafting of the metal precursor on the substrate at low temperature. To now gain insight on the nature of the grafted species and guide the XPS assignment, comparison, and contrast with the XPS data of the model molecular compound,  $\text{Ph}_3\text{SiO}-\text{W}(=\text{N}^t\text{Bu})_2(\text{NMe}_2)$ , the reaction product between BTBMW and  $\text{Ph}_3\text{SiOH}$  discussed in chapter 3 will be carried out throughout the following part.

The observation of the W 4f<sub>7/2</sub> and W 4f<sub>5/2</sub> levels corresponds to its W<sup>6+</sup> oxidation state.<sup>173</sup> The O 2p core-level showed an increased contribution of the signal at lower BE (530.7 eV) with respect to the pristine wafer (see deconvolution in Figure 4. 8). It is separated from the signal assigned to SiO<sub>2</sub> (532.88 eV) by ca. 2.0 eV, which matched well a previous XPS study report on the O 1s peaks of tungsten oxide and hydroxide bonds.<sup>164</sup> Hence, the low BE peak was attributed to the bonded complex, W–O–Si. This attribution comes in agreement with XPS analysis of the molecular product,  $\text{Ph}_3\text{SiO}-\text{W}(=\text{N}^t\text{Bu})_2(\text{NMe}_2)$ , which also displayed a low BE peak in the O 1s range supporting the W–O–Si system.

The narrow-scan XPS spectrum of the N 1s region shows the appearance of nitrogen of BTBMW at 397.97 eV with a little shoulder at 400.2 eV (red spectra 1 in Figure 4. 6). The deconvolution of the N 1s peaks identified contributions of three peaks, which were similarly assigned as the N 1s peaks observed in the molecular triphenylsiloxide complex. Imido (W=N), amido (W–N), and amine (W–NH<sub>x</sub>R<sub>2-x</sub>, where R = <sup>t</sup>Bu or Me<sub>2</sub>) groups<sup>173</sup> were estimated in a 2.7:1:1 ratio, respectively. The deficiency of amido in this ratio points to that the amine group was formed by protonolysis of the dimethylamido group rather than tert-butylimido.

The amido and imido groups are certainly the ligands of grafted BTBMW. The W=N bond withdraws more electron density from the nitrogen atom than the W–N, hence, the N of the imido group gains higher BE. The observed N 1s peaks are coherent with the previous study on the N 1s BE evolution upon the increase of metal-nitrogen bond order in alkylamido, alkylimido, and nitride complexes.<sup>160</sup> Attribution of the N 1s to amine was supported by works reporting the XPS study on the protonation of nitrogen-containing functional group<sup>27,161</sup> and incomplete liberation of HNMe<sub>2</sub>

upon protonolysis of the tungsten-dimethylamido bond.<sup>162,163</sup> Given the electron-withdrawing properties of the tungsten d<sup>0</sup> center, the coordinated amine can exhibit the N 1s signal at higher BE.

The relative ratios appear different between the molecular and the wafer-supported species. The fraction of amine-type nitrogen was almost two-fold higher in the molecular product than on the silicon wafer. This could originate from greater exposure to hydrolysis in the experiment with Ph<sub>3</sub>SiOH related to the issue of arbitrary air-tightness of the transporting box for the XPS chamber. Hydrolysis could lead not only to a coordinated amine ligand but also to W–OH and/or Si–OH moieties that can be observed as the increased contribution of a higher BE peak in the O 1s range.

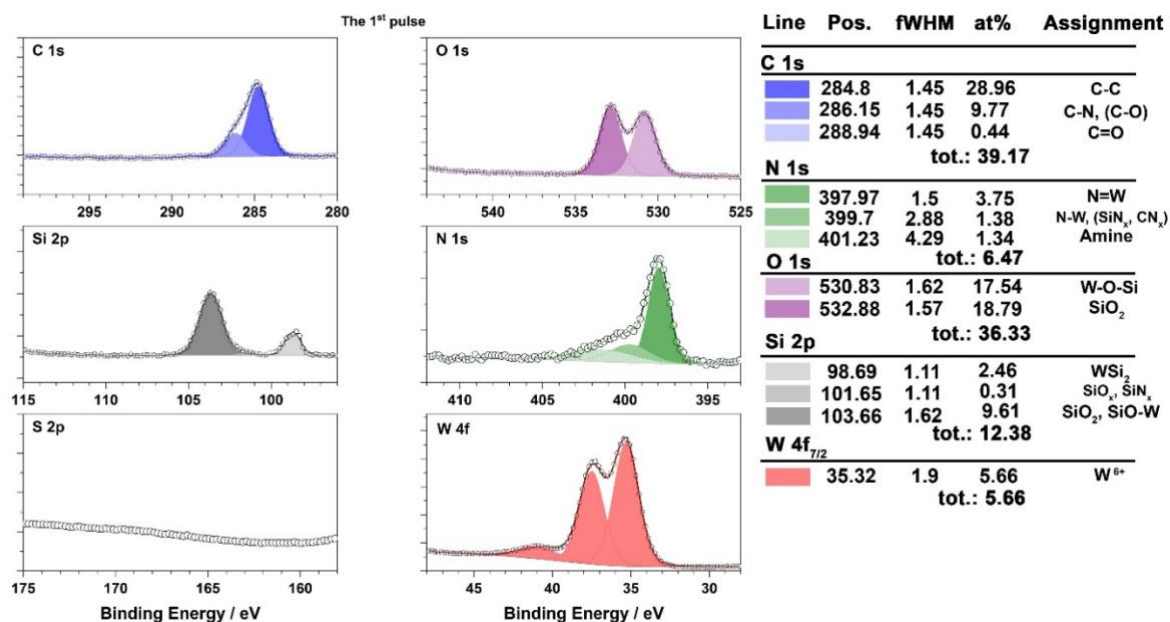


Figure 4. 8. Fitting XPS data of the C 1s, O 1s, Si 2p, N 1s, S 2p, and W 4f regions after the 1st pulse

The peak of carbon (284.8 eV), which was earlier assigned to the C–C, C–O, and C=O containing organic contamination, increased its intensity with respect to silicon and its width towards higher BE. The contribution of carbon atoms of grafted BTBMW can be observed from the greatly increased fraction of the middle peak that combines the C–N bond of the complex and traces of C–O contamination. Fitting the C 1s high-resolution spectrum allowed to determine its total atomic fraction at 39.17 %. This way, the calculated atomic ratio of C:N:W was as 6.92:1.14:1, which differs much from the ratio found upon the 1<sup>st</sup> pulse on the silica nanobeads (10:3:1). Despite the mentioned hydrolysis issue could lower the fraction of amido ligands leading to C and N deficiency, the trend of atomic fractions (at.%-C > at.%-N > at.%-W) was preserved. The signals in the Si 2p

region apparently show little shift of the main feature with respect to the pristine sample. The BE value measured for the molecular compound (Si 2p for  $\text{Ph}_3\text{SiOW}(\text{NMe}_2)(=\text{N}^t\text{Bu})$ ) is observed at 102.07 eV; substitution of electron-donating phenyl group with electron-withdrawing O groups of the silica network suggests that the silica-related moiety should have led to higher BE with respect to the molecular one. We thus expect a signal above 102.7 eV. We assign the main feature at 103.66 eV to SiO-W (in overlap with Si-O-Si). The signal due to impurities ( $\text{SiN}_x$  and  $\text{SiO}_x$ ) is still present at 101.65 eV. A small but noticeable new feature is observed at 98.69 eV, which has no analogue in the molecular study reported in Chapter 3. This BE agrees with the one reported in the literature for  $\text{WSi}_2$ .<sup>194</sup> Formation of  $\text{WSi}_2$  species can occur via the reaction of the complex with Si-H bonds on the Si surface.<sup>195,196</sup> Therefore, this suggests the possible existence of defects in the oxide layer. The XPS measurement in further ALD pulses (see fitted XPS graphs in Figure 4. 8 - Figure 4. 12) did not show this peak anymore, thus hinting to the fact that the formation of tungsten silicide,  $\text{WSi}_2$ , if any, is sub-surface. In summary, these XPS spectra suggest that for in large part, the deposition of BTBMW on the wafer was successful, where the main corroborating components were  $\equiv\text{SiO}-\text{W}(\text{VI})$ ,  $\text{W}=\text{N}$ ,  $\text{W}-\text{N}$ ,  $\text{W}-\text{amine}$ , and  $\text{C}-\text{N}$  bond systems.

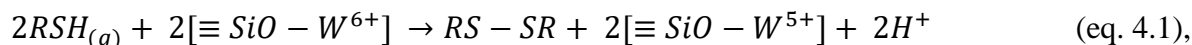
#### 4.3.1.4. *The first pulse of EDT (the 2<sup>nd</sup> half-cycle)*

As seen in chapter 2, the first pulse of EDT is expected to make the W-S bond by replacing alkylamido ligands. As discussed there, a thiol is also reported to induce a reduction by possibly proceeding to a coupling of two thiol groups (see eq. 4.1).<sup>25,165,166,167</sup> Indeed, the W 4f peaks of the wafer supported thiolates shifted to lower BE values upon the EDT pulse (Figure 4. 6). These values are located between commonly reported reference values of  $\text{WS}_2$  and  $\text{WO}_3$ , and most probably identify with the formal  $\text{W}^{5+}$  state coinciding with some works in the literature.<sup>24</sup> Atomic fractions distribute almost equally between the  $\text{W}^{5+}$  and  $\text{W}^{6+}$  states (0.78 vs 0.65 %) (see deconvolution of XPS spectra in Figure 4. 9). Here, the reductive path induced by the thiol pulse is clear despite possible air leaks leading to hydrolysis and possibly to oxidation.

The S 2p core-level deconvolution showed two major components at 161.69 eV and 163.31 eV. These values are within the 0.1 eV range of the analogous one observed for the molecular product of the reaction between  $\text{Ph}_3\text{SiO}-\text{W}(=\text{N}^t\text{Bu})_2(\text{NMe}_2)$  and EDT (at 161.79 eV and 163.25 eV, respectively) as discussed in the previous chapter. Therefore, we use the same arguments to assign two main doublets assigned to the thiolate,  $-\text{S}^-$ , thiols  $-\text{SH}$ ,<sup>27</sup> and coupled sulfur atoms  $-\text{S}-\text{S}-$  ( $\text{S}_2^{2-}$

),<sup>24</sup> thus molecularly suggesting the same ease of ethylene elimination from the ethylenedithiolate moiety on the wafer as on the molecular compound. Ethylene was also directly observed by NMR for the 2<sup>nd</sup> pulse-modeling reaction on silica nanobeads.

The equation below (Eq. 4.1 adapted from ref<sup>25</sup>) was proposed to illustrate the thiol coupling-induced oxidation-reduction transformations:



The coupled RSSR is the oxidation product of the RSH thiol,<sup>165,166</sup> whereas RSH can be not only HSCH<sub>2</sub>CH<sub>2</sub>SH (free EDT) but also ethanedithiolate ligands bonded to the tungsten center. The minor S 2p<sub>3/2</sub> component at 168.63 eV is assigned to sulfates, possibly due to adventitious hydrolysis oxidation, comprises less than 4% of the total sulfur content.

The ratio between total atomic fractions of S and W, 3.23:1, is not far from the value seen by the XPS fitting of the analogous molecular product (3.51:1). However, elemental analysis on the silica nanobeads showed a higher S to W ratio (4.27:1). Most probably, the value estimated by XPS could be lower due to possible hydrolysis during transportation.

Along with tungsten reduction, the EDT pulse induced an increase of nitrogen fraction in amine form. The proposed reaction scheme for the analogous product on silica nanobeads (see in Chapter 3) supports the possibility to make hydrogen bonding or even a proton transfer between -NMe<sub>2</sub> and -SH or =N<sup>t</sup>Bu and -SH. Besides, EDT is a potential protonating source and some amido or imido ligands can remain coordinated to the tungsten even after protonolysis of a tungsten-nitrogen bond.<sup>162,163</sup> The deconvolution of the N 1s range identified three peaks with the same assignments as in the previous pulse, but the fraction of the W=N state decreased almost 2-fold (from 0.58 to 0.28) with respect to the total nitrogen content upon the 2<sup>nd</sup> pulse (see Figure 4. 9). It may signify that amine formation occurred mainly at the expense of the imido ligands. Hence, this phenomenon comes in line with observations of the 2<sup>nd</sup> pulse on silica nanobeads, where EDT hydrogenated W=N<sup>t</sup>Bu bond to form (HSCH<sub>2</sub>CH<sub>2</sub>S)-W-NH<sup>t</sup>Bu. Here, the NH can see the hydrogen bonding with thiol<sup>197</sup> or even receive a proton from thiol,<sup>159,198</sup> which would partly form a zwitterion ((-SCH<sub>2</sub>CH<sub>2</sub>S)-W-N<sup>+</sup>H<sup>t</sup>Bu) and shift the N 1s peak to higher BE. To further complexify the possible surface chemistry, amides, imides, and other nitrogen-containing compounds were reported to catalyze thiol-ene click reactions by inducing the proton subtraction of the thiol group.<sup>175</sup> The ratio N/W was decreased upon the EDT pulse, which signifies substitution of the amido or imido groups.

Most probably the substituted nitrogen can be from the amido group because it is more subjected to the W–N bond cleavage.<sup>169</sup>

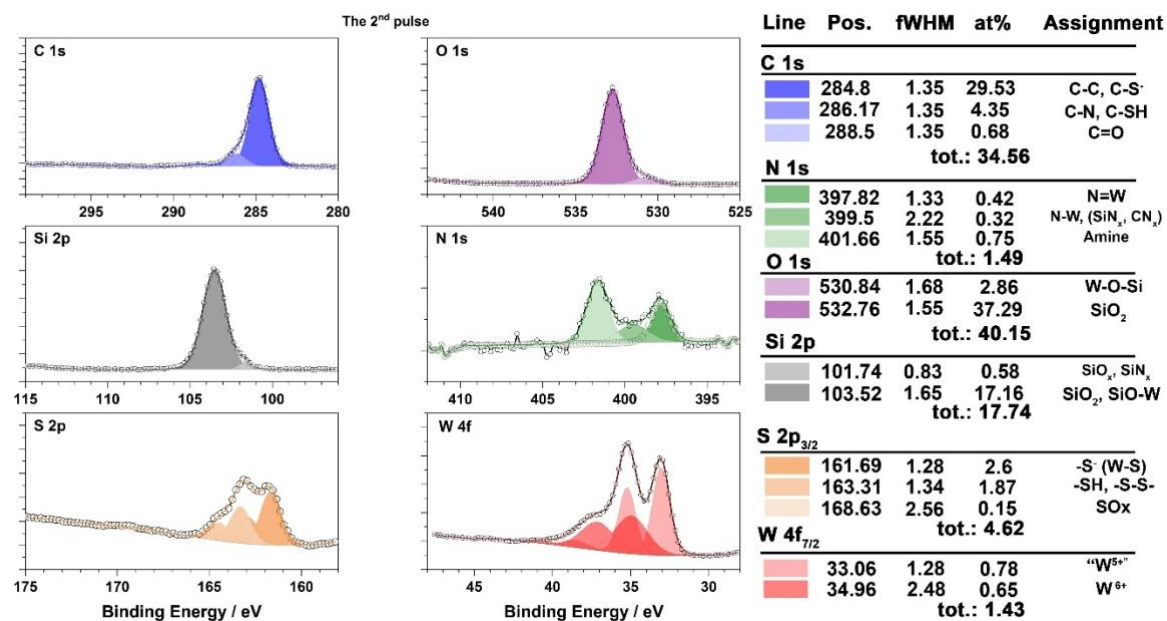


Figure 4. 9. Fitting XPS data of the C 1s, O 1s, Si 2p, N 1s, S 2p and W 4f regions after the 2<sup>nd</sup> pulse.

The C 1s range was expected to exhibit components from the C–S<sup>-</sup> and C–SH bond environments. Ataman *et al.*<sup>27</sup> assign such carbon-sulfur bonds with high energy resolution XPS. In our deconvolution, the C-thiolate and C-thiol bonds overlap with assigned C–C (284.8 eV) and C–N (286.17 eV) bonds, respectively.

The O 1s and Si 2p core-levels did not demonstrate significant modifications being remained at the same BEs (see blue spectra 2 in Figure 4. 6). This time fitted Si 2p graphs did not display the contribution of Si<sub>2</sub>W. The utilization of different wafer pieces (from initial bigger one) used for XPS analysis of each pulse might also explain this lack of WSi<sub>2</sub> throughout the XPS study.

#### 4.3.1.5. The third half-cycle (2<sup>nd</sup> pulse of BTBMW)

The increase of relative atomic fractions attributed to imido nitrogen, W<sup>6+</sup>, and decrease of total S fraction signify successful surface reaction of BTBMW with the 2nd pulse product. Preferable elimination of –NMe<sub>2</sub> ligand (as HNMe<sub>2</sub>) upon BTBMW grafting was already demonstrated in the molecular reaction (with Ph<sub>3</sub>SiOH) as well as in the surface reactions on silica nanobeads.

Therefore, growth of the relative atomic fractions of imido nitrogen (from 0.28 to 0.38) and the  $W^{6+}$  state was expected phenomena. Also, the S/W ratio decreases due to added tungsten atoms upon the third half-cycle.

The fitting of the graphs led to determine two doublets corresponding to  $W^{6+}$  and  $W^{5+}$  oxidation states in the atomic percentages ratio of 1:1 (0.77% for each, see in Figure 4. 10). It may indicate that half of the W present in the  $W^{6+}$  state could originate from the newly grafted BTBMW. The  $W^{5+}$  state might have remained from the 1<sup>st</sup> ALD cycle though additional reduction of W ( $6+ \rightarrow 5+$ ) could occur upon the elimination of ethylene that is induced by the steric pressure from the new deposition of BTBMW. The identified positions on the BE axis for the fitted spectra of W 4f come in good agreement with the provided BE values by few references.<sup>199,200</sup>

The S 2p core level remained unchanged. Deconvolution of these peaks reveals two doublets assigned to the thiolate ( $-S^-$ ), thiol, and persulfido  $-S-S-$  ( $S_2^{2-}$ ) forms of the sulfur (see in Figure 4. 10) in the same relative atomic ratio to each other as in the previous step. Since the last two components overlap and are estimated as the same unit, the preserved ratio between two sulfur peaks ( $-S^- : (SH+S_2^{2-})$ ) can signify the concurrent decrease of thiol and increase of the  $S_2^{2-}$  form.

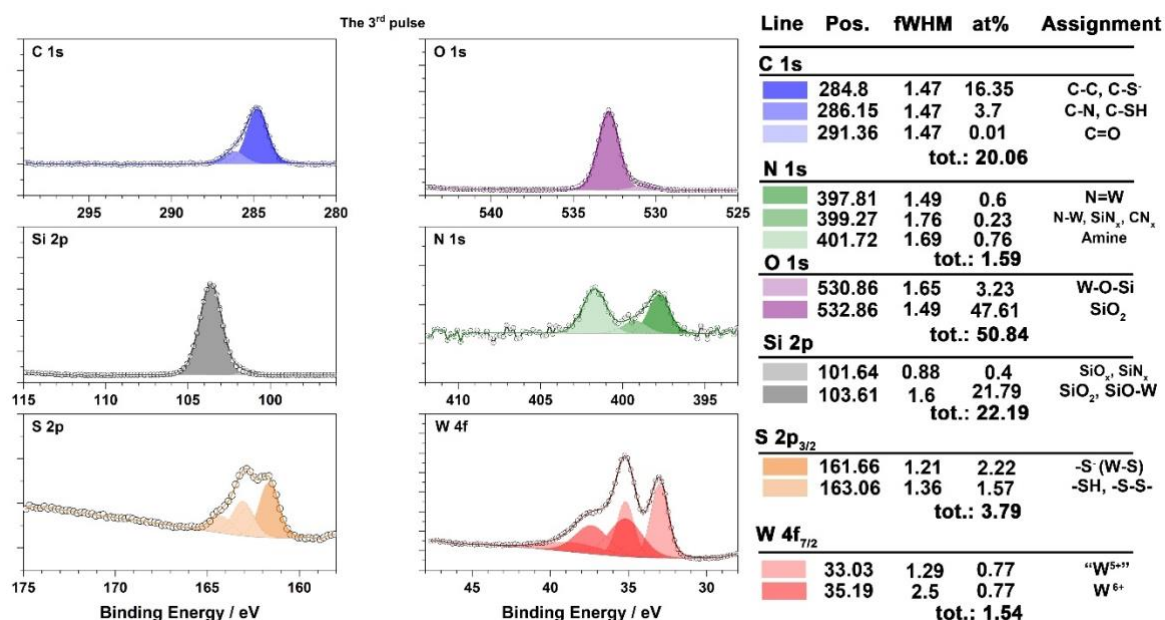


Figure 4. 10. Fitting XPS data of the C 1s, O 1s, Si 2p, N 1s, S 2p, and W 4f regions after the 3rd pulse

The binding energies of Si 2p, O 1s, and C 1s were found at 103.5, 532.8, and 284.8 eV (see green spectra 3 in Figure 4. 6), respectively, which are the same as after the 2<sup>nd</sup> pulse.

#### 4.3.1.6. *The fourth half-cycle (2<sup>nd</sup> pulse of EDT)*

The fourth pulse, that is, in fact, the 2<sup>nd</sup> pulse of EDT, reveals the W 4f, S 2p, and N 1s features similar to those of the product of the 1<sup>st</sup> pulse of EDT. The observed positions of the W 4f peaks high-resolution spectra (purple spectra 4 in Figure 4. 6) seem to lie in the range of W<sup>5+</sup> and W<sup>4+</sup> oxidation states with a bit of contribution of W<sup>6+</sup> state. The fitting of these peaks shows that they are composed of two doublets with their 4f<sub>7/2</sub> positions at 35.49 and 33.21 eV in the ratio of (1:2) (see Figure 4. 11). Analogously to the previous ALD cycle, the deposition of EDT in the 2<sup>nd</sup> cycle resulted in increasing the fraction of the W<sup>5+</sup> state. Therefore, the tungsten reduction hypothesis based on S–S coupling and ethylene elimination is supported in this pulse too.

Fitting of the S 2p peaks displayed two doublets with their 2p<sub>3/2</sub> peaks corresponding to –S<sup>–</sup> thiolate and (–SH + S<sub>2</sub><sup>2–</sup>) states in an increased 2:1 ratio. This can mean that the formation of S<sub>2</sub><sup>2–</sup> and preservation of thiol group are not as important as in the previous EDT pulse (–S<sup>–</sup> : (SH+S<sub>2</sub><sup>2–</sup>) = 2:1 vs. 1.4:1)

Deconvolution of the N 1s peaks reveals the presence of the same nitrogen states among which the fraction of the W=N form decreased (from 0.38 to 0.19) with respect to the total N. This is again a two-fold decrease of the fraction, which is consistent with affecting only one of the imido ligands. The imido group could be hydrogenated by EDT to produce (HSCH<sub>2</sub>CH<sub>2</sub>S)W–NH<sup>t</sup>Bu, whereas –NH<sup>t</sup>Bu and –SH can establish hydrogen bonding or undergo the proton exchange to yield amine. An increased fraction of the amido nitrogen is consistent with the proposed formation of –NH<sup>t</sup>Bu ligand.

No significant changes were observed in the high-resolution spectra of Si 2p, O 1s, and C 1s (see purple spectra 4 in Figure 4. 6). To summarize, collected data upon the 4<sup>th</sup> pulse suggest successful surface reaction with EDT providing similar features as after the 2<sup>nd</sup> pulse. It was shown that successive ALD cycles can be continued in this manner that maintain partial reduction of tungsten's oxidation state. Although the reduction to the formal oxidation state of M<sup>5+</sup> (where M = W, Mo) was reported in heterogeneous reactions,<sup>24,25,167,199,200</sup> no literature evidence was found from ALD works using M (VI) alkylamido complex as a starting precursor.

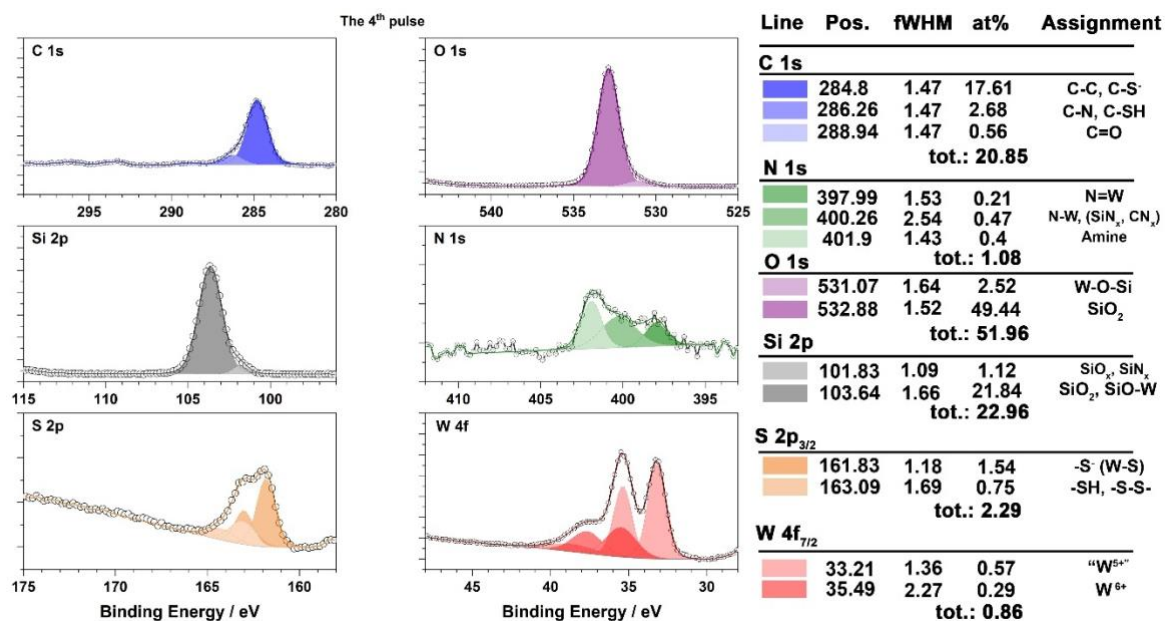


Figure 4. 11. Fitting XPS data of the C 1s, O 1s, Si 2p, N 1s, S 2p, and W 4f regions after the 4th pulse

#### 4.3.1.7. *Ex-situ annealed sample*

The annealing at 800 °C under argon flow was expected to eliminate moieties containing C, N, H, and excess S. Besides, annealing at this temperature should start turning the WS<sub>x</sub> to crystalline WS<sub>2</sub> as displayed in the phase diagram (introduction, Chap. 1).

After etching of the top layer WO<sub>3</sub> contaminant (see experimental part), the W 4f spectrum displayed contributions of three doublets, which are assigned to the W<sup>6+</sup>, W<sup>5+</sup>, and the W<sup>4+</sup> states (see Figure 4. 12). The main difference observed in this spectrum from the previous ALD steps was the shift of the main peak position toward lower BE, which is consistent with the formation of the WS<sub>2</sub>. The presence of the W<sup>6+</sup> can be explained by possible oxidation to WO<sub>3</sub> during the transfer for ex-situ annealing or residual tungsten thiolate due to incomplete thermal decomposition. The W<sup>5+</sup> state could be observed because the first layer is tungsten oxysulfide (WO<sub>y</sub>S<sub>z</sub>) rather than pure disulfide and supported by the observed disulfide S<sub>2</sub><sup>2-</sup> environment. It agrees well with the analogous works on the XPS study of Mo/W oxysulfides and a mixture of different sulfides.<sup>24,167</sup> One should note that tungsten oxysulfide is expected to remain in the first layer due to the formation of ≡Si-O-W in the first pulse of BTBMW.

The S 2p core-level revealed the same two doublets with  $2p_{3/2}$  positions at 161.72 and 162.64 eV corresponding to the  $-S^-$  and  $S_2^{2-}$  forms, respectively. One can notice that the S  $2p_{3/2}$  peak of  $S_2^{2-}$  form slightly shifted to a lower BE (-ca. 0.5 eV) which may point to the decrease of SH component in it. This is consistent with the loss of excess sulfur in the annealing. The atomic S/W ratio was only 0.4 (instead of the expected 2), which shows a high deficiency with respect to  $WS_2$  (see Figure 4. 12). This can be attributed due to not enough etching of the top surface.

Preservation of the N 1s peaks (assigned to W=N and W-N) was also unexpected to observe after the annealing. Atomic fractions ratio of N to W remained at a high level of 1.1. Therefore, incomplete annealing and surface contamination mentioned above were suggested as possible reasons.

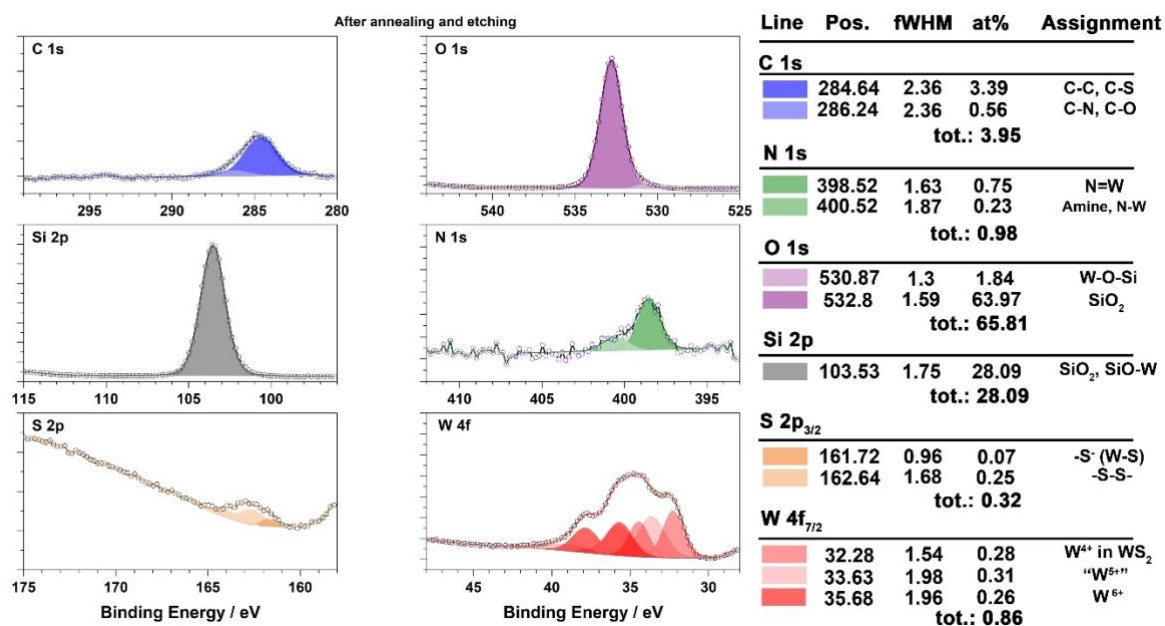


Figure 4. 12. Fitting XPS data of the C 1s, O 1s, Si 2p, N 1s, S 2p, and W 4f regions after annealing and etching the top surface for 12 minutes.

The BE maxima of Si 2p, O 1s, and C 1s core levels remained at the same values in their narrow scan XPS spectra, though it was noticed that carbon content has significantly reduced from 20.85 at.% to 3.95 at.%. A decrease of the carbon content was induced by annealing which was also seen by DRIFT spectra evolution during the *in-operando* thermal decomposition study on the silica nanobeads.

In summary, the ALD process (including the annealing step) does lead to the formation of tungsten (IV) sulfide ( $WS_2$ ). At the same time, this formation did not appear complete since residual thiolates and surface contamination could be observed.

#### 4.3.1.8. Operando XPS study of the annealing step

The XPS study presented hereto pertains to a study akin to *in situ* studies, plus a final ex-situ annealing step which led to substantial surface oxidation to  $WO_3$  (see above). One further set of XPS experiments was performed in order to carry out the annealing experiments in absence of air exposure and to do so the annealing was performed directly inside the XPS chamber. One piece of the wafer after 4 ALD pulses was introduced inside the XPS chamber with the (almost) airtight transfer and then annealed inside the XPS chamber from room temperature to 500 °C and monitored stepwise by XPS.

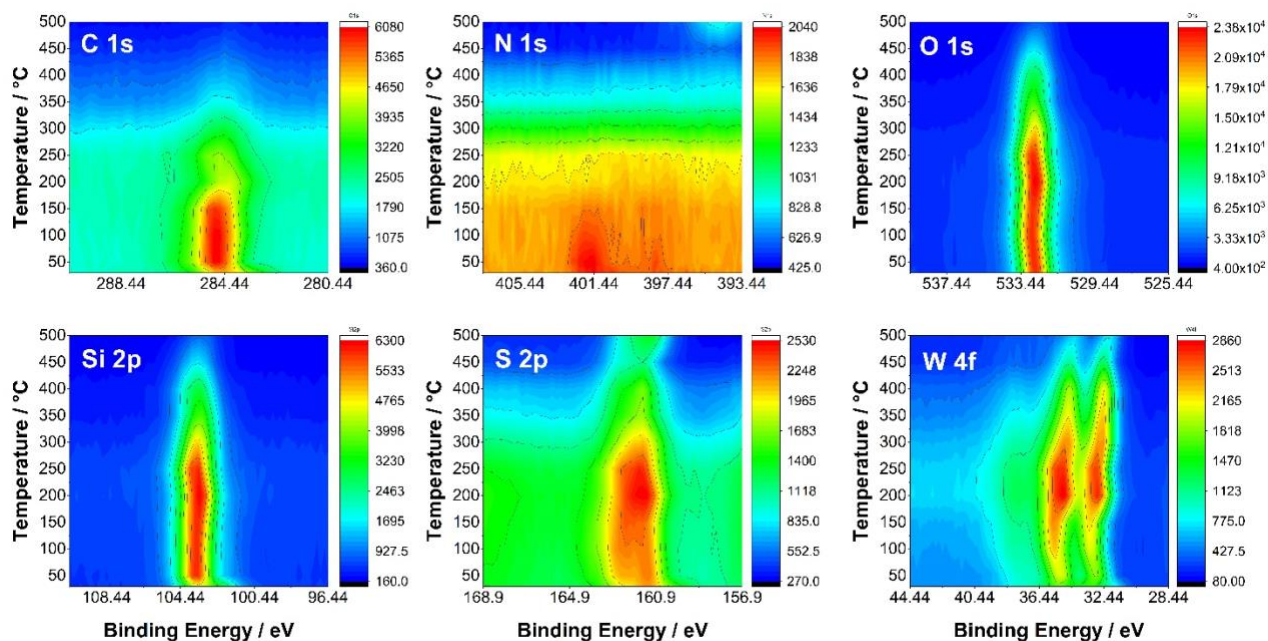


Figure 4. 13. Evolution of the high-resolution XPS spectra upon heating under an ultra-high dynamic vacuum where intensity is given by color range from blue to red

The narrow scan XPS data were recorded for the same six elements (C 1s, N 1s, O 1s, Si 2p, S 2p and W 4f) at each 50° step. At each new heating step, the wafer was maintained at the set temperature minimum for one hour before starting the analysis. The graphs were built for the

temperature and signal intensity vs. BE, where intensity is given by a color range from blue to red (see Figure 4. 13). The color transition from blue to red corresponds to the intensity rise from low to high. It can be noticed that all spectra start to lose the signal intensity above 450 °C. It is assigned to the pressure increase at the higher temperature. The decrease of the C 1s and N 1s peaks started at lower temperature. Carbon diminishes starting from 200 °C, while nitrogen diminishes above 300 °C. This comes in good agreement with the thermal decomposition study carried on silica nanobeads, where ethylene, isobutene and methylisocyanide were observed in the range of 200-350 °C by GC-MS. The reduction of the S 2p signal was observed from 250 °C, which can be attributed to the release of excess sulfur. This elimination of sulfur matched with the temperature range of thiirane, thiophene and ethanethiol released from silica and detected by GC-MS between 200 and 400 °C. Approximately at the same temperature range, we can notice a deviation of the main W 4f peak towards the lower BE, thus suggesting concomitant reduction of tungsten oxidation number. The O 1s and Si 2p core levels have not been altered much except the overall signal loss. This means the reduction of tungsten's oxidation number possibly towards  $W^{4+}$  in  $WS_2$ .

The BE variation over temperature of each element's main peak with respect to its initially determined BE is reported in Figure 4. 14. This graph shows a significant shift of the main W 4f peak towards the lower BE attributed to its reduction to the  $W^{4+}$  state, while the S 2p, Si 2p, O 1s, and C 1s peaks remained almost unchanged (in the range of the technical error). The decrease of the main W 4f peak BE was first recorded by 0.8 eV at 300 °C that is then followed by a stabilization of the peak. The N 1s peak shape was broadened and its main peak sharply changed from one assigned environment (imido, amido, and amine nitrogen) to another. Since the N 1s BE values went out of the measurement error range, its interpretation was not considered.

Fitting and deconvolution of the high-resolution spectra at each step of the annealing afforded to quantify elements. Ratios of the atomic fractions of the elements over that of tungsten are plotted versus temperature in Figure 4. 15. Graph A shows ratios of all the 5 elements over tungsten separately, and graph B is a zoom of the same data for sulfur and nitrogen elements exclusively over tungsten. All the records at 500 °C were difficult to assign and not considered reliable, because the vacuum was not so strong to get a good signal. From graph A, the release of organic moieties is obvious with the decrease of the C/W ratio in the range of room temperature to 300 °C. Both O/W and Si/W ratios steadily decrease within the whole range of annealing that can signify an overall increase of the fraction of W. The decrease in nitrogen content is concurrent with the loss of carbon moieties (see graph B). However, the trend of sulfur was not as obvious as other elements.

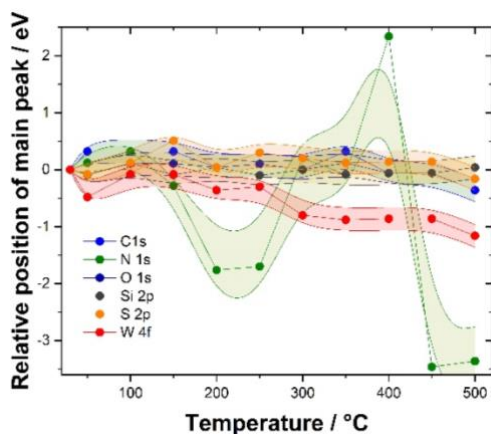


Figure 4. 14. The relative position of the main peak vs temperature in *in situ* annealing. Two lines on two sides of the recorded points signify the range of the measurement error.

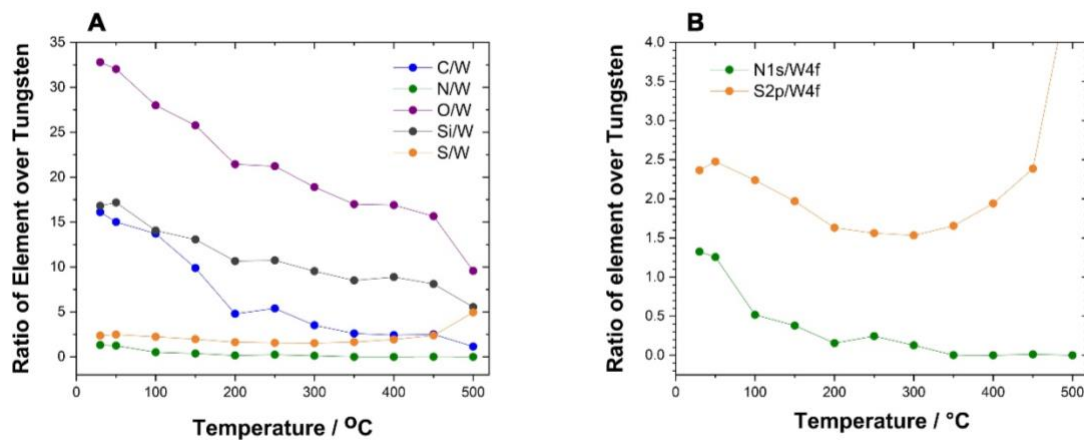


Figure 4. 15. Evolution of ratios of elements over tungsten with temperature during annealing

In the range of 20-300 °C, it diminishes most probably due to the loss of excess sulfur in parallel with carbon and nitrogen. Then from 350 °C, the sulfur content with respect to tungsten increases until the end of annealing. This was an unexpected observation and could be assigned to the back sublimation of sulfur-containing impurities. The appearance of copper and molybdenum in the survey spectra (see the black spectrum in Figure 4. 2) supports this suggestion. When the temperature reached 200 °C, it was maintained for 6 hours more because some evolution of carbon content was noticed. During those 6 hours at 200 °C, the carbon content decreased by 30 % (from 17.29 to 12.08 at.%). Fractions of other elements remained stable. In general, this *in situ* annealing in XPS displayed not only relevant results with the analogous study of thermal decomposition of

silica model after 4 pulses monitored by DRIFT and GC-MS but also complementary insights into the evolution of the oxidation states.

### 4.3.2. *In situ* annealing of ALD grown W and Mo thiolates on SiO<sub>x</sub>@Cu grid in an environmental transmission electron microscope

#### 4.3.2.1. *En route to MoS<sub>2</sub>*

The ALD growth of molybdenum thiolates using Mo(NMe<sub>2</sub>)<sub>4</sub> and EDT precursors was previously well-characterized on both 2D (SiO<sub>2</sub>@Si wafer) and 3D (silica nanobeads) substrates in our laboratory.<sup>19</sup> Therefore, it was a good model for the first *in situ* environmental TEM annealing study of ALD-grown metal thiolates on SiO<sub>x</sub>@Cu grid.

The 200 mesh Cu grid was coated with a mixture of SiO and SiO<sub>2</sub> by a supplier that does state no approximate ratio between the oxides. Nevertheless, it is expected that SiO<sub>x</sub> (where 1 < x < 2) film should possess surface hydroxyl groups capable of reacting with metal alkylamido complexes.

#### *In situ annealing under hydrogen atmosphere*

The growth procedure of Mo thiolates by 6 ALD cycles was adapted from the work of S. Cadot *et al.*<sup>19</sup> See the experimental part of this chapter for special measures applied for the growth on a partially dehydroxylated SiO<sub>x</sub>@Cu grid. Since the presence of H<sub>2</sub> gas during annealing of Mo thiolates was shown to facilitate the crystallization to form MoS<sub>2</sub>,<sup>19</sup> the initial attempt for *in situ* annealing in environmental TEM (E-TEM) was decided to perform under 2 mbar of H<sub>2</sub>. The TEM images (see Figure 4. 16A) at low magnification captured at 50 °C show the uniform film throughout the grid. The surface seems to illustrate the coating with “*pinholes*” (circular bright zones). The presence of pinholes in ALD films can be because the substrate has a low concentration of surface reactive functional groups.<sup>185</sup> Since the darker image parts signify less conduction of the current and thicker material, it may illustrate the regular distribution density of the silanol groups over the surface of the grid precoating. The surface of the bright spheres was thought to be bare silica non-containing ALD-grown sample, while dark zones were thought to be coated with thicker material. However, at higher temperatures (>300 °C), the images will confirm the deposition of

nanostructures on both the dark and bright zones, thus the difference in contrast suggests some variability in film thickness. When the grid was heated to 150 °C, the surface morphology did not change. The image taken on the border of dark and bright zones (Figure 4. 16B) reveals amorphous material on both sides with no distinct structures. The first formation of worm-like structures was observed in the next annealing step (at 300 °C). The high-resolution image (Figure 4. 16C) reveals short “worms” on both dark and silica zones. The worm-like shapes point to the beginning of the crystallization of MoS<sub>2</sub>. These layered nanodomains are oriented randomly in various directions. At 450 °C, one can notice the formation of crystalline nanoparticles with well-ordered atoms. This evidence supports the facilitated crystallization of MoS<sub>2</sub> in the presence of H<sub>2</sub> by S. Cadot *et al.*<sup>19</sup>

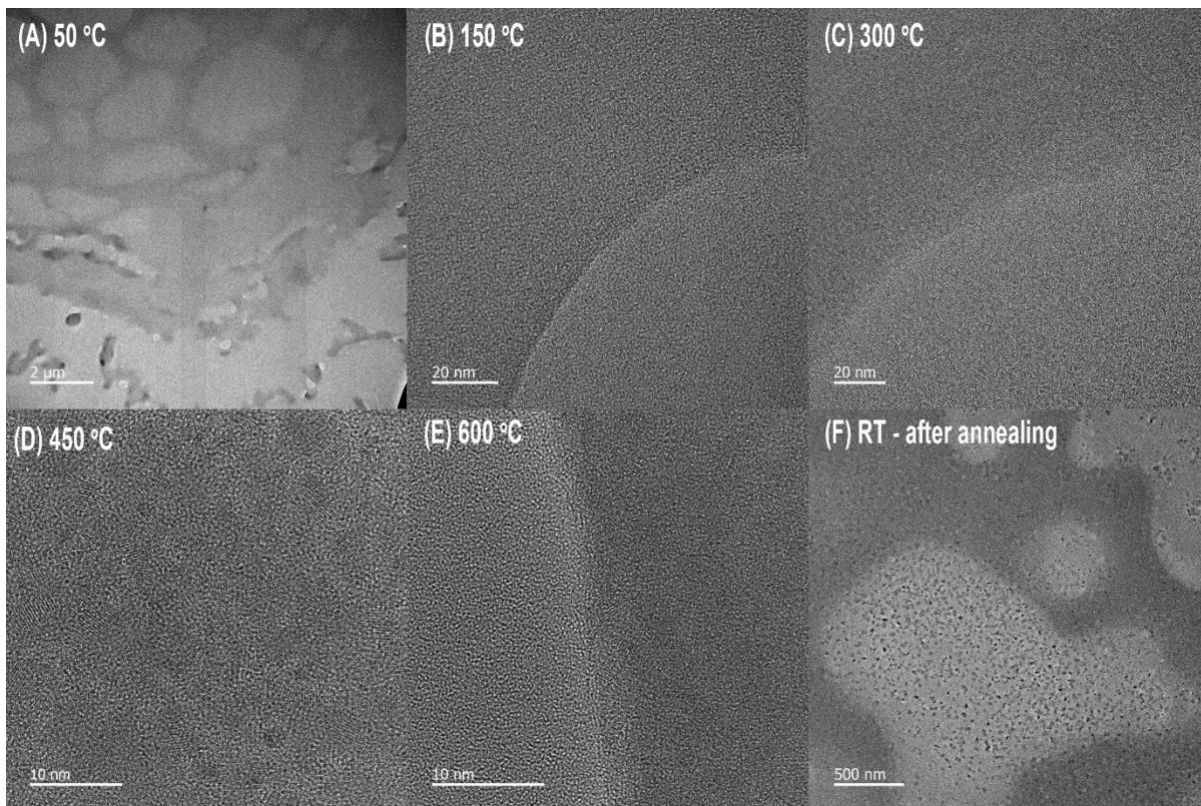


Figure 4. 16. Selected HRTEM images recorded during *in situ* annealing of SiO<sub>x</sub>@Cu<sub>grid</sub>-supported molybdenum thiolates grown by 6 ALD cycles

In the next step at 600 °C (image E), challenges related to constantly moving surface (due to unstable temperature) that is especially critical only in high-resolution images made it difficult to acquire a sharp image. In addition, at this temperature copper started to migrate over major parts of the sample surface. Nevertheless, on the less damaged parts, black nanoparticles and crystalline structures were observed on silica as well as in dark zones. A longer acquisition time lead to

decomposition of the observed sample.<sup>201</sup> Since captured images, especially in high magnification, were blurry, no indicative FFT pattern could be calculated. In the following stage, the sample was cooled to room temperature and the surface was analyzed by EDX spectroscopy. The results of the EDX and FFT analyses were not provided at the time of writing this thesis.

### *In situ annealing under argon atmosphere*

It was thought that the presence of H<sub>2</sub> facilitates not only the transformation of Mo thiolates into MoS<sub>2</sub> but also the migration of Cu from the grid, thus leading to unexpected side reactions involving Cu. Therefore, the next *in situ* annealing study was carried for ALD-grown Mo thiolates (3 cycles) in the presence of Ar gas (2 mbar). The grid's surface was imaged at RT, 50, 150, 300, 450, 600, 800 °C and finally again at RT for the possibility to conduct EDX analysis and take stable high-resolution images. See selected TEM micrographs in Figure 4. 17. The distribution of ALD-grown material had the same pattern (bright spheres and dark intersphere spaces) as previous samples analyzed under H<sub>2</sub>. Between RT and 300 °C, no distinct changes were observed on the surface that looked amorphous. The major difference was that worm-like and crystalline nanostructures became observed at higher temperatures. At 450 °C, there appeared very fine crystalline particles (<1-2 nm) that were barely noticed (Figure 4. 17A).

At 600 °C, the surface was covered not only with nanocrystalline particles but also with stick-shaped particles. In the beginning, high-magnification images (Figure 4. 17 images B, C) did not show any crystalline domains. After a longer exposure time (> 20 minutes) to the electron beam, the sticks started to show crystallinity aligned to their length. The width of the sticks was growing under the beam “*swallowing*” all the other small nanoparticles located next to them (see in Figure 4. 17D). Nevertheless, the appearance of the small crystalline nanoparticles out of the sticks reminded a layered pattern of MoS<sub>2</sub>.

At 800 °C, the surface was coated with nanoparticles of different shapes (Figure 4. 17E). Rods, triangular, pentagonal, and spherical morphologies were found all over the surface. Under the electron beam, their size continued to extend quickly (Figure 4. 17F). The HRTEM images of the rods and triangles revealed domains with well-ordered atoms of a single crystalline structure.

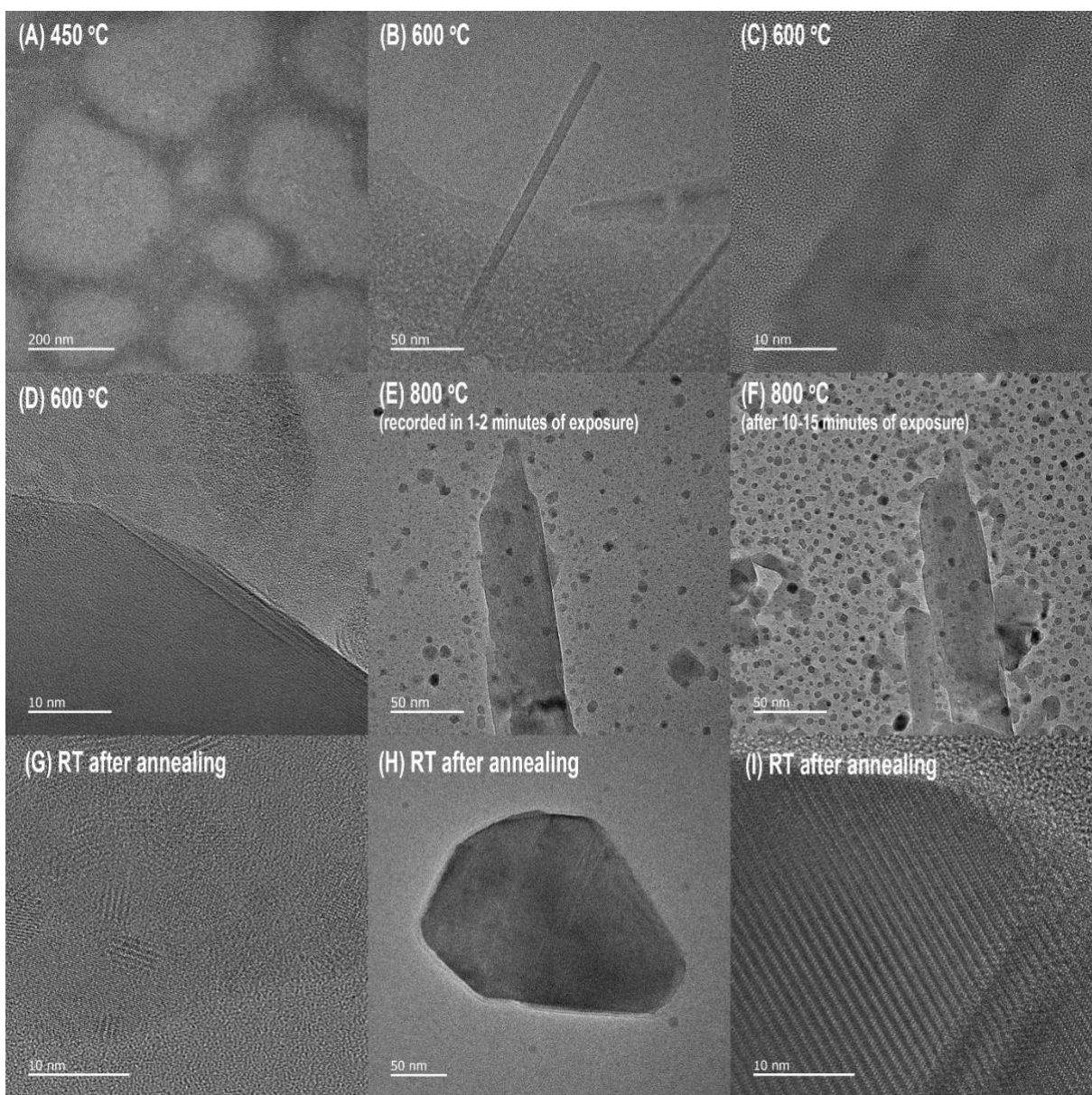


Figure 4. 17. Selected HRTEM images recorded during *in situ* annealing of SiO<sub>x</sub>@Cu<sub>grid</sub>-supported molybdenum thiolates grown by 3 ALD cycles

At room temperature, EDX analysis (see Figure 4. 3 and Table 4. 1) determined that most of the rod nanoparticles were composed of MoO<sub>3</sub> (also supported by the electron diffraction pattern parameters). Some triangle particles showed an atomic fraction of S much higher than that of Mo (S/Mo ratio > 8.2). Considering the well-ordered organization of atoms in crystalline domains, a high fraction of S may originate from the formation of CuS. EDX cannot define the real S/Cu ratio in a separate particle because the Cu signal is mostly contributed from the grid itself. However, some other triangles showed the S/Mo ratio as 2.6:1, which is closer to the expected ratio (2:1).

Nevertheless, it cannot be directly assigned to MoS<sub>2</sub>, because it can still be composed of CuS and MoO<sub>3</sub>. This proposal is supported by similar orientations of single atoms in the crystals (see in Figure 4. 17 I) of both triangles with a high S/Mo ratio and a low one. EDX found S and Mo in a 2 to 1 ratio on a brighter zone (out of black nanoparticles). Higher resolution images (Figure 4. 17G and *spectre 4* in Figure 4. 3) in the areas out of black particles shows layered patterns as well as crystalline nanodomains which are similar to those observed on silica nanobeads.<sup>19</sup>

In summary, the formation of MoS<sub>2</sub> was not out ruled, but mostly significant amount of MoO<sub>3</sub> was seen as well as spurious copper-based contamination coming from the grid. Oxidation of Mo (IV) to its Mo (VI) in oxide form was attributed to impurities present in argon. That is why the next *in situ* annealing of ALD-grown W thiolates was decided to carry in a dynamic UHV (10<sup>-6</sup> mbar).

#### 4.3.2.2. *En route to WS<sub>2</sub>*

##### *In situ annealing under an ultra-high vacuum*

Deposition of W thiolates was performed on the Cu TEM grid coated with the silica suboxide layer in the same manner as on the SiO<sub>2</sub>@Si wafers. After 3 ALD cycles, the grid was transferred onto a holder of the E-TEM for *in situ* annealing. The temperature of the grid holder was increased stepwise from 50 to 800 °C by 50 °C in each step and monitored by TEM. In the end, the temperature was lowered to RT, and the surface was analyzed by EDX spectroscopy and HRTEM. HRTEM micrographs recorded at each 100 ° between 300 and 800 °C are shown in Figure 4. 18. Between RT and 750 °C, the microscope images of low magnification showed that the surface has predominant deposition on the “islands” (see darker zones in Figure 4. 18A).

Such a pattern of the growth on the substrate can originate from the low concentration of the surface functional groups.<sup>185</sup> Several investigations in the ALD growth on the silica layer reported growth of islands.<sup>95,128,186,202</sup> The low concentration of Si–OH groups and their non-uniform distribution into spheres could originate from the nucleation of silica nanoparticles in the very first growth stages.<sup>203,204</sup> These literature precedents provide good support for the observed heterogeneity in Figure 4. 18A and evidence for the distribution of surface silanol groups into “islands” when SiOx rather than thermally grown silica is used.

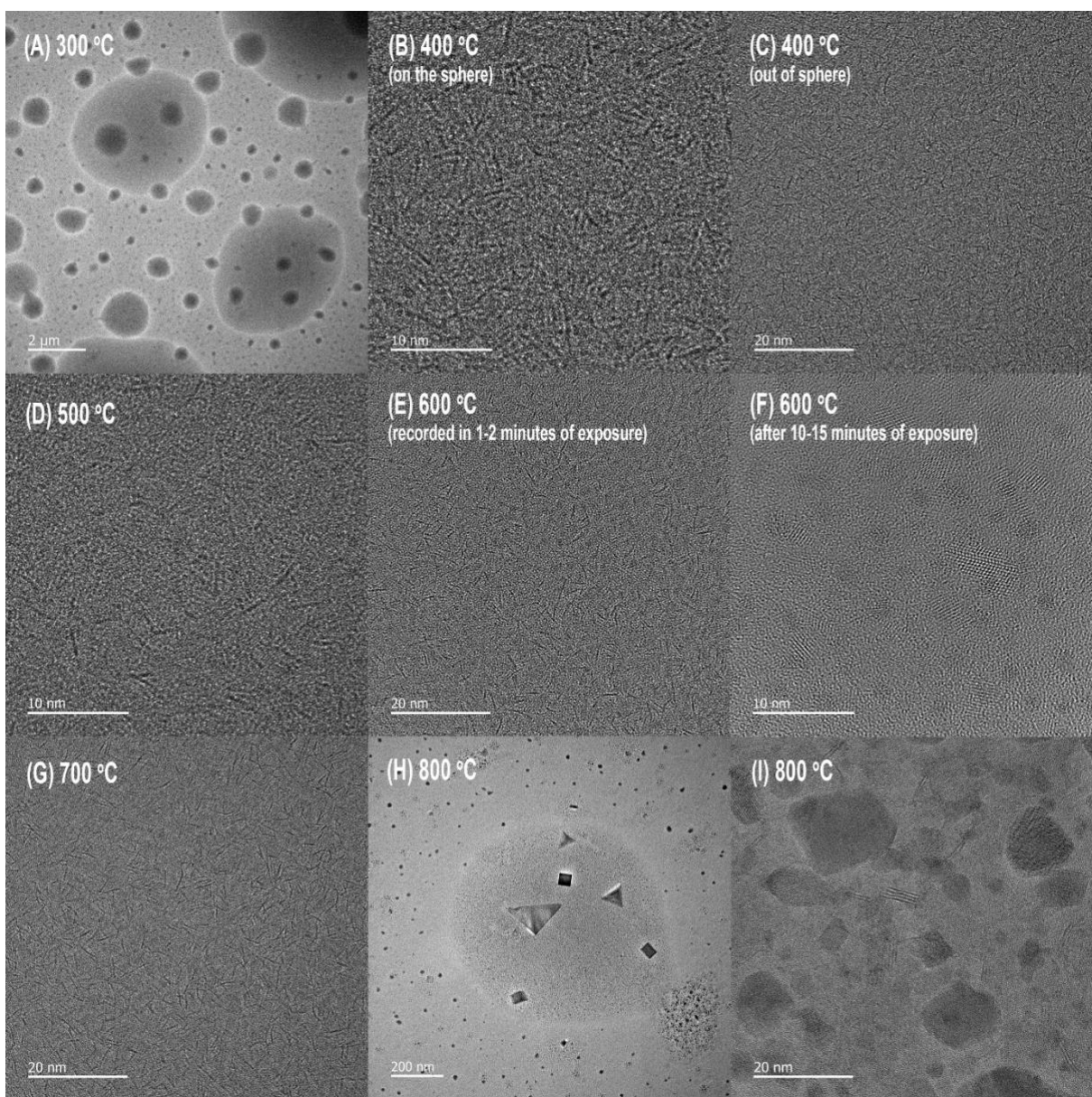


Figure 4. 18. Selected HRTEM images recorded during *in situ* annealing of  $\text{SiO}_x@Cu_{\text{grid}}$ -supported tungsten thiolates grown by 3 ALD cycles

Up to 300 °C, no distinct morphologies were seen neither on the spheres nor between the spheres (image A). The electron microscope revealed the formation of the worm-like patterns starting from 400 °C. Interestingly, these “worm” shapes were found both on spheres and on silica zones (see Figure 4. 18B and C). Hence, the conformal ALD growth is confirmed on zones of the high (spheres) and low (silica) density silanols. With a longer time of exposure (ca. 10-15 minutes) to the electron beam on the same spots, the formation of the nanocrystalline particles was observed. FFT analysis of one of such crystalline nanodomains formed under the electron beam was carried. The

results (see Figure 4. 5 in the experimental section of this chapter) suggested the beam-induced formation of crystalline tungsten sulfide of  $W_{21}S_8$  with a high deficiency of sulfur.

One of the illustrative examples of turning from worm shapes to nanocrystalline particles is demonstrated in Figure 4. 18E and F for the step at 600 °C. It should be noted that such transformation occurred at each step from 400 °C, while the step at 600 °C was selected because the particles' size was big enough for illustration. With each step to a higher temperature, the number of the worm shapes (image D and G) was slowly increasing and nanocrystalline particles were formed quicker and larger under the electron beam exposure.

At the final step (800 °C), the image of low magnification showed assemblies of dense nucleations around each sphere. Medium magnification image (image H) demonstrates black nanoparticles of different shapes (triangles, squares, rods, spheres). A close look at the spheres and out of them revealed the formation of the nanocrystalline particles with well-ordered atoms across the plane. Linear organization of more than ca. 10 atomic layers was observed in each particle. Nanodomains composed of several layers, which is a characteristic of the structure of  $WS_2$  (image I), were also seen both on the spheres and out of them. The average distance between single neighboring layers is about 0.62 nm. This value agrees with the reported distances between sulfur atoms of two neighboring stacks (0.614 nm)<sup>147,205</sup>.

After cooling to RT, different areas and individual nanoparticles were analyzed by EDX (see analyzed zones in Figure 4. 4 and atomic fractions in Table 4. 2). The relatively large area of “spectre 1”, and two black particles on the “spectre 2” and “spectre 4” areas showed sulfur deficiency with respect to targeted  $WS_2$ . Only one of the analyzed zones (spectre 3) exhibited a closer value ( $S/W = 1.7$ ). Mostly found zones showed the S to W ratio far-deviated from the expected values, thus suggesting that side reactions involving the released excess sulfur and similar to Mo thiolates samples occur at high temperatures. Besides, most of the analyzed areas showed the presence of Mn and K impurities that probably originated from the grid and/or its holder.

In summary, E-TEM characterization of the *in situ* annealing of the ALD-grown thiolates might show the formation of characteristic worm-like shapes of  $WS_2$  started around 350-400 °C under dynamic UHV. At higher temperatures, the features become more pronounced with a greater number of layered structures and crystalline nanodomains. As it was already seen by the XPS study, at temperatures above 500 °C unexpected side reactions can occur involving the Cu and excess sulfur. The FFT analysis results are not available at the time of writing this thesis, and thus could not

be included. Therefore, the more robust analysis results are being waited from the interpretation of obtained FFT at the intermediate annealing steps (400-700 °C).

## 4.4 CONCLUSION

The goal of this chapter was to test if initial pulses of ALD of  $\text{WS}_2$  on these 2D substrates follow analogous chemistry pathways as on the 3D substrates. Detailed characterization of ALD-grown samples on the  $\text{SiO}_2$ @Si wafers (and  $\text{SiO}_x$ @Cu grid) shows many similarities and some differences with respect to the results obtained on the silica powder.

ALD of W thiolates on 2D substrates ( $\text{SiO}_2$ @Si<sub>wafer</sub> wafer and  $\text{SiO}_x$ @Cu<sub>grid</sub>) has mostly displayed consistent results as it was seen by XPS, HRTEM, and EDX characterization. Unfortunately, still incomplete characterization (such as Raman and elemental analysis for example) as well as some internal inconsistencies in the ambitious *operando* approaches tried here, allows at this stage only partial conclusion.

The first pulse of BTBMW led to chemisorption of the complex in a similar manner on both silica nanobeads and silica-coated Si wafer. Surprisingly, unexpected, minority  $\text{WSi}_x$  might be involved in the first step. Then the second half-cycle generates the W–S bond and modifies the amido group as observed by XPS of the molecular analogue and by IR and elemental analyses on silica nanobeads. The successful deposition of BTBMW in the third pulse signifies the availability of free –SH groups. In the fourth pulse, EDT binds to the W, hydrogenates the amido group, and keeps the oxidation state of W “reduced”. XPS and HRTEM data collected in *in situ* annealing experiments have displayed deeper insights into the formation of  $\text{WS}_2$  from W thiolates. As it was seen from XPS data, the fractions of carbon and nitrogen decrease while tungsten remains unchanged though the binding energy of W 4f shifts down which was a clear sign for its reduction.

At this stage, little can be asserted with confidence from the ambitious and one-of-the-kind E-TEM study attempt. On a positive note, the pertinence of the approach seemed validated with results from the  $\text{MoS}_2$  system (using an ALD process developed before this thesis). In this case, uniform amorphous deposit (presumably molybdenum (IV) thiolates) evolve to the lamellar structure upon *operando* annealing, assigned to  $\text{MoS}_2$ .

The experiment with tungsten is not direct. Firstly, the initial deposit appears to be in island growth. While we rationalize this by invoking our lack of initial correct rehydration of the native  $\text{SiO}_x$  film, the island growth negatively affects the homogeneity of the phenomena studied. Secondly, no clear crystallization to  $\text{WS}_2$  is observed at moderate temperatures. Even if the worm-like structure seems to appear no stronger corroborating evidence (FFT, EDX analyses) is available. No clear large

crystalline domains are present. Analysis at higher temperatures is marred by contamination from the copper-containing sample holder (grid).

In summary, the E-TEM study is still too early in its deployment. At the same time, the strategy chosen appears pertinent and corroboration with spectral data should overall strengthen this bold new approach to merge molecular insight on 3D supports with real ALD growth on 2D ones.

**Chapter 5 - PHOTO- and  
ELECTROCATALYTIC  
PERFORMANCE OF ALD-GROWN  
WS<sub>2</sub>**

## 5.1 INTRODUCTION

This chapter will test the performance of ALD-grown thin WS<sub>2</sub> layers in energy converting devices (specifically electrocatalytic cells for CO<sub>2</sub> reduction). In this case, TiO<sub>2</sub> nanotubes (TNT's) grown on Ti disk and carbon nanotubes (CNT) have been selected, given their more established role in energy converting devices. An immediate word of caution is called before proceeding further. Growing WS<sub>2</sub> on ultimate surfaces other than silica by applying the same ALD protocol developed purposefully for silica and then jumping directly (that is without investing as much energy in questioning the validity of this translation) to testing directly the performance is at least a two-leap jump. To partly address this lack of thorough scientific rigor, this introduction offers some of the elements in the literature that seem to condone such a jump. Two families of such elements will be presented: on one hand, what is known of TiO<sub>2</sub> and carbon nanotube ultimate surfaces and how it may favorably relate to silica ultimate surface is presented, on the other hand, literature examples suggesting that “squeezing out of the middle step” appears like a common practice in relevant and interesting literature.

### 5.1.1. TiO<sub>2</sub> as an ALD substrate and its ultimate surface

Titania nanotubes arrays (TNT's) combine a photoactive oxide with highly active nanostructured surface functional groups. Titanium dioxide is well-known for its strong features in the photo(electro)chemical water splitting,<sup>206–208</sup> photochemical reduction of CO<sub>2</sub>,<sup>209–211</sup> photocatalysis of waste degradation,<sup>212</sup> in paints, as a pigment, etc. Anatase and rutile are the most commonly used polymorphs of titania among three existing ones (the third crystalline phase is brookite).

Understanding the surface functional groups lays a path towards better understanding the surface reactions. The titanol groups were previously characterized by the alumnus of the C2P2 laboratory and SINCHEM doctoral program, Dr. Tapish Saboo.<sup>213</sup> The TiO<sub>2</sub>-anatase bears three kinds of reactive hydroxyl groups that can be identified by the absorption bands in the IR range of 3600-3800 cm<sup>-1</sup> as terminal Ti–OH on (001) facet, coordinated water on the (100) facet, and bridging Ti–μ<sub>1</sub>–OH on (101) facet (in Table 5. 1).

Surface functional groups of titania were reported to be reactive towards transition metal complexes bearing allyl<sup>214</sup>, acetylacetonate<sup>215</sup>, and dimethylamido<sup>216</sup> ligands. The state of the art works on

SOMC on the titania surface are briefly described below in comparison with surface properties of silica.

Table 5. 1. IR bands and density of surface titanol groups on different titania anatase crystal planes reported in the thesis of T. Saboo

Titanol binding scheme	Corresponding crystal plane	IR band / $\text{cm}^{-1}$	Density / ( $[\times\text{OH}]/\text{nm}^2$ )
	(101)	3670	0.27
	(001)	3741	0.14
	(100)	3715	0.36

S.G. Shore et al<sup>214</sup> have conducted surface organometallic studies on grafting of  $\text{Rh}(\text{allyl})_3$  complex onto silica, titania, alumina, and magnesia. Among these supports, partially dehydroxylated  $\text{TiO}_{2-250}$ ,  $\text{SiO}_{2-(100-550)}$  and  $\text{Al}_2\text{O}_{3-350}$  behaved similarly binding bis(allyl)rhodium upon releasing propene (quantified by GC). As it was observed in IR spectra, the surface reaction paths on the three oxides proceed by the cleavage of surface  $\equiv\text{MO}-\text{H}$  bonds and metal-ligand,  $(\eta^3-\text{C}_3\text{H}_5)_2\text{Rh}-(\eta^3-\text{C}_3\text{H}_5)$ , bonds and forming  $\text{M}-\text{O}-\text{Rh}(\eta^3-\text{C}_3\text{H}_5)_2$  (where  $\text{M} = \text{Si}, \text{Ti}$  or  $\text{Al}$ ). Despite the different nature and concentration of the surface  $-\text{OH}$  bonds on the mentioned substrates, the same resulted grafted bis(allyl)rhodium species demonstrate a similar reaction mechanism.

A study of the first chemical deposition of vanadium alkylamido complex onto partially dehydroxylated silica, titania, and alumina was reported by S. Grasser and co-workers.<sup>216</sup> The authors determined that the vanadium complex undergoes mono-grafting on silica, bis-grafting on alumina, and tris-grafting on titania yielding  $\equiv\text{SiO}-\text{V}(\text{NMe}_2)_3$ ,  $(=\text{AlO})_2-\text{V}(\text{NMe}_2)_2$ , and  $(\equiv\text{TiO})_3-\text{V}(\text{NMe}_2)$  surface species, respectively. After the reaction of the oxides with tetrakis(dimethylamido)vanadium (IV), elemental analyses of vanadium and nitrogen served to estimate the N:V ratio in three grafted complexes as ca. 3:1, 2:1, and 1:1 for  $\text{SiO}_2$ ,  $\text{Al}_2\text{O}_3$ , and  $\text{TiO}_2$ , respectively. The elemental analyses were accompanied by the electron paramagnetic resonance

(EPR), IR, and solid-state NMR spectroscopy results to state the common reaction mechanism. Despite proceeding with different degrees of the substitution reactions with the surface hydroxyl groups, the formation of the V–O bond in place of the V–NMe<sub>2</sub> was assessed. Different degrees of substitution can be explained by the various density and reactivity of surface hydroxyls on these oxides depending on the pretreatment conditions.

The above-mentioned SOMC reports lead us to expect a reaction mechanism of the ALD growth on titania similar to what we could explore in molecular reactions and silica nanobeads in Chapter 2. The results on SiO<sub>2</sub>@Si wafer discussed in the previous chapter can, on the other hand, encourage us on assuming that thin film or nanotubes of TiO<sub>2</sub> grown on 2D substrates (e.g. Ti foil) are supposed to behave similarly to titania nanobeads 3D substrates.

Adequate irradiation of a semiconductor such as titania generates negatively charged electrons and positively charged holes that may undergo various paths. They may participate in the desired reduction and oxidation reactions, respectively, recombine with each other and produce heat, or to be trapped by other adsorbed species. Research work involving doping the titania with various species has greatly enhanced its photoactivity in the last few decades.<sup>210,217</sup>

Titania is a photoactive semiconductor with bandgap energies of 3.20 eV for anatase<sup>212</sup>, 2.98 eV for rutile,<sup>218</sup> and 3.26 eV for brookite<sup>212</sup> phases. The flat band energies were measured as a function of pH and defined at -0.45, -0.37 and -0.46 V (vs NHE) at pH = 7 by Di Paola et al.<sup>218</sup> These values make titania suitable for HER and OER from the thermodynamics point of view (see Figure 5. 1). The conduction band of the anatase is located higher (more negative) than the reduction potential of the 2H<sup>+</sup>/H<sub>2</sub> couple (-0.41 V vs NHE) and its valence band is at a lower potential (more positive) than the reduction potential of H<sub>2</sub>O/O<sub>2</sub> (0.82 V vs NHE). However, the photoactivity of titania is turned on only upon electronic excitation by UV-light irradiation because its absorption band is below 380 nm. Taking into account that UV light fraction in solar light is around 3%, the final effectiveness of titania itself is supposed to be low in real conditions. That is why, a possible approach to circumvent this limitation is by doping titania with metal nanoparticles<sup>206</sup>, non-metals<sup>217,219,220</sup>, sensitizing dyes<sup>221</sup>, and graphene<sup>211</sup>. Another method is to reduce pH below 7 to lower the reduction potential. This is why most of the photoelectrochemical cells (PEC) establish an acidic medium (pH=0) on the cathodic side to decrease the reduction potential of 2H<sup>+</sup>/H<sub>2</sub> couple to zero.<sup>13,222,223</sup>

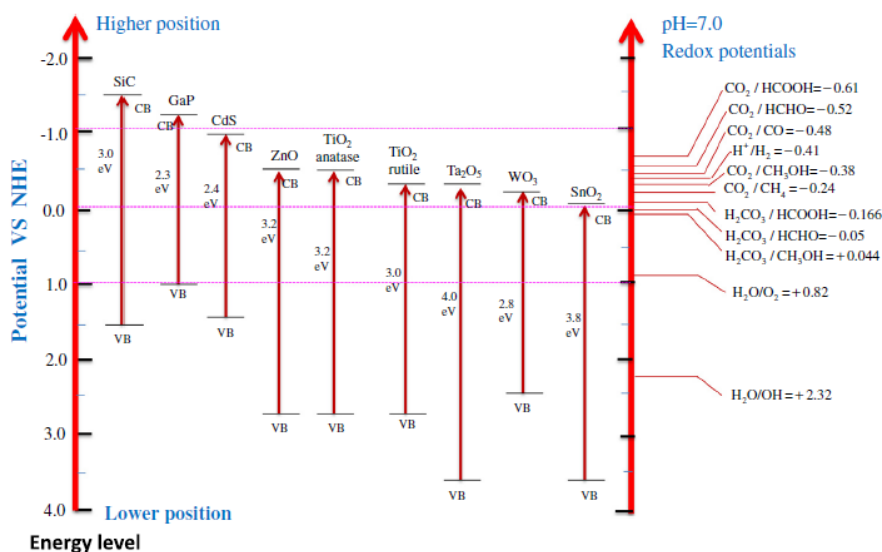


Figure 5. 1. Bandgap energies of several semiconductors including TiO<sub>2</sub> presented versus thermodynamic reduction potentials of various compounds at pH = 7. Reproduced with permission from ref<sup>210</sup>

Noteworthy, the same ALD process, Mo(NMe<sub>2</sub>)<sub>4</sub> and H<sub>2</sub>S, works on SiO<sub>2</sub>@Si wafer<sup>93</sup> and we had shown a little extra that the ALD process with Mo(NMe<sub>2</sub>)<sub>4</sub> and EDT works on SiO<sub>2</sub>@Si wafer and on silica nanobeads.<sup>19</sup> This is further evidence that supports our attempt to make the ALD process tested so far based on BTBMW and EDT on 2D and 3D SiO<sub>2</sub> and 2D TiO<sub>2</sub>.

To improve catalytic properties of the TNT's, they have also been coated with ALD-grown MoS<sub>2</sub> using Mo(NMe<sub>2</sub>)<sub>4</sub> and H<sub>2</sub>S precursors.<sup>49</sup> In a joint work between our group and Prof. Bachmann's group in U Erlangen, TiO<sub>2</sub> nanotubes were uniformly coated with MoS<sub>2</sub>. The growth of MoS<sub>2</sub> onto TNT's@Ti<sub>foil</sub> was confirmed by EDX (S:Mo = 2:1) and XPS analyses, though the XRD measurements showed no peaks corresponding to MoS<sub>2</sub>. The authors link it to the formation of an amorphous phase of the film at 95 °C.

Figure 5. 2 illustrates the nanotubes before (a) and after (b) coating with 80 ALD cycles of MoS<sub>2</sub>. As a visual confirmation of the film growth, the thicker thickness of the tube walls is observed after the coating.

The MoS<sub>2</sub>-functionalized TNT were tested for hydrogen evolution reaction (HER) (see Figure 5. 2c)

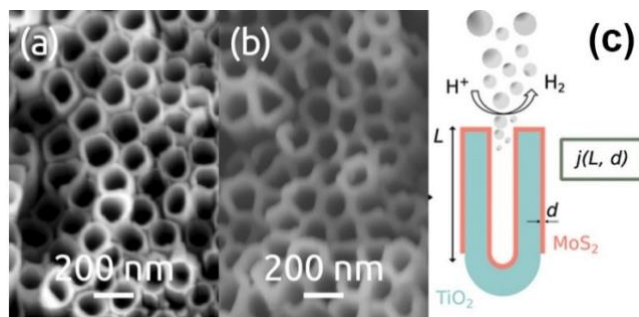


Figure 5. 2. Scanning electron microscopy images of annealed TNT's before (a) and after MoS<sub>2</sub> coating by 80 ALD cycles (b). (c) - Uniform deposition of MoS<sub>2</sub> thin film on nanostructured high aspect ratio substrate, TiO<sub>2</sub> nanotubes, by ALD. Reproduced with permission from ref<sup>49</sup>.

The electrocatalytic performance of the MoS<sub>2</sub>-coated electrodes towards HER has been greatly improved for both TiO<sub>2</sub> substrate morphologies, planar, and tubular. The current density at -0.45 V (vs SHE) increased about 10-fold comparing the bare TNT's and the coated electrodes with 30, 50, and 80 ALD cycles of MoS<sub>2</sub>. These different numbers of the cycles did not lead to a proportional increase of the current density. This is consistent with catalytic surface reactions occurring only on the active area and dense MoS<sub>2</sub> deposition. Increased catalytic activity in HER was supported by significantly lowered charge-transfer resistance from 85 kΩ for bare planar TiO<sub>2</sub> substrate down to ca. 164 Ω for MoS<sub>2</sub> coated TNT's. This way, it was well demonstrated how poor activity of one material can be greatly advanced by a uniform film of an active material grown by ALD. Taking into account similar features of WS<sub>2</sub> and MoS<sub>2</sub>, the growth of WS<sub>2</sub> thin film on TiO<sub>2</sub> should also enhance the photocatalytic properties of the substrate.

### 5.1.2. Carbon nanotubes as an ALD substrate and its ultimate surface

High-surface-area and highly conductive carbon nanotubes (CNTs) functionalized with catalytic thin films or nanoparticles were demonstrated as promising catalytic composites,<sup>224,225</sup> and are generally identified as pertinent electrode component in the electrocatalytic reduction of CO<sub>2</sub>.<sup>224,226,227</sup> Since transition metal dichalcogenides showed good efficiency towards CO<sub>2</sub> reduction,<sup>228</sup> the ALD growth of WS<sub>2</sub> onto CNTs surface for the electrocatalytic conversion of CO<sub>2</sub> is an attractive strategy.

CNTs surface is reputed to be inert towards the first cycles of ALD.<sup>79</sup> Therefore, the growth of thin films is achieved via pretreatment of CNT with strong acids or oxidants (e.g. HNO<sub>3</sub>, O<sub>3</sub>) that covalently bind various functional groups (alcohols, ketones, carboxylic acids, esters, amides, etc.)<sup>229,230</sup> to the surface enabling the reaction with ALD precursors. There are also noncovalent functionalizations that are based on adsorbing polymers, surfactants or other anchoring molecules establishing intermolecular interactions such as van der Waals,  $\pi$ - $\pi$  interactions, hydrogen bonding, electrostatic forces, etc.<sup>231-233</sup>

Precedents of successful coating CNT by ALD are present in the literature for example, for coating with Al<sub>2</sub>O<sub>3</sub><sup>234</sup>. To the best of our knowledge, there are no other precedents of ALD-grown WS<sub>2</sub> on CNT besides the contribution by Pr. N. Pinna from Humboldt University in collaboration with us.<sup>15</sup> In this work, N. Pinna and co-workers showed that the same ALD process developed for SiO<sub>2</sub>@Si wafer with BTBMW and H<sub>2</sub>S (and partly modeled by us on silica nanobeads) works also for growth onto multi-walled (MW) CNTs pretreated in concentrated HNO<sub>3</sub>.<sup>15</sup> Grown film can be seen as dark platelets on the walls of CNTs as can be seen in HRTEM micrograph (Figure 5. 3).

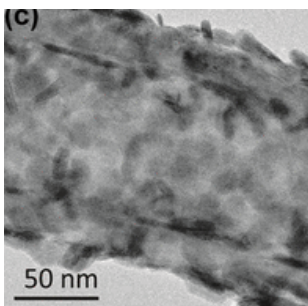


Figure 5. 3. Functionalized CNTs with 200 ALD cycles of WS<sub>2</sub> on the surface. Reproduced with permission from ref.<sup>15</sup>

Therefore, few samples with a different number of ALD cycles of WS<sub>2</sub> on MWCNTs were prepared and tested for electrocatalytic reduction of CO<sub>2</sub> in collaboration between research groups in Lyon, Messina, and Berlin universities in the framework of this thesis (see result and discussion section).

Non-ALD precedents for WS<sub>2</sub>-coated CNT exist and show relevance for energy device development. One of the previous works demonstrated a significant increase in Li-ion battery cell capacity when MWCNTs were introduced as a scaffold to the WS<sub>2</sub>-coated anode.<sup>17</sup> Cyclic voltammetry measurements in this study also revealed good intercalation features of WS<sub>2</sub> film for Li<sup>+</sup> ions.

Another literature precedent demonstrated high photocatalytic activity by a composite sample based on the interphase between carbon dots (CDs) and WS<sub>2</sub>. The hybrid structure (WS<sub>2</sub>-CD) enhanced photocatalytic degradation of Congo Red dye with respect to pristine 2D WS<sub>2</sub> monolayer as it can be seen in Figure 5. 4.

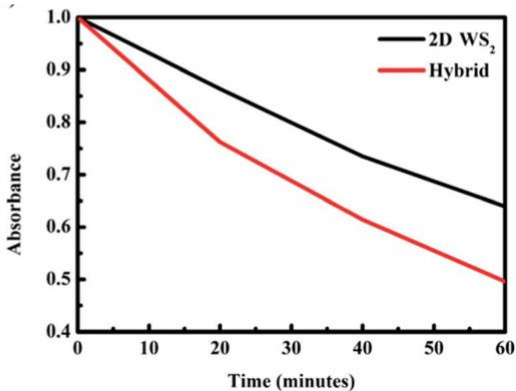


Figure 5. 4. A plot of absorbance vs. time showing photocatalysis rates of the pristine WS<sub>2</sub> and hybrid (CD-WS<sub>2</sub>) samples. Reproduced with permission from ref.<sup>235</sup>

These precedents raised the interest to study the catalytic performance of CNTs coated by a thin film of WS<sub>2</sub> via ALD. Specifically, the WS<sub>2</sub>@CNT composites developed by Pr. Pinna were tested in the electrochemical reduction of CO<sub>2</sub> as a cathode.

## 5.2 EXPERIMENTAL SECTION

### 5.2.1. Preparation and characterization of Ti disk-supported samples

#### 5.2.1.1. TNT's growth on a Ti disk by anodization

This procedure follows the protocol described elsewhere.<sup>208</sup> Before anodization, the titanium metallic disks (Alfa Aesar, a diameter of 3.5 cm, the thickness of 0.025 mm, Ti purity of 99.96 and 99.8 %) have been sonicated in 10-20 mL of isopropanol under ultrasound for 30 minutes. Electrochemical controlled growth of titania nanotubes on the surface of Ti foil has been performed in a two-electrode cell in ethylene glycol containing 0.3 wt. % ammonium fluoride and 2.3 vv. % ultrapure water by chronoamperometric anodization at 50.0 V for 45 minutes. After anodization, the disks are rinsed with isopropanol, calcined at 450 °C for 3 hours (ramp of 2 °/min) in the air, and sonicated in isopropanol for 30 seconds to remove the top amorphous layer. The chosen duration of the anodization was reported to grow TNTs of ca. 1 μm in height (see Figure 5. 6).

#### 5.2.1.2. ALD of WS<sub>2</sub> on a TNT's@Ti disk

Before ALD, the disks are dehydroxylated at 200 °C in a dynamic UHV (10<sup>-5</sup> mbar) for 1 hour and stored in the glovebox. The two separate bulbs equipped with Young's valves of the ALD glass reactor, discussed in the results section of this chapter, are loaded with 500 μL of distilled BTBMW, 200 μL of EDT, previously dried over molecular sieves. The TNT's@Ti disk was loaded in the main reactor chamber. The glass reactor is connected to the UHV line that allows establishing a static vacuum of 10<sup>-5</sup>-10<sup>-6</sup> mbar before each pulse. Each ALD cycle was composed of four main steps: (i) pulse of the BTBMW precursor for 10 minutes at 60 °C that increases pressure in the main tube up to 5·10<sup>-4</sup>-1·10<sup>-3</sup> mbar; (ii) purging under vacuum until ~5·10<sup>-5</sup> mbar for 10-15 minutes; (iii) pulse of the EDT precursor for 2 minutes at room temperature; (iv) purging under dynamic vacuum until ~5·10<sup>-5</sup> mbar for 15 minutes. After performing the desired number of ALD cycles, the disks were annealed under the flow of argon (60 sccm) at 500 °C for one hour (ramp = 2 °/minute).

#### 5.2.1.3. Photocurrent generation tests by chronoamperometry

The chronoamperometry tests were performed at the University of Messina under the supervision of Dr. F. Tavella and Dr. C. Ampelli. The Ti disks with grown TiO<sub>2</sub> nanotubes on the surface have been tested in photocurrent generation before and after ALD in a setup discussed elsewhere.<sup>236</sup> The TNT's@Ti disk was connected as a working electrode in a three-electrode cell equipped with two other electrodes: reference Ag/AgCl (3M KCl) and counter Pt. Photocurrent response was evaluated in an aqueous 0.5 M solution of Na<sub>2</sub>SO<sub>4</sub> at an applied potential of 0.3 V. The Ti disk was irradiated by a xenon lamp through a quartz window of the cell. Between the lamp and quartz window, the

shutter was positioned at a 3 cm distance and controlled to alternate off/on positions for 30 seconds at each position.

## 5.2.2. Preparation and characterization of CNTs-supported samples

### 5.2.2.1. ALD of WS<sub>2</sub> on CNTs

The samples were prepared and provided by the research group of N. Pinna *et al.* in Berlin. The preparation method was reported in ref.<sup>15</sup> Its short description is provided here. Powder of CNTs (200 mg) was dispersed in concentrated nitric acid (100 mL), stirred, and refluxed at 105 °C for 6 hours. CNTs were washed with distilled water. The acid was removed by redispersing in water and centrifugation cycles. 10 mg of dried powder (80 °C overnight) was dispersed in 2 mL ethanol by ultrasonication (30 minutes) for drop-casting on an Al foil. ALD of WS<sub>2</sub> onto CNTs was performed using BTBMW (maintained at 80 °C) and H<sub>2</sub>S precursors (no preheating) at 300 °C.

### 5.2.2.2. Electrocatalytic tests of CO<sub>2</sub> reduction

The electrocatalytic reduction measurements were performed in collaboration with research group members in the University of Messina, M. Daniele Giusi and M. Matteo Miceli. A lab-scale electrocatalytic reactor used for CO<sub>2</sub> reduction tests<sup>237</sup> was composed of liquid-phase three-electrode electrochemical cell made of Plexiglass for visual control, working electrode (on the cathodic side), saturated Ag/AgCl reference electrode (located at 0.5 cm distance from the working electrode), and Pt counter rod-shaped electrode (Amel) on the anodic side. See a schematic illustration of the reactor in Figure 5. 5. 1.6-1.7 mg of CNTs functionalized by ALD-grown WS<sub>2</sub> (50, 200, and 300 cycles using BTBMW and H<sub>2</sub>S prepared in Berlin by Prof. Pinna's group) were suspended in isopropanol (5 mL) containing liquid Nafion (50 µL), sonicated for 30 minutes and sprayed onto the working electrode (1 cm × 1.5 cm size) made of GDL by spray-coating technique. Loading of the WS<sub>2</sub>@CNT composite reached 1.1 mg/cm<sup>2</sup>. The working area of the electrode is 1 cm<sup>2</sup> out of total 1.5 cm<sup>2</sup>. A proton-conducting membrane (Nafion® 117, Ion Power) was placed between the anode and cathode compartments for physical separation. Anodic and cathodic sides were filled with KHCO<sub>3</sub> (0.5 mol·L<sup>-1</sup>) solution that served as a supporting electrolyte. The electrolyte solution was saturated with a continuous flow of pure CO<sub>2</sub> (10 ml·min<sup>-1</sup>) in an external reservoir that prevents direct striking the cathode surface with gas bubbles. A peristaltic pump continuously circulated the electrolyte solution between the cathode compartment and the external container. The total volume of solution in the cathodic part and the external container was 20 ml, while the anodic part contained 9-10 ml of the electrolyte solution. Constant voltage differences (-0.4, -0.6, and -0.8 V vs. RHE) between the working and counter electrodes were supplied by a potentiostat/galvanostat (Amel mod. 2049A).

The liquid products were analyzed by sampling the liquid from the external container and determining the composition of the solution using ion chromatography. The gas products were

detected by sampling the gaseous stream leaving the external container at regular intervals into gas-chromatography (GC-TCD, Agilent 7890A, column 5A Plot).

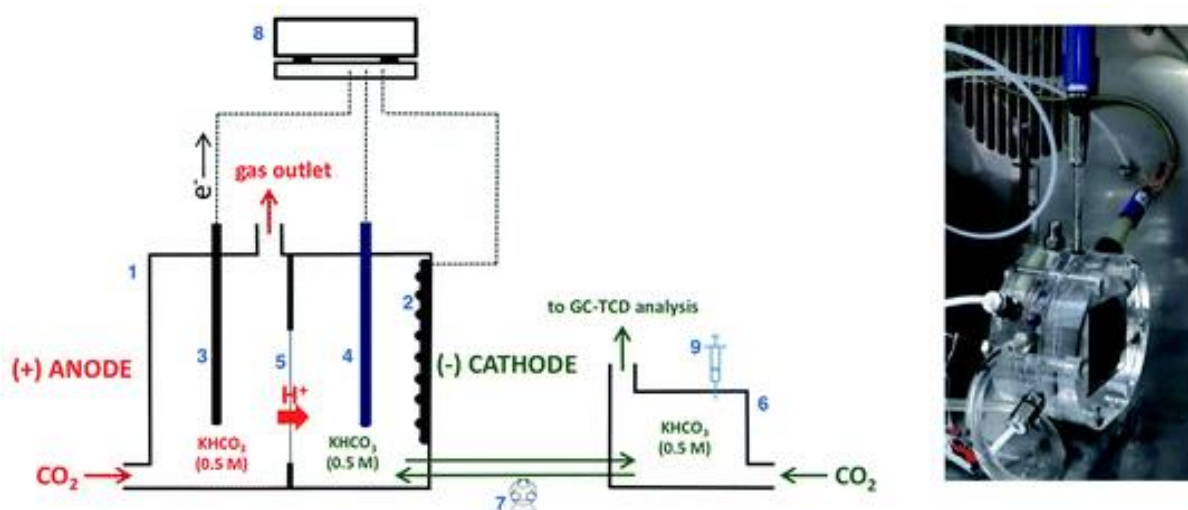


Figure 5. 5. Scheme of the electrocatalytic reactor for CO<sub>2</sub> reduction tests. 1 – liquid-phase electrochemical cell; 2 – working electrode; 3 – Pt counter electrode; Ag/AgCl reference electrode; 5 – nafion®; 6 – external container; 7 – peristaltic pump; 8 – potentiostat/galvanostat; 9 – sampling for GC-MS;. The scheme was reproduced with permission from ref.<sup>237</sup>

Two liquid electrolyte samples taken from the cathodic part of the measurement with 200-WS<sub>2</sub>@CNT and 300-WS<sub>2</sub>@CNT (both at -0.6 V) were analyzed by GC-MS Shimadzu QP 2010 equipped with the ZB-WAX Plus column (60 m × 0.25 mm × 0.25 μm) with the aim to find (at least qualitatively) light alcohols. This measurement was carried in collaboration with Dr. Nolven Guillaume at IRCELYON. This analysis did not detect any alcohol. However, it is not definitive proof of the absence of alcohol in the electrolyte after the reduction test for all the samples given the fact that only 2 out of 18 (6 liquid samples for each WS<sub>2</sub>@CNT composite ) samples were analyzed.

## 5.3 RESULTS AND DISCUSSION

### 5.3.1. WS<sub>2</sub> films grown on TiO<sub>2</sub>@Ti disk by ALD and their photocurrent production tests

Titania nanotube arrays (TNT's) have been successfully grown on titanium disk during 45 minutes of anodization at 50.0 V. This duration of the anodization was chosen because disks anodized for 45 minutes have shown the maximum H<sub>2</sub> production rate earlier.<sup>208</sup> This method of TNT's growth has been previously established by the research group at the University of Messina<sup>208,236,238–240</sup>. With 45 minutes of anodization of Ti disk at -50.0 V, TNT's extend vertically in about 1.0 μm of height. The tubes grow around 23 μm in thickness on average as observed by scanning electron microscopy (SEM) in Figure 5. 6.

The ALD growth of WS<sub>2</sub> on the 2D substrate, titania nanotube arrays grown on titanium foil (TNT's@Ti) was performed applying the methodology developed for 3D silica particles. Some process variations for ALD were also tried: (i) ALD on pre-calcined titania NT's or ALD without calcination, but in both cases followed by annealing under argon flow after ALD; (ii) performance of the BTBMW pulse at 60 and 20 °C; (iii) purity of the used Ti disk of 99.96% and 99.8%; (iv) 3, 5 and 8 ALD cycles. Samples after ALD of WS<sub>2</sub> with all information are provided in the table below (Table 5. 2).

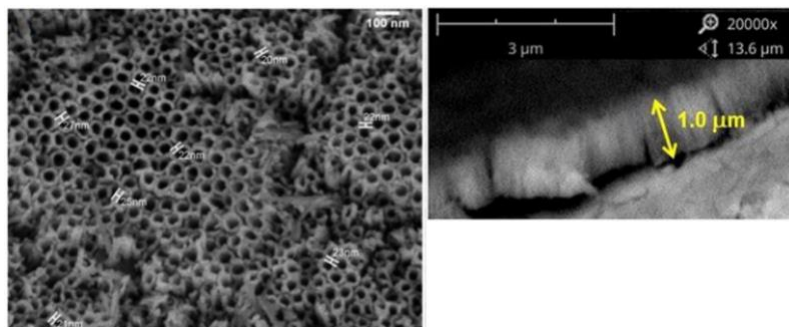


Figure 5. 6. SEM images of top view (left) and cross-section (right) of bare TNT's@Ti (adapted from ref<sup>207,208</sup>)

The ALD of WS<sub>2</sub> was carried in a glass tubular homemade reactor linked with two separate bulbs mentioned in chapter 3 (see Figure 3. 1). Via a greased key, the main chamber of the reactor is connected to the UHV line that can establish low pressure down to 10<sup>-6</sup> mbar. Young's valves allowed to open the bulbs containing BTBMW and EDT precursors to start diffusing the vapors

towards the substrate. Before the first pulse and between each BTBMW and EDT pulses, the main chamber was evacuated by making a vacuum of  $5 \cdot 10^{-5}$  mbar to ensure the elimination of excess reactant and by-products as well as good diffusion of the vapors. Through the glass walls of the reactor, it was possible to observe the color changes after initial pulses. Though we could not record the colors during ALD by a photo due to the outer grease and light reflection from the glass wall, all the transformations before and after ALD steps are illustrated by photo in Figure 5. 7. The disks of higher purity (99.96%) tended to bend strongly after calcination at 450 °C (shown in Figure 5. 7E) whereas lower purity (99.8%) disks kept its shape stable yet producing lower photocurrent (ca. ~2.5 vs. 4.2 mA). A straight line on disks appears after anodization because one of the edges is needed to use for holding. Therefore, the little part across this line remains non-anodized, and consequently, it is not covered with the TNT's layer. After ALD, a small non-anodized part maintains its initial color that was before ALD (see Figure 5. 7F and G). Image G illustrates the growth of W thiolates on the anodized part of the disk turning it to red that confirms good reactivity with the surface  $\equiv\text{Ti-OH}$  functional groups. At the same time, the non-anodized part stays inactive in the ALD that can be attributed to the poor reactivity of functional groups (Ti-H and Ti-O-Ti) on the metallic surface.

Table 5. 2. List of TNT's@Ti samples after ALD of WS<sub>2</sub> with different variations of the procedure. All the Ti disks were anodized for 45 minutes before the ALD.

Run #	Purity of Ti disk /%	Calcination <sup>a</sup>	Number of ALD cycles	Temperature of the metal pulse
1	99.96	Before	5	60 °C
2	99.8	Before	5	60 °C
3	99.8	After	3	60 °C
4	99.8	Before	5	20 °C
5	99.8	After	5	60 °C
6	99.8	After	8	60 °C

<sup>a</sup> – the TNT@Ti disk was either calcined at 450 °C in the air before the ALD of WS<sub>2</sub> or annealed at 500 °C in argon flow after the ALD

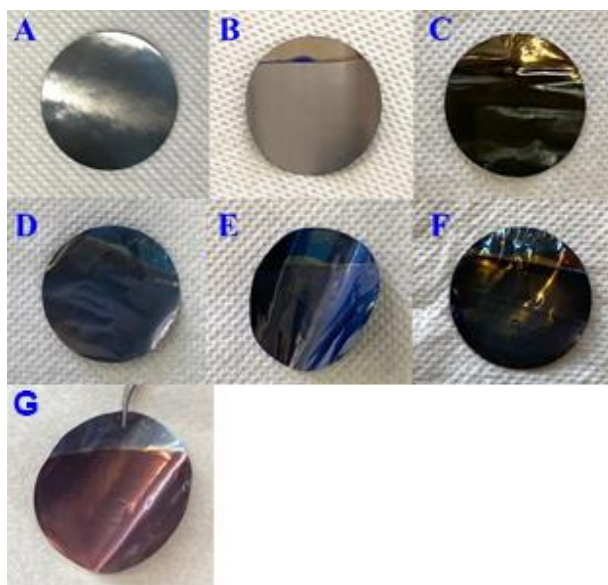


Figure 5. 7. The appearance of Ti foil discs before and after anodization and ALD: A - bare Ti disk before anodization; B – TNT's@Ti<sup>99.8%</sup> after anodization; C - WS<sub>2</sub>-TNT's@Ti<sup>99.8%</sup> after ALD and annealing; D – TNT's@Ti<sup>99.96%</sup> after anodization; E – bent disk of TNT's@Ti<sup>99.96%</sup> after anodization and before ALD; F - WS<sub>2</sub>-TNT's@Ti<sup>99.96%</sup> after ALD and annealing; G – TNT's@Ti<sup>99.96%</sup> after anodization and 3 full cycles of ALD before annealing (captured in the glovebox)

SEM measurement and EDX analysis were done on a sample obtained through 3 ALD cycles on pre-calcined TNT's@Ti<sub>disk</sub><sup>99.96%</sup> (see Figure 5. 8). The hollow parts that were seen between the TiO<sub>2</sub> nanotubes in Figure 5. 6 are not observed after ALD. It is a characteristic signature of successful ALD growth that can proceed onto the surfaces of nanostructures with 3D morphology. EDX analysis supported the successful deposition of tungsten sulfide, which is confirmed the presence of tungsten and sulfur originating from 3 deposition cycles.

The research group headed by Prof. Siglinda Perathoner and Dr. Claudio Ampelli at the University of Messina has wide experience in photoelectrochemical catalysis of water splitting. Thanks to the mobility program of the SINCHEM doctorate, it was possible to do the first photocurrent tests of the TNT's@Ti disks with a thin film of WS<sub>2</sub> on the surface grown by ALD. The photocurrent measurement was performed in a three-electrode cell equipped with a flat quartz wall on one side for irradiation of the working electrode. The setup is illustrated in Figure 5. 9, where Pt wire played the role of a counter electrode and Ag/AgCl (3M KCl) was used as a reference electrode. The disk sample was irradiated by a Xe lamp that induced the generation of electrical current. The current was measured by a potentiostat.

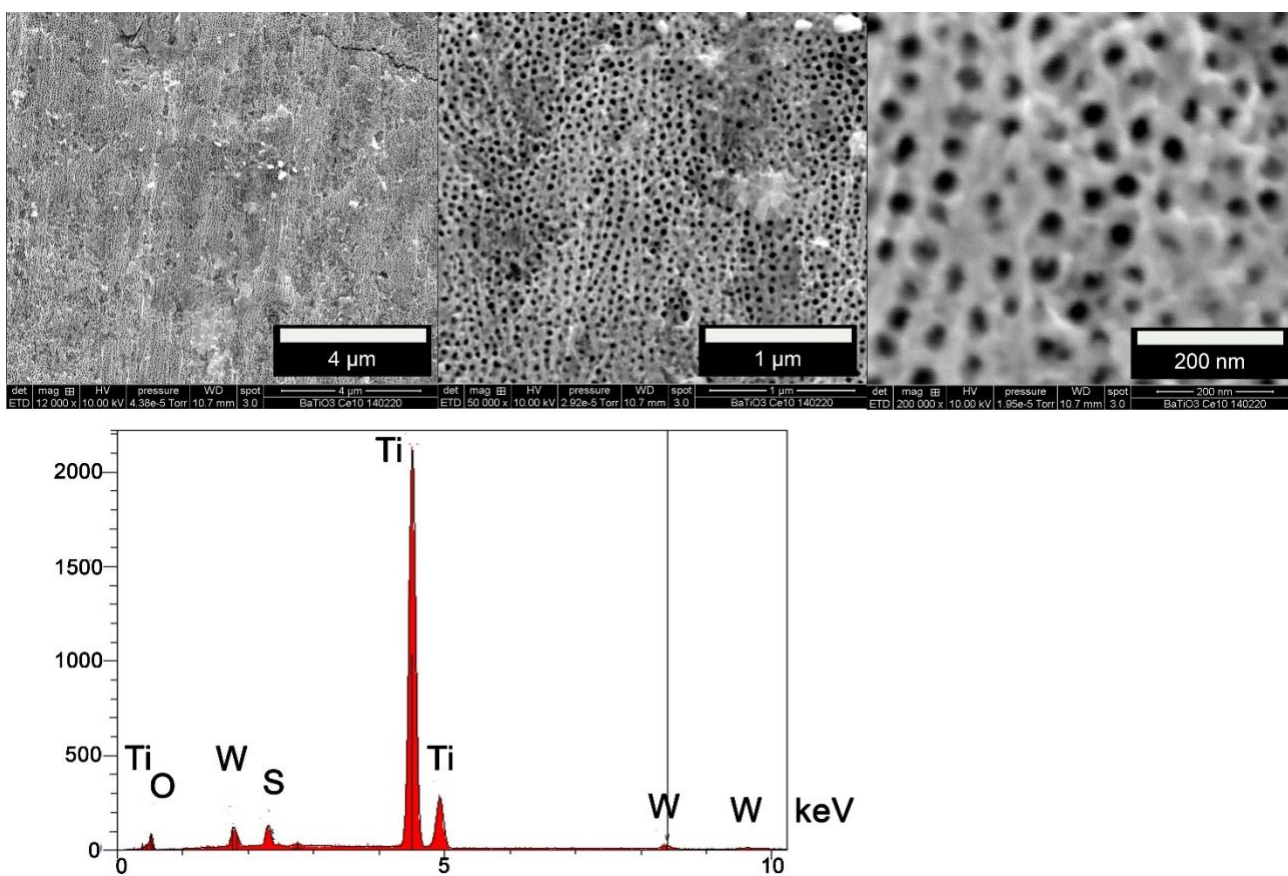


Figure 5. 8. SEM images and EDX analysis of the TNT's@Ti<sup>99.96%</sup> disk after 3 ALD cycles and annealing at 500 °C in argon flow.

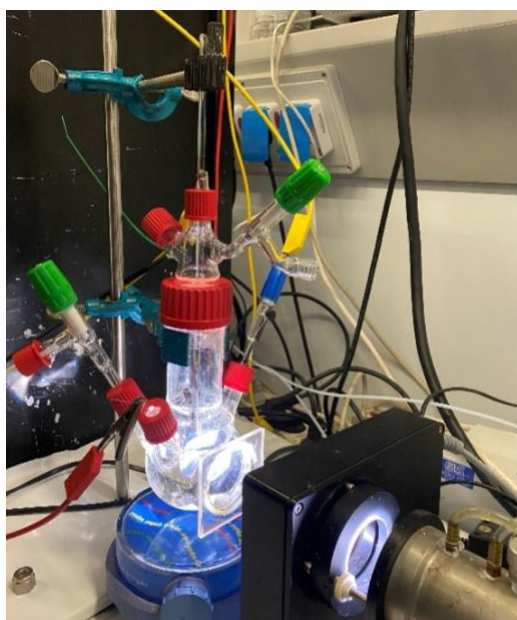


Figure 5. 9. Three-electrode setup for photocurrent measurement at the group of S.Perathoner *et al.*

In the first stage, we examined how the number of ALD cycles (none, 3, or 5) on non-calcined TNT's@Ti influences the photocurrent (see Figure 5. 10). Three ALD cycles of WS<sub>2</sub> on non-calcined TNT's@Ti have improved the photocurrent of the bare non-calcined TNT's@Ti, but five ALD cycles have decreased the photocurrent. However, due to very low absolute values of the photocurrent and the absence of the measurement for eight ALD cycles on non-calcined TNT's, it is too early to conclude that a lower number of ALD of WS<sub>2</sub> is better for performance in the photocurrent tests. Perhaps, a greater enhancement of the number of ALD cycles could result in an improvement of photoactivity. Most of the works reporting the positive improvement of photoactivity investigated a much higher number of deposition cycles (> 30 cycles) of active material.<sup>48,49,241</sup> Probably only 3 or 5 cycles were not enough to cover homogeneously all the nanotubes in depth, but only to create a thin layer of WS<sub>2</sub> on the top surface of the tubes, acting as a charge recombination layer, with the result of decreasing the overall performances of TNT's. However, a very thin layer would be more suitable in a different photoelectrochemical cell configuration<sup>236</sup> (e.g. with separation of the reaction environments for reduction and oxidation).

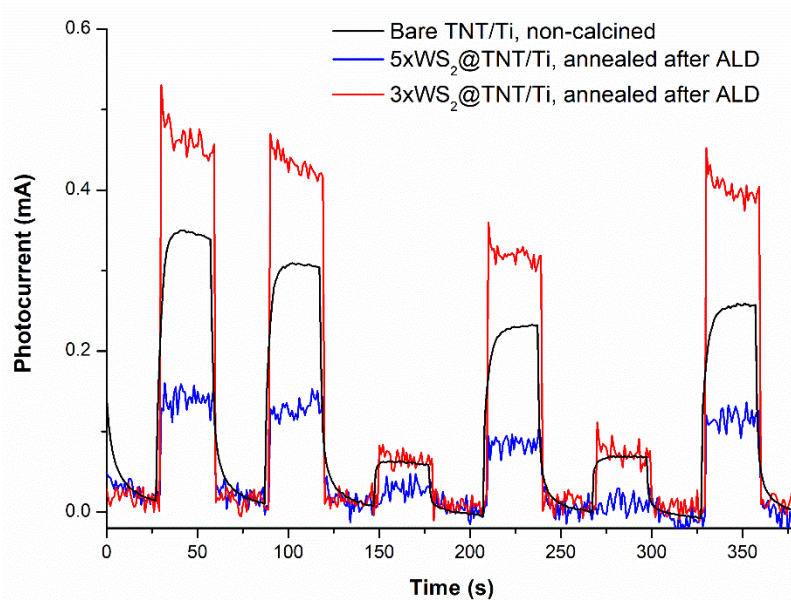


Figure 5. 10. Photocurrent measurement for the non-calcined TNT's@Ti disks with 0, 3, and 5 ALD cycles of WS<sub>2</sub>

The purity of the Ti disk used as a substrate plays a very important role too. From the graph in Figure 5. 11, it is observed that bare TNT's@Ti disks of higher (99.96 %, black line) and lower

purity (99.8 %, blue line) already differ in photocurrent production before ALD. After the same number of cycles of ALD of WS<sub>2</sub> on both calcined TNT's@Ti disks, the photocurrent drops only slightly for the high purity disk (8.3% drop) and much more for the lower purity disk (64 % drop). This comparison shows that photon-to-electron conversion is more efficient when ALD is performed on a calcined high-purity TNT's@Ti disk, while with five ALD cycles photocurrent is not improved with respect to the bare disk. With and without filters, we can observe that 5xWS<sub>2</sub>-TNT's@Ti(99.96%) overcomes the photocurrent of bare TNT's@Ti(99.8%) disk. Most probably, the less pure Ti disks conduct a lower current than the higher purity disks.

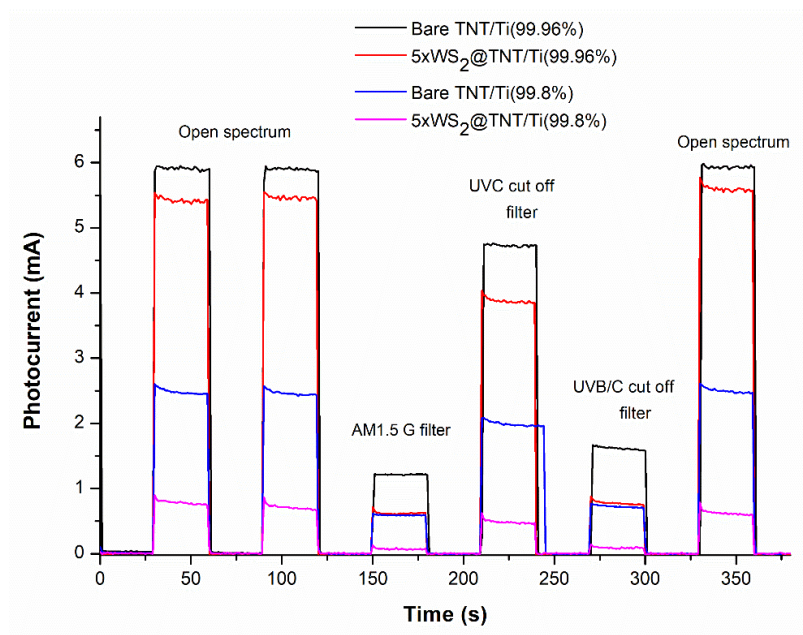


Figure 5. 11. Photocurrent measurement for the TNT's@Ti disks of higher (99.96 %) and lower purity (99.8 %) before and after 5 ALD cycles of WS<sub>2</sub>. Both disks were pre-calcined at 450 °C before ALD

A further experiment was carried out around the effect of calcination. Figure 5. 12 illustrates generated photocurrent by the bare calcined TNT's@Ti<sup>99.8%</sup> (black line), TNT's@Ti disk after 5 cycles of ALD on already calcined TNT's (red line) and TNT's@Ti disk after 5 cycles of ALD and on non-calcined TNT's (blue line), but each ALD process was followed by annealing step in argon flow. The alternating increase and decrease of the current matched off and on positions of a shutter in front of the Xe lamp. The photocurrent was tested with different wavelength light by putting filters in front of the Xe lamp: no filter – denoted as an *open spectrum*; solar simulating filter – *AM 1.5G*, *UVC* cut-off filter, *UVB/C* cut-off filter.

As it can be seen from the graph, the photocurrent of the calcined bare TNT's@Ti is higher than that generated by the disk after ALD on pre-calcined TNT's and much higher than the disk after ALD on non-calcined TNT's. Hence, it points to an important role of the calcination before ALD in the better deposition as well as better performance. A thin layer produced by ALD of WS<sub>2</sub> might cover the TNT's from the incident light, absorbs the radiation, and reduces the conversion of the radiation energy into the current due to poorly established interphase between TiO<sub>2</sub> and WS<sub>2</sub>. With such a low number of ALD cycles, the non-anodized Ti metallic surface being not a suitable substrate for investigated precursors did not receive a considerable amount of tungsten thiolates. Photocurrent generated by bare WS<sub>2</sub> (without TNT's growth) was not studied. This could be done in an ALD reactor capable of performing a high number of deposition cycles within an acceptable time, though it may suffer from the nucleation step in the initial stages.

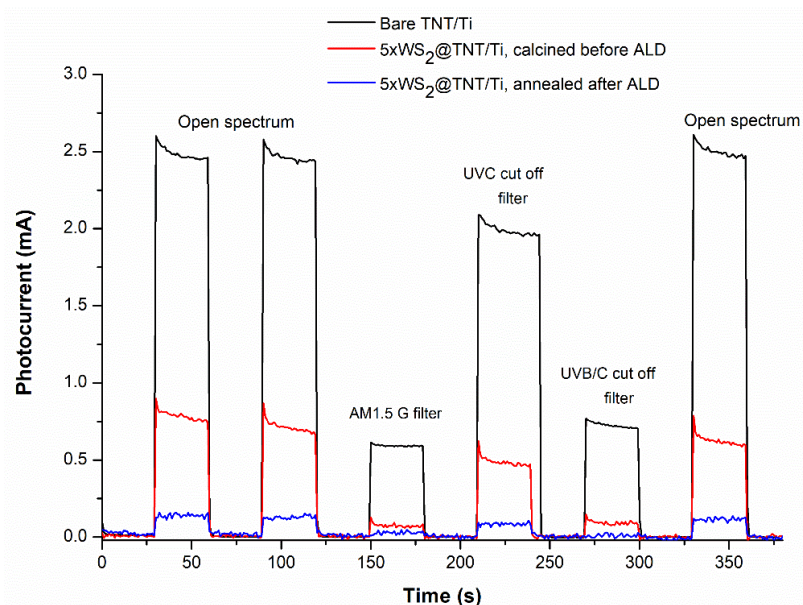


Figure 5. 12. Photocurrent measurement for bare calcined TNT's@Ti disk (black line), after 5 ALD cycles of WS<sub>2</sub> on pre-calcined TNT's@Ti (red line) and after 5 ALD cycles of WS<sub>2</sub> on non-calcined TNT's@Ti (blue line) without and with different filters

The calcination of the TNT's turns the amorphous phase into crystalline anatase/rutile phases mixture that significantly improves the photocurrent.<sup>242–244</sup>

Finally, since the metal complex BTBMW is in the liquid phase at room temperature, it was attempted to carry metal pulse without any heating. 5 ALD cycles have been performed at room temperature on pre-calcined TNT's@Ti(99.8%) and the photocurrent is compared with 5xWS<sub>2</sub>-TNT's@Ti(99.8%) deposited at 60 °C in Figure 5. 13. The latter sample was also obtained by 5 ALD cycles on pre-calcined TNT's, where the BTBMW pulse was done at 60 °C. As it can be seen, carrying a metallic pulse at 60 °C during the WS<sub>2</sub> ALD led to less photocurrent generation as compared to the sample prepared at RT. Without any filter, the photocurrent of the high-temperature sample was about 3.5 times lower (0.75 vs. 2.5 mA). In the case of solar simulating AM 1.5G, UVB/C, and UVC cut-off filters the difference between the two samples' performances remained almost at the same level (ca. 3.3-4 times lower). Since the sample prepared at RT did not differ much from the bare TNT's, it points to the fact that no considerable amount of WS<sub>2</sub> was deposited on TNT's. Although one can suppose that higher photocurrent of RT sample can be an indication of better photoactivity of deposited material, this is not such case. During ALD cycles, the color of the disk did not change in contrast to the transformation from blue to red color of the samples of ALD performed at 60 °C. In addition, its particular slight decrease of photocurrent with respect to bare

TNT's contrasted from other ALD samples of TNT's/Ti that led to a more important photocurrent decrease (with the same number of cycles).

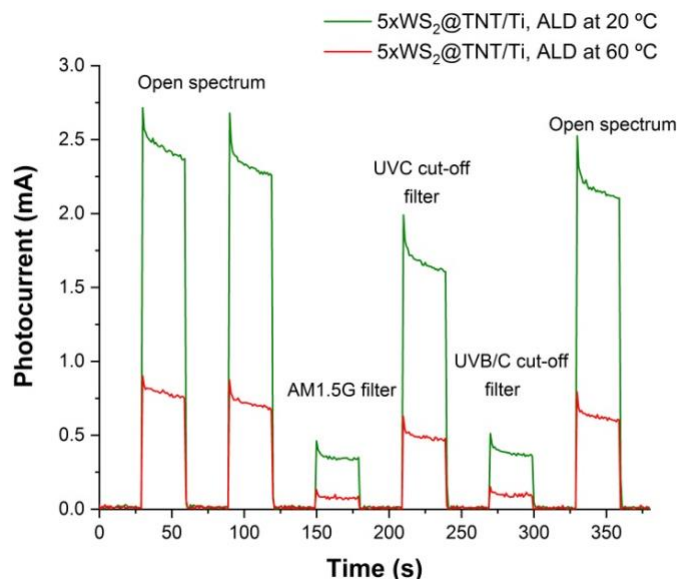


Figure 5. 13. Photocurrent measurement for the TNT's@Ti disks before ALD, and after 5 ALD cycles with metal pulses performed at 60 °C and 20 °C

The last two factors point to that the ALD at RT led to the deposition of a negligible amount of material, which can probably be due to the very low vapor pressure of the BTBMW at room temperature. Therefore, the relatively high photocurrent generated by this sample was not ascribed to the deposited material but rather ascribed to a slight decrease of the photocurrent initially produced by the bare TNT's.

In summary, the first attempts to grow a thin film of WS<sub>2</sub> by ALD seem to be successful on another 2D substrate, TNT's@Ti disk. The characteristic color change and EDX analysis provide good support for that. In these preliminary experimental tests, only a low number of deposition cycles were investigated. Although all the TNT's@Ti samples after ALD have generated lower photocurrent than bare TNT's, there are still many possibilities with ALD of WS<sub>2</sub> or other transition metal dichalcogenides that can advance the photocatalytic performance of the TNT's@Ti for water splitting. These studies point us to several paths for the enhancement of photocurrent generation in future studies so far:

- Growth of WS<sub>2</sub> performed on the high purity foil (TNT's@Ti<sup>99.96%</sup>) yields higher photocurrent than that of done on lower purity foil (TNT's@Ti<sup>99.8%</sup>). Therefore, the next studies should be done on the foil of higher purity.
- TNT's should be pre-calcined before ALD is carried on the disk because the amorphous phase is poorly photoactive and its transformation to the crystalline phase does not occur properly after the deposition.
- To have sufficient vapor pressure of the precursors, the ALD temperature should not be lower than 60 °C. After successful ALD growth of W thiolates on Si wafer and silica nanobeads at 80 °C, this temperature seems to be optimal for further attempts.
- A greater range of the number of deposition cycles should be studied. For the initial stage, 10, 20, 30 and 50 cycles may show some improvement and conclusive trend.

As many other works report photoactivity of ALD-grown material with the deposition cycles above 30, a higher number of ALD cycles of WS<sub>2</sub> on TNT's@Ti disk using our precursors has good potential to improve the photocurrent generation and final photoelectrochemical performance in water splitting. Nevertheless, a very thin layer would be more suitable in a different photoelectrochemical cell configuration (with separation of the reaction environments for reduction and oxidation). Electrode and cell design on these specific photocatalysts after these preliminary tests have suggested how to improve the interaction between WS<sub>2</sub> and TNT in relation with the electrolyte (higher number of ALD cycles, or lower thickness of TNT layer, more suited electrode assembly and type of cell configuration, different electrolyte and pH).

### 5.3.2. Electrocatalytic reduction of CO<sub>2</sub> by ALD-grown WS<sub>2</sub> on CNT

ALD-growth of thin films of WS<sub>2</sub> on MWCNT was performed by using BTBMW and H<sub>2</sub>S as precursors by the research group of Dr. Pinna (the method is described elsewhere<sup>15</sup>). The powder samples after a different number of ALD cycles (50, 200, and 300) were suspended in isopropanol, Nafion and sprayed onto a gas-diffusion layer (GDL) carbon electrode. They are further labeled as 50-WS<sub>2</sub>@CNT, 200-WS<sub>2</sub>@CNT, and 300-WS<sub>2</sub>@CNT, respectively.

Prepared electrodes were then tested in chronoamperometry mode for electrocatalytic reduction of CO<sub>2</sub> as a cathode in a compact electrochemical device, which has a design minimizing overpotential phenomena (see the reactor scheme in Figure 5. 5) (which is discussed in-detail elsewhere<sup>237</sup>). The

tests were carried out under different potentials (-0.4, -0.6 and -0.8 V vs. RHE) in order to obtain different current densities ( $0.15 - 4 \text{ mA cm}^{-2}$ ). Figure 5. 14 shows plots of measured electrical current with the duration of the applied voltages. A coherent increase of the absolute current is seen with increased voltage. However, different samples do not exhibit the same increase in the current which can be assigned to varied electrical conductivity after three different number of ALD cycles. One of the measurements at  $-0.4 \text{ V}$  for 300-WS<sub>2</sub>@CNT could not be continued after 30 minutes due to unknown technical issues. Thus, this shorter exposure to applied voltage must be taken into account when evaluating its catalytic performance.

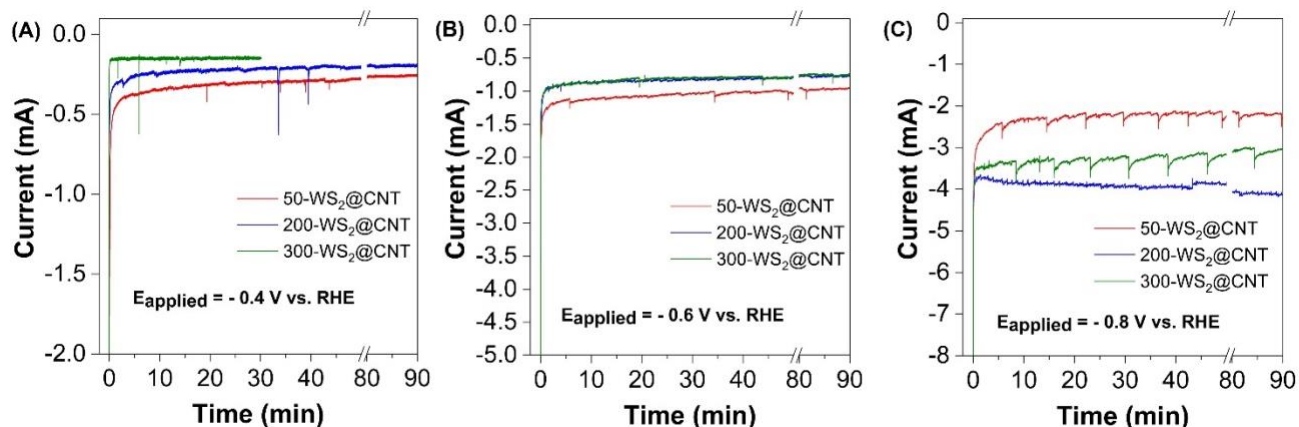


Figure 5. 14. Chronoamperometry plots of measured current vs time of applied voltage (A: -0.4 V; B: -0.6 V; C: -0.8 V vs RHE ). Red curve - 50-WS<sub>2</sub>@CNT after 50 ALD cycles; Blue curve - 200-WS<sub>2</sub>@CNT after 200 ALD cycles; Green curve - 300-WS<sub>2</sub>@CNT after 300 ALD cycles;

Results showed that formic acid and CO were the main products. The amount of produced formic acid was determined by ion chromatography analysis of liquid electrolyte samples, while CO gas was quantified from the headspace by micro GC. Their quantities estimated according to the under-peak area integration and a calibration curve of the instrument were then used to calculate the faradaic efficiency ( $\eta$ ) according to equation 5.1 below:

$$\eta = \frac{N(e^-)^{meas}}{N(e^-)^{total}} \quad (\text{eq. 5.1})$$

where  $N(e^-)^{meas}$  is the measured number of exchanged electrons to give products (formic acid or CO) and  $N(e^-)^{total}$  is the total number of exchanged electrons to give all products estimated as in eq. 5.2:

$$N(e^-)^{total} = \frac{I \times t}{n \times F} \quad (\text{eq. 5.2})$$

Where  $n$  is the number of electrons involved in the conversion from  $\text{CO}_2$  to  $\text{HCOOH}$  or to  $\text{CO}$ ,  $I$  the generated current,  $t$  the time of current passage, and  $F$  the Faraday constant ( $96485.3 \text{ C}\cdot\text{mol}^{-1}$ ). Faradaic efficiencies of formic acid and  $\text{CO}$  were estimated and plotted against the applied voltage difference (see bar graph in Figure 5. 15).

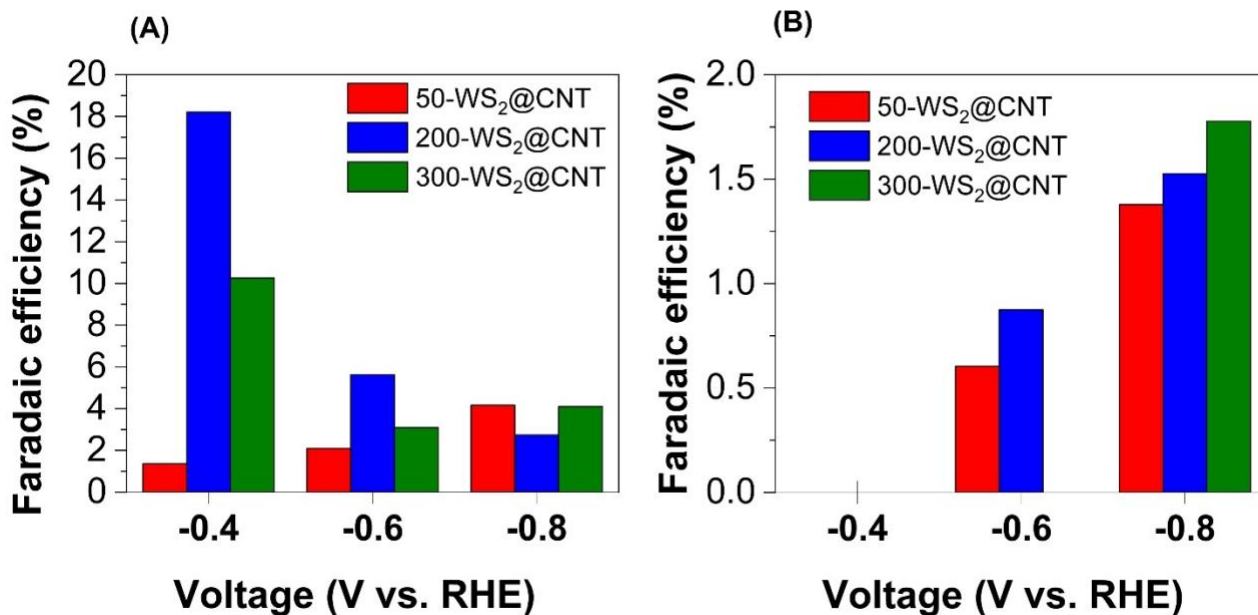


Figure 5. 15. A plot of faradaic efficiency towards the formation of (A) formic acid and (B)  $\text{CO}$  gas at three different applied voltages measured for ALD-grown  $\text{WS}_2$  samples on CNT (e.g. 50- $\text{WS}_2$ @CNT: after 50 ALD cycles).

The overall comparison of the bars on two sides (A and B) points to fact that electrons were mostly directed towards formic acid formation rather than towards  $\text{CO}$  gas formation. The increase of  $\text{CO}$  gas amount when the applied potential was increased comes along with the decrease of formic acid's faradaic efficiency. One can notice that two samples, 50- $\text{WS}_2$ @CNT and 200- $\text{WS}_2$ @CNT, demonstrated enhancement of  $\text{CO}$  gas production with higher voltage. Production of formic acid by the thinnest sample with 50- $\text{WS}_2$ @CNT was gradually enhanced with the increase of applied potential. In contrast, the sample with 200 ALD cycles (200- $\text{WS}_2$ @CNT) showed a decrease of faradaic efficiency by changing the selectivity towards  $\text{CO}$  gas. The third sample produced formic acid more efficiently at a lower potential (10.3 % that may alter due to incomplete measurement) than at -0.6 (3.1 %) or -0.8 V (4.1 %).

Two samples (200- $\text{WS}_2$ @CNT and 300- $\text{WS}_2$ @CNT) showed high faradaic efficiencies (71.7 and 85.9 %, respectively) for the formation of a side product,  $\text{H}_2$  gas, at -0.8 V (vs. RHE). It is formed

from the reduction of water as  $\text{H}_2\text{O} + 2\text{e}^- = \text{H}_2 + 2\text{OH}^-$ . Taking into account the detection limit of  $\text{H}_2$  gas by micro GC in the laboratory, hydrogen was detected only at the highest voltage, presumably because, the concentration exceeded the minimum threshold in view of high faradaic efficiency observed significant selectivity to  $\text{H}_2$  can be supposed at lower potentials too.

ALD-modified composites demonstrated positive activity in the electrocatalytic  $\text{CO}_2$  conversion. However, there are many missing points in this study. Firstly, no pristine CNTs were analyzed in the same measurement, which would give an idea of the contribution of  $\text{WS}_2$  film. Secondly, liquid electrolyte samples were not fully verified for the content of light alcohols (e.g. methanol, ethanol) which are also potential products of  $\text{CO}_2$  reduction. Note that ion chromatography was not sensitive to alcohol, besides its random unreliable detection of oxalic acid did not allow to report solid results about its formation. As the literature on both CNTs and transition metal dichalcogenides points to the enhanced catalytic activity of the composites, the ALD of  $\text{WS}_2$  on CNTs remains attractive though it needs a deeper study. As it was mentioned earlier for TNTs, deposition conditions (e.g. number of cycles, different pretreatment of CNTs, different W and S precursors, etc.) can be optimized for better performance.

## 5.4 CONCLUSION

ALD of W thiolates on the TNT's@Ti substrate appears to have been achieved. The photocurrent tests have certainly shown that the growth method is accomplished better on the pre-calcined TNT's rather than on the as-prepared amorphous titania phase. The performance of WS<sub>2</sub>-coated TNT's in the generation of the photocurrent needs further optimization steps and investigation that should involve defining optimal pretreatment temperature, the number of ALD cycles, annealing temperature, and duration.

Similar optimization of the ALD process is needed for the coating of CNTs. Besides, the electrocatalytic performance should be studied in-depth too. Along with acids and CO, electrocatalytic conversion of CO<sub>2</sub> could lead to the formation of light alcohol molecules, ethylene, and methane.<sup>225,245</sup> This needs further analysis by suitable spectroscopic tools (e.g. GC-MS, HPLC).

# Chapter 6 - **GENERAL CONCLUSION AND PERSPECTIVES**

## 6.1 Summary

The current urgency to switch from fossil fuels towards sustainable green chemistry turned ALD into one of the most attractive and powerful approaches. The ALD showed excellent usefulness not only for energy conversion applications but also in many other areas such as anti-corrosion coating, microelectronics, nano- and microelectromechanical systems, optical coatings, electroluminescent devices, etc. Crystallinity, conformality, and purity of a deposited film are essential qualities that influence the performance in a final application. Knowledge of chemistry occurring on the surface during ALD cycles affords full control over these qualities. It can guide in how to choose appropriate precursors and substrates, avoid unnecessary side reactions, and improve the overall qualities of the deposited material.

The chemistry that occurs at the interface of the substrate and the reactive gases determines the uniformity of the following layers in ALD. The first few cycles are crucially important, especially for ultrathin deposits. The growth quality of the following layered structures directly depends on the proper molecular design of the organometallic precursor and conditions of the deposition.

In this thesis, we demonstrated the effective use of SOMC tools for understanding the reaction mechanism of initial ALD cycles of WS<sub>2</sub>. Two tungsten precursors, W<sub>2</sub>(NMe<sub>2</sub>)<sub>6</sub> – HDMDW and W(=N<sup>t</sup>Bu)<sub>2</sub>(NMe<sub>2</sub>)<sub>2</sub> – BTBMW, were deployed for suitability in ALD of WS<sub>2</sub> whereas 1,2-ethanedithiol served as a sulfur precursor.

At first, chapter 2 explores the suitability of HDMDW as the ALD precursor for the WS<sub>2</sub> growth in pairing with EDT. Despite it is a dimer complex with the W≡W triple bond, it exhibited periodic features in DRIFT spectra with each ALD cycle. Consumption of –OH and –SH groups and the appearance of characteristic C–H bonds vibration was observed with each metallic pulse, while EDT pulse brought the SH groups vibration back again. The consistency was also seen between atomic ratios of S/W, N/W, and C/W from elemental analyses and proposed structures. Tests on vapor deposition of HDMDW onto solid silica nanobeads showed that surface reaction does not occur, or very poorly. Nevertheless, reactivity HDMDW was studied in the suspension of silica nanobeads in an ALD-like manner with EDT. WS<sub>2</sub> was obtained upon annealing the powder after 2 ALD cycles as the S/W ratio of about 2.1 was seen from the elemental analysis and HRTEM images of layered patterns around the silica nanobeads.

Chapter 3 showed that BTBMW is also reactive towards the ≡Si–OH group in the reaction with the molecular model of silica in solution, Ph<sub>3</sub>SiOH. <sup>1</sup>H NMR spectroscopy analysis revealed

preferential mono-substitution via the exchange of dimethylamido ligand rather than the tert-butylimido group yielding  $\text{Ph}_3\text{SiO}-\text{W}(\text{N}^i\text{Bu})_2(\text{NMe}_2)$ . The analogous reaction route was observed on partially dehydroxylated silica nanobeads. IR, Raman, NMR spectroscopies, and elemental analysis gave essential results confirming the mono-substitution via elimination of  $\text{HNMe}_2$  as well as the atomic ratios in excellent agreement with the proposed structure. The EDT precursor showed a quick reactivity towards BTBMW in solution, which thus supported good reactivity with a molecular product,  $\text{Ph}_3\text{SiO}-\text{W}(\text{N}^i\text{Bu})_2(\text{NMe}_2)$ , too. Although no product structure was proposed at this step, we could gain some important insights into the chemistry that is brought by EDT. Namely, its reductive property via sulfur-sulfur oxidative coupling was evidenced by the XPS study.

BTBMW and EDT also displayed a stable continuation of the surface reactions upon consecutive ALD pulses on silica nanobeads' surface. While each pulse of EDT brought reactive  $-\text{SH}$  thiol groups, each following pulse of BTBMW consumed them and enabled further reaction with EDT. All reactions on the surface of silica nanobeads confirmed their self-limiting feature. Pulsing excess of BTBMW or EDT yielded the loading fractions coherent with the expected density of initial  $-\text{OH}$  groups. *In-operando* thermal decomposition studied by DRIFT and GC-MS demonstrated the release of moieties constituting the proposed structure after 2 ALD cycles. The atomic ratios of S/W, N/W, and C/W determined by the elemental analysis were coherent with proposed structures of the surface sites upon each pulse. Electron microscopy images confirmed the formation of worm-like layers around silica nanobeads upon both annealing at 800 °C under argon flow and annealing at 450 °C under hydrogen flow. HRTEM also displayed crystalline nanodomains whose FFT defined unit cell parameters matching 2H- $\text{WS}_2$ .

Second, Chapter 4 discusses the successful execution of well-defined chemistry in Chapter 3 onto 2D substrates. In particular, the ALD of  $\text{WS}_2$  using the same BTBMW and EDT precursors on the  $\text{SiO}_2/\text{Si}$  wafer was extensively studied by XPS. High-resolution spectra were in good agreement with insights acquired on the 3D substrate, silica nanobeads. Besides, they provided a fundamental understanding of the evolution of oxidation states and the surrounding of the atoms with each ALD pulse as well as annealing. Interestingly, the XPS analysis confirmed a partial reduction of W (VI) already upon reaction with EDT that was coherent with findings in the literature. Removal of ethylene was confirmed by observation of the  $\text{S}_{2^{2-}}$  fraction in high-resolution XPS spectra of the S 2p spin-orbital. The extensive study of the in-situ annealing of the  $\text{SiO}_2/\text{Si}$  wafer after 2 ALD cycles by XPS was not only in good agreement with the in-situ thermal decomposition analysis by

DRIFT and GC-MS but also provided a deeper understanding of the evolution of the oxidation state of tungsten.

The developed ALD method was also applied for the growth of W thiolates on a Cu grid coated with silicon suboxide. Its in-situ annealing in HRTEM showed the formation of the worm-like layered patterns and crystalline nanodomains begins at 400 °C and advances by increasing the density of crystalline particles at higher temperatures. However, heating to 800 °C led to unexpected products involving Cu migration and its reaction with the grafted species. Nevertheless, observation of WS<sub>2</sub> crystalline nanoparticles from 400 °C comes in agreement with the observed oxidation state of W<sup>4+</sup> by *operando* XPS analysis in the range of 300-450 °C (on SiO<sub>2</sub>@Si wafer).

Our strategy for investigation of the ALD growth involving (1) a preliminary study using tools of molecular chemistry (e.g., liquid-state NMR), (2) SOMC study via grating on a high-surface-area 3D substrate using IR, Raman, (SS)NMR, elemental analysis and further (3) transition of developed growth method onto real 2D substrates (characterized by XPS, HRTEM, EDX) is unique. This thesis showed that such an approach provides a deep understanding of the surface chemistry occurring in the initial and important stage of ALD. Although the dimer tungsten complex (HDMDW) did not show good reactivity with ≡SiO–H in gas-solid interphase, our studies demonstrated that this precursor is still applicable in solution ALD.

The role of SOMC was fundamental in the successful growth of WS<sub>2</sub> by ALD on TNT's@Ti disk. Characteristic color changes on the TiO<sub>2</sub> part of the disk after EDT pulse (from blue to red), after annealing (from red to dark purple), and no color change on the metallic part of the surface were clear indications of the surface reactions. It displays the importance of the choice of the substrate for ALD and can be intentionally exploited for area-selective ALD applications. In a given time, the ALD of WS<sub>2</sub> on TNT's@Ti disks could not be completely optimized for the enhancement of the photocurrent generation as compared to the performance of a pristine TNT's@Ti disk. Even so, initial perspectives on the growth optimization were proposed being based on obtained results.

As a promising material in many electrocatalytic applications, ALD-modified (MW)CNTs were tested in CO<sub>2</sub> reduction as a cathode at the University of Messina. First CNTs coated with WS<sub>2</sub> films though ALD were prepared in collaboration with Prof. Pinna from Berlin. Functionalized CNTs demonstrated positive activity in the electrocatalytic CO<sub>2</sub> conversion mostly towards the formation of formic acid and carbon monoxide.

## 6.2 Perspectives

Although BTBMW was shown to be a suitable ALD precursor and giving well-defined chemistry, there were some uncertain observations on XPS data of ALD cycles on the SiO<sub>2</sub>@Si wafer. The Si 2p spectra of the narrow scan XPS measurements showed evidence of tungsten silicide at lower binding energy upon the deposition of BTBMW in the 1<sup>st</sup> pulse. Higher energy peak at 401.2 eV in the N 1s spectrum that was assigned to as an electron-deprived nitrogen atom in equilibrium between the coordinated amine and zwitterionic forms that was not explored in the study on silica beads.

A deeper study of the mechanism of ALD cycles using HDMDW and EDT by XPS is necessary to provide information about how the oxidation state evolves with each pulse. This would help to propose more precise structures obtained in each half-cycle.

Optimization of ALD procedure on a TNT's@Ti disk to improve photocatalytic performance. So far, due to the time constraint of the PhD mobility at the University of Messina, not many options for the growth of WS<sub>2</sub> was carried out on TNT's@Ti. Therefore, the photocurrent generation tests have not shown improved throughput comparing with the bare TNT's surface. The coating on already calcined TNT's (directly on TiO<sub>2</sub> anatase) of the higher purity (99.96 %) can still be optimized in terms of the number of deposition cycles, temperature and atmosphere of annealing to maximize photocurrent generation, and its further use in hydrogen evolution reaction catalysis.

However, similar optimization of the ALD process is needed for the coating of CNTs as mentioned for TNTs. Besides, the electrocatalytic performance should be studied in-depth too. Along with acids and CO, electrocatalytic conversion of CO<sub>2</sub> could lead to the formation of light alcohol molecules. Experiment with pristine CNTs could help to identify the contribution from the ALD-grown film. On the other hand, the reduction process could lead to the formation of other molecules (e.g. methanol, ethanol, methane, etc.) which could not be verified so far.

## REFERENCES

1. Molaei, M. J. The optical properties and solar energy conversion applications of carbon quantum dots: A review. *Solar Energy* **196**, 549–566 (2020).
2. Ismael, M. Ferrites as solar photocatalytic materials and their activities in solar energy conversion and environmental protection: A review. *Solar Energy Materials and Solar Cells* **219**, 110786 (2021).
3. Dong, C. R., Wang, Y., Zhang, K. & Zeng, H. Halide perovskite materials as light harvesters for solar energy conversion. *EnergyChem* **2**, 100026 (2020).
4. Yu, X. & Sivula, K. Layered 2D semiconducting transition metal dichalcogenides for solar energy conversion. *Current Opinion in Electrochemistry* **2**, 97–103 (2017).
5. Yu, X. & Sivula, K. Toward Large-Area Solar Energy Conversion with Semiconducting 2D Transition Metal Dichalcogenides. *ACS Energy Letters* **1**, 315–322 (2016).
6. Iqbal, M. Z., Alam, S., Faisal, M. M. & Khan, S. Recent advancement in the performance of solar cells by incorporating transition metal dichalcogenides as counter electrode and photoabsorber. *International Journal of Energy Research* **43**, 3058–3079 (2019).
7. Tsai, M. L. *et al.* Monolayer MoS<sub>2</sub> heterojunction solar cells. *ACS Nano* **8**, 8317–8322 (2014).
8. Yin, Z. *et al.* Single-layer MoS<sub>2</sub> phototransistors. *ACS Nano* **6**, 74–80 (2012).
9. Krasnozhan, D., Lembke, D., Nyffeler, C., Leblebici, Y. & Kis, A. MoS<sub>2</sub> transistors operating at gigahertz frequencies. *Nano Lett.* **14**, 5905–5911 (2014).
10. Bertolazzi, S., Krasnozhan, D. & Kis, A. Nonvolatile Memory Cells Based on MoS<sub>2</sub>/Graphene Heterostructures. *Am. Chem. Soc. Nano* **7**, 3246–3252 (2013).
11. Sun, P., Zhang, W., Hu, X., Yuan, L. & Huang, Y. Synthesis of hierarchical MoS<sub>2</sub> and its electrochemical performance as an anode material for lithium-ion batteries. *J. Mater. Chem. A* **2**, 3498–3504 (2014).
12. Xiang, Q., Yu, J. & Jaroniec, M. Synergetic effect of MoS<sub>2</sub> and graphene as cocatalysts for enhanced photocatalytic H<sub>2</sub> production activity of TiO<sub>2</sub> nanoparticles. *J. Am. Chem. Soc.* **134**, 6575–6578 (2012).
13. Yan, Y., Xia, B., Xu, Z. & Wang, X. Recent development of molybdenum sulfides as advanced electrocatalysts for hydrogen evolution reaction. *ACS Catal.* **4**, 1693–1705 (2014).
14. Sobczynski, A. *et al.* Tungsten Disulfide: A Novel Hydrogen Evolution Catalyst for Water Decomposition. *J. Phys. Chem* **92**, 2311–2315 (1988).
15. Wu, Y. *et al.* A Self-Limited Atomic Layer Deposition of WS<sub>2</sub> Based on the Chemisorption and Reduction of Bis(t-butylimino)bis(dimethylamino) Complexes. *Chem. Mater.* **31**, 1881–1890 (2019).
16. Scharf, T. W., Prasad, S. V., Mayer, T. M., Goeke, R. S. & Dugger, M. T. Atomic layer deposition of tungsten disulfide solid lubricant thin films. *J. Mater. Res.* **19**, 3443–3446 (2004).
17. Nandi, D. K., Sen, U. K., Dhara, A., Mitra, S. & Sarkar, S. K. Intercalation based tungsten disulfide (WS<sub>2</sub>) Li-ion battery anode grown by atomic layer deposition. *RSC Adv.* **6**, 38024–

38032 (2016).

18. Copéret, C. *et al.* Surface Organometallic and Coordination Chemistry toward Single-Site Heterogeneous Catalysts: Strategies, Methods, Structures, and Activities. *Chem. Rev.* **116**, 323–421 (2016).
19. Cadot, S. *et al.* A novel 2-step ALD route to ultra-thin MoS<sub>2</sub> films on SiO<sub>2</sub> through a surface organometallic intermediate. *Nanoscale* **9**, 538–546 (2017).
20. Dezelah IV, C. L. *et al.* Atomic layer deposition of tungsten(III) oxide thin films from W<sub>2</sub>(NMe<sub>2</sub>)<sub>6</sub> and water: Precursor-based control of oxidation state in the thin film material. *J. Am. Chem. Soc.* **128**, 9638–9639 (2006).
21. Dezelah IV, C. L. *et al.* A low valent metalorganic precursor for the growth of tungsten nitride thin films by atomic layer deposition. *J. Mater. Chem.* **17**, 1109–1116 (2007).
22. Koch, V. M. *et al.* A solution-based ALD route towards (CH<sub>3</sub>NH<sub>3</sub>)(PbI<sub>3</sub>) perovskite: Via lead sulfide films. *J. Mater. Chem. A* **7**, 25112–25119 (2019).
23. Wu, Y. *et al.* Atomic Layer Deposition from Dissolved Precursors. *Nano Lett.* **15**, 6379–6385 (2015).
24. Dupin, J. C., Gonbeau, D., Martin-Litas, I., Vinatier, P. & Levasseur, A. Amorphous oxysulfide thin films MO<sub>y</sub>S<sub>z</sub> (M=W, Mo, Ti) XPS characterization: structural and electronic peculiarities. *Appl. Surf. Sci.* **173**, 140–150 (2001).
25. Mukherjee, A., Sengupta, S. K., Steeves, D. M., Soares, J. W. & Whitten, J. E. Mechanism of thiol-induced color change of tungsten oxide nanoparticles. *Chem. Phys. Lett.* **752**, (2020).
26. Bachrach, S. M., Nguyen, T. T. & Demoin, D. W. Microsolvation of cysteine: A density functional theory study. *J. Phys. Chem. A* **113**, 6172–6181 (2009).
27. Ataman, E., Isvoranu, C., Andersen, J. N., Schnadt, J. & Schulte, K. Unconventional zwitterionic state of l-cysteine. *J. Phys. Chem. Lett.* **2**, 1677–1681 (2011).
28. Coutelier, O. *et al.* A new donor-stabilized ditungsten amido alkoxido species: Synthesis, crystal structure, fluxionality, and grafting onto silica. *Eur. J. Inorg. Chem.* 5541–5547 (2007). doi:10.1002/ejic.200700732
29. Chisholm, M. H., Corning, J. F. & Huffman, J. C. Bis(dimethylamine)tetrakis(tert-butyl mercaprido)di-μ-sulfido-dimolybdenum(IV). *Inorg. Chem.* **21**, 286–289 (1982).
30. Chisholm, M. H., Corning, J. F. & Huffman, J. C. The molybdenum-molybdenum triple bond. 14.<sup>1</sup> preparation and characterization of mixed alkoxy-thiolate compounds of formula Mo<sub>2</sub>(OR)<sub>2</sub>(SAr)<sub>4</sub> (M≡M). *Inorg. Chem.* **23**, 754–757 (1984).
31. Yu, X. G. *et al.* Lithium storage in conductive sulfur-containing polymers. *J. Electroanal. Chem.* **573**, 121–128 (2004).
32. Ritchie, H. & Roser, M. CO<sub>2</sub> emissions - Our World in Data. (2017). Available at: <https://ourworldindata.org/co2-emissions>. (Accessed: 30th October 2020)
33. Hoel, M. & Kverndokk, S. Depletion of fossil fuels and the impacts of global warming. *Resour. Energy Econ.* **18**, 115–136 (1996).
34. Kirsch, S. Running out? Rethinking resource depletion. *Extractive Industries and Society* **7**, 838–840 (2020).

35. Hannah Ritchie. *How long before we run out of fossil fuels? - Our World in Data. Our World in Data* (2017).
36. Dovì, V. G., Friedler, F., Huisingh, D. & Klemeš, J. J. Cleaner energy for sustainable future. *J. Clean. Prod.* **17**, 889–895 (2009).
37. Balzani, V., Credi, A. & Venturi, M. Photochemical conversion of solar energy. *ChemSusChem* **1**, 26–58 (2008).
38. Bogdanov, D. *et al.* Radical transformation pathway towards sustainable electricity via evolutionary steps. *Nat. Commun.* **10**, 1–16 (2019).
39. Li, H. & Zhang, W. Perovskite Tandem Solar Cells: From Fundamentals to Commercial Deployment. *Chemical Reviews* **120**, 9835–9950 (2020).
40. Sivula, K. Toward economically feasible direct solar-to-fuel energy conversion. *Journal of Physical Chemistry Letters* **6**, 975–976 (2015).
41. Lewis, N. S. Introduction: Solar Energy Conversion. *Chemical Reviews* **115**, 12631–12632 (2015).
42. Baltrusaitis, J., Jansen, I. & Schuttlefield Christus, J. D. Renewable energy based catalytic CH<sub>4</sub> conversion to fuels. *Catalysis Science and Technology* **4**, 2397–2411 (2014).
43. Artz, J. *et al.* Sustainable Conversion of Carbon Dioxide: An Integrated Review of Catalysis and Life Cycle Assessment. *Chemical Reviews* **118**, 434–504 (2018).
44. Stolarczyk, J. K., Bhattacharyya, S., Polavarapu, L. & Feldmann, J. Challenges and Prospects in Solar Water Splitting and CO<sub>2</sub> Reduction with Inorganic and Hybrid Nanostructures. *ACS Catal.* **8**, 3602–3635 (2018).
45. Bachmann, J. Atomic layer deposition, a unique method for the preparation of energy conversion devices. *Beilstein Journal of Nanotechnology* **5**, 245–248 (2014).
46. Zhao, H. & Lei, Y. 3D Nanostructures for the Next Generation of High-Performance Nanodevices for Electrochemical Energy Conversion and Storage. *Advanced Energy Materials* **10**, 2001460 (2020).
47. Kuang, Y., Vece, M. Di, Rath, J. K., Dijk, L. Van & Schropp, R. E. I. Elongated nanostructures for radial junction solar cells. *Reports Prog. Phys.* **76**, (2013).
48. Sarkar, S. K. *et al.* In<sub>2</sub>S<sub>3</sub> Atomic Layer Deposition and Its Application as a Sensitizer on TiO<sub>2</sub> Nanotube Arrays for Solar Energy Conversion. *J. Phys. Chem. C* **114**, 8032–8039 (2010).
49. Cao, Y. *et al.* Electrocatalytic Performance of Titania Nanotube Arrays Coated with MoS<sub>2</sub> by ALD toward the Hydrogen Evolution Reaction. *ACS Omega* **4**, 8816–8823 (2019).
50. Leskelä, M., Niinistö, J. & Ritala, M. *Atomic Layer Deposition. Comprehensive Materials Processing* **4**, (2014).
51. Winer, W. O. Molybdenum Disulfide As A Lubricant: A Review Of The Fundamental Knowledge. *Wear* **10**, 422–452 (1967).
52. Miyake, S., Sekine, Y., Noshiro, J. & Watanabe, S. Low-Friction and Long-Life Solid Lubricant Films Structured of Nanoperiod Tungsten Disulfide and Molybdenum Disulfide Multilayer. *Jpn. J. Appl. Phys.* **43**, 4338–4343 (2004).
53. Alonso, G. *et al.* Preparation of MoS<sub>2</sub> and WS<sub>2</sub> catalysis by in situ decomposition of

- ammonium thiosalts. *Catal. Letters* **52**, 55–61 (1998).
54. Fréty, R., Breyse, M., Lacroix, M. & Vrinat, M. Unsupported MoS<sub>2</sub> and WS<sub>2</sub> Model Catalysts: Influence of Textural Properties on Hydrodesulfurization and Hydrogenation Activities. *Bull. des Sociétés Chim. Belges* **93**, 663–672 (2010).
  55. Bhandavat, R., David, L. & Singh, G. Synthesis of Surface-Functionalized WS<sub>2</sub> Nanosheets and Performance as Li-Ion Battery Anodes. *J. Phys. Chem. Lett.* **3**, 1523–1530 (2012).
  56. Choi, W. *et al.* Recent development of two-dimensional transition metal dichalcogenides and their applications. *Materials Today* **20**, 116–130 (2017).
  57. Kuc, A., Zibouche, N. & Heine, T. Influence of quantum confinement on the electronic structure of the transition metal sulfide TS<sub>2</sub>. *Phys. Rev. B* **83**, 245213 (2011).
  58. Gutierrez, H. R. *et al.* Extraordinary Room-Temperature Photoluminescence in Triangular WS<sub>2</sub> Monolayers. *NanoLetters* **13**, 3447–3454 (2013).
  59. Li, Z., Meng, X. & Zhang, Z. Recent development on MoS<sub>2</sub>-based photocatalysis: A review. *J. Photochem. Photobiol. C Photochem. Rev.* **35**, 39–55 (2018).
  60. Opoku, F., Govender, K. K., Van Sittert, C. G. C. E. & Govender, P. P. Role of MoS<sub>2</sub> and WS<sub>2</sub> monolayers on photocatalytic hydrogen production and the pollutant degradation of monoclinic BiVO<sub>4</sub>: A first-principles study. *New J. Chem.* **41**, 11701–11713 (2017).
  61. Kahng, S., Yoo, H. & Kim, J. H. Recent advances in earth-abundant photocatalyst materials for solar H<sub>2</sub> production. *Adv. Powder Technol.* **31**, 11–28 (2020).
  62. Frindt, R. F. Single Crystals of MoS<sub>2</sub> Several Molecular Layers Thick. *J. Appl. Phys.* **37**, 1928–1929 (1966).
  63. Perea-López, N. *et al.* Photosensor Device Based on Few-Layered WS<sub>2</sub> Films. *Adv. Funct. Mater.* **23**, 5511–5517 (2013).
  64. Zhou, K. G., Mao, N. N., Wang, H. X., Peng, Y. & Zhang, H. L. A mixed-solvent strategy for efficient exfoliation of inorganic graphene analogues. *Angew. Chemie - Int. Ed.* **50**, 10839–10842 (2011).
  65. Coleman, J. N. *et al.* Two-dimensional nano-sheets produced by liquid exfoliation of layered materials. *Science (80-. )*. **331**, 568–571 (2011).
  66. Coleman, J. N. Liquid-phase exfoliation of nanotubes and graphene. *Adv. Funct. Mater.* **19**, 3680–3695 (2009).
  67. Shen, J. *et al.* Liquid Phase Exfoliation of Two-Dimensional Materials by Directly Probing and Matching Surface Tension Components. *Nano Lett.* **15**, 5449–5454 (2015).
  68. Mahler, B., Hoepfner, V., Liao, K. & Ozin, G. A. Colloidal synthesis of 1T-WS<sub>2</sub> and 2H-WS<sub>2</sub> nanosheets: Applications for photocatalytic hydrogen evolution. *J. Am. Chem. Soc.* **136**, 14121–14127 (2014).
  69. Lv, X. J., She, G. W., Zhou, S. X. & Li, Y. M. Highly efficient electrocatalytic hydrogen production by nickel promoted molybdenum sulfide microspheres catalysts. *RSC Adv.* **3**, 21231–21236 (2013).
  70. Wang, D., Pan, Z., Wu, Z., Wang, Z. & Liu, Z. Hydrothermal synthesis of MoS<sub>2</sub> nanoflowers as highly efficient hydrogen evolution reaction catalysts. *J. Power Sources* **264**, 229–234 (2014).

71. Lv, R. *et al.* Transition metal dichalcogenides and beyond: Synthesis, properties, and applications of single- and few-layer nanosheets. *Acc. Chem. Res.* **48**, 56–64 (2015).
72. Biyikli, N. & Haider, A. Atomic layer deposition: An enabling technology for the growth of functional nanoscale semiconductors. *Semiconductor Science and Technology* **32**, 093002 (2017).
73. Fujimoto, H. *et al.* Influence of material impurities in the hole-blocking layer on the lifetime of organic light-emitting diodes. *Appl. Phys. Lett.* **109**, 243302 (2016).
74. Park, D. G. & Kim, T. K. Effects of fluorine and chlorine on the gate oxide integrity of W/TiN/SiO<sub>2</sub>/Si metal-oxide-semiconductor structure. *Thin Solid Films* **483**, 232–238 (2005).
75. Groven, B. *et al.* Plasma-Enhanced Atomic Layer Deposition of Two-Dimensional WS<sub>2</sub> from WF<sub>6</sub>, H<sub>2</sub> Plasma, and H<sub>2</sub>S. *Chem. Mater.* **29**, 2927–2938 (2017).
76. Yeo, S. *et al.* Low-temperature direct synthesis of high quality WS<sub>2</sub> thin films by plasma-enhanced atomic layer deposition for energy related applications. *Appl. Surf. Sci.* **459**, 596–605 (2018).
77. Balasubramanyam, S. *et al.* Area-Selective Atomic Layer Deposition of Two-Dimensional WS<sub>2</sub> Nanolayers. *ACS Mater. Lett.* **2**, 511–518 (2020).
78. Delabie, A. *et al.* Low temperature deposition of 2D WS<sub>2</sub> layers from WF<sub>6</sub> and H<sub>2</sub>S precursors: impact of reducing agents. *Chem. Commun.* **51**, 15692–15695 (2015).
79. George, S. M. Atomic layer deposition: An overview. *Chem. Rev.* **110**, 111–131 (2010).
80. Heil, S. B. S. *et al.* In situ reaction mechanism studies of plasma-assisted atomic layer deposition of Al<sub>2</sub>O<sub>3</sub>. *Appl. Phys. Lett.* **89**, 131505 (2006).
81. Kim, H., Cabral, C., Lavoie, C. & Rossnagel, S. M. Diffusion barrier properties of transition metal thin films grown by plasma-enhanced atomic-layer deposition. *J. Vac. Sci. Technol. B Microelectron. Nanom. Struct.* **20**, 1321 (2002).
82. Grubbs, R. K. & George, S. M. Attenuation of hydrogen radicals traveling under flowing gas conditions through tubes of different materials. *J. Vac. Sci. Technol. A Vacuum, Surfaces, Film.* **24**, 486–496 (2006).
83. Jehn, H., Gmünd, S., Bär, G., Best, E. & Koch, E. Reactions with Sulfur. in *W Tungsten* 110–116 (Springer Berlin Heidelberg, 1993). doi:10.1007/978-3-662-08684-1\_3
84. Wildervanck, J. C. & Jellinek, F. Preparation and Crystallinity of Molybdenum and Tungsten Sulfides. *ZAAC - J. Inorg. Gen. Chem.* **328**, 309–318 (1964).
85. Voorhoeve, R. J. H. & Wolters, H. B. M. Tungsten Sulfides obtained by Decomposition of Ammonium Tetrathiotungstate. *Zeitschrift für Anorg. und Allg. Chemie* **376**, 165–179 (1970).
86. Fix Renaud, Gordon Roy G., H. D. M. Low-temperature atmospheric-pressure metal-organic chemical vapor deposition of molybdenum nitride thin films. *Thin Solid Films* **288**, 116–119 (1996).
87. Bradley, D. C. & Chisholm, M. H. Preparation and Crystallinity of Molybdenum and Tungsten Sulfides. *Inorg. Phys. Theory A*, 2741–2744 (1971).
88. Becker, J. S., Kim, E. & Gordon, R. G. Atomic layer deposition of insulating hafnium and zirconium nitrides. *Chem. Mater.* **16**, 3497–3501 (2004).

89. Liang, X., Yu, M., Li, J., Jiang, Y.-B. & Weimer, A. W. Ultra-thin microporous–mesoporous metal oxide films prepared by molecular layer deposition (MLD). *Chem. Commun.* **0**, 7140–7142 (2009).
90. Tan, L. K. *et al.* Atomic layer deposition of a MoS<sub>2</sub> film. *Nanoscale* **6**, 10584–10588 (2014).
91. Jin, Z., Shin, S., Kwon, D. H., Han, S.-J. & Min, Y.-S. Novel chemical route for atomic layer deposition of MoS<sub>2</sub> thin film on SiO<sub>2</sub>/Si substrate. *Nanoscale* **6**, 14453–14458 (2014).
92. Mattinen, M. *et al.* Atomic Layer Deposition of Crystalline MoS<sub>2</sub> Thin Films: New Molybdenum Precursor for Low-Temperature Film Growth. *Adv. Mater. Interfaces* **4**, 1700123 (2017).
93. Jurca, T. *et al.* Low-Temperature Atomic Layer Deposition of MoS<sub>2</sub> Films. *Angew. Chemie Int. Ed.* **56**, 4991–4995 (2017).
94. Knapas, K. & Ritala, M. *In Situ* Studies on Reaction Mechanisms in Atomic Layer Deposition. *Crit. Rev. Solid State Mater. Sci.* **38**, 167–202 (2013).
95. Knemeyer, K. *et al.* Mechanistic studies of atomic layer deposition on oxidation catalysts-AlO<sub>x</sub> and PO<sub>x</sub> deposition. *Phys. Chem. Chem. Phys.* **22**, 17999–18006 (2020).
96. Lemaire, P. C., King, M. & Parsons, G. N. Understanding inherent substrate selectivity during atomic layer deposition: Effect of surface preparation, hydroxyl density, and metal oxide composition on nucleation mechanisms during tungsten ALD. *J. Chem. Phys.* **146**, 52811 (2017).
97. Soethoudt, J. *et al.* Diffusion-Mediated Growth and Size-Dependent Nanoparticle Reactivity during Ruthenium Atomic Layer Deposition on Dielectric Substrates. *Adv. Mater. Interfaces* **5**, 1800870 (2018).
98. Ott, A. W., Klaus, J. W., Johnson, J. M. & George, S. M. Modification of Porous Alumina Membranes Using Al<sub>2</sub>O<sub>3</sub> Atomic Layer Controlled Deposition. *Chem. Mater.* **9**, 707–714 (1997).
99. Dendooven, J. *et al.* In situ X-ray fluorescence measurements during atomic layer deposition: Nucleation and growth of TiO<sub>2</sub> on planar substrates and in nanoporous films. *J. Phys. Chem. C* **115**, 6605–6610 (2011).
100. Mathey, L. *et al.* Functionalization of Silica Nanoparticles and Native Silicon Oxide with Tailored Boron-Molecular Precursors for Efficient and Predictive p -Doping of Silicon. *J. Phys. Chem. C* **119**, 13750–13757 (2015).
101. Alphazan, T. *et al.* Monolayer Doping of Silicon through Grafting a Tailored Molecular Phosphorus Precursor onto Oxide-Passivated Silicon Surfaces. *Chem. Mater.* **28**, 3634–3640 (2016).
102. Roussey, A. *et al.* Cu nanoparticles on 2D and 3D silica substrates: controlled size and density, and critical size in catalytic silicon nanowire growth. *J. Mater. Chem. C* **1**, 1583 (2013).
103. Yermakov, Y. I. Supported Catalysts Obtained by Interaction of Organometallic Compounds of Transition Elements with Oxide Supports. *Catal. Rev.* **13**, 77–120 (1976).
104. Zhuravlev, L. T. The surface chemistry of amorphous silica. Zhuravlev model. *Colloids Surfaces A Physicochem. Eng. Asp.* **173**, 1–38 (2000).

105. Sneh, O. & George, S. M. Thermal stability of hydroxyl groups on a well-defined silica surface. *J. Phys. Chem.* **99**, 4639–4647 (1995).
106. Nyns, L. *et al.* HfO<sub>2</sub> Atomic Layer Deposition Using HfCl<sub>4</sub>/H<sub>2</sub>O: The First Reaction Cycle. *ECS Trans.* **16**, 257–267 (2019).
107. Simões, M., Baranton, S. & Coutanceau, C. Electro-oxidation of glycerol at Pd based nano-catalysts for an application in alkaline fuel cells for chemicals and energy cogeneration. *Appl. Catal. B Environ.* **93**, 354–362 (2010).
108. Taoufik, M. *et al.* Alumina supported tungsten hydrides, new efficient catalysts for alkane metathesis. in *Topics in Catalysis* **40**, 65–70 (2006).
109. Le Roux, E. *et al.* Development of Tungsten-Based Heterogeneous Alkane Metathesis Catalysts Through a Structure-Activity Relationship. *Angew. Chemie Int. Ed.* **44**, 6755–6758 (2005).
110. Merle, N. *et al.* On the track to silica-supported tungsten oxo metathesis catalysts: Input from <sup>17</sup>O solid-state NMR. *Inorg. Chem.* **52**, 10119–10130 (2013).
111. Rhers, B. *et al.* A Well-Defined, Silica-Supported Tungsten Imido Alkylidene Olefin Metathesis Catalyst. *Organometallics* **25**, 3554–3557 (2006).
112. Chisholm, M. H. *et al.* Chemistry of Compounds Containing Metal-to-Metal Triple Bonds between Molybdenum and Tungsten. *Acc. Chem. Res.* **11**, 356–362 (1978).
113. Putkonen, M. & Niinistö, L. Organometallic Precursors for Atomic Layer Deposition. *Precursor Chem. Adv. Mater.* 125–145 (2005). doi:10.1007/b136145
114. Song, J. G. *et al.* Layer-controlled, wafer-scale, and conformal synthesis of tungsten disulfide nanosheets using atomic layer deposition. *ACS Nano* **7**, 11333–11340 (2013).
115. Persson, C. & Andersson, C. WCl<sub>4</sub>(DME): A Facile Entry into Bis(cyclopentadienyl) Complexes of Tungsten(IV). Synthesis of Bis(cyclopentadienyl)tungsten Dihydride. *Organometallics* **12**, 2370–2371 (1993).
116. Mark L. Listemann, John C. Dewan, R. R. S. Monomeric Tungsten(IV) Phenoxide and Thiolate Complexes. *J. Am. Chem. Soc.* **107**, 7207–7208 (1985).
117. IJsselstijn M. *Synthesis of Conformationally Restricted β-Turn Mimics*. (Ponsen & Looijen BV, 2006).
118. Samantaray, M. K. *et al.* WMe<sub>6</sub> Tamed by Silica: ≡Si–O–WMe<sub>5</sub> as an Efficient, Well-Defined Species for Alkane Metathesis, Leading to the Observation of a Supported W–Methyl/Methylidyne Species. *J. Am. Chem. Soc.* **136**, 1054–1061 (2014).
119. Kleinhenz, S., Pfennig, V. & Seppelt, K. Preparation and Structures of [W(CH<sub>3</sub>)<sub>6</sub>], [Re(CH<sub>3</sub>)<sub>6</sub>], [Nb(CH<sub>3</sub>)<sub>6</sub>]<sup>-</sup>, and [Ta(CH<sub>3</sub>)<sub>6</sub>]<sup>-</sup>. *Chem. A Eur. J.* **4**, 1687–1691 (1998).
120. Schrock, R. R. *et al.* Tungsten(VI) Neopentylidyne Complexes. *Organometallics* **1**, 1645–1651 (1982).
121. Mattinen, M. *et al.* Crystalline tungsten sulfide thin films by atomic layer deposition and mild annealing. *J. Vac. Sci. Technol. A* **37**, 020921 (2019).
122. Balasubramanyam, S. *et al.* Plasma-enhanced atomic layer deposition of tungsten oxide thin films using (<sup>t</sup>BuN)<sub>2</sub> (Me<sub>2</sub>N)<sub>2</sub>W and O<sub>2</sub> plasma. *J. Vac. Sci. Technol. A Vacuum, Surfaces, Film.* **36**, 01B103 (2018).

123. Becker, J. S. & Gordon, R. G. Diffusion barrier properties of tungsten nitride films grown by atomic layer deposition from bis(tert-butylimido)bis(dimethylamido)tungsten and ammonia. *Appl. Phys. Lett.* **82**, 2239–2241 (2003).
124. Becker, J. S., Suh, S., Wang, S. & Gordon, R. G. Highly Conformal Thin Films of Tungsten Nitride Prepared by Atomic Layer Deposition from a Novel Precursor. *Chem. Mater.* **15**, 2969–2976 (2003).
125. Ikeda, Y. & Ueno, K. Low-temperature growth of crystalline tungsten disulfide thin films by using organic liquid precursors. *Jpn. J. Appl. Phys.* **59**, (2020).
126. Hai, Z. *et al.* Nano-thickness dependence of supercapacitor performance of the ALD-fabricated two-dimensional WO<sub>3</sub>. *Electrochim. Acta* **246**, 625–633 (2017).
127. Sowa, M. J., Yemane, Y., Prinz, F. B. & Provine, J. Plasma-enhanced atomic layer deposition of tungsten nitride. *J. Vac. Sci. Technol. A Vacuum, Surfaces, Film.* **34**, 1–7 (2016).
128. Dasgupta, N. P., Meng, X., Elam, J. W. & Martinson, A. B. F. Atomic Layer Deposition of Metal Sulfide Materials. *Acc. Chem. Res.* **48**, 341–348 (2015).
129. Ho, T. A. *et al.* Edge-On MoS<sub>2</sub> Thin Films by Atomic Layer Deposition for Understanding the Interplay between the Active Area and Hydrogen Evolution Reaction. *Chem. Mater.* **29**, 7604–7614 (2017).
130. Kwon, D. H., Jin, Z., Shin, S., Lee, W. S. & Min, Y. S. A comprehensive study on atomic layer deposition of molybdenum sulfide for electrochemical hydrogen evolution. *Nanoscale* **8**, 7180–7188 (2016).
131. Kang, K. *et al.* High-mobility three-atom-thick semiconducting films with wafer-scale homogeneity. *Nature* **520**, 656–660 (2015).
132. Chisholm, M. H., Cotton, F. A., Extine, M. & Stults, B. R. The Tungsten-Tungsten Triple Bond. 1. Preparation, Properties, and Structural Characterization of Hexakis(dimethylamido)ditungsten(III) and Some Homologues. *J. Am. Chem. Soc.* **98**, 4477–4485 (1976).
133. Gauvin, R. M. *et al.* A well-defined silica-supported dinuclear tungsten(III) amido species: synthesis, characterization and reactivity. *Dalt. Trans.* 3127–3130 (2007). doi:10.1039/B708356B
134. Chisholm H. Malcolm & Martin D. James. Hexakis(dimethylamido)ditungsten and tungsten (IV) chloride. *Inorg. Synth.* **29**, 137–140 (1992).
135. Cadot, S. Élaboration de monocouches de dichalcogénures de métaux de transition du groupe (VI) par chimie organométallique de surface. (2017).
136. Quadrelli, E. A. & Basset, J. M. On silsesquioxanes' accuracy as molecular models for silica-grafted complexes in heterogeneous catalysis. *Coordination Chemistry Reviews* **254**, 707–728 (2010).
137. DuBois, D. L., Miller, W. K. & DuBois, M. R. Kinetic Studies and a Molecular Orbital Interpretation of Reactions at Bridging Sulfur Ligands in Dimeric Molybdenum Complexes. *J. Am. Chem. Soc.* **103**, 3429–3436 (1981).
138. Feng, Q. *et al.* Oxidative-addition reactions of [W<sub>2</sub>(η-C<sub>5</sub>H<sub>4</sub>R)<sub>2</sub>X<sub>4</sub>] (R = Pr<sup>i</sup> or Me; X = Cl or Br): reversible addition of dihydrogen to a tungsten–tungsten triple bond and X-ray crystal structures of [W<sub>2</sub>(η-C<sub>5</sub>H<sub>4</sub>Pr<sup>i</sup>)<sub>2</sub>Cl<sub>4</sub>(μ-H)(μ-PPh<sub>2</sub>)] and [W<sub>2</sub>(η-C<sub>5</sub>H<sub>4</sub>Pr<sup>i</sup>)<sub>2</sub>Cl<sub>3</sub>(μ-Cl)(μ-H)(μ-

- PPh<sub>2</sub>(PMe<sub>3</sub>)]\*. *J. Chem. Soc., Dalt. Trans.* 1397–1406 (1991). doi:10.1039/DT9910001397
139. Chisholm, M. H., Corning, J. F., Folting, K. & Huffman, J. C. Triple bonds between molybdenum and tungsten atoms supported by thiolate ligands: (RS)<sub>3</sub>M≡M(SR)<sub>3</sub>. *Polyhedron* **4**, 383–390 (1985).
  140. Hadži, D. & Prevošek, D. Infra-red absorption bands associated with the NH group-III\* Hydroxamic acids and derivatives. *Spectrochim. Acta* **10**, 21–37 (1957).
  141. Flett, M. S. C. Studies of the band near 3 μ in some hydroxy compounds. *Spectrochim. Acta* **10**, 21–37 (1957).
  142. Camp, C. *et al.* Two-electron versus one-electron reduction of chalcogens by uranium(iii): Synthesis of a terminal U(v) persulfide complex. *Chem. Sci.* **5**, 841–846 (2014).
  143. Vanin, A. F., Vasilyeva, S. V., Streltsova, D. A. & Mikoyan, V. D. EPR Characterization of Mononuclear Dinitrosyl Iron Complex with Persulfide as a New Representative of Dinitrosyl Iron Complexes in Biological Systems: An Overview. *Applied Magnetic Resonance* **45**, 375–387 (2014).
  144. Kan, B.-C., Boo, J.-H., Lee, I. & Zaera, F. Thermal Chemistry of Tetrakis(ethylmethanimido)titanium on Si(100) Surfaces †. *J. Phys. Chem. A* **113**, 3946–3954 (2009).
  145. Bouman, M. & Zaera, F. Reductive eliminations from amido metal complexes: Implications for metal film deposition. *J. Electrochem. Soc.* **158**, (2011).
  146. Zaera, F. The surface chemistry of atomic layer depositions of solid thin films. *Journal of Physical Chemistry Letters* **3**, 1301–1309 (2012).
  147. He, J., Hummer, K. & Franchini, C. Stacking effects on the electronic and optical properties of bilayer transition metal dichalcogenides MoS<sub>2</sub>, MoSe<sub>2</sub>, WS<sub>2</sub>, and WSe<sub>2</sub>. *Phys. Rev. B - Condens. Matter Mater. Phys.* **89**, 75409 (2014).
  148. Groven, B. *et al.* Two-Dimensional Crystal Grain Size Tuning in WS<sub>2</sub> Atomic Layer Deposition: An Insight in the Nucleation Mechanism. *Chem. Mater.* **30**, 7648–7663 (2018).
  149. Sundaram, G. Laser-assisted atomic layer deposition of 2D metal chalcogenide films. *US Patent Office* 1–8 (2015).
  150. Veyre, L. Pumping installation for obtaining a high vacuum and pumping method using such an installation, WO2011FR52547 20111031, Centre National De La Recherche Scientifique - CNRS- ; Universite Lyon 1 Claude Bernard. 1–38 (2012).
  151. Socrates, G. *Infrared and Raman Characteristic Group Frequencies Contents*. (JOHN WILEY & SONS, LTD, 2001).
  152. Sugeta, H. Normal vibrations and molecular conformations of dialkyl disulfides. *Spectrochim. Acta Part A Mol. Spectrosc.* **31**, 1729–1737 (1975).
  153. Bensebaa, F. *et al.* Raman characterization of metal-alkanethiolates. *Spectrochim. Acta - Part A Mol. Biomol. Spectrosc.* **55**, 1229–1236 (1999).
  154. Sushchinskii, M. M. & Rousseau, D. L. Raman Spectra of Molecules and Crystals. *Phys. Today* **26**, 61–62 (1973).
  155. Trofimov, B. A., Sinegovskaya, L. M. & Gusarova, N. K. Vibrations of the S-S bond in elemental sulfur and organic polysulfides: A structural guide. *Journal of Sulfur Chemistry* **30**,

- 518–554 (2009).
156. Bradley, D. C., Chisholm, M. H. & Extine, M. W. Hexakis(dimethylamido)tungsten(VI). *Inorg. Chem.* **16**, 1791–1794 (1977).
  157. Bradley, D. C. & Gitlitz, M. H. Metallo-organic compounds containing metal–nitrogen bonds. Part VI. Infrared and nuclear magnetic resonance of dialkylamidoderivatives of titanium, vanadium, zirconium, niobium, hafnium, tantalum, and thorium. *J. Chem. Soc. A* 980–984 (1969). doi:10.1039/J19690000980
  158. Shirazi, M., Kessels, W. M. M. & Bol, A. A. Initial stage of atomic layer deposition of 2D-MoS<sub>2</sub> on a SiO<sub>2</sub> surface: A DFT study. *Phys. Chem. Chem. Phys.* **20**, 16861–16875 (2018).
  159. McDonald, R. S., Patterson, P., Rodwell, J. & Whalley, A. Intramolecular nucleophilic participation by the thiol group during amide hydrolysis. Part 2. The imidazole catalysis dilemma. *Can. J. Chem.* **70**, 62–67 (1992).
  160. Wu, J. B. *et al.* Correlation between N 1s XPS binding energy and bond distance in metal amido, imido, and nitrido complexes. *Inorg. Chem.* **42**, 4516–4518 (2003).
  161. Stevens, J. S. *et al.* Proton transfer, hydrogen bonding, and disorder: Nitrogen near-edge X-ray absorption fine structure and X-ray photoelectron spectroscopy of bipyridine-acid salts and co-crystals. *Cryst. Growth Des.* **15**, 1776–1783 (2015).
  162. Akiyama, M. *et al.* The Tungsten-Tungsten Triple Bond. 8.<sup>1</sup> Dinuclear Alkoxides of Tungsten(III) and Structural Characterization of Hexaisopropoxybis(pyridine)ditungsten, the First Compound with Four-Coordinated Tungsten Atoms United by a Triple Bond. *Inorg. Chem.* **18**, 2266–2270 (1979).
  163. Bradley, D. C., Chisholm, M. H., Extine, M. W. & Stager, M. E. Some Reactions of Hexakis(dimethylamido)tungsten(VI). *Inorg. Chem.* **16**, 1794–1801 (1977).
  164. Vasilopoulou, M. *et al.* Hydrogenated under-stoichiometric tungsten oxide anode interlayers for efficient and stable organic photovoltaics. *J. Mater. Chem. A* **2**, 1738–1749 (2014).
  165. Ghorbani-Choghamarani, A., Nikoorazm, M., Goudarziafshar, H., Shokr, A. & Almasi, H. Metal-free oxidative coupling of thiols to disulfides using guanidinium nitrate or nitro urea in the presence of silica sulfuric acid. *J. Chem. Sci.* **123**, 453–457 (2011).
  166. Salehi, P., Farrokhi, A. & Gholizadeh, M. Oxidative coupling of thiols by pyridinium chlorochromate in solution and solvent free conditions. *Synth. Commun.* **31**, 2777–2781 (2001).
  167. Benoist, L. *et al.* X-ray photoelectron spectroscopy characterization of amorphous molybdenum oxysulfide thin films. *Thin Solid Films* **258**, 110–114 (1995).
  168. Roux, E. Le *et al.* Well-defined surface tungstenocarbene complexes through the reaction of [W(≡C<sup>t</sup>Bu)(CH<sub>2</sub>tBu)<sub>3</sub>] with silica. *Organometallics* **24**, 4274–4279 (2005).
  169. Novak, I., Kovač, B. & Jokić, M. Electronic Structure of Two Precursors for Nanofabrication: [(CH<sub>3</sub>)<sub>3</sub>CN]<sub>2</sub>W[N(CH<sub>3</sub>)<sub>2</sub>]<sub>2</sub> and Ti(NMe<sub>2</sub>)<sub>2</sub>(NEt<sub>2</sub>)<sub>2</sub>. *J. Phys. Chem. A* **118**, 5636–5641 (2014).
  170. Lozano, R., Alarcón, E., Doadrio, A. L. & Doadrio, A. Binuclear tungsten(V) oxo-complexes with 1,1-dithiolate ligands. *Polyhedron* **2**, 435–441 (1983).
  171. Kim, T. & Zaera, F. Surface chemistry of pentakis(dimethylamido)tantalum on Ta surfaces. *J. Phys. Chem. C* **115**, 8240–8247 (2011).

172. Dorneles de Mello, M. *et al.* Phosphonate-Modified UiO-66 Brønsted Acid Catalyst and Its Use in Dehydra-Decyclization of 2-Methyltetrahydrofuran to Pentadienes. *Angew. Chemie - Int. Ed.* **59**, 13260–13266 (2020).
173. Wu, J.-B., Yang, Y.-W., Lin, Y.-F. & Chiu, H.-T. Surface reaction of bis(tertbutylimido)bis(diethylamido)tungsten precursor on Si(100)-(2×1). *J. Vac. Sci. Technol. A Vacuum, Surfaces, Film.* **21**, 1620–1624 (2003).
174. Yu, B., Chan, J. W., Hoyle, C. E. & Lowe, A. B. Sequential thiol-ene/thiol-ene and thiol-ene/thiol-yne reactions as a route to well-defined mono and bis end-functionalized poly(N-isopropylacrylamide). *J. Polym. Sci. Part A Polym. Chem.* **47**, 3544–3557 (2009).
175. Lowe, A. B. Thiol-ene ‘click’ reactions and recent applications in polymer and materials synthesis. *Polymer Chemistry* **1**, 17–36 (2010).
176. Elías, A. L. *et al.* Controlled synthesis and transfer of large-area WS<sub>2</sub> sheets: From single layer to few layers. *ACS Nano* **7**, 5235–5242 (2013).
177. Berkdemir, A. *et al.* Identification of individual and few layers of WS<sub>2</sub> using Raman Spectroscopy. *Sci. Rep.* **3**, 1755 (2013).
178. Liu, C. C. & Maciel, G. E. The fumed silica surface: A study by NMR. *J. Am. Chem. Soc.* **118**, 5103–5119 (1996).
179. Tilli, M. & Haapalinna, A. Properties of silicon. in *Handbook of Silicon Based MEMS Materials and Technologies* 3–17 (Elsevier, 2020). doi:10.1016/B978-0-12-817786-0.00001-3
180. Bergholz, W. & Gilles, D. Impact of research on defects in silicon on the Microelectronic industry. *Phys. Status Solidi Basic Res.* **222**, 5–23 (2000).
181. Chen, L. *et al.* Friction and Tribochemical Wear Behaviors of Native Oxide Layer on Silicon at Nanoscale. *Tribol. Lett.* **65**, 1–8 (2017).
182. Gräf, D., Grundner, M., Schulz, R. & Mühlhoff, L. Oxidation of HF-treated Si wafer surfaces in air. *J. Appl. Phys.* **68**, 5155–5161 (1990).
183. Morita, M., Ohmi, T., Hasegawa, E., Kawakami, M. & Ohwada, M. Growth of native oxide on a silicon surface. *J. Appl. Phys.* **68**, 1272–1281 (1990).
184. Gösele, U. *et al.* Fundamental issues in wafer bonding. *J. Vac. Sci. Technol. A Vacuum, Surfaces, Film.* **17**, 1145–1152 (1999).
185. Eränen, S. *et al.* Thin Films on Silicon. in *Handbook of Silicon Based MEMS Materials and Technologies* 124–205 (Elsevier, 2015). doi:10.1016/B978-0-323-29965-7.00006-3
186. Green, M. L. *et al.* Nucleation and growth of atomic layer deposited HfO<sub>2</sub> gate dielectric layers on chemical oxide (Si-O-H) and thermal oxide (SiO<sub>2</sub> or Si-O-N) underlayers. *J. Appl. Phys.* **92**, 7168–7174 (2002).
187. Thin films on silicon. in *Handbook of Silicon Based MEMS Materials and Technologies* 133–213 (Elsevier, 2020). doi:10.1016/b978-0-12-817786-0.00006-2
188. Morgan, D. J. Core-level spectra of powdered tungsten disulfide, WS<sub>2</sub>. *Surf. Sci. Spectra* **25**, 014002 (2018).
189. Blachnik, R. & Müller, A. The formation of Cu<sub>2</sub>S from the elements II. Copper used in form of foils. *Thermochim. Acta* **366**, 47–59 (2001).

190. Bychkov, P. S. B. С. государственного аэрокосмического университета имени академика М. . Ф. . П. & Vlasov, O. A. Phase Composition Change of Copper Oxides During Sulfidization. *Bull. M.F. Reshetnyov Sib. State Aerosp. Univ.* 43–46 (2006).
191. Hsiao, C. The volatility of metallic sulfides and their treatment by vacuum metallurgy. (1950).
192. Ma, Q., Guo, H., Gordon, R. G. & Zaera, F. Surface chemistry of copper(I) acetamidates in connection with atomic layer deposition (ALD) processes. *Chem. Mater.* **23**, 3325–3334 (2011).
193. Dai, M., Kwon, J., Halls, M. D., Gordon, R. G. & Chabal, Y. J. Surface and interface processes during atomic layer deposition of copper on silicon oxide. *Langmuir* **26**, 3911–3917 (2010).
194. Louro, C., Cavaleiro, A. & Montemor, F. How is the chemical bonding of W-Si-N sputtered coatings? *Surf. Coatings Technol.* **142–144**, 964–970 (2001).
195. Corey, J. Y. Reactions of Hydrosilanes with Transition Metal Complexes. *Chemical Reviews* **116**, 11291–11435 (2016).
196. Jansson, U. Ultra-high vacuum CVD of W and WSi<sub>2</sub> films by Si reduction of WF<sub>6</sub>. *Appl. Surf. Sci.* **73**, 51–57 (1993).
197. Loehr, T. M., Wada, K., Mino, Y., Sanders-Loehr, J. & Matsubara, H. Hydrogen Bonding of Sulfur Ligands in Blue Copper and Iron-Sulfur Proteins: Detection by Resonance Raman Spectroscopy. *Biochemistry* **26**, 8059–8065 (1987).
198. Eckert, S. *et al.* Molecular structures and protonation state of 2-Mercaptopyridine in aqueous solution. *Chem. Phys. Lett.* **647**, 103–106 (2016).
199. Chen, T. Y. *et al.* Comparative study on MoS<sub>2</sub> and WS<sub>2</sub> for electrocatalytic water splitting. *Int. J. Hydrogen Energy* **38**, 12302–12309 (2013).
200. Yun, Y. *et al.* Activation of Tungsten Oxide for Propane Dehydrogenation and Its High Catalytic Activity and Selectivity. *Catal. Letters* **147**, 622–632 (2017).
201. Griffiths, A. J. V & Walther, T. Quantification of carbon contamination under electron beam irradiation in a scanning transmission electron microscope and its suppression by plasma cleaning. *J. Phys. Conf. Ser.* **241**, 012017 (2010).
202. Hoyas, A. M. *et al.* The impact of the density and type of reactive sites on the characteristics of the atomic layer deposited WN<sub>x</sub>C<sub>y</sub> films. *J. Appl. Phys.* **99**, 063515 (2006).
203. Angermann, H., Gref, O. & Stegemann, B. Effect of wet-chemical substrate smoothing on passivation of ultrathin-SiO<sub>2</sub>/n-Si(111) interfaces prepared with atomic oxygen at thermal impact energies. *Cent. Eur. J. Phys.* **9**, 1472–1481 (2011).
204. Neuwald, U., Feltz, A., Memmert, U. & Behm, R. J. Chemical oxidation of hydrogen passivated Si(111) surfaces in H<sub>2</sub>O<sub>2</sub>. *J. Appl. Phys.* **78**, 4131–4136 (1995).
205. Schutte, W. J., De Boer, J. L. & Jellinek, F. Crystal structures of tungsten disulfide and diselenide. *J. Solid State Chem.* **70**, 207–209 (1987).
206. Rahul, T. K., Mohan, M. & Sandhyarani, N. Enhanced Solar Hydrogen Evolution over in Situ Gold-Platinum Bimetallic Nanoparticle-Loaded Ti<sup>3+</sup> Self-Doped Titania Photocatalysts. *ACS Sustain. Chem. Eng.* **6**, 3049–3059 (2018).

207. de Brito, J. F. *et al.* Role of CuO in the modification of the photocatalytic water splitting behavior of TiO<sub>2</sub> nanotube thin films. *Appl. Catal. B Environ.* **224**, 136–145 (2018).
208. Ampelli, C., Tavella, F., Perathoner, S. & Centi, G. Engineering of photoanodes based on ordered TiO<sub>2</sub> nanotube arrays in solar photo-electrocatalytic (PECa) cells. *Chem. Eng. J.* **320**, 352–362 (2017).
209. Chen, Y. *et al.* Two-dimensional nanomaterials for photocatalytic CO<sub>2</sub> reduction to solar fuels. *Sustainable Energy and Fuels* **1**, 1875–1898 (2017).
210. Tahir, M. & Amin, N. S. Advances in visible light responsive titanium oxide-based photocatalysts for CO<sub>2</sub> conversion to hydrocarbon fuels. *Energy Convers. Manag.* **76**, 194–214 (2013).
211. Liang, Y. T., Vijayan, B. K., Gray, K. A. & Hersam, M. C. Minimizing graphene defects enhances titania nanocomposite-based photocatalytic reduction of CO<sub>2</sub> for improved solar fuel production. *Nano Lett.* **11**, 2865–2870 (2011).
212. Shibata, T. *et al.* Comparison of photochemical properties of brookite and anatase TiO<sub>2</sub> films. *Phys. Chem. Chem. Phys.* 1359–1362 (2004). doi:10.1039/b315777f
213. Saboo, T. Surface organometallic chemistry on Titania. (2019).
214. Dufour, P. *et al.* Surface Organometallic Chemistry: Reaction of Tris-Allyl Rhodium with Surfaces of Silica, Alumina, Titania and Magnesia. *J. Am. Chem. Soc.* **114**, 4248–4257 (1992).
215. Guzman, J., Kuba, S., Fierro-Gonzalez, J. C. & Gates, B. C. Formation of gold clusters on TiO<sub>2</sub> from adsorbed Au(CH<sub>3</sub>)<sub>2</sub>(C<sub>5</sub>H<sub>7</sub>O<sub>2</sub>): Characterization by X-ray absorption spectroscopy. *Catal. Letters* **95**, 77–86 (2004).
216. Grasser, S., Haeßner, C., Köhler, K., Lefebvre, F. & Basset, J. M. Structures of paramagnetic V<sup>IV</sup> amido complexes grafted onto metal oxide surfaces: Model systems for heterogeneous vanadium catalysts. *Phys. Chem. Chem. Phys.* **5**, 1906–1911 (2003).
217. Devi, L. G. & Kavitha, R. A review on non metal ion doped titania for the photocatalytic degradation of organic pollutants under UV/solar light: Role of photogenerated charge carrier dynamics in enhancing the activity. *Appl. Catal. B Environ.* **140–141**, 559–587 (2013).
218. Di Paola, A., Bellardita, M., Ceccato, R., Palmisano, L. & Parrino, F. Highly active photocatalytic TiO<sub>2</sub> powders obtained by thermohydrolysis of TiCl<sub>4</sub> in water. *J. Phys. Chem. C* **113**, 15166–15174 (2009).
219. Xiong, Y., He, D., Jaber, R., Cameron, P. J. & Edler, K. J. Sulfur-Doped Cubic Mesoporous Titania Films for Use as a Solar Photocatalyst. *J. Phys. Chem. C* **121**, 9929–9937 (2017).
220. Kachina, A. *et al.* A new approach to the preparation of nitrogen-doped titania visible light photocatalyst. *Chem. Mater.* **24**, 636–642 (2012).
221. Ma, T., Akiyama, M., Abe, E. & Imai, I. High-efficiency dye-sensitized solar cell based on a nitrogen-doped nanostructured titania electrode. *Nano Lett.* **5**, 2543–2547 (2005).
222. Voiry, D. *et al.* The role of electronic coupling between substrate and 2D MoS<sub>2</sub> nanosheets in electrocatalytic production of hydrogen. *Nat. Mater.* **15**, 1003–1009 (2016).
223. Nguyen, T. P. *et al.* Transition Metal Disulfide Nanosheets Synthesized by Facile Sonication

- Method for the Hydrogen Evolution Reaction. *J. Phys. Chem. C* **120**, 3929–3935 (2016).
224. Messias, S., Nunes da Ponte, M. & S. Reis-Machado, A. Carbon Materials as Cathode Constituents for Electrochemical CO<sub>2</sub> Reduction—A Review. *C — J. Carbon Res.* **5**, 83 (2019).
  225. Genovese, C., Ampelli, C., Perathoner, S. & Centi, G. Electrocatalytic conversion of CO<sub>2</sub> on carbon nanotube-based electrodes for producing solar fuels. *J. Catal.* **308**, 237–249 (2013).
  226. Genovese, C., Ampelli, C., Perathoner, S. & Centi, G. A Gas-phase Electrochemical Reactor for Carbon Dioxide Reduction back to Liquid Fuels. in **32**, (2013).
  227. Marepally, B. C. *et al.* Enhanced formation of >C1 Products in Electroreduction of CO<sub>2</sub> by Adding a CO<sub>2</sub> Adsorption Component to a Gas-Diffusion Layer-Type Catalytic Electrode. *ChemSusChem* **10**, 4442–4446 (2017).
  228. Asadi, M. *et al.* Nanostructured transition metal dichalcogenide electrocatalysts for CO<sub>2</sub> reduction in ionic liquid. *Science (80-. )*. **353**, 467–470 (2016).
  229. Hirsch, A. Functionalization of single-walled carbon nanotubes. *Angewandte Chemie - International Edition* **41**, 1853–1859 (2002).
  230. Banerjee, S., Hemraj-Benny, T. & Wong, S. S. Covalent surface chemistry of single-walled carbon nanotubes. *Advanced Materials* **17**, 17–29 (2005).
  231. Peng, Q., Spagnola, J. C., Daisuke, H., Park, K. J. & Parsons, G. N. Conformal metal oxide coatings on nanotubes by direct low temperature metal-organic pyrolysis in supercritical carbon dioxide. *J. Vac. Sci. Technol. B Microelectron. Nanom. Struct.* **26**, 978 (2008).
  232. Wang, C. *et al.* Proton Exchange Membrane Fuel Cells with Carbon Nanotube Based Electrodes. *Nano Lett.* **4**, 345–348 (2004).
  233. Eder, D. & Windle, A. H. Carbon-inorganic hybrid materials: The carbon-nanotube/TiO<sub>2</sub> interface. *Adv. Mater.* **20**, 1787–1793 (2008).
  234. Lee, J. S. *et al.* Al<sub>2</sub>O<sub>3</sub> nanotubes and nanorods fabricated by coating and filling of carbon nanotubes with atomic-layer deposition. *J. Cryst. Growth* **254**, 443–448 (2003).
  235. Atkin, P. *et al.* 2D WS<sub>2</sub>/carbon dot hybrids with enhanced photocatalytic activity. *J. Mater. Chem. A* **4**, 13563–13571 (2016).
  236. Ampelli, C. *et al.* Analysis of the factors controlling performances of Au-modified TiO<sub>2</sub> nanotube array based photoanode in photo-electrocatalytic (PECa) cells. *J. Energy Chem.* **26**, 284–294 (2017).
  237. Ampelli, C. *et al.* Electrocatalytic conversion of CO<sub>2</sub> to produce solar fuels in electrolyte or electrolyte-less configurations of PEC cells. *Faraday Discuss.* **183**, 125–145 (2015).
  238. Saboo, T. *et al.* Water splitting on 3D-type meso/macro porous structured photoanodes based on Ti mesh. *Sol. Energy Mater. Sol. Cells* **178**, 98–105 (2018).
  239. Ampelli, C., Centi, G., Passalacqua, R. & Perathoner, S. Synthesis of solar fuels by a novel photoelectrocatalytic approach. *Energy Environ. Sci.* **3**, 292–301 (2010).
  240. Tavella, F., Ampelli, C., Leonardi, S. G. & Neri, G. Photo-electrochemical sensing of dopamine by a novel porous TiO<sub>2</sub> array-modified screen-printed Ti electrode. *Sensors (Switzerland)* **18**, 3566 (2018).

241. Li, X. *et al.* A pressure tuned stop-flow atomic layer deposition process for MoS<sub>2</sub> on high porous nanostructure and fabrication of TiO<sub>2</sub>/MoS<sub>2</sub> core/shell inverse opal structure. *Appl. Surf. Sci.* **422**, 536–543 (2017).
242. Jung, K. Y., Park, S. Bin & Anpo, M. Photoluminescence and photoactivity of titania particles prepared by the sol-gel technique: Effect of calcination temperature. *J. Photochem. Photobiol. A Chem.* **170**, 247–252 (2005).
243. Jung, K. Y. & Park, S. Bin. Effect of Calcination Temperature and Addition of Silica, Zirconia, Alumina on the Photocatalytic Activity of Titania. *Korean J. Chem. Eng.* **18**, 879–888 (2001).
244. Wu, H., Ma, J., Zhang, C. & He, H. Effect of TiO<sub>2</sub> calcination temperature on the photocatalytic oxidation of gaseous NH<sub>3</sub>. *J. Environ. Sci. (China)* **26**, 673–682 (2014).
245. Junge Puring, K. *et al.* Electrochemical CO<sub>2</sub> Reduction: Tailoring Catalyst Layers in Gas Diffusion Electrodes. *Adv. Sustain. Syst.* 2000088 (2020). doi:10.1002/adsu.202000088